DISSERTATION

DESIGN AND TESTING OF A NEW AIRCRAFT-BASED CLOUD WATER SAMPLING SYSTEM

Submitted by

Derek J. Straub

Department of Atmospheric Science

In partial fulfillment of the requirements

for the Degree of Doctor of Philosophy

Colorado State University

Fort Collins, CO

Fall 2002

ProQuest Information and Learning Company
300 North Zeeb Road
P.O. Box 1346
Ann Arbor, MI 48106-1346

COLORADO STATE UNIVERSITY

August 6, 2002

WE HEREBY RECOMMEND THAT THE DISSERTATION PREPARED UNDER OUR SUPERVISION BY DEREK J. STRAUB ENTITLED DESIGN AND TESTING OF A NEW AIRCRAFT-BASED CLOUD WATER SAMPLING SYSTEM BE ACCEPTED AS FULFILLING IN PART REQUIREMENTS FOR THE DEGREE OF DOCTOR OF PHILOSOPHY.

Committee on Graduate Work

Adviser

Department Head/Director

ABSTRACT OF DISSERTATION

DESIGN AND TESTING OF A NEW
AIRCRAFT-BASED CLOUD WATER SAMPLING SYSTEM

Experimental studies of cloud processing mechanisms necessitate the collection of representative samples of cloud water for chemical analysis. In order to provide samples from clouds that are inaccessible from ground-based sampling stations, a new aircraft-based cloud water collection system has been developed. The objective of the design process was to produce an automated collector that can acquire well-characterized cloud water samples and is portable between multiple research aircraft. Issues such as cloud drop shatter and re-entrainment, structural integrity, system size and weight, material compatibility with the anticipated chemical analyses, and ease of use during field operation were all considered during the design process. The new cloud water collection system utilizes an axial-flow cyclone to centrifugally separate cloud drops from the air stream. Up to seven individual samples can be stored over the course of a single research flight.

An analysis of the axial-flow cyclone was performed with a finite volume based computational fluid dynamics (CFD) code. Solutions were obtained for air flow patterns and cloud drop trajectories. The predicted continuous phase (air) velocity field indicates that the axial-flow cyclone generates a strong rotational flow field with a tangential velocity of 85 m s^{-1}. Based on simulations of cloud drop trajectories, centrifugal force in the rotational flow field is sufficient to quickly move entrained cloud drops to the wall of the axial-flow cyclone duct where they can be removed for storage. Collection efficiency as a function of drop size was ascertained

and the 50% cut diameter was determined to be approximately 8 microns. An experimental laboratory calibration involving monodisperse fluorescein-tagged drops verified the numerical modeling results.

The system was deployed during the Dynamics and Chemistry of Marine Stratocumulus, Phase II (DYCOMS-II) field project in July 2001. The DYCOMS-II campaign served as a testing and evaluation program for the system as well as an opportunity to study the chemical composition of stratocumulus clouds in the remote marine environment. Over the course of the project, 50 samples were obtained during seven nighttime and two daytime flights. Sample pH was measured on-site after each flight. Peroxide, formaldehyde, S(IV), trace metals and major ions (Cl^-, NO_3^-, SO_4^{2-}, Na^+, NH_4^+, K^+, Ca^{2+}, and Mg^{2+}) were preserved on site and analyzed after the field campaign. The analyses were used to characterize the composition of the sampled clouds and to investigate cloud processing mechanisms, including the potential for rapid aqueous phase oxidation of S(IV) to sulfate.

Derek J. Straub
Atmospheric Science Department
Colorado State University
Fort Collins, CO 80523
Fall 2002

ACKNOWLEDGMENTS

I would first like to express my gratitude to my advisor, Professor Jeffrey Collett, for his guidance and support throughout my time as a Ph.D. candidate. I appreciate the time he invested in this project and the many valuable contributions he made which resulted in a considerably stronger dissertation. I would also like to thank Darrel Baumgardner for initiating the development of a new aircraft-based cloud water collector and promoting it as a viable project for my Ph.D. research. I am grateful to my committee members, Sonia Kreidenweis, Richard Johnson, Robert Meroney, and David Rogers, for taking the time to evaluate my progress and for sharing their insightful comments and suggestions. Above all else, I am thankful for the encouragement and patience of my wife Kathy, and for the ever present support of my family.

The development of a new aircraft-based instrument, from conceptual design to operational status, can not be completed without significant contributions from others. I would first like to acknowledge the assistance of Jack Fox and the rest of NCAR's Design and Fabrication Services staff. Their expertise in the areas of aircraft instrumentation, materials selection, fabrication techniques, and mechanical design was a principal factor in the on-time completion of a high quality, fully operational instrument. I would like to specifically thank Steve Rauenbuehler for his many hours of dedicated work and for his ingenious solutions to the various design problems that we encountered. I am grateful to Dean Lauritsen for supplying a critical LabVIEW subroutine for the data acquisition system and to Errol Korn for his knowledgeable answers to all of my LabVIEW and data acquisition questions. The successful operation of the electronics in the collection system can largely be attributed to the advice and guidance of Dave McFarland, who also loaned all the required equipment for electronic systems development and testing. I would like to thank Bill Irwin and Kurt Zrubek for their assistance in

integrating the new cloud water collection system onto the NSF/NCAR C-130 aircraft in time for the DYCOMS-II field project. Brent Kidd and Kip Eagan offered valuable guidance in the RAF machine shop. Over the course of my time at NCAR, Ron Ruth and the ATD systems administrators offered much needed computer support.

Wind tunnel testing and laboratory evaluation of the new cloud water collection system was performed with equipment loaned from various sources. The Atmospheric Technology Division (ATD) made the NCAR low speed wind tunnel facility available for testing purposes at no charge. Jim Dye supplied a water drop generation system and generously allowed its complete disassembly. Al Cooper and the Advanced Study Program provided lab space and various pieces of equipment required for wind tunnel testing and flow meter calibration. For the quantitative laboratory calibration of the axial-flow cyclone, Sonia Kreidenweis offered the use of the Vibrating Orifice Aerosol Generator (VOAG) and Jeff Collett supplied a wide range of equipment, from blowers and flow meters to the microscope imaging system.

I am also indebted to many individuals for their help before, during, and after my participation in the DYCOMS-II field campaign. Taehyoung Lee deserves special recognition for volunteering a considerable amount of his time to conduct the IC and TOC analyses of the DYCOMS-II cloud water samples. I would also like to express my gratitude to Hui Chang for completing the trace metal analysis. The efforts of Bjorn Stevens and Don Lenshow in organizing and executing the DYCOMS-II mission should be acknowledged. Their hard work was a major factor in the success of the field project. The logistical planning of Krista Laursen and Dick Friesen further contributed to the overall success of the DYCOMS-II field project. Their efforts also paved the way for a smooth and trouble free initial deployment of the cloud water collection system during DYCOMS-II. I would also like to acknowledge Jeff Stith and the rest of the RAF staff for operating the large suite of microphysical and meteorological instrumentation aboard the C-130 during the DYCOMS-II field project. Data from many of those

instruments have been used in this dissertation to aid in the interpretation of DYCOMS-II cloud water solute composition.

Finally, I am grateful to Al Cooper and the Advanced Study Program (ASP) for financial support offered through an ASP Graduate Fellowship. The ASP also contributed financially to the fabrication of the cloud water collector hardware. Additional financial support for the development of the new cloud water collection system was provided by the National Science Foundation (ATM-0084696).

TABLE OF CONTENTS

LIST OF FIGURES

LIST OF TABLES

1 Introduction

This dissertation describes the design, operation, evaluation, and deployment of a new cloud water collection system. The collection system was developed to obtain samples of cloud water from an aircraft platform for chemical analysis. This introductory chapter will focus on the motivating factors that led to the development of the collector, including the importance of clouds in the atmospheric system and the limitations of previous cloud water sampling instrumentation. In this chapter the objectives of this project will also be presented and the content of the remaining chapters will be briefly summarized.

1.1 Interactions between cloud drops, aerosol particles, and trace gases

Cloud drops interact with atmospheric aerosol particles and trace gases through a variety of mechanisms, not all of which are fully understood. Cloud drops form through heterogeneous nucleation on aerosol particles at atmospherically relevant supersaturations (Pruppacher and Klett, 1997). The subset of aerosol particles that are capable of nucleation at a given supersaturation are referred to as cloud condensation nuclei (CCN). The concentration of cloud drops that form in a rising parcel of air has been reliably predicted from direct measurements of sub-cloud CCN number concentration and updraft velocity measurements (Snider and Brenguier, 2000; Yum et al., 1998). However, the relationship between the total aerosol population and the subset that acts as CCN, which is a function of both aerosol size and composition, is not as well established. Predictions of CCN number concentration that are based on measured aerosol physical and chemical properties and Kohler theory have been found to sometimes disagree with measured CCN concentrations (Chuang et al., 2000; Covert et al., 1998; Bigg, 1986; Gras, 1995). The cause of these discrepancies remain an outstanding issue and may be attributable to

instrumentation limitations, uptake of soluble gases, or aerosol composition effects, such as the presence of organic species, which are not considered by theory (Feingold and Chuang, 2002; Stevens et al., 2002; Charlson et al., 2001; Chuang et al., 2000).

After cloud formation, cloud drops can modify the environment in a number of ways. Cloud drop collision-coalescence processes and aerosol scavenging through Brownian motion and inertial impaction tend to redistribute aerosol mass as multiple aerosol particles are combined into single cloud drops. In non-precipitating clouds, which have been estimated to account for 90% of all clouds (Seinfeld and Pandis, 1998), cloud drop evaporation yields aerosol particles on a 1:1 basis (Mitra et al., 1992; Hudson and Frisbie, 1991). Therefore, collision-coalescence and scavenging processes result in the depletion of aerosol number and a related increase in the mean particle diameter while conserving total aerosol mass (Flossman, 1994; Feingold et al., 1996).

Cloud drops can also act to generate aerosol mass, most notably through the absorption of gas phase SO_2 followed by oxidation to non-volatile sulfate. Karamchandani and Venkatram (1992) have estimated that in-cloud oxidation is responsible for 40 – 90% of sulfate production in the summer stratus clouds they studied. Lelieveld and Heintzenberg (1992) propose that 80 – 90% of total sulfur dioxide to sulfate conversion occurs in the aqueous phase. In non-precipitating clouds, the in-cloud production of sulfate tends to increase total aerosol mass while preserving total number concentration. Mass addition due to aqueous phase sulfate production has been measured in laboratory experiments (Hoppel et al., 1994) and field studies (Husain et al., 2000; 1989; Rattigan et al., 2001; Reilly et al., 2001; Birmili et al., 1999; Liu et al., 1993; Hegg and Hobbs, 1988; 1986) and predicted in modeling studies (Bower and Choularton, 1993; Feingold et al., 1998). Sulfate production tends to acidify cloud drops, as can the absorption of gas phase nitric acid and other acidic gas phase species.

The processes that occur over the lifetime of a non-precipitating cloud can significantly modify the aerosol chemical composition and size distribution. Observed bimodal size distributions in marine environments have been attributed to a combination of aerosol mass

redistribution and production affecting activated CCN (Hoppel et al., 1986; Garrett and Hobbs, 1995; Birmili et al., 1999). The modification of aerosol particles through cloud processing has a number of implications. Alteration of the CCN spectrum can influence the formation, lifetime, and precipitation rate of clouds in subsequent cloud cycles (Zhang et al., 1999; Feingold et al., 1998; Bower and Choularton, 1993). In addition, cloud processing may affect radiative forcing directly due to changes in aerosol scattering properties and indirectly due to changes in cloud albedo as modified aerosols participate in future cloud formation (Boucher and Lohmann, 1995; Jones et al., 1994; Charlson et al., 1991; Twomey, 1991; 1977; 1974).

Cloud drops that become incorporated into precipitation can be removed from the atmosphere along with trace species previously scavenged by, or produced in, the drops (Xu et al., 1998; Collett et al., 1991a; Borys et al., 1988). This is the dominant removal method for accumulation mode aerosol particles. Wet removal of acidic species, such as sulfate, nitrate, and organic acids can lead to stream and lake acidification to the detriment of vegetation and aquatic life (e.g. Mason, 1992). In addition, the removal of trace species through direct deposition of fog drops to ground surfaces can be important in locations that frequently experience fog episodes (Collett et al., 2002a; 1991b; Lillis et al., 1999; Bergin et al., 1996; Fuzzi et al., 1985).

The homogeneous production of sulfuric acid particles (Hegg et al., 1990; Hegg, 1990) and the vertical transport of trace species (Donnell, et al., 2001; Dickerson et al., 1987) have also been attributed to the presence of clouds, although not as a direct result of condensed phase cloud processes.

1.2 Cloud water sampling and instrument limitations

In an effort to examine cloud drop interactions with aerosol particles and trace gases, including cloud drop formation mechanisms and the role of clouds as processors of trace species, a wide range of instrumentation has been developed to capture samples of cloud water for chemical characterization. Numerous ground-based cloud water samplers have been documented

in the literature (Moore, 2001). Although ground-based samplers have provided a wealth of information related to cloud water characterization and cloud processing, their use is limited to the collection of fogs and clouds that are accessible at the surface, from towers, or from high elevation sites.

As an alternative, researchers have turned to aircraft to extend sampling capabilities to include cloud types and environments not accessible from ground-based sampling stations. Thus, the development of aircraft-based instrumentation has progressed through the years, although not to the same extent as ground-based samplers. Historically, the most widely used aircraft-based cloud water samplers have been slotted-rod collectors (e.g. Winters et al., 1979; Daum et al., 1984a; 1984b; Huebert et al., 1988). Although several different configurations have been developed, these devices typically consist of multiple cylindrical Teflon or Delrin rods, each having a slot at its forward stagnation point. The rods are mounted on the aircraft fuselage and extend into the airstream during flight. As air flows around the cylinders, cloud drops having sufficient inertia deviate from the air streamlines and are collected through inertial impaction. The accumulated drops then coalesce on the inner surface of the slot and flow under the influence of gravity and aerodynamic drag into a sample container. Cloud water samples obtained with slotted-rod collectors have been used to examine cloud drop scavenging of sulfate and nitrate, aqueous phase sulfate production, CCN characteristics, partitioning of species between the gas and aqueous phases, and other topics. A full review of the design and operation of slotted-rod collectors, along with other aircraft-based cloud water collectors, will be provided in Chapter 2.

Although aircraft-based collectors have been deployed on numerous field projects and have produced useful data for analysis, there are limitations associated with many previous collector designs. As with all aircraft instrumentation, aircraft-based cloud water samplers have to contend with size, weight, and power restrictions, high velocity ambient air flows, rapid variations in temperature and pressure and limited testing and deployment opportunities (Daum and Springston, 1993). These adverse conditions may be responsible, in part, for limitations

associated with aircraft-based cloud water samplers that have been developed to date. A few of these limitations will be discussed in the following sections.

1.2.1 Evaluation of collection characteristics

More often than not, an assessment of the collection characteristics of aircraft-based cloud water collectors has been neglected. The majority of the literature that describes the design and operation of aircraft-based cloud water collectors makes no mention of collection efficiency or else admits that collection efficiency is unknown. Theoretically derived collection efficiency curves or 50% cut diameters are presented occasionally, however, there is little in the way of experimental evidence to support the theoretical predictions. For a few collectors, a bulk collection efficiency is derived from field observations to describe the fraction of total cloud liquid water that is collected. Unfortunately, bulk collection efficiencies do not convey any information about the collection efficiency for individual drop sizes, an important consideration in determining whether or not the population of collected drops is representative of the sampled cloud. If an unidentified subset of the drop population routinely remains uncollected in a bulk sampler, or if an unidentified subset of the drop population is routinely enhanced, cloud water chemical measurements will be biased in an unknown way relative to the sampled cloud. These biases can arise because cloud water chemistry has been found to vary with drop size (e.g. Rao and Collett, 1995, 1998; Bator and Collett, 1997; Laj et al., 1998; Schell et al., 1997; Vong et al., 1997). A quantitative measure of collection efficiency as a function of drop size for a given sampler can identify any collection biases that may exist.

Slotted-rod collectors have been the most frequently used aircraft-based cloud water collectors and have also received the most extensive evaluation through wind tunnel testing and field assessment. Unfortunately, slotted-rod collection efficiencies have been found to be widely variable, even under well-controlled wind tunnel conditions, ranging between 10% and 62%

(Huebert and Baumgardner, 1985). A range of factors were found to influence collection efficiency, in some cases contrary to theory and expectation.

Flight tests have also revealed variability in slotted-rod bulk collection characteristics (Huebert et al., 1988; Kim and Boatman, 1992; Liu et al., 1993), although it remains unclear the extent to which flow field interactions with the aircraft structure contributes to the variations in collection efficiency. At typical research flight speeds of 60–120 m s^{-1}, air streamlines are significantly distorted around the curved surfaces of the airframe, especially the fuselage. Due to their inertia, cloud drops may be unable to follow the distorted streamlines, resulting in regions where cloud drop number concentrations are enhanced or depleted by a factor of two or more (Twohy and Rogers, 1993; Norment, 1988; King, 1984). Huebert and Baumgardner (1985) suggest that airflow/airframe interactions may be responsible for the higher collection efficiency observed during flight operation than their wind tunnel evaluation. Nearly all aircraft-based cloud water collectors are mounted on or near the fuselage of the aircraft where modifications in drop number concentrations may be more severe than wing mount locations (MacPherson and Baumgardner, 1988).

1.2.2 Drop shatter and re-entrainment

Liquid drops that impact on a solid surface with sufficient kinetic energy can shatter and fragment into small secondary drops (e.g. Rein, 1993; Cossali et al., 1997; Stow and Hadfield, 1981). When this occurs in a cloud water collector, the secondary drops may be of small enough size that they can be re-entrained into the airflow rather than collected. Conditions that contribute to drop shatter include high impact velocities and large drop sizes. Because research aircraft necessarily travel at high speeds, those conditions are easily met in inertial impactors that operate at free stream velocities, making the collection of cloud drops from an aircraft platform susceptible to drop shatter.

The effects of drop shatter are rarely discussed in conjunction with aircraft-based cloud drop collection. However, there is evidence that drop shatter and re-entrainment could significantly affect the collection efficiency of inertial impaction devices. Data from the wind tunnel evaluation of slotted-rod collectors by Huebert and Baumgardner (1985) have suggested that drop shatter and re-entrainment does occur for those collectors. Other inertial impaction type cloud water collectors operating at similar conditions will most likely experience drop shatter and re-entrainment effects as well.

1.2.3 Portability and aircraft structural modifications

Many airborne collectors appear to have been designed for deployment on a particular aircraft for a particular field project (e.g. Parungo et al., 1982; Khemani et al., 1987; Walters et al., 1983; Bogen, 1974). Their mounting structures were therefore not necessarily designed with portability in mind, making it difficult to transfer a single collector from one aircraft to another for use in multiple field projects. In addition, many collectors require a penetration through the fuselage for the purpose of moving the instrument into and out of the airstream or for in-flight sample retrieval (e.g. Winters et al., 1979; Huebert et al., 1988; Isaac and Daum, 1987; Maser et al., 1994; Scott, 1978). Transferring instruments with specialized mounting structures, possibly requiring access through the fuselage wall, to multiple research aircraft can incur high costs for aircraft modification and can raise safety concerns that necessitate air worthiness certification.

1.3 Objectives of this work

To improve upon the limitations of past aircraft-based cloud water collectors, the development of a new aircraft-based cloud water collection system was undertaken. The objective of the design process was to create an instrument capable of providing consistent, well-characterized cloud water samples that can be used to describe the chemical composition of warm-based clouds and ultimately examine cloud processing mechanisms. The system was

intended to have the capacity to store multiple sequential samples per research flight to allow variations in cloud water composition with time or location to be studied.

To extend the applicability of the collection system, portability of the system was an additional priority. By creating a portable system, it was hoped that the collector could be deployed on any of the various atmospheric chemistry and cloud microphysics research aircraft with typical cruising speeds of approximately 120 m s^{-1} or less. Transfer of the collector between research aircraft was intended to be straightforward and require little or no modification of the collection system. As part of this objective, major modifications to the aircraft structure were necessarily avoided, which resulted in the added benefits of reduced costs and safety concerns.

Deployment of the new collection system on an aircraft-based field project comprised the final objective of this project. Participation in a field campaign provided an opportunity to evaluate the system under flight conditions. Verifying the operation of individual mechanical components and assessing the cloud water collection characteristics were both of interest. In addition, it was hoped that samples obtained over the course of the field project could be used to examine cloud water chemistry and cloud processing mechanisms in the study region.

These objectives influenced the choice of collection technique, system layout, mounting technique, and the selection of materials. The objectives further necessitated the use of evaluation techniques to quantify the collection characteristics of the sampling system. These evaluation techniques took the form of computational fluid dynamics (CFD) analysis and experimental calibration, in addition to flight testing during field project deployment. CFD analysis was used extensively throughout the development of the new cloud water collector for component design and to predict internal flow dynamics. In addition, CFD-based cloud drop trajectory simulations provided an estimate of collection efficiency as a function of drop size. Trajectory calculations permitted drop shatter and re-entrainment issues to be addressed in the design phase.

Finally, automation of the collection system became a requirement as the development of the collection system progressed. Due to the mounting location eventually selected for the collection system, direct access to the system was not possible and a remote data acquisition and control system was needed.

1.4 Dissertation format

The remaining chapters of this dissertation describe the work performed for the development, evaluation, and deployment of the new aircraft-based cloud water sampler.

Chapter 2 provides a review of past aircraft-based cloud water collectors. The physical layouts of existing cloud sampling instruments are described individually along with principles of operation, performance evaluation when available, and field use. The review was undertaken to establish the advantages and disadvantages of previous designs and served as a basis from which the new collection system was developed.

Chapter 3 describes the new aircraft-based cloud water collector and provides a detailed account of the design process. This chapter includes descriptions of individual components, system operation, fabrication techniques, and the methodology used in making design choices. Operational procedures for the installation and removal of the collection system are also discussed.

Chapter 4 summarizes the CFD analysis of the cloud water sampler. A brief description of CFD theory and the submodels selected for this work is followed by an account of the flow domain, fluid properties, initial conditions, and boundary conditions. The resulting air flow solution and cloud drop trajectory simulations are reported, as are predictions of collection efficiency, sample collection rates, drop shatter and evaporation.

Chapter 5 details the setup and results of experimental work performed to evaluate the collection characteristics of the new sampler. Qualitative low speed wind tunnel analysis and a quantitative laboratory calibration technique were both employed. The laboratory calibration

revealed drop deposition patterns in the interior of the new sampler and offered a method for verifying the CFD-based trajectory calculations.

Chapter 6 describes the deployment of the cloud water sampler on the Dynamics and Chemistry of Marine Stratocumulus, Phase II (DYCOMS-II) field project. The overall objectives of the mission are recounted along with a description of flight details and the sampling environment. The chemical composition of the collected samples was ascertained through various analytical techniques and interpreted in the context of the supporting aerosol, cloud microphysics, and trace gas measurements.

Chapter 7 provides conclusions that arose from the various aspects of the collector development and recommendations for future improvements of the collection system.

The appendices supply detailed information supporting various topics throughout the dissertation.

2 Review of past aircraft-based cloud water collectors

The quest to sample cloud water from aircraft has led to the development of a variety of instruments, most of which rely on one of two primary collection techniques: inertial impaction and centrifugal separation. Inertial impaction occurs as a stream of cloud drop laden air is deflected by a solid surface such as a flat plate or cylindrical rod (Figure 2.1). While the air streamlines diverge around the surface, cloud drops larger than a critical size are unable to follow due to their inertia, causing them to impact on the surface where they accumulate and can be removed for analysis. Ideally, all drops larger than the critical diameter are captured and all drops smaller than the critical diameter remain with the airstream.

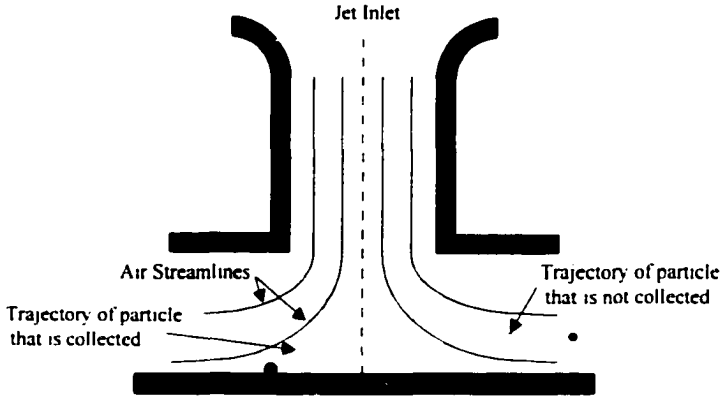

Figure 2.1. Trajectories of collected and uncollected particles in an inertial impactor. An aircraft mounted inertial impactor can take advantage of the forward motion of the aircraft to generate air flow past the impaction surface.

Centrifugal separation relies on a rotational flow field to separate cloud drops from the airstream. Typically, vanes extending outward from a central hub actively or passively interact with the air stream to generate a rotating air flow field in which centrifugal force acts on

entrained cloud drops to move them to a collection surface. Again, the accumulated water is removed from the collection surface for analysis.

In either case, the efficiency with which drops are collected generally varies as a function of drop size. A collection efficiency curve is usually employed to describe the variation of collection efficiency with drop size, and the drop diameter associated with a collection efficiency of 50% is referred to as the 50% cut diameter, or Dp_{50}. The 50% cut diameter is intended to identify the delineation between larger cloud drops that are collected and smaller drops that are not, although inevitably some fraction of drops smaller then the 50% cut diameter will be captured and some drops larger than the 50% cut diameter will remain uncollected.

In this chapter, the design, operation, and collection characteristics of aircraft-based cloud water samplers that have been used on a range of research aircraft and in a variety of environments will be reviewed.

2.1 Slotted-rod collectors

The most common instrument for collecting warm-based cloud water samples from an aircraft platform has been the slotted-rod collector, which employs inertial impaction as the collection mechanism. The first slotted-rod collector intended for aircraft installation was developed at the State University of New York (SUNY) – Albany (Winters et al., 1979; Mohnen, 1980, Tanner, 1987). The collector consisted of seven 0.95 cm diameter cylindrical rods arranged in two rows with 0.95 cm spacing between rods (Figure 2.2). The rods were mounted vertically on the exterior of the airframe, perpendicular to the airflow. Each of the rods incorporated a 2 mm wide and 4 mm deep slot into its forward stagnation point to allow cloud drops that impact on the rod to accumulate rather than being swept off the rod. Cloud water flowed down the slot under the influence of gravity until it reached the base of the collector. There, Teflon tubing transported the water into a storage bottle with the aid of a suction flow. The theoretical 50% cut diameter of these slotted-rods was calculated to be approximately 3 μm at 50 m s^{-1} and 2 μm at

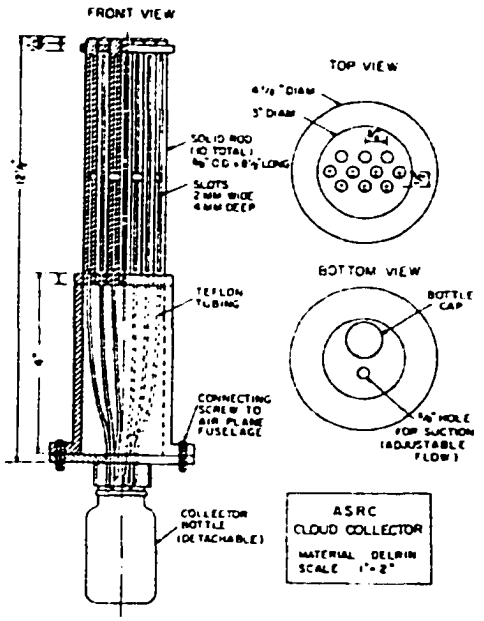

Figure 2.2. The original slotted-rod cloud water collector design (Mohnen, 1980).

100 m s^{-1} (Mohnen, 1980). These collectors, often referred to as Mohnen slotted-rod collectors, have been used on a range of experimental field campaigns.

A series of six aircraft-based field projects conducted by the Atmospheric Environment Service of Canada, with some involvement from Brookhaven National Laboratory, utilized the original slotted-rod collector design to obtain warm and supercooled cloud samples. Over the course of these six field projects, the collectors were flown on two aircraft, a Twin Otter operated by the National Aeronautical Establishment (NAE) of the Canadian National Research Council and a DC-3 operated by the Canada Centre for Remote Sensing. The first of these field campaigns took place in September and October of 1981 over southern Ontario, and yielded 4 cloud water samples. Four of the field projects targeted the North Bay region of central Ontario, covering the periods June-July 1982 (39 samples), January-February 1984 (150 samples), July-August 1988 (113 samples), and March-April 1990 (111 samples). One field project was carried out in the vicinity of Syracuse, New York during October and November, 1984 (92 samples). The aircraft in use during these six field projects supported a similar array of cloud and aerosol

microphysics instrumentation. Generally, the collected cloud water samples were analyzed for pH and major ions, and occasionally H_2O_2.

Details regarding these six related field projects, including cloud water chemical data, were reported in a number of articles in the scientific literature. Depending on the objectives of the authors, various subsets of the six studies were composited and summarized in each article. Leaitch et al. (1986a) investigated the scavenging of sulfate and nitrate and in-cloud sulfate production using the data from the 1981 and 1982 studies. An overview of the 1984 winter study, along with a comparison between cloud water, aircraft collected precipitation, and ground collected precipitation composition was provided by Isaac and Daum (1987). Strapp et al. (1988) also used the 1984 winter data to evaluate the extent to which below cloud soluble aerosol particle and trace gas composition can be used to predict cloud water composition at cloud base. Leaitch et al. (1992) used the data from the 1982, 1984 autumn, 1984 winter, and 1988 studies to examine how cloud drop number concentration is influenced by anthropogenic pollution, and attempted to find and quantify the relationship between cloud drop number concentration and cloud water sulfate concentration. The data from the 1982, 1984 autumn, and 1984 winter studies were composited into a single data set by Isaac et al. (1990) in order to describe the vertical profile of sulfate and nitrate in the study region. Leaitch et al. (1986b) initialized an adiabatic cloud model with data from the 1982, 1984 autumn, and 1984 winter studies in order to compare sulfate concentrations at ground level to those measured at higher altitudes and to determine how well cloud base aerosol particle number concentration can predict cloud drop number concentration. Macdonald et al. (1995) used the data from the 1988 and 1990 flights to examine aqueous and gas phase H_2O_2 behavior and equilibrium. Liu et al. (1993) made use of the 1988 data to examine sulfate production. Couture et al. (1998) applied the data from the 1984 winter, 1984 autumn, 1988, and 1990 studies to compare free tropospheric cloud water samples with cloud water samples obtained from two high elevation ground-based sites in southern Quebec.

While the standard slotted-rod collectors were deployed during periods when warm-based clouds (both cumuliform and stratiform) were present, the winter flights encountered supercooled cloud drops on most occasions. In order to collect cloud drops under these conditions, the rods were allowed to rime followed by retraction of the entire slotted-rod collector into the cabin, where the rimed rods were stored in polyethylene bags until analysis. On several occasions, a 22 cm by 3 cm sheet of polyethylene mesh was attached across the rods to provide a greater surface area for supercooled drops to accumulate upon (Isaac and Daum, 1987) (Figure 2.3).

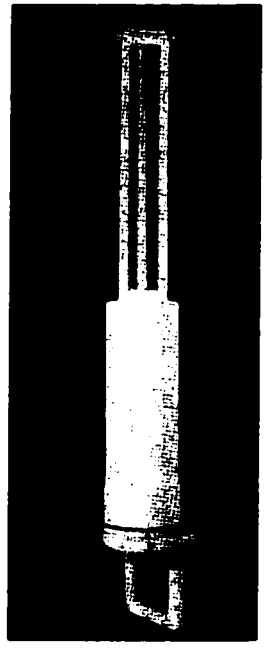

Figure 2.3 A slotted-rod cloud water collector with mesh attachment for sampling supercooled clouds (Isaac and Daum, 1987).

Experimentally derived bulk collection efficiencies were not reported for the slotted-rod collectors used to obtain either warm or supercooled cloud drops on any of the six field projects, except for the 1988 study (Liu et al., 1993). In that case, the bulk collection efficiency for the standard Mohnen slotted-rods was 10% to 35% greater than predictions based on theoretically calculated efficiency curves and King probe hot wire LWC measurements. The elevated collection efficiency was observed at both center and port mounting positions, both located just aft of the windshield on top of the Twin Otter fuselage. An explanation of this behavior was not

provided by the authors. One other qualitative observation regarding the collection efficiency of the slotted-rod collectors was made regarding the 1981 and 1982 flights: "total collection efficiency is usually very much less than that indicated by theory" (Leaitch et al., 1986a).

Daum et al. (1984a) measured the composition of cloud water using a slotted-rod collector flown on the Brookhaven National Laboratory Atmospheric Sciences aircraft in the vicinity of Charleston, South Carolina in an effort to study precipitation acidification. Over the course of 4 flights through warm-based stratus clouds, 27 samples were collected. Conductivity and pH were measured continuously as the cloud water sample passed through a specially designed cell prior to entering the storage container. Samples were analyzed post-flight for pH and major ions. The data from these 4 flights, along with 10 additional flights conducted over the southern U.S., yielding 61 samples, were reported by Daum et al. (1984b). Kelly et al. (1985) reported further on these field projects and examined cloud water H_2O_2 measurements. As in the six studies supervised by the Atmospheric Environment Service of Canada, no measure of collection efficiency was reported for these southern U.S. studies.

Mohnen slotted-rod collectors have also been used in aircraft-based studies in the Los Angeles Basin (Richards et al., 1983). In this study, based on the Sonoma Technology, Inc. Beechcraft Queen Air, 13 samples from five flights were analyzed for pH, sulfate, S(IV), HCHO, and H_2O_2 and were used to investigate the complexation of S(IV) with HCHO. Although concentrations for those species are provided, meteorological data, sample duration, and experimental collection efficiency are not discussed. Richards (1995) reports further on these 13 samples and an additional, unreported number of samples obtained on later flights in the Los Angeles Basin.

Mohnen slotted rods were deployed on the University of Washington's B-23 aircraft (Hegg et al., 1984a) along with a centrifugal cloud water collector (to be described in the following section) to obtain samples of cumulus and stratus clouds. These two collectors provided a total of 36 samples during flights from 1981 to 1983. 18 samples were from isolated

cumulus clouds, 13 from stratus clouds, and 4 from intermediate cases referred to as stratocumulus clouds. In addition to cloud water samples, filter samples were acquired directly below the sampled clouds in order to measure pre-cloud particulate sulfate and nitrate. Measurements of cloud water pH, nitrate, and sulfate were made and subsequently used to investigate the scavenging efficiency of particulate sulfate and nitrate by clouds and to estimate in-cloud sulfate production. Additional cloud water samples obtained in 1983 using slotted-rod collectors on the UW B-23 aircraft are described by Hegg et al. (1984b).

Despite the widespread use of slotted-rod collectors for cloud water chemistry studies, until 1985 the devices had received little in the way of evaluation or calibration. In an effort to provide this information, and add validity to the data generated by past cloud water studies, Huebert and Baumgardner (1985) performed a series of wind tunnel experiments and flight tests to define the collection characteristics of slotted-rod collectors. The wind tunnel portion of their study was carried out in the NRC wind tunnel in Ottawa, Ontario. Collection efficiency was calculated by dividing the mass of collected water by the mass of water that would be swept out by the cross sectional area of the slot. During their testing, they found low and widely variable collection efficiencies ranging between 10% and 62%, dependent on a range of factors that included the rod material, the mounting angle of the rods with respect to air streamlines, air speed, drop size, rod spacing, and even the machining techniques used to fabricate the rods.

During the test program, evidence of drop shatter may have been revealed. When the drop size distribution was shifted to larger sizes while maintaining other parameters constant, the collection efficiency was observed to decrease from 39% for a mean volume diameter of 12 μm to 34% for a mean volume diameter of 20 μm to 22% for a mean volume diameter of 40 μm. The authors attributed this counterintuitive decrease in collection efficiency to drop shatter and re-entrainment effects. Further evidence of drop shatter arose during runs in which the wind tunnel velocity was increased from 51 m s^{-1} to 77 m s^{-1} to 93 m s^{-1} to 103 m s^{-1} while maintaining a constant drop size distribution. In this series of runs, the collection efficiency decreased from

62% to 50% to 45% to 34%, respectively. This decrease in collection efficiency is contrary to inertial impaction theory which predicts that the cut diameter should decrease with increasing velocity. Based on this theory, a larger fraction of the total drop population should therefore be collected at higher velocities and bulk collection efficiency should rise rather than fall. Again, an increasing occurrence of drop shatter as drop impact velocities increase may be responsible for the unexpected reduction in collection efficiency. Empirically derived relationships that predict when drop shatter is likely to occur will be presented in Chapter 5.

Based on their experience, they offered several suggestions for improved performance, such as tilting the rods forward by 10 to 12 degrees, strengthening the rods to prevent them from deflecting backwards at high velocity, and increasing the spacing between rods to minimize flow interference.

2.2 Modified slotted rod collectors

Based on the findings of Huebert and Baumgardner (1985), a number of researchers have modified the original slotted-rod design in the hopes of enhancing collection efficiency and providing more consistent and representative cloud water samples. For example, modified Mohnen slotted-rod collectors were used during the 1985 Dynamics and Chemistry of Marine Stratocumulus (DYCOMS) project (Huebert et al., 1988), based on the NCAR Electra aircraft (flight speed ~105 m s^{-1}). Teflon and Delrin rods with a stainless steel backing were used to prevent the rods from deflecting during flight, making the rods elongated rather than cylindrical in cross section (Figure 2.4). The 28 cm long rods possessed 22.9 cm long, 2 mm wide, and 6 cm deep slots at their leading edges, and the hole at the bottom of the slot which passed collected water to the storage bottle was enlarged to 0.357 cm to promote water flow into the sample bottle. For this application, three rods were arranged in a single row with an increased spacing of 2.86 cm between rods to minimize airflow interaction between rods. The rods were angled forward at

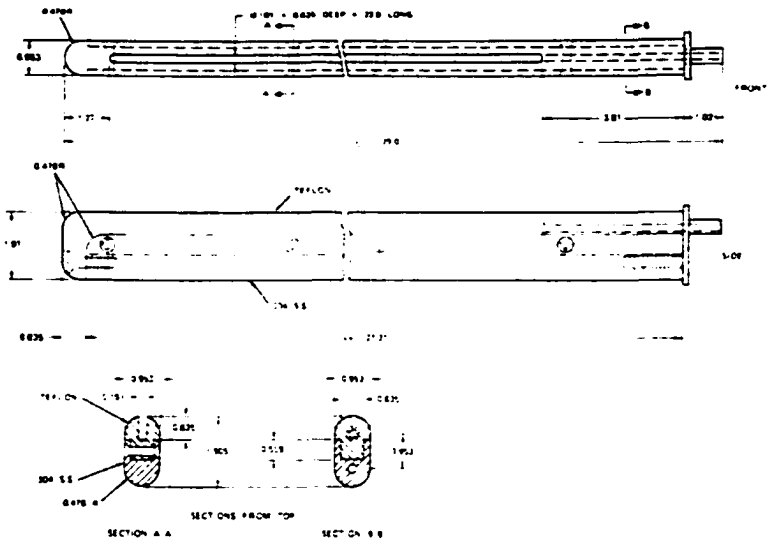

Figure 2.4. Schematic of a modified slotted-rod cloud water collector. Dimensions are in cm (Huebert et al., 1988).

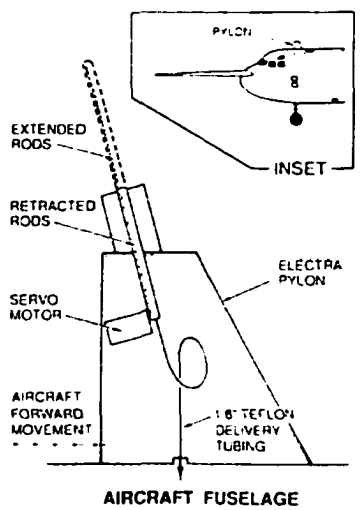

Figure 2.5. The modified slotted-rod cloud water collector mounted on the NCAR Electra aircraft (Huebert et al., 1988).

15° with respect to the fuselage so that when coupled with a 3° aircraft angle of attack during flight, the rods would be oriented at a 12° angle with respect to the airflow assuming no deflection of the rods. The rods were mounted 61.5 cm above the fuselage on a pylon (Figure 2.5) into which the rods could be retracted to prevent contamination of the collection surfaces during takeoff, landing, and other periods when the aircraft was not in clouds.

Although no cloud water composition results are supplied for their 28 samples, estimates of collection efficiency were made for the modified slotted-rod collector based on its use during DYCOMS. The authors found that collection efficiencies for the first three flights averaged just 27%, but rose to 84% ±15% on the remaining five flights. The calculation of collection efficiency was based on King probe hot wire LWC measurements. The increase in collection efficiency between the first three and remaining five flights was attributed to a conditioning of the rods over an initial period of usage, although the type of conditioning was not identified nor was the mechanism for increased collection efficiency. In addition, although the modified slotted-rod collector was mounted away from the fuselage on a pylon, the authors were unable to discount cloud drop concentration alterations due to airflow/airframe interactions for influencing collection efficiency throughout the field project. In fact, they suggest that those types of effects may have been responsible for the unusually low collection efficiency that was observed for an experimental rod that contained a slot only on its lower half. While expecting the half slot to exhibit a collection efficiency exactly 50% of the adjacent full length slots, the observed lower collection efficiency could have been evidence of drop depletion in the region nearest the fuselage.

A modified slotted-rod collector similar to that used by Huebert et al. (1988) was operated by Kim and Boatman (1992). To increase the sample collection rate, they increased the length of the Delrin rods to 32.3 cm and widened the slot as well. The collector was deployed on five flights on the NOAA King Air (~66 m s^{-1}) for the ACID-MODES field project over Harrisburg, PA. A theoretical collection efficiency curve was calculated for the flight conditions encountered during the field campaign, and a 50% cutoff diameter of 5.5 μm was reported. Based on corrected forward-scattering spectrometer probe (FSSP) LWC measurements, the observed bulk collection efficiencies were greater than unity throughout the mission, averaging 160% ± 36%. The authors put forward several theories to explain the unrealistically high collection efficiency, including a systematic underestimation of LWC by the FSSP, collection of

cloud or precipitation drops larger than the upper range of the FSSP, and aircraft/airframe effects that distort the cloud drop concentrations at either the FSSP or slotted-rod sampling locations. These theories were not quantitatively investigated and no results from the chemical analysis were reported.

In addition to describing the collection efficiency of a standard slotted-rod collector as mentioned above, Liu et al. (1993) also report on the use of a modified slotted-rod collector during the 1988 Eulerian Model Evaluation Field Study (EMEFS I) taking place on the National Research Council of Canada Twin Otter. The modified collector contained rods that were one-half the diameter of the standard rods in an attempt to enhance the collection efficiency at small drop sizes. The modified collector was mounted in one of two positions on the aircraft during the study, both on the top of the fuselage, just aft of the windshield. One position was located in the center of the fuselage and the second on the port side. While the standard collector exhibited a collection efficiency 10% to 35% greater than theoretical in both locations, the modified collector experienced a collection efficiency within 20% of theoretical in the port location but 30% to 50% less than theoretical in the center location. The authors speculate that the lower collection efficiency of the modified collector when mounted in the center location could have resulted from misalignment of the rods with the local air streamlines. However, this theory could not be confirmed as no measure of collector orientation with respect to local streamlines was available for either mounting location. No statistical difference was detected in the concentrations of SO_4^{2-}, NO_3^-, and NH_4^+ from samples obtained from the modified and standard collectors during periods of simultaneous deployment. Based on the assumption that different populations of drops were being sampled by the standard and modified collectors, the lack of measurable differences in chemical composition led the authors to report that no change in chemical composition with drop size was observed during the study. The authors used the cloud water compositional data to estimate the production of in-cloud sulfate in summer clouds over central Ontario via three separate techniques.

Although no mention is made of collection efficiency, Hegg and Hobbs (1986) report on the use of a modified slotted-rod collector to obtain 42 samples of cloud water from the western portion of Washington State in 1983 and 1984. The collector was modified from the original Mohnen slotted-rod design by lengthening the rods by a factor of two in order to increase sample collection rates. In addition, as suggested by the work of Huebert and Baumgardner (1985) the rods were strengthened with stainless steel struts, tilted slightly forward into the airstream, and the spacing between adjacent rods was doubled. The objective of their work was to make direct estimates of sulfate production in cumuliform clouds by measuring below cloud sulfate aerosol concentrations, cloud water sulfate concentrations, and interstitial sulfate concentrations. The University of Washington's B-23 aircraft served as the platform for the cloud water collector and a wide range of other cloud microphysics and aerosol instrumentation. Samples were obtained in non-precipitating, ice-free regions of cumulus and stratocumulus clouds.

Further studies of in-cloud sulfate and nitrate production were conducted by Hegg and Hobbs in 1986 and 1987 (Hegg and Hobbs, 1988) using the same modified slotted-rod collector in this case mounted on the University of Washington's C-131A. Cloud water samples were collected off the coast of North and South Carolina and along the Pacific Northwest coast. Barth et al. (1989) selected 27 samples from the 1986 portion of the study to investigate winter concentrations of cloud water H_2O_2. The selected samples were acquired on flights that targeted cumulus clouds and rainbands off the coast of North and South Carolina. Continuous gas phase H_2O_2 data recorded during these flights were used to determine the extent to which gas and aqueous phase H_2O_2 were in equilibrium.

Marine stratus clouds were sampled by Leaitch et al. (1996) over the north Atlantic using a single row of slotted-rods half the diameter of the original design. The sampling was performed as part of the North Atlantic Regional Experiment (NARE) and was based on the National Research Council of Canada Twin Otter. A total of 28 cloud water samples were obtained over 14 flights conducted in August and September 1993. The samples were analyzed for inorganic

and organic ions, H_2O_2, trace metals, HCHO, and black carbon. Only inorganic and organic ion concentrations were reported by Leaitch et al., while black carbon concentrations were reported by Chylek et al. (1996). The sampling was carried out to investigate the relationships between aerosol particle number concentrations, cloud drop number concentrations, cloud water chemical composition, and turbulence. No mention of collection efficiency was made.

The most recent deployments of a modified slotted-rod collector occurred in 1994 and 1997 over the Japan Sea and in 1996 over the northwestern Pacific Ocean (Watanabe et al., 2001). The modified collector used for these studies was mounted on a Cessna 404 for the Japan Sea flights and on a Super King Air for the Pacific Ocean flights. The collector contained a single row of three slotted cylindrical rods that were longer than the original rod design. The Teflon rods measured 430 mm long, 10 mm in diameter, and possessed a 3 mm deep slot. Drainage of accumulated cloud water down the slot was not required as the sampler was withdrawn into the cabin after every cloud pass, lasting 3 to 10 minutes, for sample removal. In supercooled clouds the rods were allowed to rime; collected rime was melted in the cabin before storage. A total of 10 samples were gathered over the Japan Sea and 6 samples were gathered over the Pacific Ocean and analyzed for pH, major inorganic ions, and H_2O_2 after landing. Unfortunately, pH measurements were unavailable for a number of samples and in-situ cloud LWC was not measured, resulting in a rather limited data set.

2.3 Other inertial impaction devices

In addition to Mohnen slotted-rods, there have been several other aircraft based cloud water collection devices that have relied on cylindrical rods as inertial impaction surfaces. Parungo et al. (1982) describes two such devices that were developed for use on the NOAA P-3 during the Hawaii Mesoscale Energy and Climate (HAMEC) project. The first of the collectors, referred to as Scoop, consisted of a single 120 cm long, 3.6 cm diameter stainless steel tube that could be extended horizontally through the cabin wall to sample clouds from the free stream

airflow (Figure 2.6). A 62 cm^2 opening along the leading edge of Scoop was intended to collect cloud water which would then be transported into a sample bottle in the interior of the aircraft. Due to its poor performance during flight trials, however, it was determined that Scoop was better suited as a rain water collector than a cloud water collector.

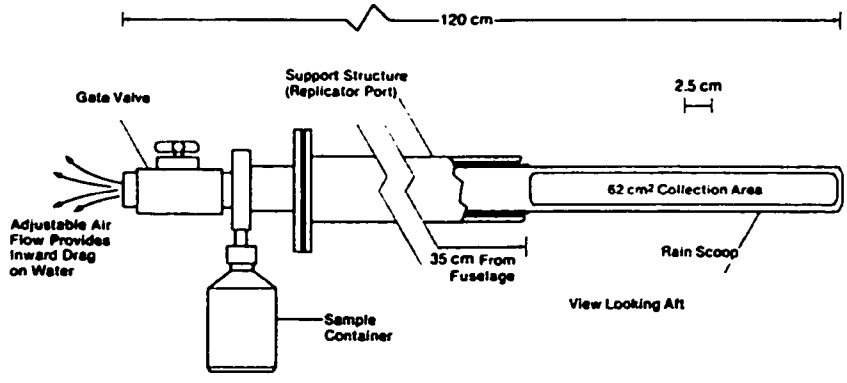

Figure 2.6. The Scoop cloud water collector (Parungo et al., 1982).

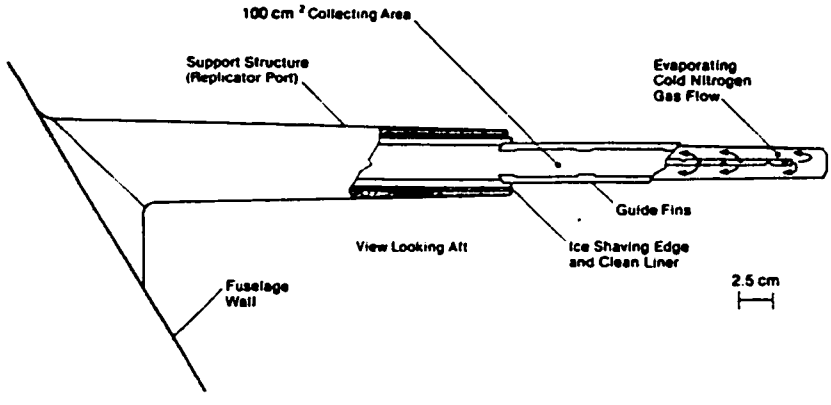

Figure 2.7. The Cold Finger cloud water collector (Parungo et al., 1982).

The second collector described by Parungo et al. (1982), dubbed Cold Finger, was similar in design to Scoop but included an internal flow of liquid nitrogen to cool the 100 cm^2 collection surface to between -10° and -20° C (Figure 2.7). The intention was to freeze cloud drops as they made contact with the cold impaction surface and accumulate cloud drops as rime ice. The entire collector could then be withdrawn into the cabin for sample removal. The authors provide an

estimate of water vapor collection due to condensation on the cold impaction surface, and indicate that the collection of vapor is negligible compared to cloud drop collection. However, in their calculations the authors assume that the accumulation of water vapor on the collector surface is a result of pure diffusion. Ventilation effects arising from the 100 m s^{-1} air flow past the collector are neglected. Inclusion of ventilation terms should significantly enhance predictions of vapor collection. The bulk collection efficiency of the Cold Finger is mentioned briefly as being greater than 60% for LWC in the range of 0.1 to 1.0 g m^{-3}, although no details are provided. During the HAMEC project, six samples were obtained on June 14 and 22, 1980 and analyzed for pH and major ions.

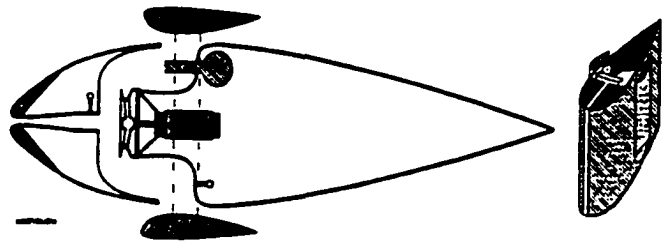

Figure 2.8. The Isokinetic Cloud Probing System (ICPS) (Maser et al., 1994).

The Isokinetic Cloud Probing System (ICPS) (Maser et al., 1994; Maser and Jaeschke, 1992) is a jet impactor that employs a vertically oriented, rectangular, flat plate impaction surface integrated into a standard wing section enclosure (Figure 2.8). Air enters an inlet located along the leading edge of the wing section and passes through a decelerating diffuser before being directed toward a polymethylmethacrylate impaction surface. Aerodynamic drag forces the accumulated water toward the edges of the impaction surface where it is extracted. Secondary wing sections at the collector outlets can be adjusted until isokinetic sampling conditions are created. Theoretical calculations indicate that the 50% cut diameter is 5 μm at 62 m s^{-1}. The ICPS was used during the Cloud Experiment Ober-Pfaffenhofen And Transports (CLEOPATRA) project, which was based on a Piper Navajo Chieftain PA31 aircraft. In addition to the ICPS

collector, a modified Mohnen slotted-rod collector with a reported theoretical Dp_{50} of 5.8 μm (Jaeschke, 1986), a modified ICPS collector lacking wing sections and assumed to have the same collection efficiency as the regular ICPS (Figure 2.9), and a porous plate "round jet impactor" with a theoretical Dp_{50} of 8.8 μm (Figure 2.10) were flown during CLEOPATRA. Few details regarding these latter collectors are provided. During CLEOPATRA, 53 total cloud water samples were obtained although individual samples are not attributed to specific collectors and no bulk collection efficiencies are reported for the sample periods. Details regarding the chemical analysis of these samples are provided by Sinner et al. (1994) and Preiss et al. (1994).

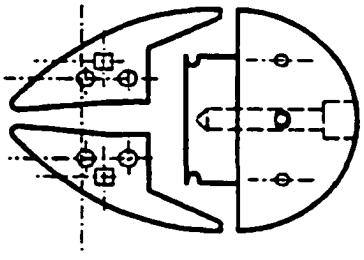

Figure 2.9. The modified ICPS (Maser et al., 1994).

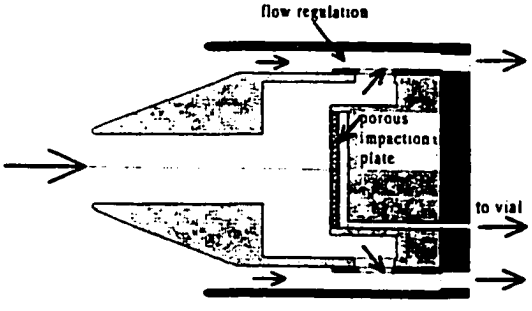

Figure 2.10. A porous plate round jet impactor (Maser et al., 1994).

The only aircraft-based collector designed for drop size segregated cloud water sampling is a two-stage impactor described by Jaeschke and Gunther (2001) (Figure 2.11). The rectangular jet cascade inertial impactor was designed to capture cloud drops larger than 10 μm in the first stage while drops larger than 5 μm are expected to be retained in the second stage. Flat surfaces

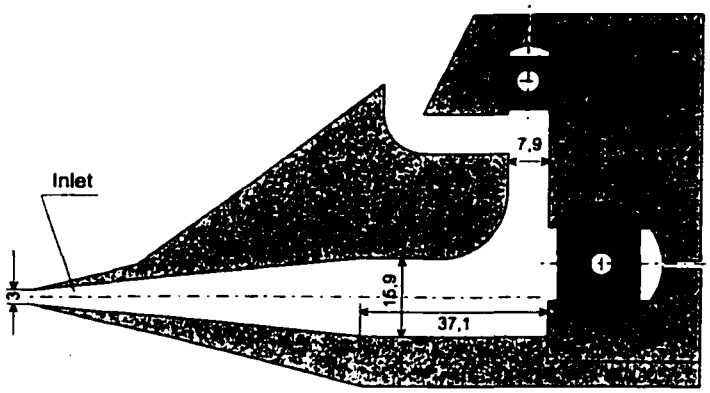

Figure 2.11. A two-stage cascade inertial impactor for size segregated cloud water sampling (Jaeschke and Gunther, 2001).

machined onto cylinders serve as impaction surfaces. The cylinders are housed in cylindrical cavities in which they can be rotated. After cloud drops accumulate on the impaction surfaces for a given duration, the cylinders are rotated 180° to transport the accumulated cloud water to a channel on the reverse side of the cylindrical housing. From there the sample is flushed out of the channel with the aid of a rinsing solution. The cutoff diameters were calculated according to the guidelines of Marple and Rubow (1986). A semi-quantitative calibration of the impactor was performed although results of the calibration are not provided. The two-stage impactor was evaluated under flight conditions in maritime clouds over the North Sea and continental clouds over Germany, which yielded an unspecified number of samples for chemical analysis. Representative results presented by Jaeschke and Gunther (2001) for these two cases indicate that compositional variations did exist between the two sampled drop size fractions of cloud water.

An unnamed inertial impaction device (Khemani et al., 1987; Khemani et al., 1982) consists of 14 U-shaped stainless steel channels arranged radially in the shape of a funnel with a diameter of 210 mm and a half angle of 23 degrees (Figure 2.12). The collector is mounted directly on the aircraft fuselage and exposed to the freestream airflow during flight. The channels serve as impaction surfaces as well as guides to direct the accumulated water toward the center of

the funnel, where it flows through a tube into the interior of the aircraft. The authors report that the collection efficiency of this device has not been evaluated either theoretically or experimentally. The collector was used to sample cloud water from warm stratocumulus and cumulus clouds in the Pune region of India during the summer monsoons of 1983, 1984, and 1985. Over the three year period, 47 cloud water samples were obtained in non-precipitating clouds and 43 samples were obtained in precipitating clouds.

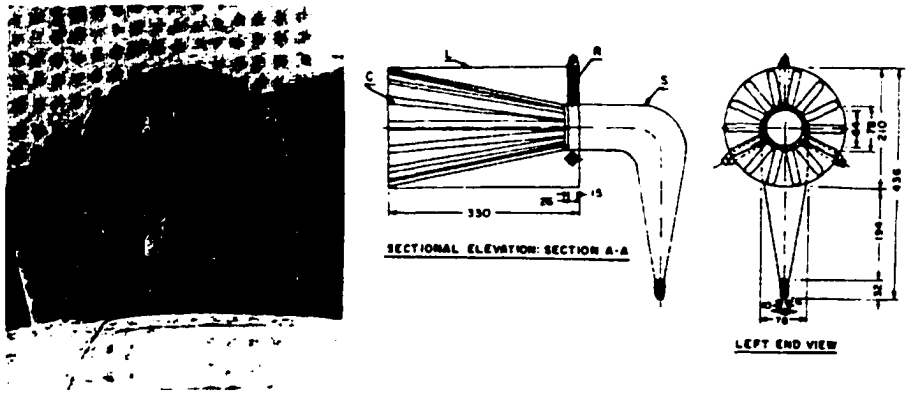

Figure 2.12. A simple funnel cloud water collector (Khemani et al., 1987).

A rectangular channel collector was operated from a Queen Air 65-65 to sample cloud water over Heidelberg, Germany (Bogen, 1974). During a 1971 field campaign, hundreds of milliliters of water were gathered per research flight. The samples were analyzed for 17 trace elements and compared to rain water samples obtained from the same area. The sampler consisted of a 10 cm × 20 cm curved rectangular channel that extended through an emergency window opening and was oriented with the open end facing the direction of flight (Figure 2.13). Cloud drops intercepted by the channel opening were swept along the channel and into the interior of the aircraft where accumulated water drained into a sample bottle. Drops larger than 4 μm in diameter were estimated to have been collected at flight speeds of 83 m s^{-1}.

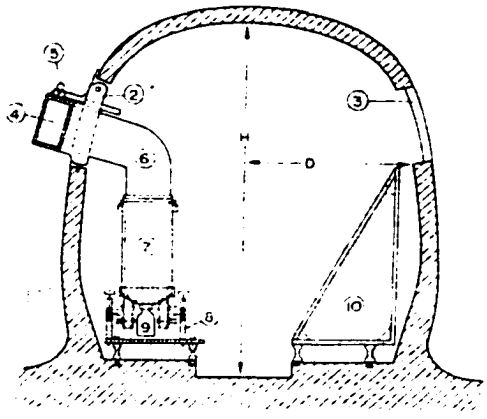

Figure 2.13. A rectangular curved duct cloud water collector extends through the cabin wall of a Queen Air 65-65 (Bogen, 1974).

Scott (1978) placed a simple funnel device on a movable boom mounted just above the left wing on the fuselage of a Cessna 402 aircraft (Figure 2.14). A Teflon scarf tube positioned at the apex of the nylon funnel promoted air flow through the device. Sample collection occurred during flight as cloud drops impacted the walls of the funnel and flowed to the center where tubing transported the sample to a storage container. Although collection efficiency was not investigated through theoretical or experimental means, the authors admit that the efficiency was low, especially for small drop sizes. The device required 10 to 20 minute sample periods to obtain a sufficient volume of cloud water for analysis. 15 samples were obtained with this device in the vicinity of Sidney, Australia in 1976 and analyzed for pH.

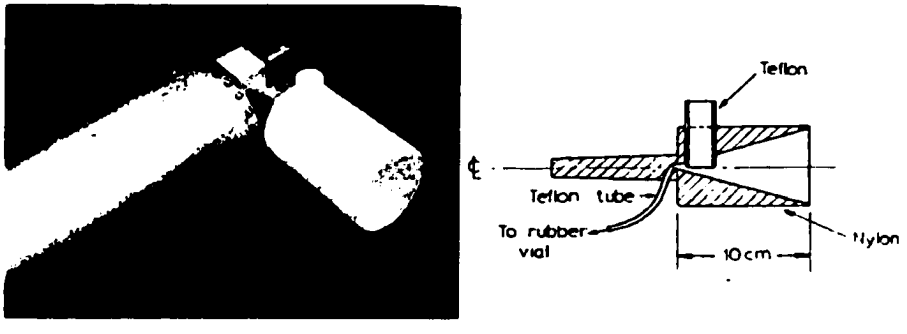

Figure 2.14. A Nylon funnel with scarf tube (Scott, 1978).

Inspired by the ground-based collection of supercooled cloud drops on mesh collectors referred to as cloud sieves (Hindman et al., 1992), Hindman (1988) developed a conceptual aircraft-based version of the cloud sieve. The airborne cloud sieve incorporates four sets of cylinders having diameters of 0.3, 1.27, 3.18, and 5.0 cm as impaction surfaces to capture four different drop populations simultaneously. The cylinders were designed to collect supercooled cloud drops with theoretically derived 50% cut diameters of 4, 8, 13, and 18 μm at a flight speed of 60 m s^{-1}. However, because the airborne cloud sieve was never built or flown, it remains a collector in concept only.

Finally, several inertial impaction cloud water collection devices mentioned in the literature, but not described in detail, include a nylon wand that is extended into the airstream through a hole in the fuselage (Scott and Laulainen, 1979), a Teflon sampler flown on a Twin Otter aircraft that required 20-30 minute sample periods (Lei et al., 1997), an unspecified device used to capture hundreds of cloud water samples in the USSR (Petrenchuk and Drozdova, 1966; Petrenchuk, 1973), and a polyethylene coated aluminum rod used for supercooled cloud water collection (Hegg and Hobbs, 1981). In addition, a simple funnel device has been used to capture rain rather than cloud samples (Oddie, 1962), and a glass slide impactor has been used to determine cloud drop size and number concentration but not drop chemical composition (Jiusto, 1967).

2.4 Centrifugal devices

The second main technique used to collect cloud water from an aircraft platform is centrifugal separation. Scott (1978) designed a centrifuge which incorporated angled vanes to harness the freestream airflow to produce rotation (Figure 2.15). In theory, air enters the inlet nearly isokinetically and is forced to larger radii due to the presence of an internal cone. The resulting air flow pattern causes cloud drops to collect on the inner surface of the outer cone and accumulate in the annular space at the base of the outer cone. After cloud penetration, the entire

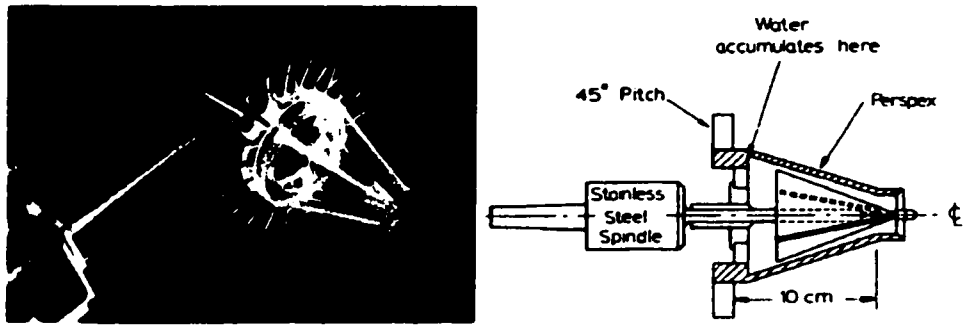

Figure 2.15. An actively rotated centrifuge collector (Scott, 1978). For the schematic cross section, air flow is from right to left.

unit was brought into the cabin for sample retrieval. Unfortunately the high rate of rotation (10,000 rpm) attained by this device led to structural failure after the sixth passage through cloud. No theoretical or experimental efficiency calculations were performed, although the authors surmise that drops with diameters below 1 micron should easily be separated from the airstream.

A modified version of Scott's centrifugal device was used to collect cloud water samples from the University of Washington's B-23 research aircraft over Los Angeles and Western Washington (Hegg and Hobbs, 1981; Hegg et al., 1984a). The fins of the modified centrifugal collector were eliminated and instead a motor was employed to rotate the apparatus at 3400 rpm to reduce the likelihood of mechanical failure. The interior pyramid was also modified in an attempt to improve collection efficiency; however, the bulk collection efficiency was stated to be approximately 10%, presumably determined through field measurements. The authors report that only drops greater than 6 μm in diameter were captured for a flight speed of 60 m s^{-1}. Samples obtained with this collector were generally analyzed for pH and sulfate in an effort to investigate the scavenging and production of sulfates in clouds.

Walters et al. (1983) developed a centrifugal cloud water separator that incorporates fixed, curved vanes into a two inch diameter duct (Figure 2.16). As air and cloud drops are drawn into the separator and encounter the stainless steel vanes, a rotational flow field develops. As the flow rotates about the duct centerline, cloud drops are removed to the walls of the duct by

centrifugal force. The accumulated cloud water flows along the wall and is then extracted at a circumferential grove located downstream of the vanes. The centrifugal collector was installed in the cabin of a Lockheed Hercules by placing it in a 47 mm ID, 2.3 m long curved duct with a forward facing inlet and rear facing exhaust (Figure 2.17) that extend through the aircraft fuselage. Optimal vane outlet angles were established through parametric wind tunnel testing which also qualitatively confirmed predictions of sample collection rates. Flight tests indicated the bulk collection efficiency to be approximately 80% for a cloud LWC of 0.3 g m^{-3}. The flight tests appear to have been performed for evaluation purposes only, and no chemical analyses were conducted.

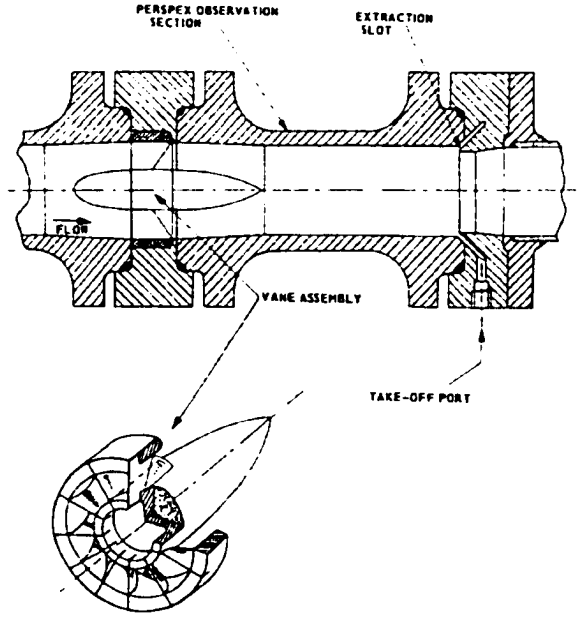

Figure 2.16. A fixed vane centrifugal cloud water collector (Walters et al., 1983).

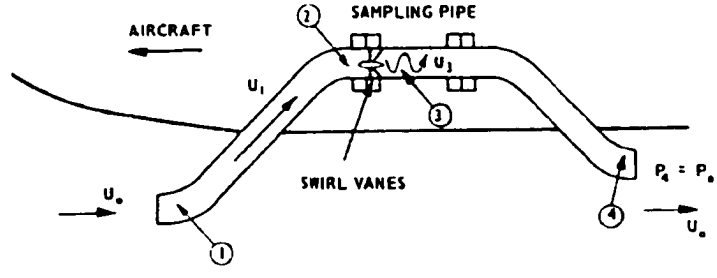

Figure 2.17. The fixed vane centrifugal cloud water collector mounted on an aircraft (Walters et al., 1983).

2.5 The counterflow virtual impactor

The counterflow virtual impactor (CVI) does not collect samples of cloud water for the direct measurement of aqueous phase chemical concentrations, but instead provides samples of non-volatile cloud drop residuals that can be analyzed for chemical composition. The CVI, sometimes referred to as a droplet to aerosol converter, was originally developed for aircraft-based sampling (Laucks and Twohy, 1998; Twohy et al., 1997; 1989; Dixon and Charlson, 1994; Strom et al., 1994; Noone et al., 1993; Ogren et al., 1985) but has been adapted for sampling from ground-based sites as well (Anderson et al., 1994; Noone et al., 1991; 1990; 1988a; 1988b; Heintzenberg et al., 1989; Ogren et al., 1989).

The CVI inlet consists of two concentric stainless steel tubes adjoined at their leading edges (Figure 2.18). A heated carrier gas flows through the annular region between the tubes and through a porous section of the inner tube. The flow rate of the carrier gas is adjusted such that a portion of the carrier flow exits the tip of the CVI (excess flow) while the bulk of the carrier flow moves in the opposite direction through the inner tube to sampling instruments (sample flow). A zero velocity stagnation plane develops where the excess flow and sample flow diverge in the inner tube. The location of the stagnation plane is dependent upon the length of the porous tube and the ratio of sample flow rate to total carrier gas flow rate.

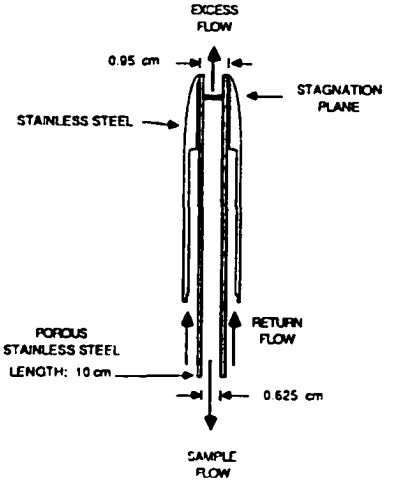

Figure 2.18. One version of the counter-flow virtual impactor (CVI) inlet (Noone et al., 1988a).

For aircraft deployment, the CVI inlet is oriented into the direction of flight. Aerosol particles and small haze drops are unable to penetrate the excess flow exiting the CVI tip and simply flow around the inlet. Cloud drops, on the other hand, possess enough inertia to enter the CVI inlet. If cloud drops are large enough to penetrate the stagnation plane as well, they enter the heated, dried sample gas flow where water and volatile components evaporate rapidly. The remaining non-volatile residuals are transported to sampling instruments where they can be counted, sized, or collected on filters for post-flight chemical analysis. The evaporated water and volatile species can be measured in the sample stream if desired. The 50% cut diameter of the CVI can be adjusted by altering the ratio of sample to total carrier gas flow rate, allowing size dependent variations in chemistry to be investigated. Typical 50% cut diameters range between 4 and 30 μm for ground-based and aircraft-based applications.

2.6 Concluding remarks

Interest in cloud drop nucleation mechanisms, cloud water acidification, aerosol mass generation, and other interactions between cloud water, aerosol particles, and trace gases have prompted the development and use of instrumentation designed specifically to collect samples of cloud water from aircraft platforms. Most of these aircraft-based cloud water collectors were built for and operated during field projects conducted in the 1980s or earlier. There has been very little airborne cloud water sampler development work in recent years, despite evidence that past designs have a range of shortcomings.

The most popular aircraft-based cloud water sampler through the years has been the slotted-rod design which relies on inertial impaction for cloud drop collection. The slotted-rod collector is relatively simple in concept, design, and construction making its use attractive. Despite being widely used in the field, however, there was no experimental evaluation of the slotted-rod design until 1985 when wind tunnel tests were performed. The wind tunnel testing exposed a widely variable collection rate but also provided suggestions for improvements that

were incorporated into later versions. Through the years, slotted-rod collectors have successfully obtained samples of cloud water for inorganic ion, H_2O_2, HCHO, S(IV), and pH analysis. To date, though, there has still not been a systematic calibration of slotted-rod collectors to determine collection efficiency as a function of drop size.

Apart from slotted-rod collectors, the majority of aircraft-based samplers have been developed for specific field projects based on specific aircraft and have only been deployed a limited number of times. These collectors have generally employed inertial impaction on cylindrical rods or flat plates as a collection technique, although several rely on centrifugal separation to remove cloud drops from the air stream. Theoretical 50% cut diameters are typically reported to be between 2 μm and 10 μm. Only one aircraft-based collector has been designed for drop size segregated cloud water sampling, although collection of cloud drop residual particles as a function of drop size has been performed. As with slotted-rod collectors, there has been little in the way of evaluation of most cloud sampling instruments and, for the most part, collection efficiency as a function of drop size has not been assessed.

3 Design of a new aircraft-based cloud water collection system

The development of a new aircraft-based cloud water collection system was initiated in July, 1999. At that time, the intention was to produce a finalized version of the collection system for deployment during NCAR's Megacity Impact on Regional and Global Environment – Mexico City (MIRAGE-Mexico) mission, a field project scheduled for the summer of 2000. This presented a limited time frame for system development and construction. The MIRAGE-Mexico field project offered an excellent opportunity to participate in a study with an emphasis on cloud and aerosol interactions, and an aircraft platform that would include a range of instrumentation necessary to investigate those interactions. However, to accommodate this accelerated deployment schedule it was necessary to pattern the new collector, at least in part, after an existing design rather than develop an entirely new collection method. In the end, the MIRAGE-Mexico campaign was indefinitely postponed and the collector was first deployed on the DYCOMS-II field project in the summer of 2001.

A review of the existing aircraft-based cloud water collection systems identified the advantages and disadvantages of past designs and helped determine a collection technique that would satisfy our requirements. After the review process, an axial-flow cyclone design, based on that of Walters et al. (1983), was chosen to separate cloud drops from the ambient airstream. It was expected that an axial-flow cyclone would provide more consistent samples than inertial impaction devices, especially slotted rod collectors which have low collection efficiencies that are sensitive to slight changes in true air speed, angle of attack, materials used in construction, and even manufacturing processes (Huebert and Baumgardner, 1985). It was also expected that an axial-flow cyclone would be less susceptible to drop shatter and re-entrainment than inertial

impaction devices. Finally, the ability of an axial-flow cyclone to process relatively large quantities of air in a compact space, with a geometry suitable for incorporation into a Particle Measurement Systems (PMS) canister, made this design attractive.

The main component of the cloud water collection system is an axial-flow cyclone, which separates cloud drops from the ambient airstream. In addition to the axial-flow cyclone, several additional components complete the collection system. These components include: a retractable inlet cover, an automated sample storage system, and electronics, all of which are housed in the PMS canister. A LabVIEW-based control and data collection system is used to remotely operate the system from the cabin of the aircraft. The components of the cloud water collection system will be described in the following sections of this chapter.

3.1 The axial-flow cyclone

Like all cyclone separators, an axial-flow cyclone utilizes centrifugal force to separate solid or liquid particles from a rotating gas. Strauss (1975) provides an extensive review of cyclone theory and a description of the various types of cyclone separators that have been developed. The axial-flow cyclone differs from the more widely used tangential reverse-flow cyclone (Figure 3.1) in that the inlet and outlet are aligned and the airflow never reverses direction (Figure 3.2). Although conventional reverse-flow cyclones are used more regularly and have received extensive theoretical and experimental evaluation (e.g. Griffiths and Boysan, 1996; Kim et al., 2001; Kim and Lee, 2001; Mothes and Loffler, 1988), the layout and operation of fixed and rotating vane axial-flow cyclones, primarily for high flow rate industrial gas cleaning applications, have been described as well (Strauss, 1975; Ogawa, 1984; Burkholz, 1989). A simple mathematical model has been developed to describe the performance of laminar axial-flow cyclones for use as aerosol samplers (Maynard, 2000). Axial-flow cyclones have also been developed to remove dust from high temperature flue gasses (Akiyama and Marui, 1989), for

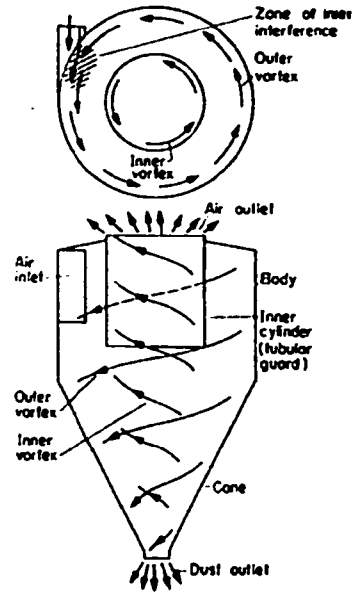

Figure 3.1. Gas flow pattern in a conventional reverse flow cyclone. Particle laden flow enters the separator tangentially, creating a descending rotational flow field where particle separation occurs. The rotating flow then ascends and particle free gas is discharged from an outlet that is perpendicular to the inlet. (Strauss, 1975).

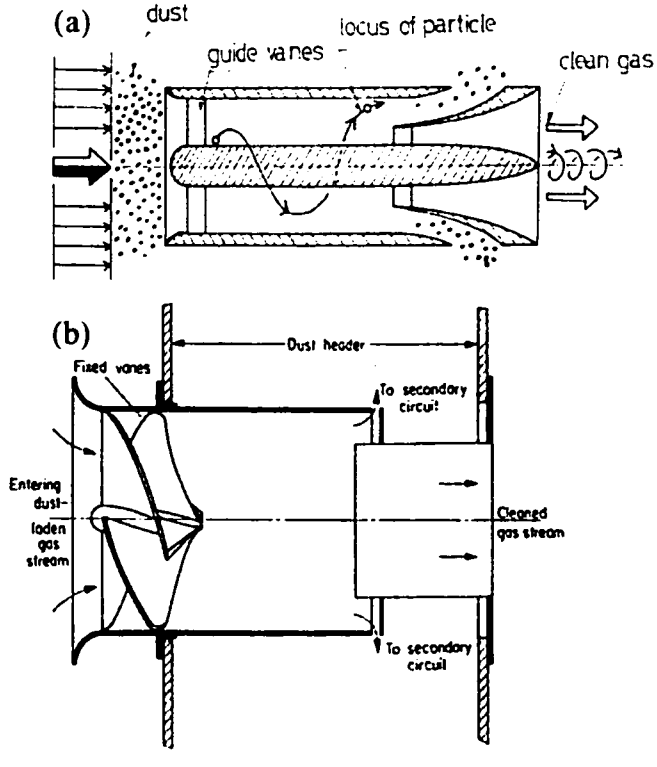

Figure 3.2. Two examples of axial-flow cyclones for industrial gas cleaning applications. The inlet and outlet are aligned and gas flow does not reverse direction. Rotation is generated by fixed swirl vanes. Particles migrate to the duct wall due to centrifugal force and are removed along with a secondary flow while clean gas is discharged from the outlet. (a) (Ogawa, 1984); (b) (Strauss, 1975).

particle separation at low gas flow rates (Vaughan, 1988), and for the separation of liquid drops from a liquid of a different density (Nieuwstadt and Dirkzwager, 1995).

The axial-flow cyclone designed for the new cloud water collection system consists of an 80 cm long, 6 cm inner diameter duct that is placed on the exterior of the aircraft and exposed to the airflow. The duct is aligned with the external airflow and positioned with the inlet facing the direction of flight, allowing ram pressure to drive air and cloud drops through the duct. Mounted inside the duct, approximately 15 cm downstream of the inlet, is a non-rotating vane unit consisting of eight curved vanes that extend radially from a 3.0 cm diameter aerodynamically shaped center hub to the outer duct wall (Figure 3.3). As the incoming air encounters these stationary vanes, the flow is redirected to produce a rotational flow field about the duct centerline.

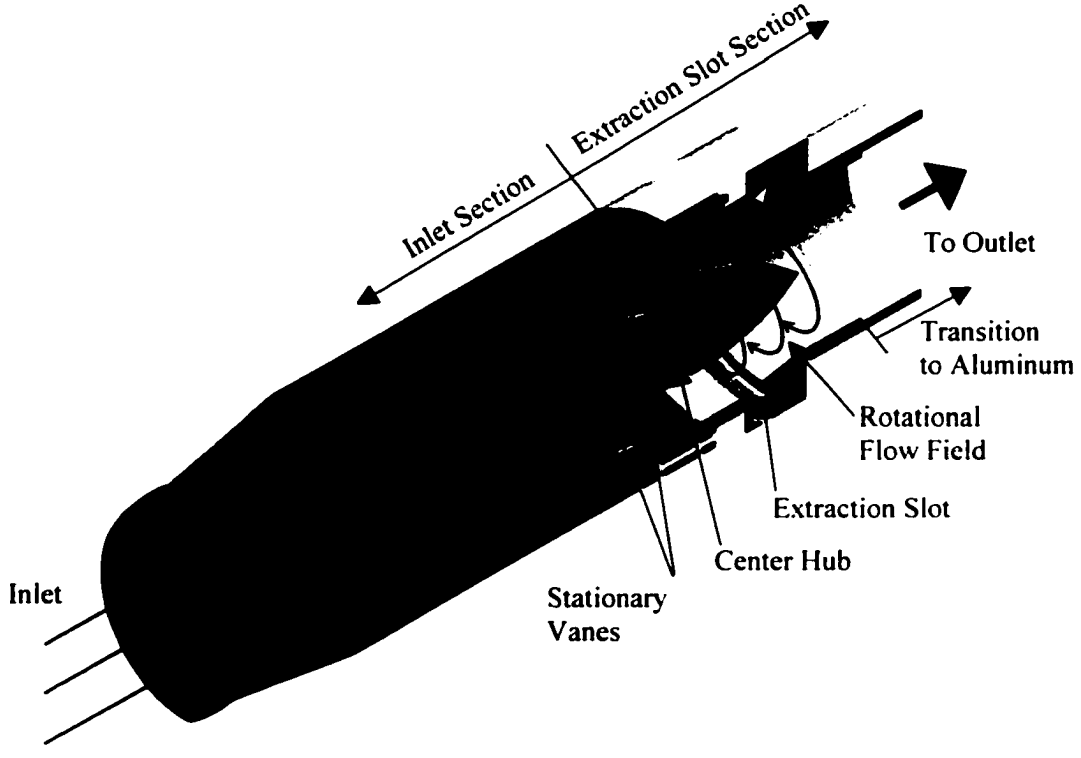

Figure 3.3. Cut-away view of the axial-flow cyclone showing the inlet, the stationary curved vanes, and extraction slot. The inlet and extraction slot sections are machined from polycarbonate and the curved vane assembly is fabricated from glass filled nylon. The inlet is 6 cm in diameter.

Rotation is clockwise when viewed from the front of the collector. In the rotational flow field, centrifugal action quickly moves cloud drops to the duct wall. As drops accumulate on the duct wall, shear flow from the rotating air flow drives the drops along the surface of the duct until they reach a 0.6 cm deep circumferential extraction slot located approximately 5.5 cm downstream of the vane assembly. Cloud water is drawn out of the extraction slot through two ports and subsequently directed to the sample storage system.

Due to the presence of the stationary curved vanes, a pressure drop through the system was unavoidable and resulted in subisokinetic sampling conditions. A system in which the vanes are actively rotated could produce isokinetic flow through the system, however, the tradeoff in mechanical complexity, added cost, and complexity of flow field analysis prevented the pursuit of an actively rotated system in the limited development schedule.

The feasibility of the stationary vane axial-flow cyclone design was investigated through a relatively simple analysis employing the Bernoulli equation and empirically derived expressions for pressure loss in a duct (Munson et al., 1990) and pressure loss through an axial-flow turbine vane unit (Horlock, 1966). This analysis indicated that the axial-flow cyclone would indeed be subisokinetic, with an inlet velocity of approximately 40 m s^{-1}, equivalent to a 6700 l min^{-1} flow rate, for a 65° vane outlet angle and 115 m s^{-1} freestream conditions (representative of aircraft flight speed). Aspiration efficiency calculations based on the correlations of Zhang and Liu (1989), along with internal collection efficiency based on the radial motion of drops in the collector as calculated through a simplified force balance, provided an estimation of collection efficiency as a function of drop size. At each drop size, collection efficiency was defined as the number of cloud drops that reach the interior duct wall upstream of the extraction slot divided by the number of drops that would be swept out by the 6 cm diameter cross sectional area of the axial-flow cyclone duct. These calculations predicted a 50% cut diameter of approximately 5 μm.

3.1.1 Design of the flow-through duct

The forward 30 cm of the axial-flow cyclone duct was machined at NCAR's Design and Fabrication Services (DFS) from polycarbonate, a material that is structurally adequate for aircraft applications yet will not compromise the chemistry of the cloud water that comes into contact with it. The polycarbonate portion of the duct is divided into two separate sections. The first section, referred to as the inlet section, (dark shading in Figure 3.3) extends from the leading edge of the inlet to the location of the curved vane assembly. The second section, referred to as the extraction slot section, (light shading in Figure 3.3) starts at the curved vane assembly and extends 4 cm downstream of the extraction slot. At the junction of these two sections, recesses are machined into the interface to accommodate the vane unit.

The extraction slot was machined into the inner surface of the polycarbonate duct 5.5 cm downstream of the leading edge of the curved vanes. Its design was aided by CFD analysis which will be further described in Section 4.4.4. Two ports extend through the duct and into the extraction slot to facilitate the removal of accumulated cloud water from the axial-flow cyclone. Downstream of the extraction slot, the duct transitions to aluminum and serves as a support structure for many of the remaining system components. Additional details regarding the design of the axial-flow cyclone duct can be found in Appendix A.

3.1.2 Design of the curved vane assembly

The development of the curved vane assembly began with the design of the aerodynamically shaped center hub that would secure the root of each of the curved vanes. No guidelines were available to suggest the appropriate dimensions of the center hub, so a 3 cm diameter, 9.37 cm long hub was selected (Figure 3.4). In order to minimize distortion of the airflow through the duct, an elliptical leading edge and a tapered trailing edge were specified. At the mounting location of the center hub, the diameter of the duct was enlarged in an effort to maintain an approximately constant cross sectional flow area through the duct. Therefore, the

duct inner diameter in the region of the center hub transitions from 6.0 cm to 7.0 cm through a 9° expansion. Downstream of the center hub, the duct then transitions back to a 6.0 cm inner diameter through an 11° contraction.

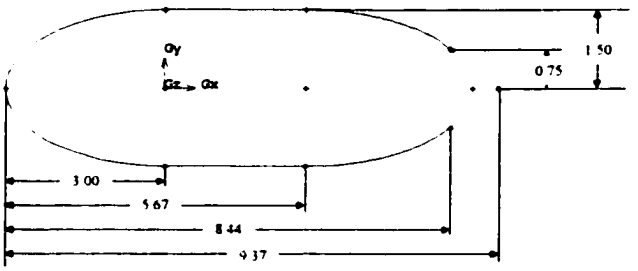

Figure 3.4. Geometry of the curved vane assembly center hub. Dimensions are in cm.

The development of the vane geometry followed guidelines presented by Horlock (1966) and Wilson and Korakianitis (1998) for the optimal design of axial flow turbine blades. These guidelines supplied the principal dimensions that were incorporated into a simplified blade geometry. The design process required the selection of the number of blades; eight were chosen for the axial-flow cyclone cloud water collector. Based on the number of blades and the dimensions of the axial-flow cyclone duct and center hub, parameters describing the two dimensional geometry of the blade cross section could be derived. The camber line, which defines the cross sectional shape of the blade, was constructed from a straight line segment positioned at the desired outlet angle and an arc that is tangential to that line segment and also possesses an axially-directed leading edge (Figure 3.5). An outlet angle of 65° was selected to provide a compromise between pressure drop and the ability to extract collected cloud water from the duct walls (Walters, 1983). The two dimensional geometry was then extended into three dimensions to fully define the curved vane assembly. A detailed description of the blade geometry design process is included in Appendix A.

The complex geometry of the curved vane assembly proved difficult to fabricate through traditional machining techniques, and would have required specially manufactured molds and

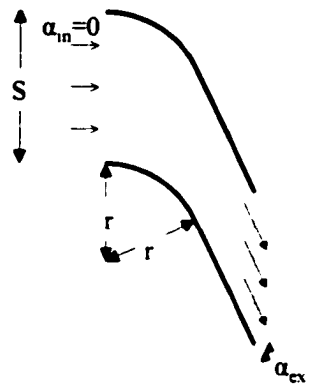

Figure 3.5. Cross sectional geometry of the curved vanes.

presses and extensive joining techniques that would have limited the choice of materials and increased costs substantially. In consultation with Steve Rauenbuehler in NCAR's DFS, a rapid prototyping fabrication procedure was selected as an alternative. In this process, the center hub, the eight curved vanes, and a portion of the exterior duct were constructed as a single component (Figure 3.6). Selective Laser Sintering (SLS), one of the many rapid prototyping processes, was selected for its ability to generate high strength, complex components that can be used directly as they are made. In the SLS process, a solid component is built up from a succession of cross sectional layers as a computer guided laser sinters one thin layer of powdered material at a time. The curved vane assembly was fabricated in this way from glass filled nylon at Rapid Prototyping Corporation (Longmont, CO 80504).

Figure 3.6. The curved vane assembly fabricated through SLS. The curved vane assembly is a single component that incorporates the center hub, eight curved vanes, and a section of the duct wall.

3.2 Collector housing

One of the design objectives in the development of the new cloud water collection system was portability between multiple research aircraft. To this end, a PMS canister was selected to house the entire cloud water collection system.

3.2.1 Particle Measurement Systems canister

As illustrated in Figure 3.7, a PMS canister is a 61 cm long, 18 cm outer diameter aluminum cylinder that was originally developed to accommodate Particle Measurement Systems' optical probes which measure aerosol and cloud drop size distributions. Because these optical probes are used on a wide range of aerosol and cloud microphysics research flights, many research aircraft have standard mechanical mounts and electrical interfaces to accommodate PMS canisters. By placing the cloud water collector in one of these canisters, the system could potentially be used without major modifications on any aircraft of suitable flight speed that supports PMS optical probes.

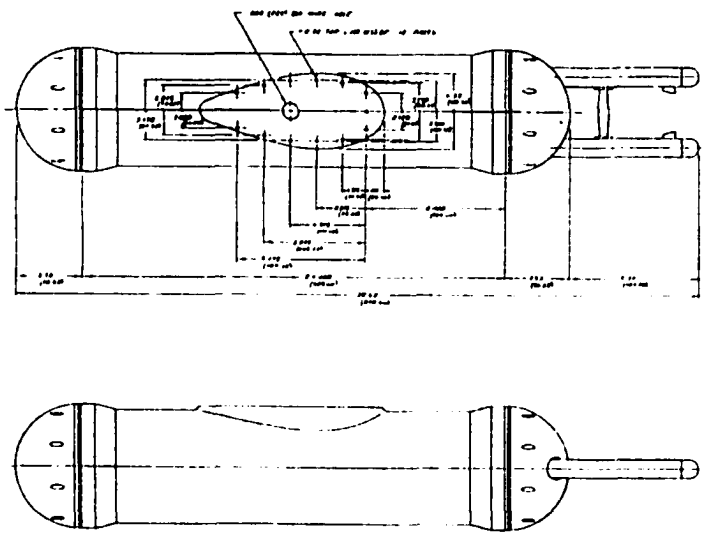

Figure 3.7. Schematic of a standard Particle Measurement Systems canister. The canister is 61 cm long and has an outer diameter of 18 cm.

The use of a PMS canister enclosure and associated mounting location also made fuselage modifications and cabin penetrations unnecessary, and use of a proven structure made

flight worthiness certification straightforward. The major disadvantages of adopting a PMS canister are the severe size limitations that are imposed on instrumentation design and the remote placement of the canisters on the aircraft making remote control necessary and preventing in-flight modifications and repairs. Considerable time and expense was invested in finding miniature components (valves, fittings, electronics, sensors, sample bottles, etc.) that could fit in the limited available space. In addition, a significant expenditure of time was made orienting, positioning, and often modifying the components in such a way that each could operate separately as intended and that all could operate in tandem as a functional cloud water collection system.

Most PMS optical probes rely on a hemispherical end cap with one or more small openings to cover the forward end of the canister and a solid hemispherical end cap to cover the aft end of the canister. To accommodate the cloud water collector and its large diameter flow through design, new end caps were required. Forward and aft end caps were machined by NCAR's DSF from aluminum stock, followed by anodization to prevent corrosion. The axial-flow cyclone's polycarbonate inlet extended through a 9.4 cm diameter opening in the forward end cap while the aluminum exit duct extended through a 6.35 cm diameter opening in the aft end cap (Figure 3.8). The forward end cap was press fit onto the polycarbonate inlet of the axial-flow cyclone and sealed with an O-ring. Each end cap was secured to the canister with eight stainless steal hex-head bolts.

To provide the maximum usable space in the interior of the PMS canister for the remaining components of the collection system, the axial-flow cyclone duct is mounted in the upper right quadrant of the PMS canister when viewed from the front. This configuration allows the sample storage bottles to be mounted vertically to the left of the duct. The minor modifications necessary for installation of the collection system in a standard PMS canister are described in Appendix C.

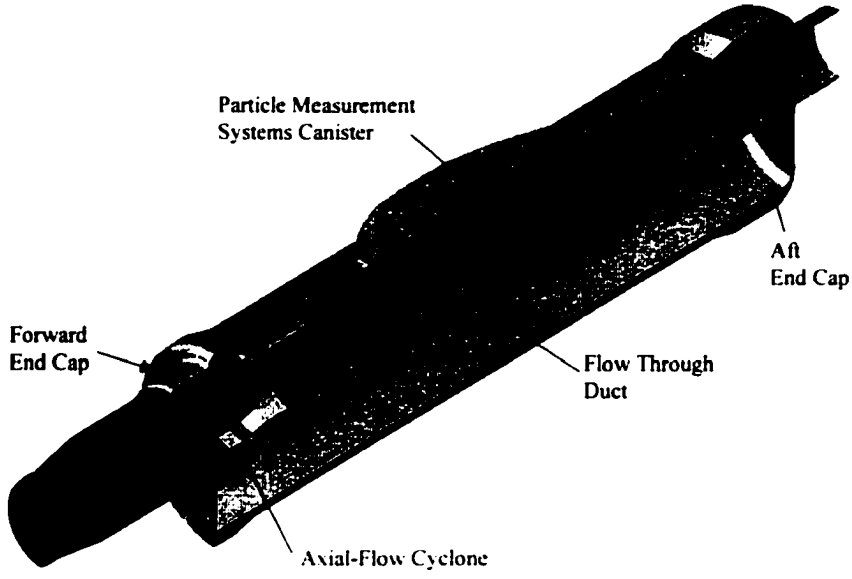

Figure 3.8. Cut-away view of the axial-flow cyclone mounted in a PMS canister. The forward and aft end caps of the canister hold the axial-flow cyclone in position. The remaining components of the cloud water collection system are structurally supported by the aluminum duct and occupy the space surrounding the duct.

3.2.2 NSF/NCAR C-130 mounting location

The cloud water collection system was primarily developed for deployment on the NSF/NCAR C-130 aircraft which has a capacity of 10 PMS canisters; two on each wing tip, and three on each mid-wing instrumentation pod. At these locations, the canisters may not be subject to the more severe airflow distortions near the fuselage that may be responsible for enhancing or depleting cloud drop number concentrations by a factor of two or more due to inertial effects (Twohy and Rogers, 1993; Norment, 1988). Unfortunately, flow distortions and cloud drop number modification may be present at the wing tip and instrumentation pod locations as well, although there is no analysis currently available to quantify this.

The canister and cloud water collector were mounted on the instrumentation pod located below the right wing of the NSF/NCAR C-130, outboard of the two engines. The instrumentation pod is capable of supporting three PMS canister – one horizontally outboard of the pod, one at a 45° angle, and one hanging vertically below the pod. For the first deployment of the cloud water

collector, the lower pod position was selected as the mounting location (see Figures 6.2 and 6.7) because it offered convenient access for the routine removal and replacement of the collector that was necessary between flights for sample retrieval. However, the collector could be installed in any of the canister locations on the NSF/NCAR C-130 aircraft.

On the C-130, PMS canisters are air worthiness certified for weights up to approximately 18 kg. In order to remain below that total weight and therefore avoid a recertification process, attention to component weight was necessary during the design process. An added benefit for weight reduction was the production of a more maneuverable and transportable instrument. The final weight of the cloud water collector, including PMS canister, was 16 kg.

3.3 Inlet cover

The concentrations of relevant species in cloud water are on the order of μM, requiring strict attention to the cleaning of all surfaces that are exposed to cloud water to prevent sample contamination. In addition, appropriate steps must be taken to ensure that cleaned surfaces remain uncontaminated until sampling commences and after sampling is complete. For this reason, a cover mechanism, designed primarily by Steve Rauenbuehler in NCAR's DFS, was developed to close off the inlet during periods when sampling was not occurring (Figure 3.9). The objective was to prevent contaminants such as runway debris and aerosol particles from entering the collector and compromising the cloud water chemical composition.

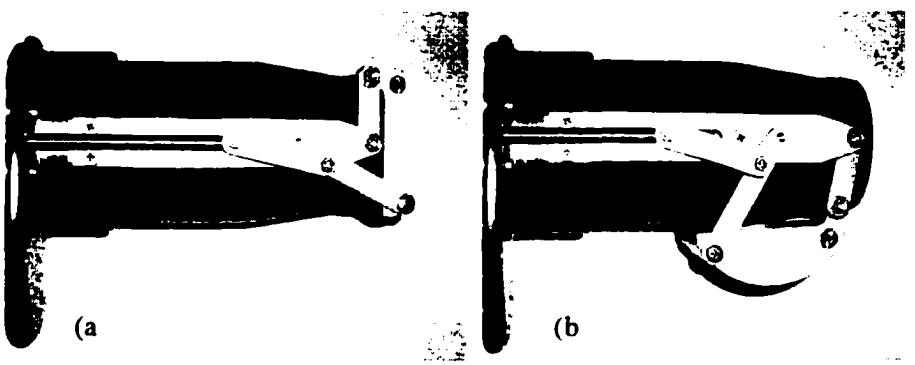

Figure 3.9. A view of the inlet cover in the closed (a) and open (b) positions. The cover transitions from the closed position to the open position in approximately 30 s as the rods are retracted into the canister via the inlet cover motor and chain drive. The cover is kept closed during non-sampling periods in order to minimized contamination of the interior collection surfaces.

The inlet cover was machined from a single polycarbonate block and incorporated an aerodynamically shaped leading edge and a circular depression on the reverse side that precisely fits over the axial-flow cyclone inlet when the cover is in the closed position (Figure 3.9a). A series of hinges allows the cover to transition between the closed and open positions by rotating and swinging down below the inlet (Figure 3.9b). The transition from the fully open to fully closed position, and vice-versa, required approximately 30 s.

3.4 Sample storage system

In order to store accumulated cloud water for the duration of a research flight, a sample storage system was developed. For the prototype collector, seven sample bottles were incorporated into the system so that seven separate samples could be stored on a single flight (Figure 3.10). Standard wide-mouth 125 ml polypropylene bottles (Nalgene 2105-0004) were selected as storage containers due to their inert composition, availability at low cost, appropriate size, and their ability to be easily removed from the collector after each flight for transport, weighing, and storage of the enclosed sample. Fresh bottles are placed on the collector before every flight.

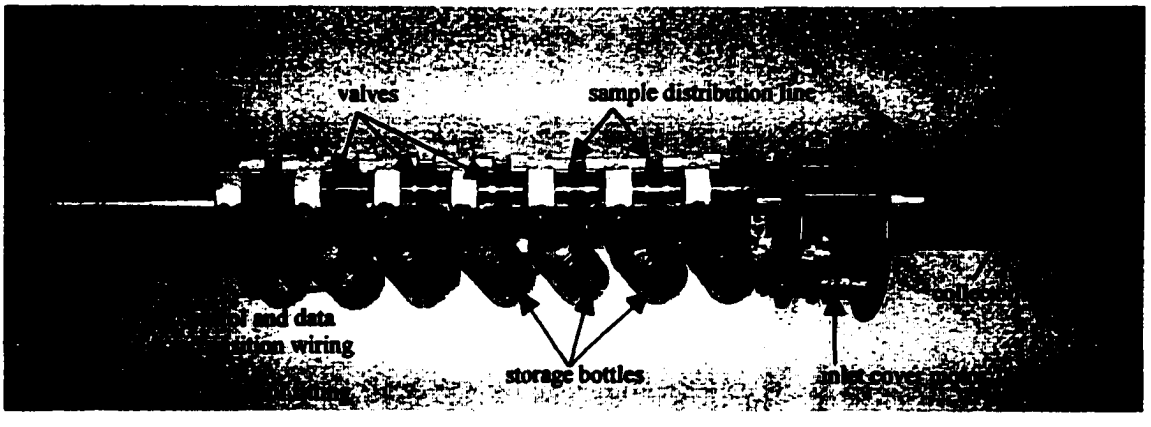

Figure 3.10. A photo of the cloud water collection system showing the inlet cover and sample storage subsystems. The electronics housing and vacuum system flow meter are not visible in this view. All collector subsystems are incorporated into a single structure slides into a PMS canister for rapid installation and removal.

Cloud water is transported from the extraction slot to the storage bottles through a Teflon tubing distribution line. Multiple Teflon solenoid valves (Bio-Chem Valve, 100T2-S804) mounted along the length of the distribution line control the flow of cloud water sample to individual bottles. The storage bottle lids are permanently attached to the outlets of the solenoid valves. Thus, only the sample bottle is removed and replaced between flights. A schematic diagram of the storage bottle setup is provided in Figure 3.11. The storage bottles are angled forward slightly so that seven bottles can be accommodated in the PMS canister (Figure 3.12). Further information regarding the transport of cloud water from the extraction slot to the storage bottles is available in Appendix A.

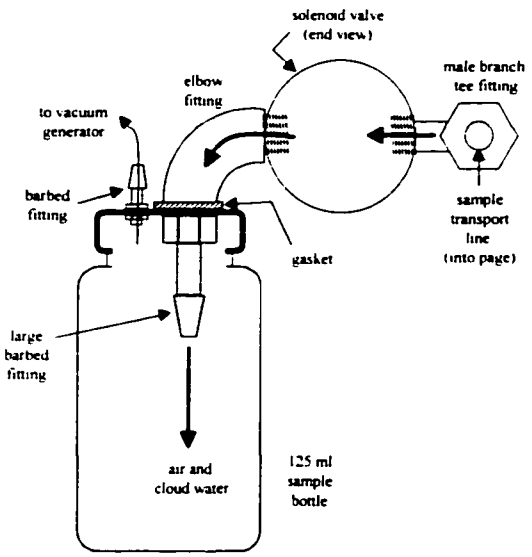

Figure 3.11. Schematic view of a sample storage bottle attached to a Teflon valve. Cloud water travels through the sample transport line from the extraction slot to the storage bottle. When the valve is opened, a suction flow through the small barbed fitting draws the cloud water sample into the bottle through the large barbed fitting.

To promote the flow of cloud water out of the extraction slot, through the sample transport lines and valves, and into the collection bottles, a suction flow is applied to each bottle. Each sample bottle lid therefore supports a second small barbed fitting through which the suction air is drawn (Figure 3.11). A short length of flexible 0.25 in OD polypropylene tubing leads from the small barbed fitting on each bottle to an aluminum manifold and flow meter which are

mounted on the axial-flow cyclone duct (Figure 3.13). The flow meter, in turn, leads to a vacuum generator consisting of a 10 cm long, 1.27 cm OD thin wall aluminum scarf tube that is permanently mounted on the aft end cap of the PMS canister. The flexible line between the flow meter and the scarf tube contains a quick disconnect fitting so that the aft end cap can be separated from the rest of the collection system.

Figure 3.12. The sample storage bottles arranged in series along the aluminum duct of the axial-flow cyclone.

Figure 3.13. Components of the cloud water collector vacuum system mounted on the axial-flow cyclone aluminum duct.

The scarf tube extends into the free stream air flow from the aft end-cap of the PMS canister (Figure 3.14). The exposed end of the scarf tube is cut at an angle to produce a low

pressure region at the tip. Although little information is published regarding the design of scarf tubes, an outlet angle of 22.5° has been used successfully in the past (Schanot, 2000). When traveling at 100 m s^{-1}, the air flow disturbance at the scarf tube tip sufficiently lowers the pressure at that location to induce a suction flow through the entire sample storage system. In flight measurements show that the scarf tube draws approximately 15 l min^{-1} through the sample storage system. While the scarf tube produces a vacuum at all times during flight, a suction flow in the storage system is only realized when one of the upstream storage system valves is opened to complete the flow path. Because a vacuum is drawn on the sample storage system, air-tight fittings and connections were required to prevent air leaks into the system during flight. Two in-flight tests indicated that the vacuum exerted on the sample storage bottles does not cause any sample evaporation over the course of a 10 hour flight.

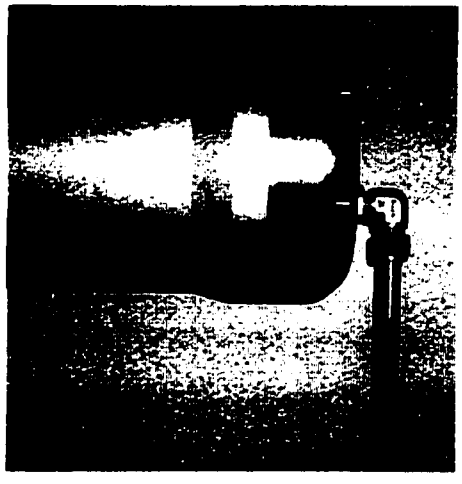

Figure 3.14. Scarf tube located on the aft canister end cap.

3.5 Electronics, sensors, and control system

5.5.1 Power supply

Electrical power on the NSF/NCAR C-130 aircraft is supplied at 115 V AC 400 Hz, 115 V AC 60 Hz, and 28 V DC, all of which are available in the instrumentation pods. The 28 V DC supply was thought to be the most versatile for directly powering the array of electrical

components in the cloud water collection system, and was therefore selected. The major disadvantage of using the C-130 28 V DC power supply, which was not recognized during the design phase, is that the 28 V DC supply is available only after the C-130 lifts off from the ground and becomes airborne. Because the 28 V DC power is typically used for anti-ice applications, that power supply is disconnected in order to prevent overheating while the aircraft is not in motion. The lack of an aircraft generated power supply while parked made it difficult to integrate the system on the C-130 and test its operation. An independent power supply, grounded to the aircraft electrical system, was required for system testing purposes.

The storage system valves were rated for continuous operation at 24 V DC; however, operation of the valves at that voltage for an anticipated 10 to 15 minute sampling period created considerable heat. To decrease the amount of heat produced while the valves were energized, the supply voltage was decreased from the 28 V aircraft supply to 15 V with the use of a DC/DC switching converter (Lambda, PM20-24S15). The return terminal pins on the high and low voltage sides of the DC/DC converter were connected in order to reference the 15 V supply to aircraft ground. Testing showed that while the valves still became warm when operated at 15 V, the aluminum valve mounts conducted the heat rapidly to the aluminum duct and then to the PMS canister, making heating in the interior of the canister negligible. Apart from the inlet cover motor which was driven directly by the 28 V aircraft supply, the 15 V power was used to supply the rest of the system components as well.

Sensors in the cloud water collection system (see below), which draw very little current, share the common 15 V power supply with the storage system valves which draw considerably more current. The operation of the valves can sufficiently perturb the power supply so that sensor output can be affected at times. The valve activity can be detected as spikes in the sensor signals, primarily the temperature signal. Fortunately the disruptions are transitory as the valves are operated only intermittently. In the future, isolation of the sensor power supply from the other components could prevent this minor problem.

3.5.2 Sensors

A Honeywell microbridge mass airflow sensor (AWM5104VN) was installed in the vacuum system line to monitor the storage system suction flow rate. Details regarding the power supply, additional circuitry required for proper operation, and a calibration of the flowmeter are included in Appendix A. A National Semiconductor LM35 integrated circuit temperature sensor was also included in the cloud water collection system, primarily to indicate if the system temperature dropped below 0° C. Operation of the collection system below 0° C should be avoided due to potential problems with ice formation in the sample lines and valves. Appendix A supplies additional information about the temperature sensor.

3.5.3 Actuation

Remote operation of the collection system components, including the inlet cover motor and storage system valves was accomplished with the use of solid state DC/DC relays. A 5 V signal sent from the data acquisition and control laptop in aircraft cabin was used for switching the relays. Each valve in the storage system had a dedicated relay (Crydom MODC5). The relays were configured in a normally open mode so that no power would be supplied to the valves until the 5 V signal was supplied. In this way, the valves ordinarily remained closed. With the application of the 5 V signal to a given relay, the high voltage circuit would be completed and the associated valve would be energized. The single DC/DC relay (NAIS TXS2SA-4.5V) used to operate the inlet cover motor employed a more complicated configuration because it was required to reverse the voltage potential across the motor in order to open or close the cover. More specific information describing the relays used in the axial-flow cyclone cloud water collector is included in Appendix A.

3.5.4 Electronics housing and wiring

All of the electronics were arranged, in a very compact configuration, onto a 4.5 cm by 25.5 cm perforated protoboard and soldered by hand. Micro relays and miniature power supply

components were selected because of the limited space. The circuit board is mounted in an aluminum and lexan enclosure and secured to the axial-flow cyclone aluminum duct via two aluminum mounting rings. The electronics housing is sealed with silicone in order to prevent any water that may be present in the canister, either from a leak in the collection system or from condensation, from entering the housing and shorting out the system.

Twenty three component lead wires pass into and out of the enclosure through a sealed fitting. The lead wires connect relays and power supplies within the electronics enclosure to the motor, storage system valves, and sensors outside the enclosure. Also exiting the electronics housing through a sealed fitting is a bundle of 19 wires for data acquisition, control, and power that arrive from the aircraft cabin. A detailed description of system wiring, including the colors of lead wires and data acquisition and control wires that correspond to various components, is presented in Appendix A.

The schematic diagram in Figure 3.15 shows the wiring diagram for all of the electronic components housed in the PMS canister as well as the routing of individual wires from the PMS canister to the aircraft power supply in the instrumentation pod and to the data acquisition and control laptop in the aircraft cabin. The schematic also indicates the corresponding terminal numbers for each of the Amphenol and Bendex fittings that were required between the PMS canister and the aircraft cabin. Finally, the schematic depicts the configuration of the LabVIEW terminal board located in the aircraft cabin.

3.5.5 Data acquisition and control system

Because the cloud water collector is located externally on the C-130 instrumentation pod, direct access to the collection system is not possible, and all components of the collection system need to be controlled and monitored remotely. For this task, a stand-alone LabVIEW-based control and data acquisition system was developed. A control and data acquisition program (referred to as a virtual instrument or VI) was written and executed in National Instruments'

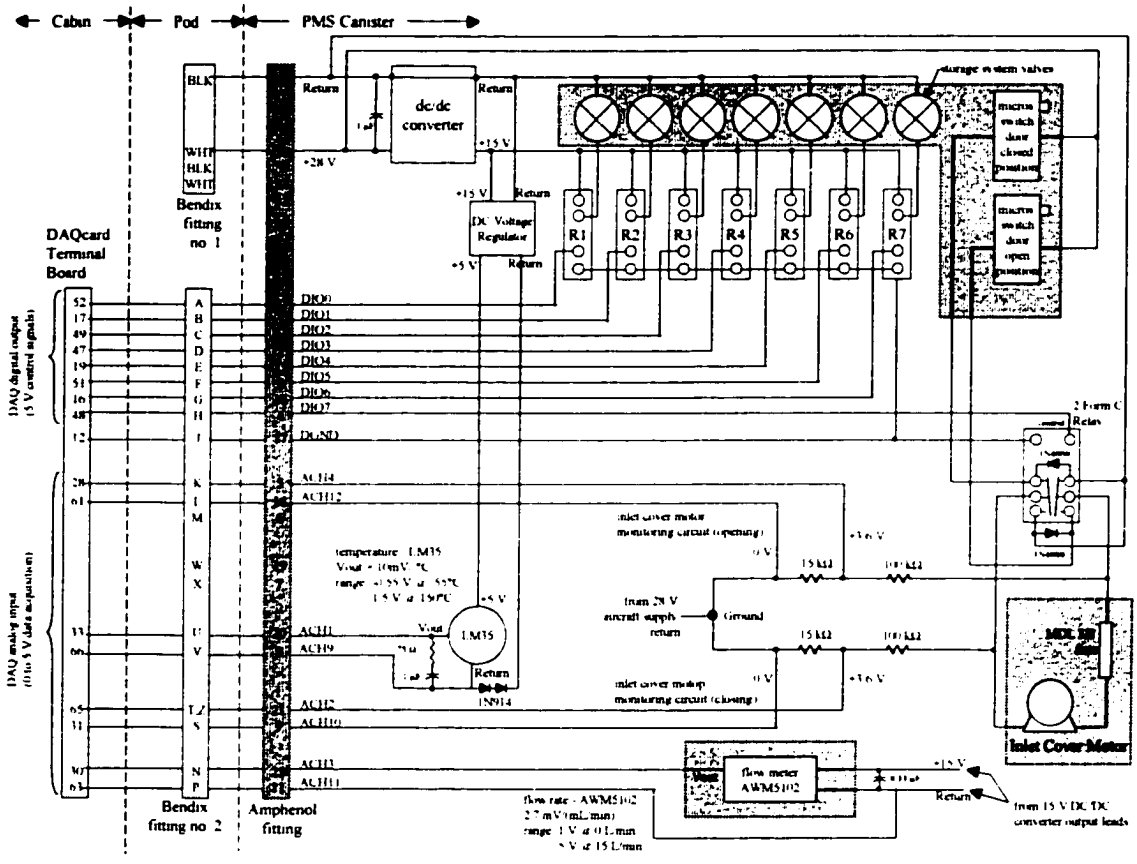

Figure 3.15. Wiring diagram for the axial-flow cyclone control and data acquisition electronic components and connectors. The vertical dashed lines indicate if the component or connector is located in the PMS canister, the instrumentation pod, or in the aircraft cabin. For the components in the PMS canister, the shaded regions indicate components that are mounted outside of the electronics housing. The remaining components are enclosed within the electronics housing.

LabVIEW v5.1 graphical programming environment running on a 697 MHz laptop computer with the Windows 2000 operating system. The LabVIEW program permits sensor output data to be written to the hard drive, provides virtual buttons to trigger events, and displays information graphically in real time to allow an operator to monitor system parameters. The LabVIEW software was coupled with a DAQCard-AI-16XE-50 data acquisition module which interfaced with the collection system's electronics. The capabilities of the DAQCard-AI-16XE-50 more than satisfied the requirements for this application. These capabilities include 16 single end analog inputs with a 0 to ±10 V range, a 200 kHz analog to digital conversion rate, and 8 digital outputs. With space at a premium in the aircraft cabin, the DAQCard also provided the benefit of

small size, occupying a single PCMCIA slot in the laptop computer. A 68 pin cable (National Instruments, PSHR68 and SH6868) connects the DAQCard to a 68 screw unshielded terminal block (National Instruments, CB-68LP) which is mounted in one of the instrumentation racks in the aircraft cabin. The terminal block provides a transition to the 17 wire cable that extends through the C-130 wing to the instrumentation pod and on to the cloud water collector housed in the PMS canister.

All eight of the DAQCard digital I/O lines are used to activate relays in the cloud water collection system. One digital line is associated with each of the seven storage system valve relays and one digital line is associated with the inlet cover motor relay. The digital ground wire is tied into one of the two control terminals on each of the relays to establish a return line. The eight digital I/O lines are configured to normally have a 0 voltage potential with respect to the digital ground line. Individual relays are then triggered by setting the desired digital I/O line to +5 V with respect to the digital ground. The 5 V differential across the relay control terminals is sufficient to trip the relays. The voltage states of the digital I/O lines are controlled within the LabVIEW software.

The LabVIEW VI written for the aircraft cloud water collection system was modified and revised a number of times before the operational version "collector_v5.vi" was finalized. In this VI, four two-wire analog input signals are acquired by the DAQCard and converted to a digital signal at 100 Hz. The four analog inputs correspond to the flow meter, the temperature sensor, the inlet cover motor opening monitor circuit, and the inlet cover motor closing monitor circuit. The LabVIEW VI then averages the 100 Hz data to produce 1 Hz data which is written to a data file and also displayed in real time on the LabVIEW front panel (Figure 3.16). The file name is specified in the LabVIEW front panel, has "_data.xls" appended, and is written to "C:\data\". A time stamp obtained from the laptop internal clock is also written to the data file.

The cloud water collector LabVIEW VI also acquires data from the C-130 aircraft data system for display and recording. The aircraft data system, which reads and stores hundreds of

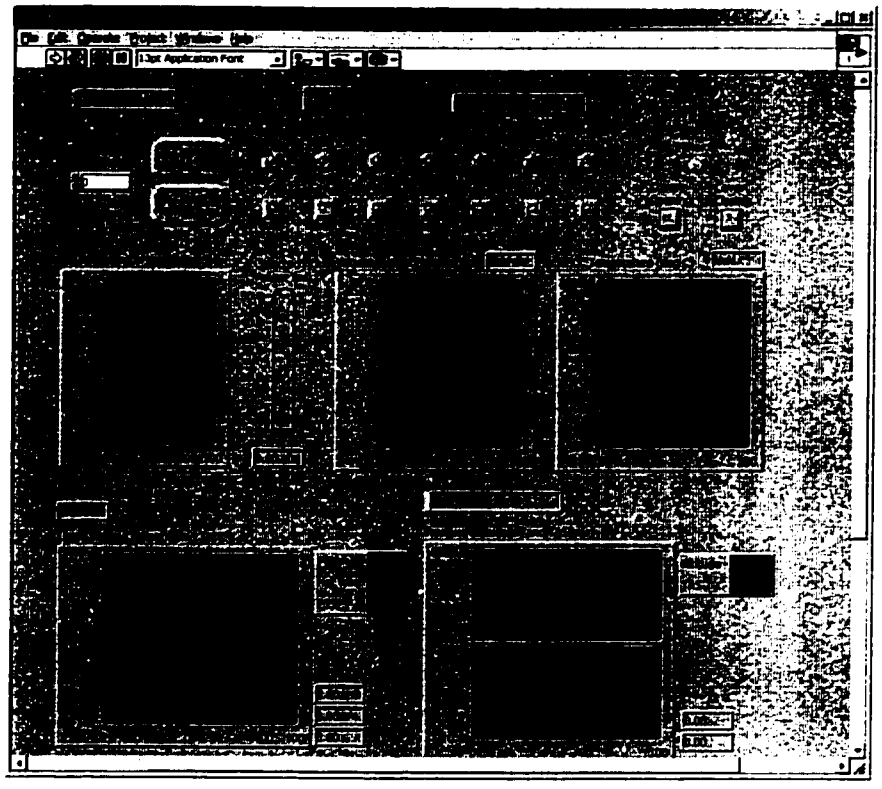

Figure 3.16. The LabVIEW VI front panel showing the graphical displays, indicator lights, and control switches.

inputs from a wide range of instrumentation, transmits a text stream containing the values of selected variables once per second. This text stream is read through the COM1 port by a serial read sub-VI (Prgm_ACFT – Aircraft Data Acquisition (top level).vi) developed by Dean Lauritson (NCAR/ATD). Three independent LWC measurements, the PVM (XGLWC), the hot-wire King probe (PLWCC), and the SPP-100 (PLWCF_LPI) are acquired in real time in this way. In addition, pressure altitude in m (PALT), true air speed in m s^{-1} (TAS), external temperature in °C (ATX), and the aircraft data system time stamp are obtained. In addition to being displayed in graphical form in real time on the front panel, these aircraft data system variables are written to the specified data file along with the cloud water collection system sensor measurements. The variables that are included in the C-130 data system serial text string are changed from one field project to the next. Therefore, future deployments of the cloud water collection system will most likely require the assignment of new index numbers to the index array elements in the LabVIEW

VI. Index numbers corresponding to the locations of desired variables in the C-130 data stream should be used, keeping in mind that the first three variables in the data stream correspond to the aircraft time stamp in hours, minutes, and seconds.

The LabVIEW VI contains a set of virtual switches that can be used to open and close the inlet cover and storage system valves as needed. By selecting the valve or motor number in the appropriate input box on the VI front panel and clicking the button marked "Open Valve/Cover" the appropriate digital I/O line is set to +5 V and the relay in the PMS canister is triggered. Clicking the button marked "Close Valve/Cover" returns the digital line to 0 V and the relay returns to its normally open state and the valve or inlet cover closes. The storage system valves are numbered from 1 to 7, with valve number 1 occupying the forward position in the PMS canister and valve number 7 occupying the aft position. The inlet cover motor is assigned the number 8.

When a storage system valve is opened in this way, an indicator light is illuminated just below the corresponding valve label. The indicator light remains lit until the valve is closed. At the time the valve is opened, a loop is activated to continually update an estimate of the volume of water accumulating in the associated storage bottle. The volume of water entering the storage bottle is predicted once per second by multiplying the PVM LWC measurement by the nominal flow rate through the axial-flow cyclone and by an enhancement factor derived from CFD drop trajectory modeling. This prediction is summed while the valve remains open to produce a total accumulated volume estimate. The accumulated sample volume estimate is displayed graphically on the VI front panel to indicate when a storage bottle is potentially full and the valve should be closed. Following valve closure, a second indicator light is activated. This second light remains illuminated for the duration of the flight as a reminder that that particular bottle has been filled. Further, the final estimate of the accumulated volume of water for that bottle is displayed below the second indicator light. The graphical display of accumulated sample volume resets to zero in preparation for the next sample period.

As with the storage system valves, when the inlet cover is opened an indicator light is illuminated and remains lit until the cover is closed. In addition, while the motor is operating to open the cover, a second indicator light appears to signify that the cover is actually opening. This second indicator is triggered by the 3.6 V output of the motor monitoring circuit, and is extinguished as soon as the cover reaches the fully opened position. A similar indicator light is used to signify when the motor is operating to close the inlet cover.

Whenever an action is initiated via the virtual front panel switches, such as opening a sample storage valve or closing the inlet cover, a text statement describing that command is written to a file in order to form a record of sampling activities. The short text statement simply indicates the type of activity that was performed, the associated valve or motor number, and the local CPU time stamp. Using this file, sample period initiation and termination times are recorded and sample durations can be easily calculated. This information is written to a file with the same name as the data file described earlier, although "_action.xls" is now appended to the name.

In preparation for a research flight, the laptop computer running LabVIEW is placed in an instrumentation rack in the cabin of the aircraft and the DAQCard is connected to the terminal block via 68 pin cable. The cloud water collector VI is initiated and preliminary checks of voltages and aircraft data acquisition can be made. The 28 V DC power is not activated until after takeoff, so sensor readings from the cloud water collector are unavailable until that time. After takeoff, the vacuum system flow rate and canister temperature readings will be displayed on the LabVIEW VI front panel. When the in-cloud target region is reached, cloud LWC can be monitored via the graphical VI front panel display to determine an appropriate time to initiate sampling. The inlet cover is first opened via the front panel virtual controls. Following the indication that the cover has reached its fully open position, one of the sample storage system valves can be opened to start the flow of cloud water sample to the associated bottle. The filling of sample bottles is not restricted to any particular order. The estimated volume of water

accumulating in the sample storage bottle can be monitored and the valve closed after sufficient sample has been obtained. Successive samples can then be gathered immediately by opening additional valves in sequence. Alternatively, if further samples are desired at a later time, the inlet cover can be closed between sample periods.

3.6 Collector installation, removal, and cleaning

The entire cloud water collection system was designed as a single, self-supported, lightweight structure that could be easily inserted into and removed from a PMS canister. This requirement arose from the need to access the collector after every research flight for cleaning and sample bottle removal and replacement, while the PMS canister itself remains affixed to the aircraft. During field projects, the time available between flights can be limited and working conditions are often less than ideal, so the removal and replacement of the cloud water collector structure was designed to be as straightforward and rapid as possible. To accomplish this, a self-contained structure that could easily slide into and out of the canister was developed. The backbone of the entire collector is the axial-cyclone duct to which the front end cap, inlet cover, valves, sample bottles, sensors, and electronics are all secured. The only component that is separate from the rest of the structure is the aft canister end cap, which supports the scarf tube.

After minor modifications are made to a PMS canister (Appendix C), the cloud water collection system can be simply inserted into the front end of the canister and pushed into place. The front end cap is first secured to the canister with the appropriate bolts, the electrical and vacuum fittings are reconnected, and then the aft end cap is bolted to the canister. The installation or removal of the collection system requires 5 to 10 minutes to complete. Detailed procedures for these activities can be found in Appendix C.

Following a research flight, the collection system can be quickly removed from the aircraft and placed in a specially designed stand for transport and servicing. Sample bottles are removed and weighed to determine the amount of sample collected, and aliquots are prepared for

composition analysis. The collection system can then be cleaned with DI water in preparation for subsequent flights. The cleaning process requires some disassembly of the axial-flow cyclone duct in order to access interior surfaces and is fully described in Appendix C.

4 CFD analysis of the cloud water collector

An analysis of the axial-flow cyclone collector design was performed with the finite volume based Computational Fluid Dynamics (CFD) software package, FLUENT v5.0 (Fluent, Inc., Lebanon, NH). The numerical analysis provided predictions of air flow patterns in and around the collector, the flow rate and pressure drop through the collector, and profiles of temperature and pressure in the interior of the collector. In addition, simulations of cloud drop trajectories enabled predictions of collection efficiency, drop splash, and evaporation. In the past, CFD modeling has been applied successfully to a range of multiphase flows (e.g. Asgharian and Godo, 1997; Chen and Ahmadi, 1997; McFarland et al., 1997; Laucks and Twohy, 1998; Jurcik and Wang, 1995; Muyshondt et al., 1996; Swanson et al., 1996). Straub and Collett (1999, 2001, 2002) applied FLUENT's multiphase capabilities to the analysis of two ground-based multi-stage cascade inertial cloud drop impactors with satisfactory results.

The numerical modeling of the axial-flow cyclone was performed with the UNIX versions of FLUENT and the preprocessor GAMBIT running on a four processor Sun Sparc workstation with the Solaris 2.8 (SunOS 5.8) operating system, 1024 MB of real memory, and 3171 MB of swap space.

4.1 Description of the CFD model

Details regarding the theory, solution procedure, and selected parameterizations of the FLUENT CFD model will be presented in this chapter. In reference to the axial-flow cyclone modeling, the term 'continuous phase' refers to air and 'discrete phase' refers to cloud drops.

4.1.1 Continuous phase

The Navier-Stokes equations provide a mathematical description of fluid flow; however, exact analytical solutions to these equations are only available for a limited range of simplified problems. In the case of flow through complex geometries in which an exact solution is not possible, the flow domain can be decomposed into finite control volumes to which the Navier-Stokes equations can be applied, thereby conserving mass and momentum on a control volume basis. The mass and momentum conservation equations are integrated over each control volume in the computational domain to produce a set of algebraic equations that can be linearized and solved numerically.

Because the algebraic equation set is coupled and non-linear, FLUENT employs an iterative method to obtain a solution for steady state problems. The iterative method involves successive linearizations and solutions of the equation set. During each iteration, FLUENT uses a sequential approach to solve the governing equations, resulting in the solution of only one dependent variable at a time. First, the momentum equations, one for each coordinate direction, are sequentially solved using values of pressure and mass fluxes from the previous iteration to generate a velocity field. The resulting velocity field may not satisfy the mass conservation equation and so a correction equation, derived from the continuity equation, is used to ensure mass conservation and update velocity, pressure, and mass flux fields. For this work, the Semi-Implicit Method for Pressure Linked Equations (SIMPLE) (Patankar, 1980; Fluent, 1999) algorithm was selected as the correction equation. During this process, each dependent variable is solved over the entire solution domain using a Gauss Seidel linear equation solver employing a multi-grid technique. After scalar quantities are evaluated and a convergence check is made, further iterations are performed if needed. Convergence is monitored for each conserved variable through residual values, which represent summations over all control volumes of the imbalance in the governing equations. Solutions were deemed to be converged after residuals decrease by three orders of magnitude (normalized residuals $< 10^{-3}$).

The algebraic form of the conservation equations include vector and scalar values at control volume faces, however, only control volume center values are stored. FLUENT provides several interpolation schemes to provide control volume face values. For this work, a second order interpolation method, the Quadratic Upstream Interpolation for Convective Kinematics (QUICK) scheme (Leonard, 1979), was used to reduce the effects of numerical diffusion (Freitas, 1995; Ferziger and Peric, 1999).

In the numerical modeling, continuous phase turbulence was taken into account through Reynolds averaging of the governing equations (Fluent, 1999) followed by closure of the turbulent equation set with a Reynolds Stress Model (RSM). The non-isotropic RSM solves transport equations for individual Reynolds stresses and therefore requires the solution of additional equations beyond those required for two-equation type turbulence parameterizations. This incurs added computational expense and can lead to convergence difficulties; however, the RSM is considered to have superior accuracy in complex flow fields (Launder, 1989).

Explicit calculation of flow properties in the viscosity affected region near wall surfaces was avoided through the use of non-equilibrium wall functions (Launder and Spalding, 1974; Fluent, 1999). Wall functions are semi-empirical equations that are used for the determination of mean velocity, temperature, and turbulence quantities in control volumes adjacent to wall surfaces that would otherwise require an excessively fine mesh for resolution. Wall functions have been successfully utilized in previous modeling efforts designed to investigate gas/particle flows (Griffiths and Boysan, 1996; Gong et al., 1993).

Compressibility effects can become important for flows characterized by a Mach number greater than 0.3 (Munson et al., 1990). For typical NSF/NCAR C-130 research flight speeds of 115 m s^{-1}, the Mach number is approximately 0.3, so compressibility effects were included in the numerical modeling. This was accomplished by calculating the density via the ideal gas law and activating the energy equation to account for the coupling between temperature and pressure.

Finally, only steady state solutions were generated for the continuous phase flow through the axial-flow cyclone. Therefore, any large-scale time dependent flow features that may exist in the flow field were not captured in the numerical modeling performed here. High Reynolds number flows may not reach steady state due to flow separation effects and vortex shedding. A time dependent flow solution would be required to investigate the validity of the steady state assumption.

4.1.2 Discrete phase

Lagrangian particle trajectories are predicted in FLUENT by constructing and then integrating a force balance on individual particles. The force balance relates the acceleration of a particle to the forces acting on it, on a per mass basis. The force balance in the x-coordinate direction is:

$$\frac{du_p}{dt} = F_D(u - u_p) + g_x \frac{(\rho_p - \rho)}{\rho_p} + \left(\frac{\rho}{\rho_p}\right) u_p \frac{du}{dx} + F_x \tag{4.1}$$

where u_p is the discrete phase velocity, ρ_p is the discrete phase density, u is the continuous phase velocity, ρ is the continuous phase density, g is the gravitational vector, and F_X represents additional forces that can be considered. $F_D(u-u_p)$ represents the drag force per unit mass. F_D is the inverse of particle relaxation time and is given by:

$$F_D = \frac{18\mu}{\rho_p D_p^2} \frac{C_D \mathrm{Re}}{24} \tag{4.2}$$

where μ is the continuous phase dynamic viscosity, D_p is the drop diameter, and the Reynolds number, Re, and the drag coefficient, C_D, are given by:

$$\mathrm{Re} = \frac{\rho D_p |u_p - u|}{\mu} \tag{4.3}$$

$$C_D = a_1 + \frac{a_2}{\mathrm{Re}} + \frac{a_3}{\mathrm{Re}^2} \tag{4.4}$$

and a_1, a_2, and a_3 are flow regime dependent constants defined by Morsi and Alexander (1972). The third term on the right hand side of equation 4.1 accounts for continuous phase pressure gradients that influence drop motion. This is a potentially important term in the axial-flow cyclone as low pressure develops along the duct centerline and high pressure develops at the duct walls as a result of the rotational flow field.

Two modifications can be made to the drag force coefficient in order to extend its applicability. The Cunningham slip correction factor is available in FLUENT to address non-continuum effects, but can only be used in conjunction with the Stokes form of the drag law which is valid for particle Reynolds numbers less than 0.1. The particle Reynolds number often exceeds this value in the axial-flow cyclone making the use of the Cunningham slip correction and Stokes drag law inappropriate. Non-continuum effects are greatest for submicron particles (Seinfeld and Pandis, 1998), though there may be some minor influence for the smallest drop sizes modeled in this work. In addition, the drag force can be adjusted by a shape factor in order to predict the trajectories of non-spherical particles, although this was not necessary for the modeling of liquid water drops in this work. Cloud drop Reynolds numbers reach maximum values (Re = 200 for 50 μm drops) for a short duration at the inlet of the axial-flow cyclone where the majority of drop deceleration occurs. Although liquid drops begin to deform at $20 \leq Re \leq 300$, drag force coefficients change by less than 1% for $Re \leq 300$ (Pruppacher and Klett, 1997).

A number of forces that can influence the motion of particles or drops under certain conditions were not included in the particle force balance in this work. The Bassett force, virtual mass force, and Magnus force can be neglected if the particle density is much greater than the continuous phase density and if the flow is dilute (Shirolkar et al., 1996). Thermophoresis, diffusiophoresis, and Brownian motion were all neglected due to the super-micron size of the drops studied (Seinfeld and Pandis, 1998).

The effects of particle/particle interactions are not captured in the Lagrangian discrete phase modeling scheme in FLUENT. For this reason, a maximum discrete phase volume fraction

of 10 to 12% is recommended to ensure a dilute flow in which particle/particle interactions can be neglected. The volume fraction of water in a cloud is typically less than 1×10^{-6}, well below the recommended volume loading, indicating that the absence of particle interaction effects in the trajectory simulations should not significantly affect the modeling results.

FLUENT provides a mechanism to simulate the effects of continuous phase turbulence on particle motion. The Discrete Random Walk (DRW) model, a stochastic eddy lifetime parameterization (Fluent, 1999; Crowe et al., 1998), can be used to generate instantaneous velocity fluctuations that can be added to the mean continuous phase velocity in equation 4.1. The velocity fluctuations are statistically derived from continuous phase turbulence parameters. Including the effects of instantaneous velocity fluctuations on particle motion appears to be beneficial in certain multiphase flow regimes such as inertial impaction (Straub and Collett, 1999; 2001). However, turbulent influences on particle motion can also lead to significant overprediction of particle deposition to wall surfaces, primarily when particles are flowing parallel and adjacent to a wall surface (Straub and Collett, 1999; 2001; 2002). Excessive drop collection in these situations may be the result of inaccuracies in the eddy-lifetime model used for turbulent particle dispersion (MacInnes and Bracco, 1992; Crowe et al., 1998). Random walk models used to simulate the dispersion of particles may erroneously tend to concentrate particles in regions of low turbulent intensity at the expense of regions of high turbulence intensity (MacInnes and Bracco, 1992). Because a significant fraction of cloud drops entering the cloud water collector flow next to the duct wall, cloud drop trajectory calculations were based solely on the mean continuous phase velocity field to avoid excessive deposition of drops to the duct wall. Supplemental trajectory simulations that included DRW turbulent velocity fluctuations resulted in similar predictions of drop collection patterns in the interior of the collector, suggesting that turbulent influences are minor for this case.

Mass transfer from the discrete phase to the continuous phase due to evaporation was explored, and will be discussed in Section 4.4.6.

4.2 Modeling of the axial-flow cyclone

As the design of the axial-flow cyclone progressed, new models with updated geometries were created for CFD flow field analyses. The initial models contained simplified vane and duct geometries and focused on the proper definition of upstream and downstream boundaries. Later models added progressively more complex features, such as the extraction slot geometry, finite vane thickness, and the parabolic inlet leading edge curvature. In all, flow solutions for a series of 12 models with varying geometries were generated. The effects of each added feature on the continuous phase flow field could then be examined. This effort culminated in a final model representing the geometry of the axial-flow cyclone as it was built. Only this final geometry will be discussed in this chapter.

4.2.1 Geometry setup

Geometry creation and mesh generation for all the numerical models was performed with GAMBIT v1.3, the solid model and mesh preprocessor supported by Fluent, Inc. The interior of the axial-flow cyclone was modeled to examine pressure and temperature profiles through the collector as well as the effectiveness of the curved vanes in producing a rotational flow field. To reduce model run time, a 90° sector of the axial-flow cyclone duct was modeled, with rotationally periodic boundary conditions to simulate the existence of a full cyclone duct (Figure 4.1).

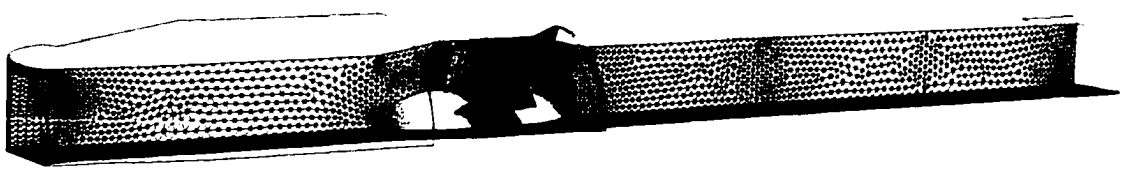

Figure 4.1. The interior flow domain of the axial-flow cyclone cloud water collector containing the curved vane assembly and the extraction slot. The use of rotationally periodic boundary conditions allowed a 90° sector of the duct to be modeled.

Conforming to the "as built" geometry of the collector, the modeled duct has a 6 cm interior diameter which transitions to 7 cm in the region of the curved vane assembly. The

leading edges of the curved vanes are 18.8 cm downstream from the inlet of the collector. The curved vanes are 0.04 in thick, and the center body is 9.37 cm long.

Regions upstream of the inlet and downstream of the outlet were included in the model in order to apply free stream boundary conditions and to study free stream airflow interactions with the inlet and exit geometries (Figure 4.2). The parabolic upstream flow region extends 93 cm upstream of the inlet and the downstream parabolic flow region extended 40 cm downstream of the exit. The entire computational domain was discretized with an unstructured mesh consisting of 152,000 tetrahedron, hexahedron, pyramid, and wedge elements.

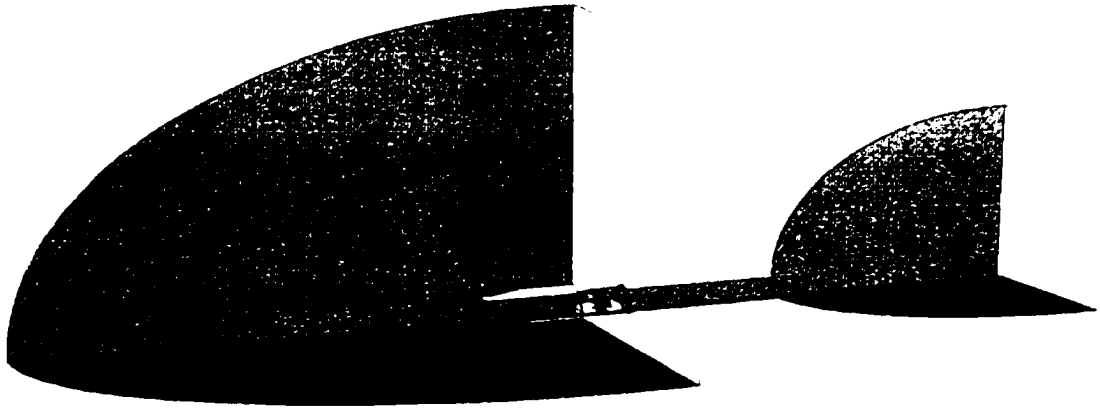

Figure 4.2. The full computational flow domain. Regions upstream of the inlet and downstream of the outlet were included to investigate flow interaction with the inlet and outlet. A freestream velocity of 115 m s^{-1} was applied at the domain boundaries.

4.2.2 Continuous phase properties and boundary conditions

Continuous phase properties were selected to match the standard atmosphere for two altitudes, 3000 m and 1000 m. Air density was calculated via the ideal gas law and was continuously updated throughout the solution procedure in order to account for the effects of compressibility. In order to study the effects of evaporation in the axial-flow cyclone, the continuous phase was assumed to be a mixture of air and water vapor. The heat capacity of the air/water vapor mixture was assumed to be constant at 1000 J kg^{-1} K^{-1}. The thermal conductivity and viscosity were assumed to be independent of temperature and pressure and were calculated

by a mass-weighted mixing law. Thermal conductivity and viscosity averaged 0.0242 w m^{-1} K^{-1} and 1.69×10^{-5} kg m^{-1} s^{-1}, respectively, over the solution domain. The mass diffusivity for water vapor in air was set to 2.88×10^{-5} m^2 s^{-1}.

Boundary conditions that required specification at the domain boundaries included continuous phase velocity, temperature, water vapor mixing ratio, and turbulence properties. The velocity at the domain inlet boundary was specified to be 115 m s^{-1} in the x-direction to simulate collector operation at C-130 research flight cruising speeds. The boundary temperature was 268 K for the 3000 m case and 281 K for the 1000 m case. Air at the domain inlet boundary was assumed to be saturated at the boundary temperature; a condition imposed by setting water vapor mass fractions to 0.0038 for the 3000 m case and 0.0075 for the 1000 m cases. A turbulence intensity of 3% and a turbulence length scale of 1 cm were selected, although previous work suggests that the model is fairly insensitive to these parameters when internally generated turbulence dominates (Straub and Collett, 1999; Muyshondt et al., 1996). Boundary conditions to simulate suction flow at the extraction slot were not included in the model. The domain outlets were specified to have a gauge static pressure of 0 Pa.

4.2.3 Discrete phase properties and boundary conditions

In order to simulate the behavior of liquid water cloud drops, the discrete phase density was specified to be 1000 kg m^{-3}. The heat capacity, thermal conductivity, and latent heat of the liquid drops were assumed to have constant values of 4182 J kg^{-1} K^{-1}, 0.6 w m^{-1} K^{-1}, and 2.26×10^{6} J kg^{-1}, respectively.

For each drop size under investigation, drops were injected into the continuous phase from a 90° sector of a 6 cm diameter circular surface. This injection surface, essentially a projection of the inlet of the modeled collector, was located 30 cm upstream of the leading edge of the collector inlet. The drops were evenly distributed across the injection surface with a spacing of 0.1 cm, resulting in a total of 705 drops injected for each drop size. The drops were

given an initial velocity of 115 m s^{-1} to match the free stream air flow velocity. Initial conditions for the discrete phase were provided in external files which specified position, velocity, and diameter for each series of drops.

Wall surfaces in the model were set to an escape boundary condition for the discrete phase. This boundary condition halts trajectory calculations the moment drops come into contact with a wall surface, simulating the deposition, without splashing or rebound, of cloud drops on the surfaces of the collector. Drop trajectories were calculated in 0.01 cm increments, and the maximum number of calculations per drop was set to 80,000 in order to allow all drop trajectories to come to completion.

4.3 Continuous phase flow solution

In the following sections, the continuous phase flow solution is described in terms of velocity, pressure, and temperature fields. Although the flow solution was generated in a three-dimensional domain, two-dimensional contour, velocity vector, and scatter plots are used to convey information in a clear and comprehensible manner. The two-dimensional plots represent data from a single cross-sectional plane that passes through the duct centerline. Although the velocity, pressure, and temperature fields could potentially vary if the cross-sectional plane is rotated about the duct centerline, the steady state flow solution appears to be symmetrical about the centerline suggesting that any single cross-sectional plane will provide a good representation of the entire three-dimensional domain.

4.3.1 Velocity fields

Contours of the continuous phase velocity along a representative slice through the solution domain are depicted in Figure 4.3. Contours in Figure 4.3 represent total velocity magnitude not just the components of velocity aligned with the plane that is displayed. The velocity at the domain upstream boundary is 115 m s^{-1}, as prescribed in the model boundary conditions. Due to the partial obstruction that the curved vanes present to the airflow in the

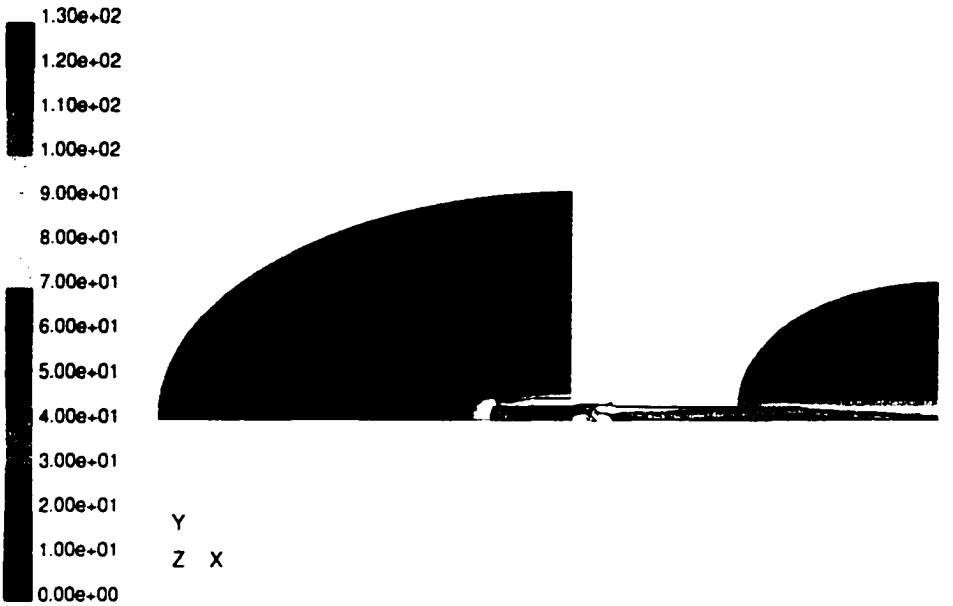

Figure 4.3. Contours of velocity in the axial-flow cyclone (m s^{-1}).

interior of the collector, the air decelerates as it approaches the inlet of the collector, reaching approximately 30 m s^{-1} in the inlet region, which corresponds to a flow rate of approximately 4,900 l min^{-1} (for the 3000m case). Based on the air velocity, the diameter of the duct, and the physical properties of the air flow, the Reynolds number is approximately 9.5×10^4. The subisokinetic inlet condition results in a fraction of the flow diverting around, rather than through, the inlet (Figure 4.4) and has implications for cloud drop aspiration efficiency that will be discussed in section 4.4.2.

The total velocity field can be decomposed into axial, tangential, and radial components. Figure 4.5 shows axial velocity contours and Figure 4.6 shows tangential velocity contours in the vicinity of the inlet and curved vane assembly. In the interior of the collector, the velocity is purely axial in direction upstream of the curved vanes. The axial component of velocity, when averaged over the duct cross section is fairly constant at 30 m s^{-1} through the length of the axial-flow cyclone duct as would be expected through mass conservation arguments.

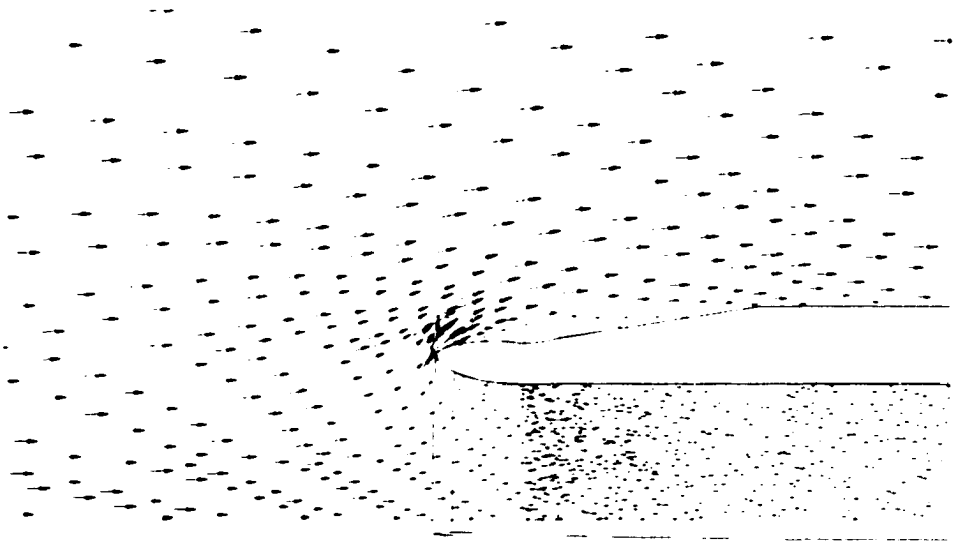

Figure 4.4. Velocity vectors at selected control volume centers in vicinity of axial-flow cyclone inlet. The axial-flow cyclone inlet is subisokinetic.

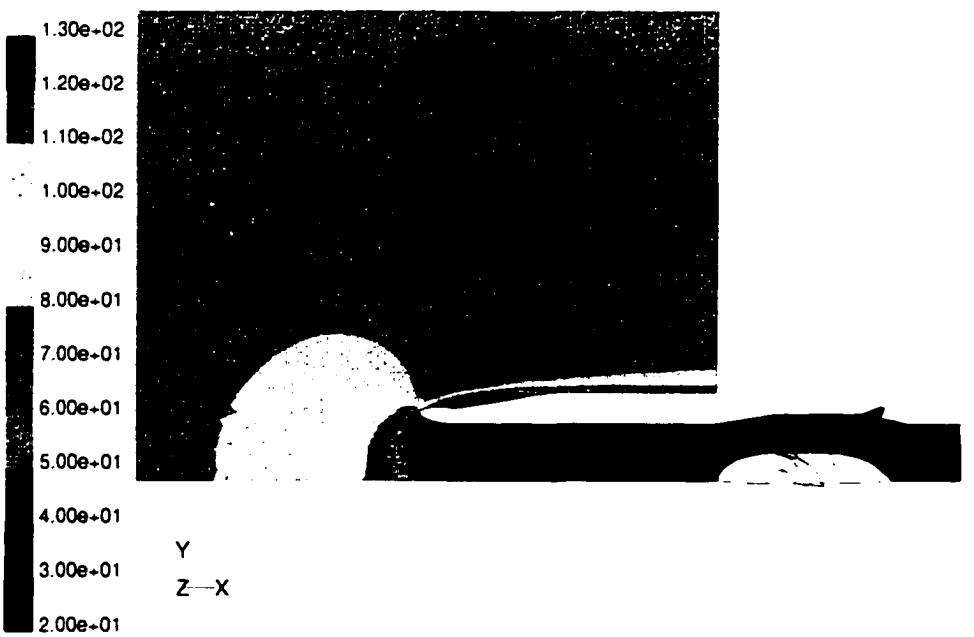

Figure 4.5. Contours of axial velocity in the inlet region of the axial-flow cyclone (m s^{-1}). The freestream axial velocity is 115 m s^{-1} while the velocity in the interior of the axial-flow cyclone duct is approximately 30 m s^{-1}.

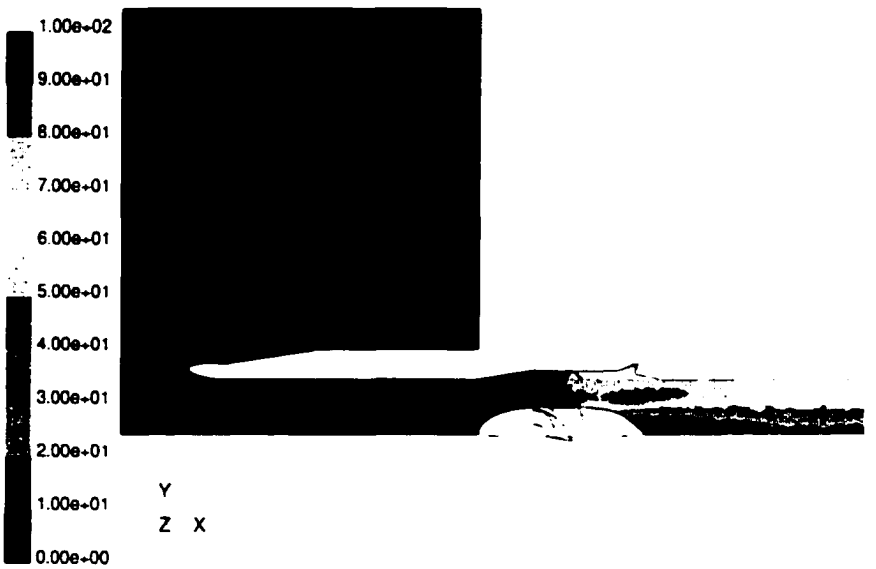

Figure 4.6. Contours of tangential velocity in the inlet region of the axial-flow cyclone (m s^{-1}). Tangential velocity is zero upstream of the curved vane unit and approximately 85 m s^{-1} immediately downstream of the vane unit. Drop separation occurs in the rotating flow field downstream of the vane unit.

The tangential velocity is negligible upstream of the curved vane assembly. However, as the flow passes through the vanes, the tangential velocity immediately accelerates to approximately 85 m s^{-1}. This abrupt increase in the tangential velocity creates a strongly rotational flow field which persists past the extraction slot and slowly decays through the remainder of the duct.

The axial and tangential components of velocity are also presented as a scatter plot which shows velocity as a function of distance through the solution domain (Figure 4.7). The velocities are taken from a single line that passes through the solution domain midway between the vane hub and duct wall. An outline of the collector is included at the top of the figure to identify the location of the inlet, the start of the fixed vane unit, the extraction slot, and collector outlet.

There is no indication of flow separation as the axial-flow cyclone duct diameter increases from 6.0 cm to 7.0 cm through the 9° expansion that maintains a constant cross sectional area in the vicinity of the center hub. However, the numerical modeling indicates that a region of reversed flow develops at the duct centerline downstream of the vanes (Figure 4.8).

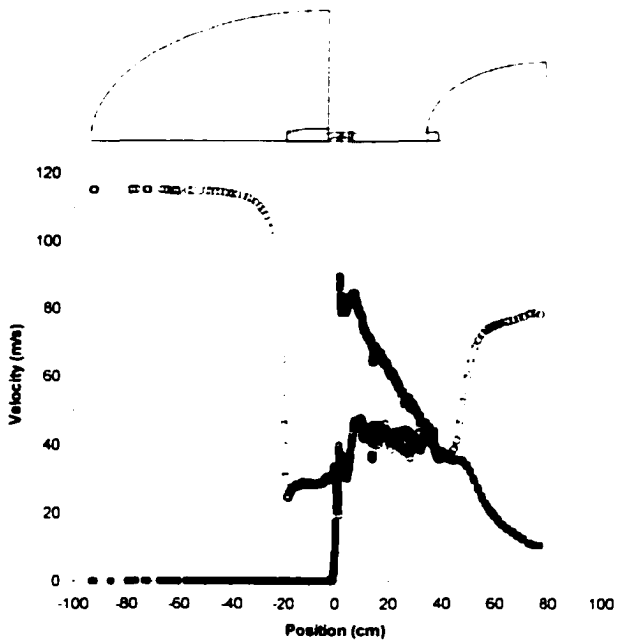

Figure 4.7. Axial (open circles) and tangential (solid squares) components of velocity as a function of position through the axial-flow cloud water collector. The inlet is located at –18 cm, the vanes at 0 cm, and the exit at +37 cm. The axial component of velocity decreases as the flow approaches the collector inlet due to partial stagnation conditions. The tangential component is negligible before increasing to 85 m s^{-1} immediately downstream of the vanes. The tangential velocity then decays through the remainder of the duct.

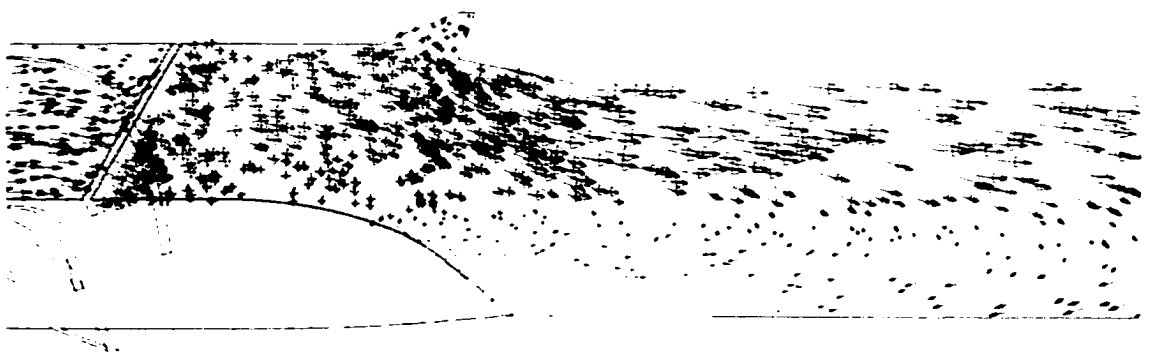

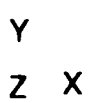

Figure 4.8. Velocity vectors at selected control volume centers showing a region of reversed flow that develops downstream of the vane unit.

The reversed flow is the result of low pressure that arises at the duct centerline due to the rotational flow field. The low pressure region acts to draw downstream air back towards the vane assembly along the duct centerline. Although this effect does not influence drop collection directly, it does contribute to a further deceleration of the air flow and an associated static pressure rise in the axial-flow cyclone duct. This effect is most likely responsible for the CFD calculated flow rate (4900 l min^{-1}) being lower than the flow rate calculated using simple theory (6700 l min^{-1}) mentioned in Section 3.1. The rotational flow field is sufficient for the collection of cloud drops through centrifugal action (see section 4.4), however, the reduction in flow rate due to flow reversal contributes to the subisokinetic sampling conditions that bias collection toward larger drop sizes. Various geometry modifications were investigated through additional numerical modeling in an effort to reduce or eliminate flow reversal in the axial-flow cyclone duct, however, no practical solutions were found.

4.3.2 Pressure fields

Contours of static pressure through the axial cyclone duct are presented in Figure 4.9. Static pressure in Figure 4.9 is shown as gauge pressure, or a deviation from the baseline operating pressure of 70,120 Pa (701 mb) in the model, which corresponds to the standard atmosphere at 3000 m. A baseline pressure of 89,880 Pa was used for the 1000 m case. Gauge static pressure is also shown in scatter plot format as a function of distance through the collector in Figure 4.10.

As the air slows at the inlet of the collector, dynamic pressure ($\frac{1}{2}\rho V^2$) is converted into a static pressure rise, the magnitude of which can be approximated through the Bernoulli equation:

$$P_{static,inlet} = P_{static,freestream} + \frac{1}{2}\rho V^2_{freestream} - \frac{1}{2}\rho V^2_{inlet} \qquad (4.5)$$

where $P_{static,inlet}$ is the inlet static pressure, $P_{static,freestream}$ is the freestream static pressure, ρ is the air density, $V_{freestream}$ is the freestream velocity, and V_{inlet} is the inlet velocity. For airflow along a given streamline, and assuming incompressible flow and a gauge freestream static pressure of 0,

the inlet static pressure ($P_{static,inlet}$) should be approximately 5600 Pa, a value reflected in the numerical modeling.

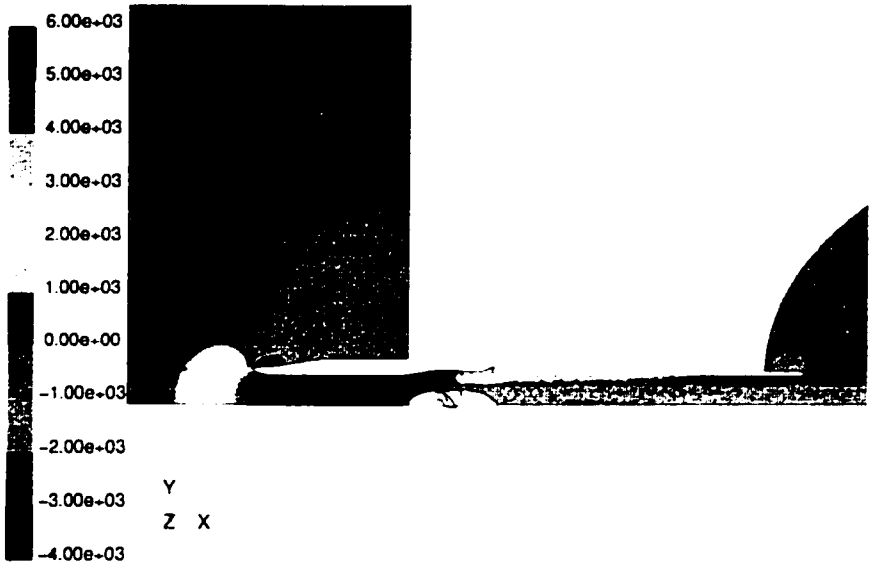

Figure 4.9. Contours of static pressure in the axial-flow cyclone duct (Pa). Contours indicate pressure deviations from the baseline operating pressure of 70,120 Pa and 89,880 Pa for the 3000 m and 1000 m altitude cases, respectively.

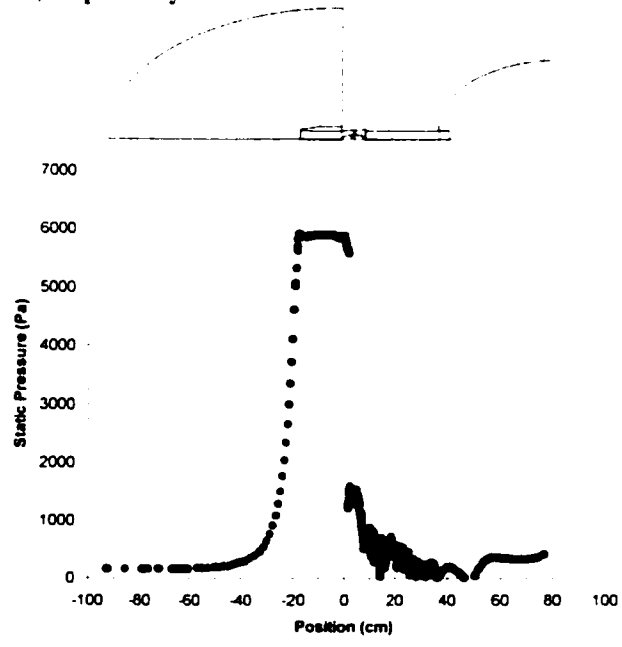

Figure 4.10. Static pressure as a function of position in the axial-flow cyclone (Pa). Pressure is shown as a deviation from the baseline operating pressure of 70,120 Pa and 89,880 Pa for the 3000 m and 1000 m altitude cases, respectively. The inlet is located at –18 cm, the vanes at 0 cm, and the exit at +37 cm. The pressure rise in the first 20 cm of the duct results from the presence of the curved vane assembly which partially obstructs the flow.

4.3.3 Temperature fields

The deceleration of the airstream in the axial-flow cyclone inlet results in compressional heating of the sample stream. A temperature contour plot for the 3000 m case is displayed in Figure 4.11. In addition, Figure 4.12 shows a scatter plot of temperature as a function of distance through the axial-flow cyclone. The temperature increases from the freestream value of 268 K to 274 K in the inlet for the 3000 m case and from 281 K to 287 K for the 1000 m case. This temperature rise results in an increase in the saturation vapor pressure and has implications for evaporation of the cloud water sample, which will be discussed in Section 4.4.6.

4.4 Discrete phase solution

Following the steady state airflow solution, cloud drop trajectories were calculated via integration of a force balance on individual drops. These trajectory simulations were used for predicting collection efficiency, drop shatter, and evaporation.

4.4.1 Cloud drop trajectories

Trajectory calculations for drops 1 μm in diameter and for drops 2 to 50 μm in diameter, in 2 μm increments, proceeded until a wall was encountered or the drops exited the computational domain. For illustrative purposes, 10 sample trajectories for drops 1, 10, and 30 μm in diameter are shown in Figure 4.13.

Due to the subisokinetic sampling conditions of the axial-flow cyclone, some cloud drops approaching the inlet of the collector tend to follow the air streamlines that diverge around the exterior of the inlet (Figure 4.13a). This effect is more pronounced for smaller drops with low inertia, and in the limit only those drops within the limiting air streamlines will enter the collector. On the other hand, as drop diameter and inertia increase, drops can cross the limiting streamline and enter the collector. At sizes larger than approximately 20 μm, 90% of the drops released from the 3 cm radius injection surface enter the collector.

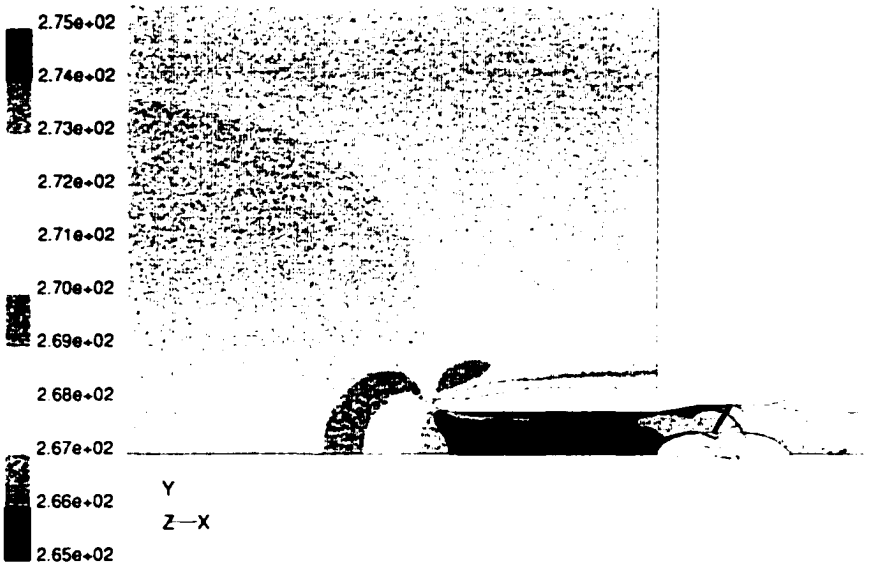

Figure 4.11. Temperature contours in the axial-flow cyclone duct (K).

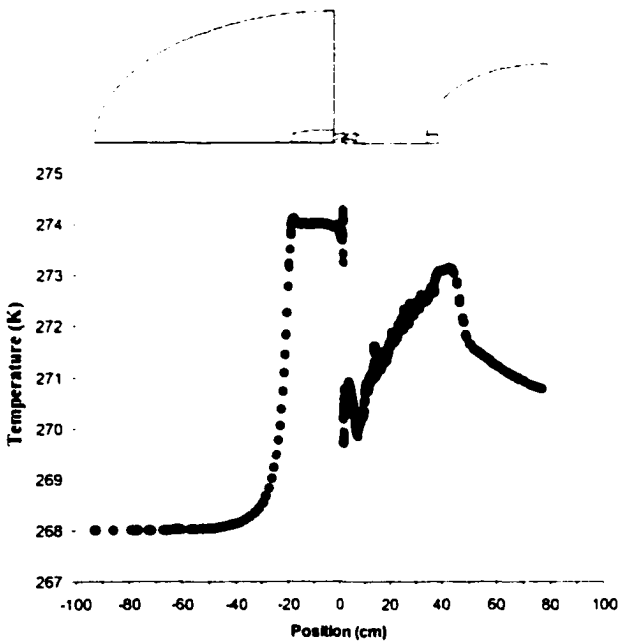

Figure 4.12. Temperature as a function of position in the axial-flow cyclone (K). The inlet is located at –18 cm, the vanes at 0 cm, and the exit at +37 cm. Compressional heating results in a 6 K rise in temperature in the first 20 cm of the duct. The temperature drops as the air re-accelerates in the rotational flow field but then rises again as the flow slows through the remainder of the duct.

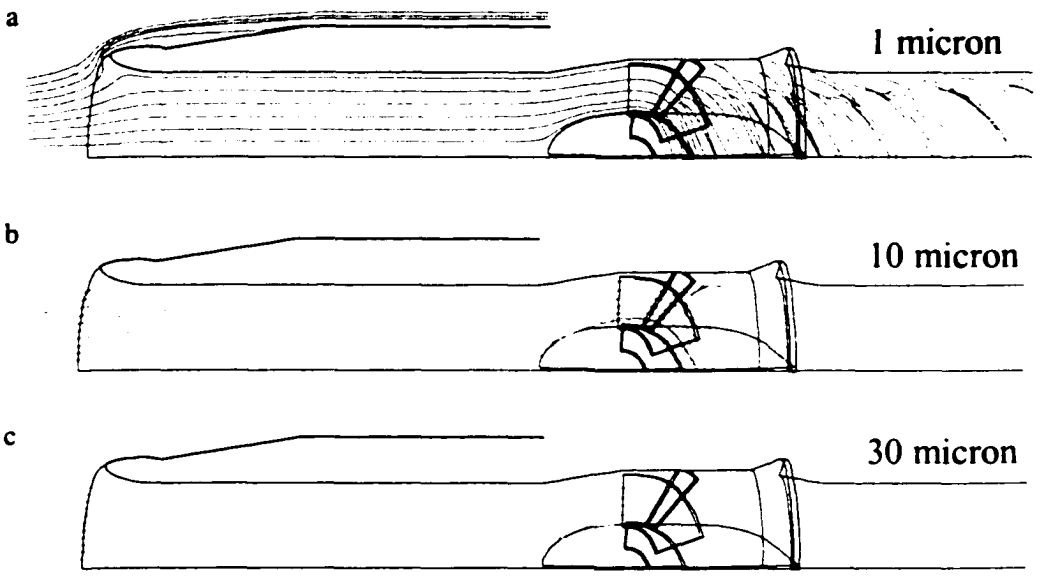

Figure 4.13. Sample trajectories for (a) 1 μm, (b) 10 μm, and (c) 30 μm drops. A fraction of 1 μm drops follow air streamlines around the inlet of the axial-flow cyclone, while the remainder reach the duct wall downstream of the extraction slot and are therefore not collected. 10 μm drops reach the duct wall upstream of the extraction slot and should be collected. 30 μm drops possess enough inertia to impact on the surfaces of the curved vanes.

The drops that enter the inlet travel axially until reaching the rotational flow field. The rotational flow field that develops immediately downstream of the vane unit exerts sufficient centrifugal force on the entrained cloud drops to quickly move them to the duct wall. As indicated in Figure 4.13, large cloud drops migrate to the duct wall rapidly while smaller drops migrate more slowly. Drops one micron in diameter do not reach the wall until well downstream of the extraction slot while ten micron drops move quickly to the duct wall in the rotational flow field and deposit on the wall surface upstream of the extraction slot. 30 micron drops possess enough inertia that they are unable to follow the air flow past the curved vanes and instead impact on the surfaces of the vanes. It was expected that drops impacting on the vanes would be shed off the vane surfaces and into the rotational flow field where they would be quickly removed to the duct wall.

4.4.2 Collection efficiency

The collection efficiency of the axial-flow cyclone was evaluated by releasing drops into the computational domain from an injection surface located 30 cm upstream of the inlet. The escape wall boundary condition, in which trajectory calculations are terminated upon drop contact with a wall surface, allowed the number of drops depositing on any given wall surface to be recorded. Drops from 1 to 50 microns in diameter were used to examine collection efficiency as a function of drop size.

The overall collection efficiency of the axial-flow cyclone was investigated in two parts, an external aspiration efficiency and an internal collection efficiency, which helps to identify the processes that influence the collection of cloud drops in the axial-flow cyclone. The external aspiration efficiency was defined as the percentage of drops released from the injection surface that enter the inlet of the collector. The curved surface of the leading edge of the inlet presents a limited surface area for drops to impact upon. Due to the geometry of the inlet leading edge, a stagnation point develops just inside the lip of the inlet (Figure 4.14).

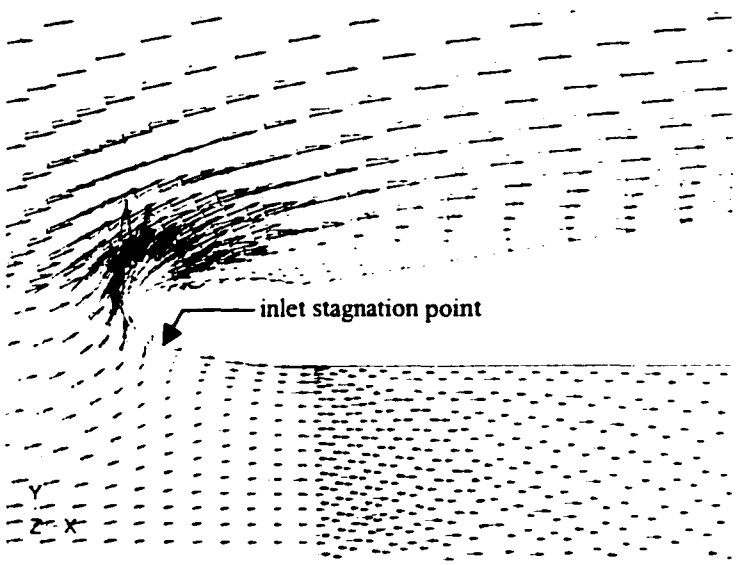

Figure 4.14. Velocity vectors at the inlet of the axial-flow cyclone duct. Cloud drops that impact the duct wall upstream of the stagnation point should be swept out of the inlet while cloud drops that impact the duct wall downstream of the stagnation point should be driven along the duct wall until they reach the extraction slot and are collected.

This stagnation point delineates air that does not enter the inlet from air that does enter the inlet. Cloud drops that impact on the small area upstream of the stagnation point were assumed to be swept out of the inlet by the air flow and therefore not collected. Cloud drops impacting downstream of the stagnation point were assumed to be collected as they should be driven by the airflow along the length of the inlet wall surface and ultimately to the extraction slot. Subject to these assumptions, the external aspiration efficiency is illustrated in Figure 4.15 for the 1000 m and 3000 m cases. Because the collector operates at subisokinetic conditions, collection efficiency is lowest at small drop sizes and increases with increasing drop size. As particles become larger, their increased inertia allows additional drops to cross through the limiting air streamline and pass through the partial stagnation at the inlet of the collector.

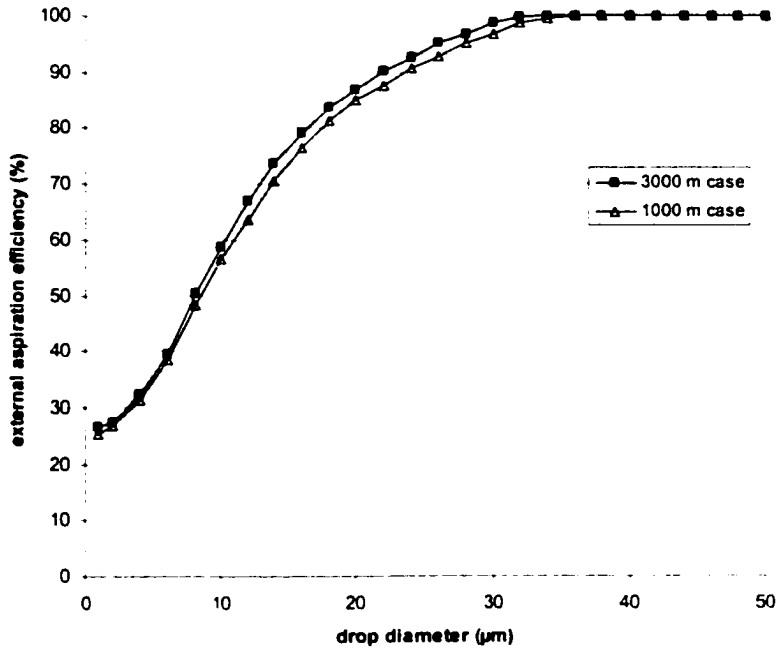

Figure 4.15. External aspiration efficiency for the 3000 m case (filled squares) and 1000 m case (open triangles).

The internal collection efficiency of the axial-flow cyclone was calculated as the percentage of drops entering the collector that reach the duct wall upstream of the extraction slot. This definition of collection efficiency assumes that all drops that reach the duct wall upstream of

the extraction slot flow under the influence of the adjacent rotational shear flow along the duct wall, into the extraction slot, and are removed for storage. Cloud drops that impact on the curved vane assembly, including the vanes and the center body, were assumed to flow off of these surfaces, enter the rotational flow field, and reach the duct wall upstream of the extraction slot and therefore be collected. Because the flow of liquid water on wall surfaces could not be easily modeled, the validity of these assumptions was unknown prior to flight and laboratory testing. Laboratory testing has since suggested that drops that impact on the vanes do reach the duct wall upstream of the extraction slot, drops that impact the center body do not reach the duct wall upstream of the extraction slot and therefore remain uncollected, and water that accumulates on the duct wall upstream of the extraction slot is not necessarily extracted with perfect efficiency (for details regarding the laboratory testing see Chapter 5). With the extraction slot in its final location at 5.5 cm downstream of the vane leading edge, internal collection efficiency increased rapidly with increasing drop diameter for the 1000 m and 3000 m cases (Figure 4.16). Figure 4.17 shows internal collection efficiency for the two cases if drops that impact on the center hub remain uncollected. At small drop sizes, the effect is minor because the drops can follow the airflow around the center hub. However, as drop size and inertia increase, a higher fraction of drops tends to impact on the center hub, accounting for the fates of approximately 15% of 50 μm drops.

Combining the external aspiration efficiency and the internal collection efficiency, the resulting overall collection efficiency for the axial-flow cyclone as a function of drop size is shown in Figure 4.18 for the 1000 m and 3000 m cases. This overall collection efficiency represents the number of cloud drops that reach the duct wall upstream of the impaction surface divided by the number of drops that would be swept out by the cross-sectional area of the axial-cyclone inlet. In Figure 4.18, curves that assume that cloud drops impacting on the center hub are collected are shown together with curves that assume that drops impacting on the center hub remain uncollected. By comparing the external aspiration efficiency, the internal collection

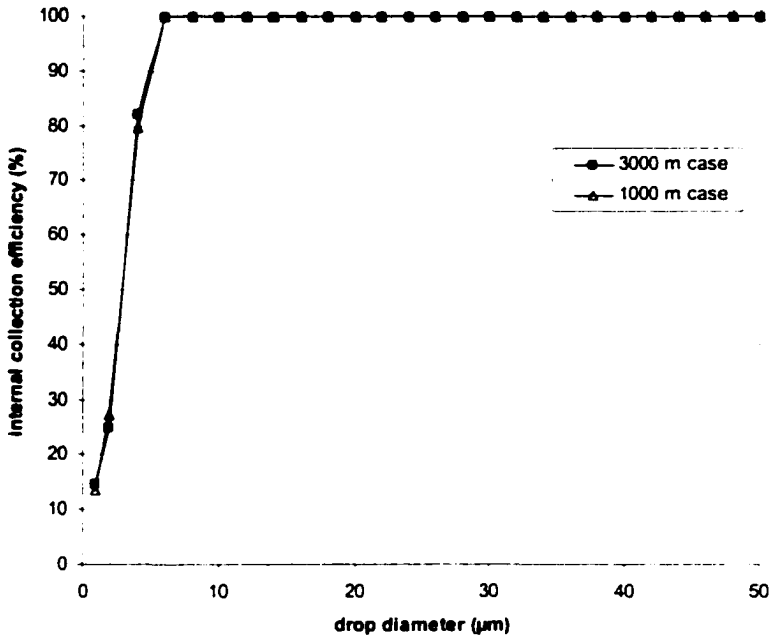

Figure 4.16. Internal collection efficiency curves for the 3000 m case (filled squares) and 1000 m case (open triangles).

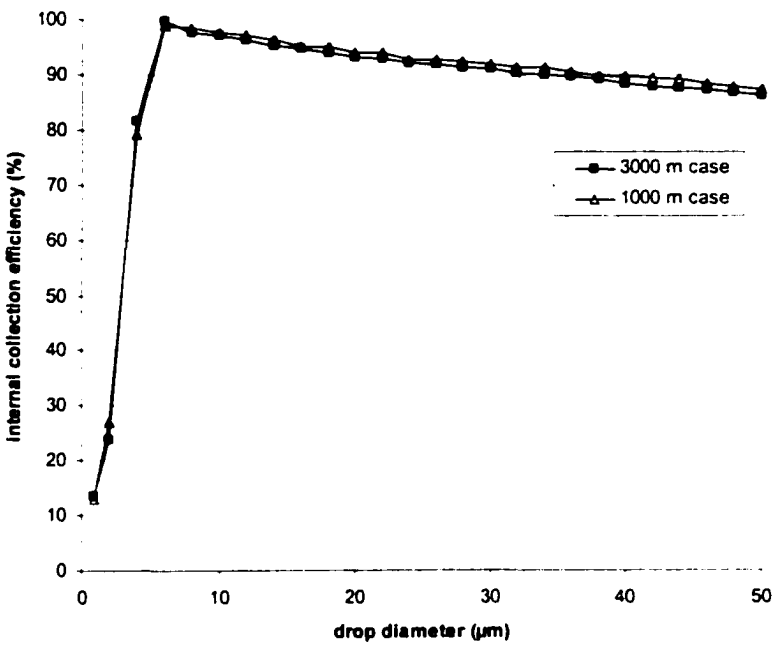

Figure 4.17. Internal collection efficiency curves assuming that drops that deposit on the center hub remain uncollected. Curves are shown for the 3000 m case (filled squares) and 1000 m case (open triangles).

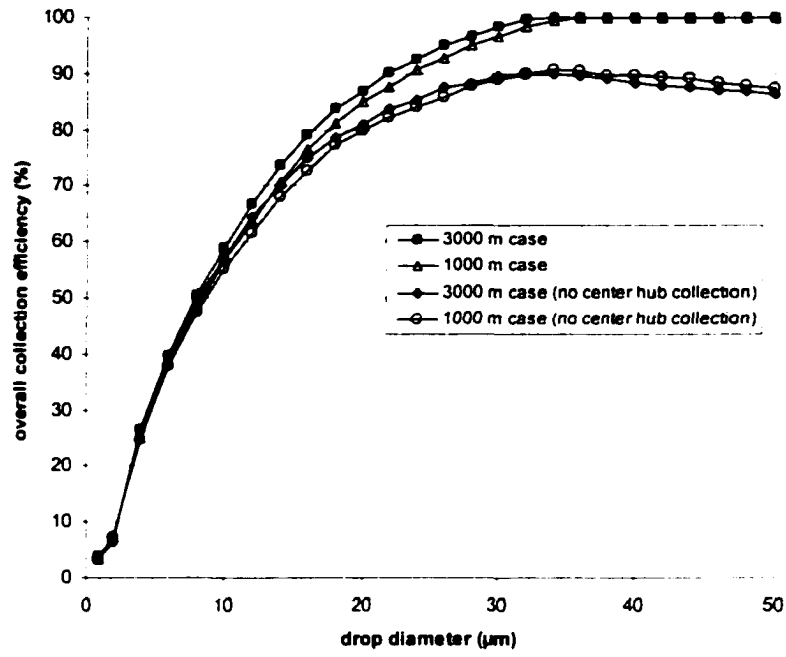

Figure 4.18. Total collection efficiency curves for the axial-flow cyclone cloud water collector. Curves for four cases are represented: based on the assumption that drops depositing on the center hub are collected for operation at 3000 m (filled squares) and 1000 m (open triangles), and based on the assumption that drops depositing on the center hub remain uncollected for operation at 3000 m (filled diamonds) and 1000 m (open circles).

efficiency, and the overall collection efficiency, it can be seen that the subisokinetic sampling conditions are primarily responsible for the collection behavior at small drop sizes. The overall Dp_{50}, the diameter at which 50% of the drops are collected, is approximately 8 microns.

As a side note, a numerical model was constructed with a vane outlet angle of 30° as opposed to the baseline 25° outlet angle. The collection efficiency was found to be nearly identical to the 25° case, and was not pursued further.

4.4.3 Inlet misalignment modeling

Experimental evidence has suggested that the passing efficiency of aircraft-based aerosol sampling inlets is sensitive to mounting location on the aircraft and orientation with respect to the free stream airflow (Baumgardner and Huebert, 1993). Similar orientation and misalignment effects were considered as a potential problem for the aspiration of cloud drops into the axial-flow cyclone cloud water collector. During flight, the NSF/NCAR C-130 typically assumes a 4°

angle of attack resulting in flow streamlines that are oriented at a 4° angle relative to the axis of the collector, provided that local streamlines are not further modified by the structure of the aircraft. This was not accounted for in the CFD-based flow field analysis and cloud drop trajectory simulations described in the previous section, which assumed isoaxial flow conditions, i.e. that the freestream flow field was aligned with the axial-cyclone duct. It was not known if the misalignment of the inlet with the air streamlines would sufficiently influence the motion of cloud drops so as to prevent their entry into the inlet of the collector.

The original model, which reduced the computation domain to a 90° sector of the axial-flow cyclone duct, could not be used to capture non-isoaxial flow effects. A model containing the full 3-D geometry of the axial-flow cyclone, mounted in a PMS canister, was developed in order to investigate inlet misalignment effects (Figure 4.19). The interior of the duct was not modeled; rather, interior duct conditions from the original modeling effort were used to constrain the flow rate through the axial-flow cyclone. Drops from 2 to 50 μm were injected into the flow field in a fashion similar to the previous modeling. Figure 4.20 shows the external aspiration efficiency as a function of drop size for the axial-flow cyclone at a 4° angle of attack. The original 0° angle of attack external aspiration efficiency is also included in Figure 4.20, and suggests flow field modification at low angles of attack should not significantly alter the collection efficiency and sample collection rate.

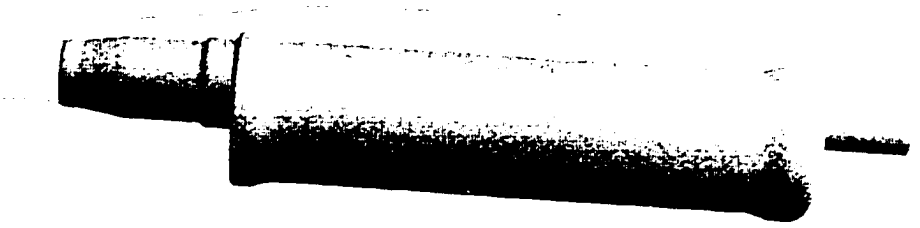

Figure 4.19. 10 μm drop trajectories for collector operation at a 4° angle of attack.

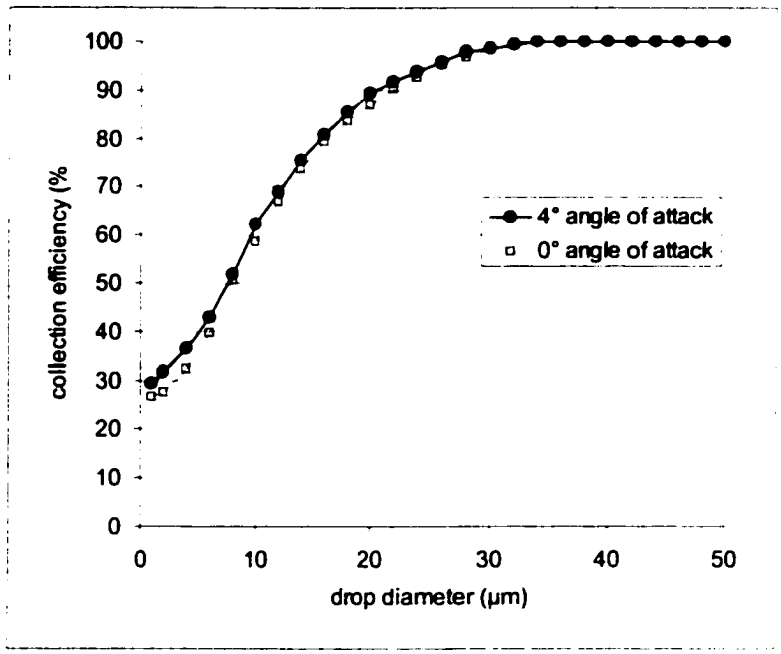

Figure 4.20. External aspiration efficiency for the 0° (open squares) and 4° (filled circles) angle of attack cases.

This modeling also indicates that flow perturbations created by the blunt forward end cap of the PMS canister are minor and have little effect on inlet aspiration. Other airflow/airframe interactions that may distort local streamlines have not been investigated. The NSF/NCAR C-130 wing and instrumentation pod on which the collector is mounted are the most likely structures that may influence the flow field around the collector.

The passing efficiency of aircraft aerosol inlets is also hampered by the deposition of a significant fraction of aerosol particles in the turbulent region in the interior of inlets. The turbulence results primarily from flow separation at sharp inlet edges (Wilson and Seebaugh, 2001; Huebert et al., 1990). Flow separation was not observed to occur in the modeled axial-flow cyclone inlet, most likely as a result of subisokinetic inlet conditions and the blunt shape of the inlet leading edge. However, if inlet turbulence is responsible for cloud drop deposition on the interior of the axial-flow cyclone, the cloud drops that deposit should simply be transported along the wall due to aerodynamic drag and should eventually reach the extraction slot and be collected.

4.4.4 Extraction slot geometry and placement

The CFD based cloud drop trajectories aided in the placement of the extraction slot in the axial-flow cyclone duct. After examining the distances required for drops to reach the wall of the axial-flow cyclone downstream of the curved vane assembly, the location of the circumferential extraction slot was selected such that drops greater than 5 μm impact the duct wall upstream of the slot and smaller drops impact the duct wall downstream of the slot. This configuration allows the majority of cloud drops to be captured while excluding most interstitial aerosol particles and unactivated haze drops.

The geometry of the extraction slot was derived from the slot geometry of Walters et al. (1983). The cloud water separator of Walters et al. relied on a suction flow rate of approximately 55 lpm to draw water out of the extraction slot and into sample bottles. After modeling the Walters et al. geometry (Figure 4.21), it was theorized that the small width (1.5 mm) of the extraction slot inhibited the rotational flow field from extending through the depth of the slot, preventing the cloud water from being centrifugally forced to the bottom of the slot where it could be removed. In addition, a strong radial flow away from the slot was observed (Figure 4.21b) which may have hindered water from flowing into the slot. A high extraction flow rate may have been required to compensate for these problems.

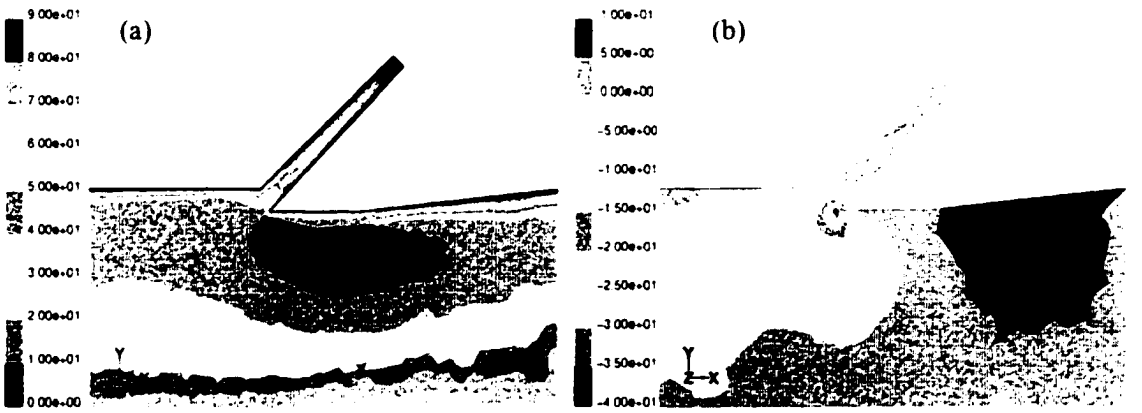

Figure 4.21. Contours of tangential (a) and radial (b) air velocity in the region of the extraction slot for the Walters et al. (1983) centrifugal separator geometry (m s^{-1}). The strong rotational flow field fails to extend through the depth of the extraction slot (a). In addition, air flowing in the radial direction away from the extraction slot (b) may have necessitated an excessive suction flow rate to draw water out of the slot. The 55 l min_{-1} suction flow was not included in these simulations.

For the new axial-flow cyclone, a wider, shallower slot design was employed. By increasing the width and reducing the depth of the slot, it was hoped that the rotational flow would persist throughout the slot to promote the flow of water to the bottom of the slot where it could be easily extracted. In addition, a sharp protruding lip was avoided in an effort to perturb the flow as little as possible. Through these modifications it was hoped to develop a more efficient system for the removal of water from the duct wall at lower suction flow rates. The numerical modeling showed that the rotational flow field developed by the curved vanes did uniformly extend through the depth of the slot, that there was no radial flow away from the slot along the forward edge and overall flow disruption was minor, and that cloud drops would accumulate in the slot if drops were allowed to rebound from wall surfaces. However, as mentioned earlier, it was impossible to model the actual flow of liquid water along a wall surface, so the ultimate outcome of these modifications was unknown prior to flight testing. Flight testing and subsequent laboratory flow testing revealed that despite the promising continuous phase flow field indicated by the modeling effort, water did not readily flow into the extraction slot for collection. There is some indication that water flowed over the slot rather than into it, the cause of which is not easily identifiable (see Chapter 5 for further discussion).

4.4.5 Drop shatter and re-entrainment

Cloud drops that enter the collector inlet with enough inertia to impact the curved vanes rather than pass through to the rotational flow field may shatter if the kinetic energy at impact is sufficiently high (Rein, 1993). Drop shatter can result in the formation of multiple secondary drops that may be too small to be effectively collected. Through experimental analysis and the use of dimensionless parameters to describe drop/surface interactions at impact, regimes in which the outcome of a drop/surface collision is likely to result in drop deposition or shattering have been identified (Cossali et al., 1997; Rein, 1993; Mundo et al., 1995). The non-dimensional groups commonly used to define the limits of deposition and shattering are the Weber number

(We), the drop Reynolds number (Re), and the Ohnesorge number (Oh), which are defined as follows:

$$We = \frac{\rho V^2 D_p}{\sigma} \tag{4.6}$$

$$Re = \frac{\rho V D_p}{\mu} \tag{4.7}$$

$$Oh = \frac{\mu}{(D_p \sigma \rho)^{1/2}} \tag{4.8}$$

where ρ is liquid density, D_p is drop diameter, V is drop velocity at impact, σ is liquid surface tension, and μ is liquid dynamic viscosity. Although the Weber, Reynolds, and Ohnesorge numbers are frequently used to describe drop shatter phenomena, they do not represent three independent dimensionless groups. The Weber, Reynolds, and Ohnesorge numbers can be related as follows: $Oh=We^{1/2} Re^{-1}$.

Experimental studies by Mundo et al. (1995) covered a range of conditions for the impact of drops on a solid, dry surface. The authors determined the drop deposition/splash limit to be:

$$(Oh\ Re^{1.25})_L = 57.7 \tag{4.9}$$

This implies that that drops tend to splash if the value of $Oh \cdot Re^{1.25} > 57.7$, and drops completely deposit on a surface if $Oh \cdot Re^{1.25} < 57.7$. Their results were independent of impact angles between 35° and 87° and independent of surface roughness for values of non-dimensional surface roughness (R_{nd} = mean roughness height / drop diameter) of 0.03 and 0.86. Stow and Hadfield (1981) found that surface roughness does affect the drop deposition/splash limit, although their results only deviate from those of Mundo et al. (1995) for $R_{nd} < 0.01$, in which case the energy required for drop shatter increases as surface roughness decreases. Further work that verifies the findings of Stow and Hadfield (1981), and also indicates that drop splash may be dependent on surface roughness is provided by Range and Feuillebois (1998). In any event, the 1.0 μm surface roughness for the Duraform GF glass-filled nylon used in the SLS fabrication of the curved vanes

results in a non-dimensional roughness ranging between 1.0 and 0.02 for drops from 1 to 50 μm in diameter, indicating that the deposition/splash limit of Mundo et al. (1995) is applicable for the axial-flow cyclone.

In the collector, after the curved vanes are initially wetted, drop impact may be influenced by the presence of a liquid film on the vane surface. Cossali et al. (1997) studied the phenomenon of drop shatter for drop impact on a thin liquid film, finding the following relation to describe the deposition/splash limit:

$$(Oh^{-0.4}\ We)_L = 2100+5880\ \delta^{1.44} \tag{4.10}$$

where δ is the non-dimensional film thickness:

$$\delta = \frac{h}{D_p} \tag{4.11}$$

and h is the film thickness. The drop deposition/splash limit is valid for $0.1 < \delta < 1.0$ and for $Oh > 0.007$.

Using drop impact velocities calculated during the numerical trajectory simulations, and the drop deposition/shatter limits defined above, the propensity for drop shatter in the axial-flow cyclone was evaluated. The relevant impact velocity is the velocity normal to the impact surface (Mundo et al., 1995). Impact velocities derived from the initial axial-flow cyclone geometry in which the curved vane unit was placed 8.8 cm downstream of the inlet leading edge indicated that drop shatter would be likely for drops larger than 18 μm (assuming impact on a dry surface) or 30 μm (assuming the presence of a thin film). In order to lessen the chance of drop shatter, the inlet was extended by 10 cm, allowing additional time for cloud drops to decelerate in the low velocity inlet flow field before impacting the curved vanes. The total and surface-normal drop impact velocities in the "as-built" axial-flow cyclone geometry are displayed in Figure 4.22. Drops between 22 and 24 μm are able to slow to the inlet air velocity (~30 m s^{-1}) by the time they impact. Smaller drops slow to the inlet air velocity, but are reaccelerated as they pass into the converging portion of the vanes before impact. Due to their inertia, larger drops are unable to

completely decelerate from 115 m s^{-1} before impacting the blade surfaces and therefore have impact velocities greater than 30 m s^{-1}. Based on the geometry of the curved vanes, the component of velocity normal to the vane surface was determined.

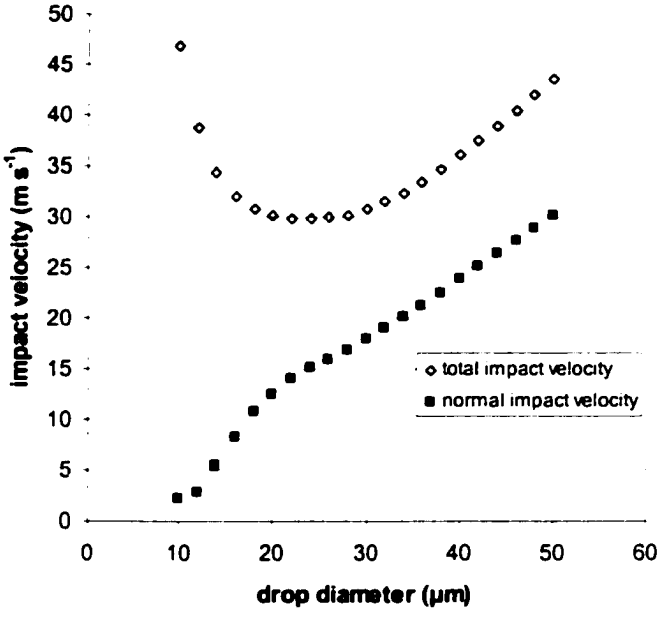

Figure 4.22. The impact velocity of drops that deposit on the surfaces of the curved vanes. Total velocity (open diamonds) and the component of velocity normal to the wall surface (filled squares) are shown.

If the curved vanes are assumed to be dry, the correlations of Mundo et al. (1995) predict that drops larger than 30 μm should shatter upon impact. Incidentally, the same result is obtained if a critical Weber number of 150 is used to define the drop deposition/splash limit, although there is some dispute as to the validity of that practice (Rein, 1993; Moore, 2001).

If a liquid film is present, the calculation of the drop deposition/splash limit, $(Oh^{-0.4}\ We)_L$, is dependent upon the non-dimensional film thickness (δ) which varies with actual film thickness and drop diameter. The drop deposition/splash limits for film thicknesses of 2, 5, and 10 μm are shown in Figure 4.23 as a function of drop size. Also shown in Figure 4.23 is the value of $Oh^{-0.4}$ We for the impact of drops on the curved vanes in the axial-flow cyclone as a function of drop size. Splashing can be expected when $(Oh^{-0.4}\ We) > (Oh^{-0.4}\ We)_L$. If a film thickness of 5 μm is

assumed to be present on the vane surfaces, the drop deposition/splash limit of Cossali et al. (1997) predicts that only drops larger than 46 μm will shatter, ensuring that the majority of cloud drops impacting the vane surfaces will simply deposit there. An increase in film thickness will shift the drop deposition/splash limit to larger sizes, while a decrease in film thickness will shift the limit to smaller sizes. Unfortunately, the relations of Cossali et al. (1997) are not valid for $\delta < 0.1$, which occurs for thin film thicknesses and large drop diameters. In this case, the drop deposition/splash limit should probably revert to the dry surface case.

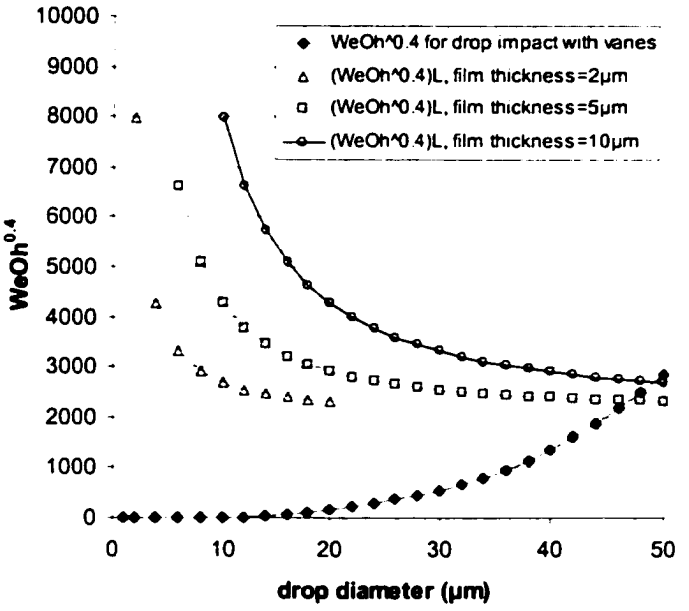

Figure 4.23. The quantity ($WeOh^{0.4}$) for the conditions encountered in the axial-flow cyclone cloud water collector (filled diamonds). Also included are values of ($WeOh^{0.4}$) that designate the drop deposition / splash limit for thee film thicknesses: 2 μm (open triangles), 5 μm (open squares), and 10 μm (open circles). Drop splash is expected for $(WeOh^{0.4}) > (WeOh^{0.4})_L$.

Larger drops, ranging in size from the typical cloud drop limit of 50 μm up to precipitation drops on the order of mm, are therefore likely to shatter if they impact the curved vanes. The experimental work of (Mundo et al., 1995) indicates that the secondary drops that form should have diameters between 10 – 20% of the original drop diameter for conditions similar to those experienced in the axial-flow cyclone. If this is the case, the secondary drops would be large enough to be collected in the rotational flow field of the axial-flow cyclone.

Further information regarding the characteristics of secondary drops can be found in Samenfink et al. (1999).

4.4.6 Evaporation

The temperature rise in the inlet of the axial-flow cyclone due to deceleration of the airflow raises the saturation vapor pressure of water and can therefore result in evaporation of cloud drops or cloud water on the cyclone wall. Evaporation of the cloud water can lead to biases in the measurement of chemical concentrations. To quantify the extent to which evaporation may occur in the collector, estimates of evaporation were made for suspended drops flowing through the collector and for a liquid water film on wall surfaces of the collector.

4.4.6.1 Evaporation of suspended drops

FLUENT offers a vaporization scheme which allows the evaporation from liquid drops to be evaluated. This is accomplished by defining the discrete phase as "droplets" rather than inert particles and initiating Law 2 for mass transfer between the discrete and continuous phases. The change in mass for an evaporating drop is given by the following expression (Fluent, 1999):

$$m_p(t+\Delta t) = m_p(t) - N_i' A_p M_i \Delta t \tag{4.12}$$

where m_p and $m_p(t+\Delta t)$ represent the mass of the drop at times t and $(t+\Delta t)$, A_p is the surface area of the drop, M_i is the molecular weight of species i', and N_i' is the molar flux of vapor defined by:

$$N_i' = k_c\left(C_{i',s} - C_{i',\infty}\right) \tag{4.13}$$

Here, the mass flux from the drop to the continuous phase is proportional to the gradient in water vapor concentration from the drop surface to the bulk continuous phase (Fluent, 1999), with k_c representing the mass transfer coefficient, and $C_{i',s}$ and $C_{i',\infty}$ representing the molar water vapor concentration at the drop surface and in the bulk continuous phase, respectively. The mass transfer coefficient is obtained through a Nusselt correlation for forced convection around a

sphere which incorporates the drop Reynolds and Schmidt numbers (Bird et al., 1960; eqn. 21.2-24). The bulk continuous phase water vapor concentration is defined through the governing continuous phase transport equations. For this work, the bulk continuous phase water vapor concentration was dictated by the mass concentrations specified at the domain upstream boundary and was not modified by evaporation from the discrete phase. The drop surface water vapor concentration is derived from the saturation vapor pressure at the drop temperature, a function of temperature only and defined by a seventh order polynomial fit adapted from Table 15.2 of Seinfeld and Pandis (1998) for temperature (T) in K and saturation vapor pressure (P_{sat}) in Pa:

$$P_{sat} = a_0 + a_1 T + a_2 T^2 + a_3 T^3 + a_4 T^4 + a_5 T^5 + a_6 T^6 \qquad (4.14)$$

where a_0=6.95433526×10^5, a_1=-1.88222246×10^4, a_2=2.12717924×10^2, a_3=-1.28577113×10^0, a_4=4.38717045×10^{-3}, a_5=-8.01803174×10^{-6}, and a_6=6.13682093×10^{-9}. This treatment ignores the solute effect and may therefore over predict the evaporation rate for small drop sizes. A heat transfer equation which balances the heat storage in the drop, the convective heat transfer to the drop, and the latent heat required for evaporation is solved simultaneously with the mass transfer equation to determine the drop temperature.

Evaporation of cloud drops during transit through the collector was investigated through this mass/heat transfer scheme for the 3000 m and 1000 m cases. The percent loss in mass due to evaporation was calculated for the period from drop entry into the solution domain until deposition of the drops downstream of the vanes or on the curved vanes. The predicted percent mass loss as a function of drop diameter is illustrated in Figure 4.24. Significant mass loss through evaporation is predicted at small drop sizes. Depending on altitude, a loss of 78 to 91% is expected for 2 μm drops and 23 to 27% for 4 μm drops. However, evaporational losses decrease rapidly with increasing drop size. Drops 10 μm in diameter should experience a 3 to 5% loss and drops greater than 20 μm should lose less than 1% of their mass. Evaporation is greater

for the 1000 m case despite an identical temperature rise in the collector (~7 K) for the two cases. This result is due to the non-linear increase in saturation vapor pressure with temperature.

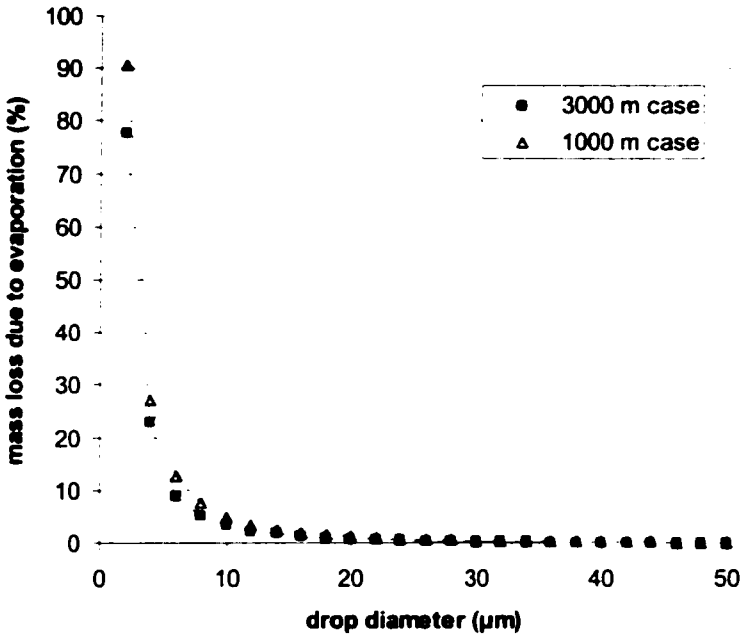

Figure 4.24. Evaporation of suspended drops in the axial-flow cyclone.

The evaporation of drops as predicted through the numerical modeling was corroborated with drop evaporation calculations employing the classic cloud drop condensation/evaporation equation (e.g. Seinfeld and Pandis, 1998 Eqn. 15.74), which includes solute effects and was modified to include ventilation effects (Pruppacher and Klett, 1997) on mass transfer. Drop velocities and continuous phase temperature and pressure were extracted from the numerical modeling trajectory calculations in order to define the conditions experienced by a cloud drop passing through the collector. Due to limitations in the output products of the numerical modeling, the process was fairly cumbersome and only 10 μm drops for the 3000 m case were studied. Using this technique, the percent mass loss due to evaporation for 10 μm drops was 2.3%, slightly lower than the numerical modeling prediction of 3.25%. The lower evaporation rate obtained here may be due to the inclusion of solute effects that lower water vapor pressure over the drop.

Because chemical concentrations measured in bulk cloud water samples will be typically governed by large drops which typically contribute the most to collected sample volume, the effects of small drop evaporation on measured concentrations should not be significant. In addition, the collection efficiency of the axial-flow cyclone at small drop sizes is relatively low, so that few small drops would be included in the sample to begin with. More concern would be warranted if drop size segregated samples were being collected. Drops larger than 6 μm experience less than a 5% decrease in diameter, suggesting that evaporation should not affect collection efficiency due to changes in the inertial characteristics of the drops.

4.4.6.2 Evaporation from wall surfaces

The majority of cloud drops that enter the inlet of the axial-flow cyclone collector deposit on the duct wall just upstream of the extraction slot due to centrifugal forces in the rotational flow field or impact the curved vanes if they possess enough inertia. However, drops also deposit on the duct wall upstream of the curved vane unit due to the influence of the radially diverging flow field at the collector inlet resulting from the subisokinetic flow in which a component of velocity is directed toward the wall of the duct. The cloud drops that accrete on the duct wall upstream of the curved vanes flow under the influence of aerodynamic drag toward the extraction slot where they would theoretically be collected. The accumulated cloud water flowing along the duct surface will be subject to evaporation in the elevated temperature region in the collector.

To bound evaporation from the duct wall in the axial-flow cyclone, mass and heat balances (Bird et al., 1960 Eqns. 21.1-2 and 13.1-1) were applied to a liquid water film that was assumed to cover all wall surfaces in the collector. These surfaces included the duct wall from the inlet to the extraction slot, the extraction slot itself, the vanes, and the center hub. The mass and heat balances were combined, along with the Clausius-Clapeyron equation, following a procedure similar to the one detailed by Seinfeld and Pandis (1998) for the coupling of mass and

heat transfer for drop condensation/evaporation. The resulting equation predicts the mass loss from a wall surface due to evaporation:

$$\frac{dm}{dt} = \frac{S_\infty - 1}{\frac{RT}{Ak_c M_w e_s(T_\infty)} + \frac{h_{fg} M_w}{RT_\infty}\frac{h_{fg}}{hAT_\infty}} \tag{4.15}$$

where S is the saturation ratio ($e(T_\infty)/e_s(T_\infty)$) in the bulk continuous phase, R is the universal gas constant, T is the wall surface temperature, T_∞ is the bulk continuous phase temperature, A is the wall area, M_w is the molecular weight of water, $e_s(T_\infty)$ is the saturation vapor pressure at T_∞, k_c is the mass transfer coefficient, and h is the heat transfer coefficient. The heat and mass transfer coefficients were taken from correlations given in Bird et al. (1960) for highly turbulent (Re > 20,000) flow through pipes. The correlations are given by:

$$\frac{hD_p}{k} = 0.026(\mathrm{Re})^{0.8}(\mathrm{Pr})^{\frac{1}{3}} \tag{4.16}$$

$$\frac{k_c D_p}{D_v} = 0.026(\mathrm{Re})^{0.8}(Sc)^{\frac{1}{3}} \tag{4.17}$$

where D_p is the duct diameter, k is thermal diffusivity, D_v is mass diffusivity, Re is the Reynolds number, Pr is the Prandtl number, and Sc is the Schmidt number. The heat (h) and mass (k_c) transfer coefficients were calculated to be 88.9 w m^{-2} K and 0.099 m s^{-1}, respectively.

Wall evaporation rates were calculated for flight conditions at 3000 m and 1000 m using equation 4.15, which assumes that the bulk continuous phase saturation ratio remains constant despite the addition of water vapor due to evaporation. At the predicted rate of evaporation (see below), the water vapor density only increases by 0.1%, which negligibly impacts the saturation ratio and makes the above assumption valid. In addition, equation 4.15 assumes that the liquid water film has no heat capacity, and that there are no surface curvature or solute effects. If the entire 509 cm^2 interior surface of the axial-cyclone duct were covered with a film of water, the expected evaporation rates would be 0.24 g min^{-1} at 3000 m flight conditions and 0.32 g min^{-1} at

1000 m flight conditions. These evaporation rates are compared to potential collection rates on the order of 3 to 5 g min^{-1} for LWC in the range of 0.2 to 0.3 g m^3. Consequently, sample evaporation and corresponding solute concentration increases are expected to be less than 10% for typical sampling conditions.

A reduction in evaporation could be achieved by reducing the time that cloud drops are exposed to high temperature, sub-saturated conditions, and reducing the potentially wetted surface areas of the collector. However, a reduction in these values leads to higher drop impact velocities. There is a competing need to slow drops in low velocity regions to prevent drop splash at impact and to reduce the exposure to low velocity regions that warm and become sub-saturated.

4.4.7 Predictions of collection rate

Based on the collection efficiency curves derived from the numerical trajectory simulations, estimates of sample collection rates could be made and required durations for sample collection could be predicted. The rate of sample collection depends not only on the collection characteristics of the collector, but also on the LWC of the cloud and the drop volume size distribution. In an effort to examine collection rates for a range of possible sampling conditions, a series of lognormal size distributions were used to represent the drop size distributions for typical stratocumulus clouds. Each lognormal distribution was represented by a geometric mean diameter (Dp_g) and a geometric standard deviation (σ_g). Cloud water collection rates were predicted for geometric mean diameters between 6 and 26 μm. In order to predict collection rates solely as a function of LWC and Dp_g, a constant sigma value of 1.2 was selected for all lognormal cloud drop distributions. This value of σ_g has been found to be representative of non-precipitating cloud drop distributions (Feingold and Heymsfield, 1992; Feingold et al., 1998).

The lognormal distributions were first used to partition a given LWC into 2 μm increment bins. The maximum water available for collection in each bin, in g min^{-1}, could then

be determined from the bin LWC, the aircraft velocity, and the area of the collector inlet. The CFD derived collection efficiency curve could be applied to this distribution of available water to determine the fraction of water that would theoretically be collected; this predicted collection rate could be further reduced through estimates of evaporation losses. An example of this process for a LWC of 0.4 g m^{-3} and a drop size distribution possessing a mean diameter of 16 μm and a geometric standard deviation of 1.2 is illustrated in Figure 4.25. The maximum cloud water available for collection, equivalent to the collection rate if the system was 100% efficient and evaporation was negligible, is shown as a function of drop diameter in Figure 4.25. Because collection efficiency and the evaporation of suspended drops are both functions of drop size, collection rates that take these effects into account are also plotted as a function of drop size. Evaporation from wall surfaces in the axial-flow cyclone is treated as independent of drop size:

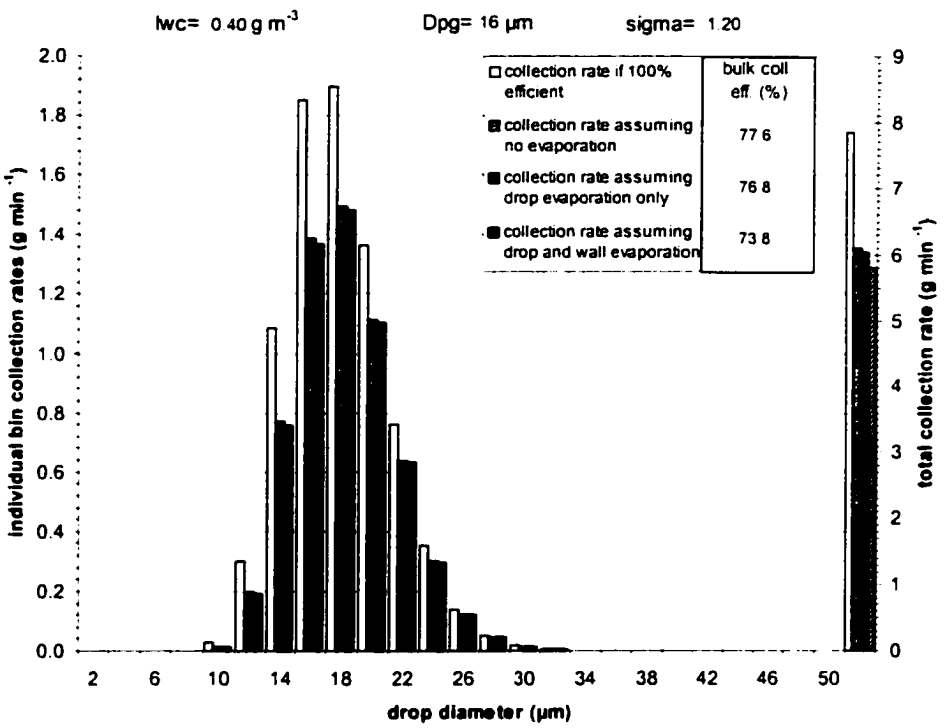

Figure 4.25. Collection rate as a function of drop diameter based on CFD derived collection efficiency and evaporation.

therefore, the reduction in collection rate due to wall evaporation is only included in the group of bars that sum collection rates for all drop sizes. The collection efficiency curve used to generate Figure 4.25 assumes that sampling was occurring at 3000 m and that drops that impact the cyclone's center hub remain uncollected. As can be seen in Figure 4.25, at small drop sizes where collection efficiency is low, a significant fraction of the available water remains uncollected due to subisokinetic sampling conditions. The reduction in collection rate due to drop evaporation is also more prevalent at small drop sizes, as would be expected.

By summing the collection rates in each of the bins, total cloud water collection rates could be predicted. The rightmost grouping of bars in Figure 4.25 shows the total collection rates for the example conditions stated above. The maximum available water for collection is 7.85 g min^{-1}, of which 6.10 g min^{-1} should enter the inlet of the collector and be collected, if evaporation is neglected. If evaporation of suspended drops flowing through the axial-flow cyclone duct is considered, the bulk collection rate falls slightly to 6.03 g min^{-1}. As discussed in Section 4.4.6, evaporation from wall surfaces is assumed to be a function of the wetted wall surface area of the collector rather than a function of drop size, and was calculated to be 0.24 g min^{-1} for the 3000 m case. When this is included, the final collection rate is predicted to be 5.79 g min^{-1}. It is apparent that evaporation from wall surfaces, at least as calculated in Section 4.4.6, is a more significant factor than evaporation from suspended drops.

Total collection rates were predicted for sampling conditions exhibiting LWC in the range of 0.1 g m^{-3} to 0.8 g m^{-3} and mean drop diameters from 6 to 26 μm. Geometric standard deviations were held constant at 1.2. Predicted collection rates that neglect evaporation range from less than less than 2 g min^{-1} to greater than 13 g min^{-1}, and are displayed in Figure 4.26. Calculations of suspended drop evaporation and wall evaporation suggest that collection rates will be reduced by the percentages given in Figure 4.27, with evaporation from wall surfaces accounting for the majority of total evaporation as indicated in Figure 4.28.

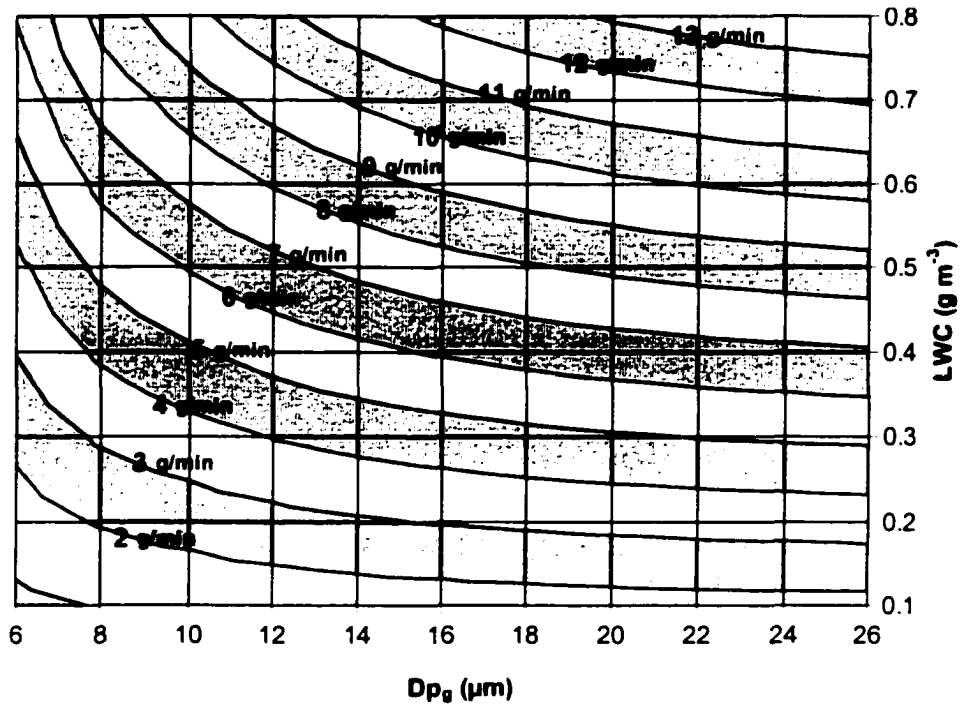

Figure 4.26. Total predicted collection rate as a function geometric mean diameter. Evaporation is neglected.

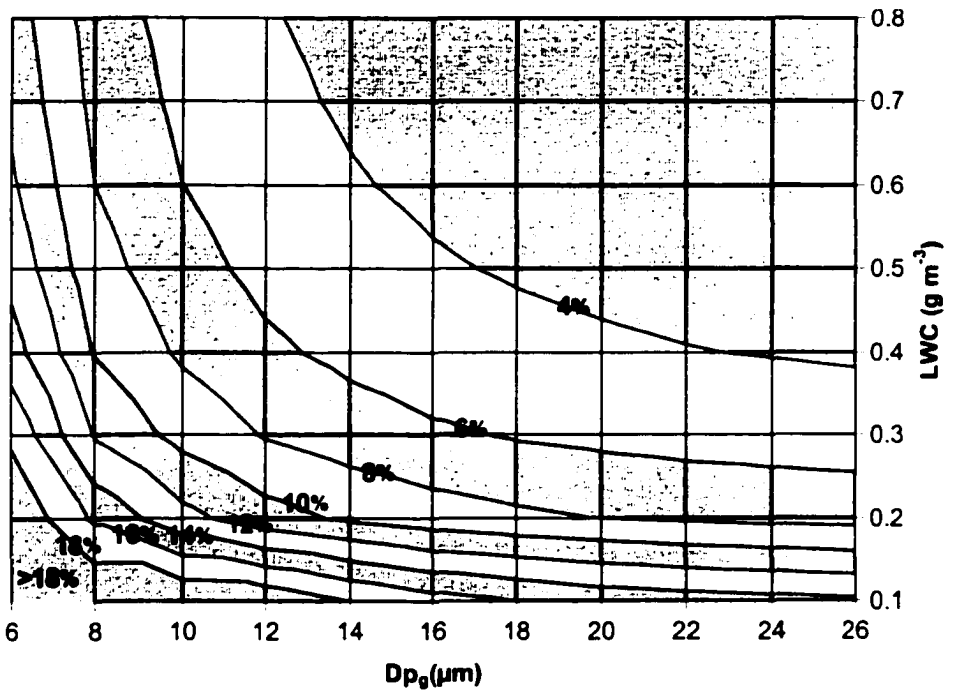

Figure 4.27. Percent reduction in total collection rates due to the evaporation of suspended drops and from wall surfaces.

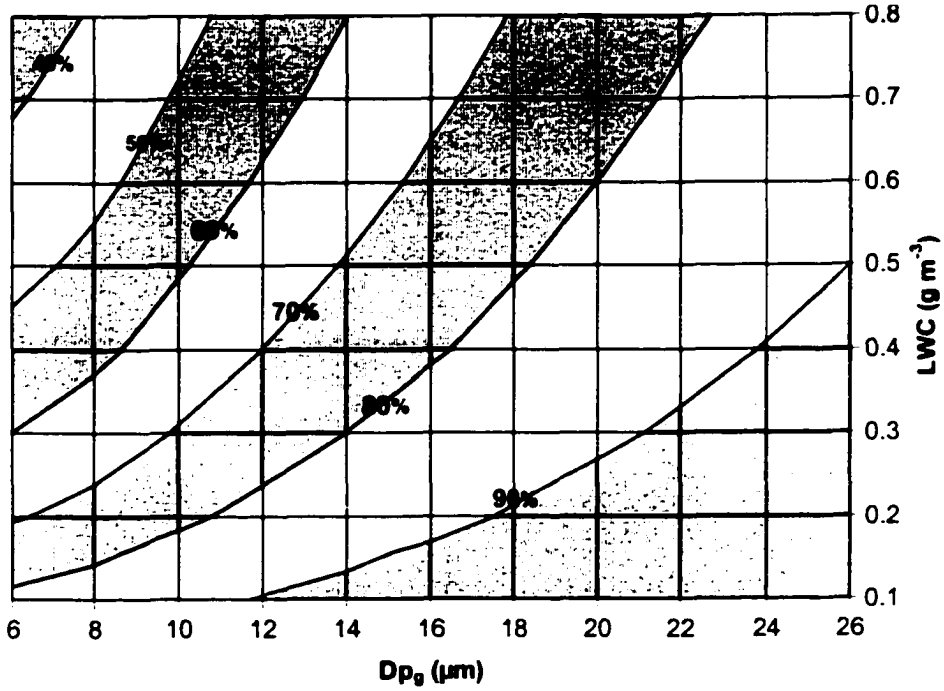

Figure 4.28. Fraction of total evaporation due to evaporation from wall surfaces.

5 Experimental evaluation of collector performance

The ability to visualize and quantify flow fields and particle trajectories through CFD analysis proved invaluable in the design of the axial-flow cyclone cloud water collector. The CFD analysis offered a preliminary assessment of the chosen design to generate the desired flow rates, flow dynamics, and cloud drop separation characteristics.

As mentioned previously, a great deal of research reported in the literature suggests that CFD analysis can successfully predict flow fields and particle trajectories for a wide range of flow environments. However, there are situations in which CFD may not perfectly represent actual fluid dynamics, especially for multi-phase flow in which particle trajectories are being studied (e.g. Straub and Collett, 2002; 2001; 1999; MacInnes and Bracco, 1992; Crowe et al., 1998). In part, this may be due to the many levels of approximation required to generate a continuous phase flow solution using a finite volume approach, and the unavoidable errors associated with those approximations (Ferziger and Peric, 1999; Anderson, 1992). Further errors may result if a single steady state solution is obtained for a turbulent flow that may not actually reach steady state conditions. Discrete phase solutions then require further approximations (Crowe et al., 1998) that can generate additional errors. It is therefore considered prudent to perform some level of experimental flow analysis in order to verify model predictions. Experimental evaluation of the axial-flow cyclone proceeded via qualitative and quantitative approaches that will be described in this chapter.

5.1 NCAR wind tunnel testing

Following their design, the axial-flow cyclone duct and curved vane unit were the first components of the collection system to be fabricated. Before committing to the construction of

the remaining components of the system (e.g. storage system, PMS canister modifications, inlet cover, etc.), a verification the CFD-based predictions of the axial-cyclone's ability to separate cloud drops from air was desired. The optimal approach for verifying the CFD analysis would be to subject the axial-flow cyclone to well-controlled air flow and LWC conditions (similar to those modeled) while monitoring sample collection rates. This type of activity would ideally take place in a wind tunnel. Unfortunately, wind tunnels capable of producing air velocities representative of aircraft flight and liquid water drop distributions representative of real clouds are rare, and obtaining test time in the few tunnels that can satisfy these conditions is time consuming and prohibitively expensive. After plans to use the former PMS wind tunnel in Boulder, CO fell through in early 2001, alternate test facilities were explored. The low speed NCAR wind tunnel was considered as an alternative primarily due to its immediate availability and cost-free operation. Although flight-like velocities could not be generated in NCAR's facility, a rapid evaluation of the axial-flow cyclone was required in order to allow sufficient time to complete the collector before deployment on the DYCOMS-II field project in July 2001.

To ascertain whether the use of the 25 m s^{-1} NCAR wind tunnel would provide meaningful insight into the operation of the axial-flow cyclone, a low velocity numerical modeling exercise was performed. The boundary conditions of the final numerical model of axial-flow cyclone were modified to reflect the 25 m s^{-1} maximum velocity that can be achieved in the NCAR wind tunnel. Apart from modifying the boundary velocity and changing air properties to represent conditions at 1500 m, all other continuous and discrete phase parameters were identical to the modeling described in Section 4.2. For an external air velocity of 25 m s^{-1}, the inlet velocity was approximately 6 m s^{-1}. As in the simulations of collector operation at aircraft velocities, a rotational flow field developed immediately downstream of the curved vanes, with a tangential velocity of approximately 20 m s^{-1}. Based on the injection of drops ranging in diameter from 2 to 50 μm, the external aspiration efficiency was found to be lower than for the aircraft velocity case, due to the reduced inertia of drops traveling at 25 m s^{-1} rather than 115

m s^{-1}. Despite the fact that fewer drops enter the inlet of the collector at 25 m s^{-1}, the CFD analysis predicted that the rotational flow field was sufficiently strong to force the majority of drops larger than approximately 8 μm to the duct wall upstream of the extraction slot. The predicted internal collection efficiency for the 25 m s^{-1} case is shifted to larger drop sizes by about 4 μm when compared to the 115 m s^{-1} case (Figure 5.1). Thus, it appeared that the internal collection characteristics of the axial-flow cyclone were not radically altered for operation at a freestream velocity of 25 m s^{-1}, and that wind tunnel testing at 25 m s^{-1} could provide an indication of collector performance.

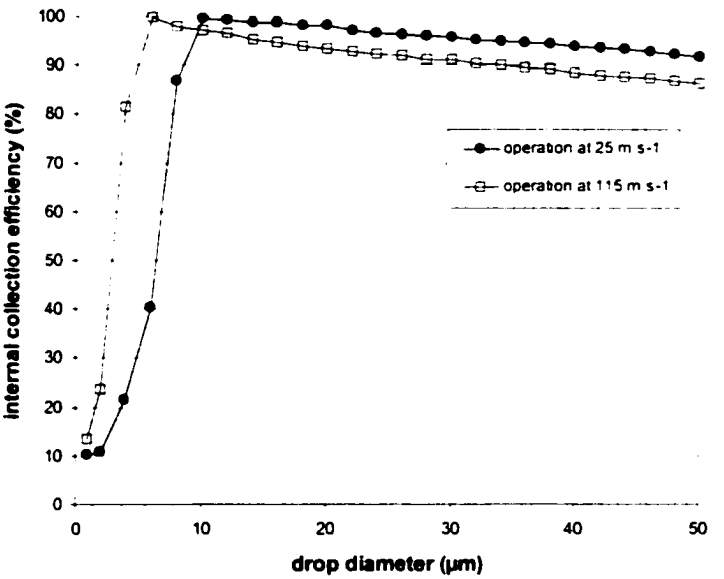

Figure 5.1. Axial-flow cyclone internal collection efficiency for operation at 115 m s^{-1} (open squares) and 25 m s^{-1} (filled circles).

A quantitative determination of the internal collection efficiency at low velocity conditions would have been ideal for comparison to the low velocity CFD analysis; however, time constraints prevented the development of a rigorous experimental setup. Instead, a qualitative evaluation was performed in the NCAR wind tunnel (Figure 5.2). The NCAR wind tunnel is a 7.32 m long open tunnel housed in a closed room, featuring a 0.89 m diameter test section and a maximum velocity of 25 m s^{-1} (Brock et al., 1995). Wind tunnel operation is

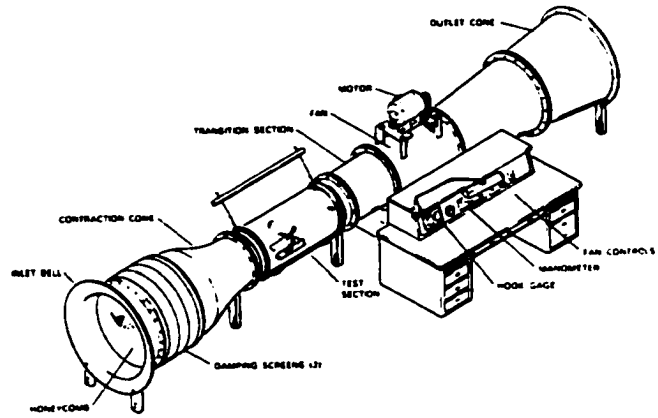

Figure 5.2. Schematic of the NCAR wind tunnel. The axial-flow cyclone was mounted in the 0.89 m diameter test section where the maximum velocity is 25 m s^{-1}.

monitored from an adjacent control room. The axial-flow cyclone, without PMS canister, inlet cover, or sample storage system, was mounted in the center of the test section and a spray generator was used to inject liquid water drops into the airstream. The spray generator utilized a 0.25 mm orifice atomizing nozzle and pressurization system borrowed from the NCAR spray calibrator (Dye, 1983). The nozzle produces a drop distribution with a volume mean diameter of 15 μm and very little mass below 6 μm, insensitive to the input water and air pressure (Dye, 1983). The nozzle was mounted 75 cm upstream of the collector in the wind tunnel. The drop size distribution and LWC were not verified during the experiments.

Several experiments were conducted in which the wind tunnel velocity was slowly increased and allowed to stabilize at its maximum value, approximately 24 m s^{-1} as indicated by the primary pitot tube velocity measurement. The spray system was then activated for one minute, after which the wind tunnel velocity was slowed back to zero. Because the axial-flow cyclone was fabricated from polished Lexan, a visual inspection could then be made of the internal surfaces. Water drops that accumulated on interior surfaces were clearly visible, and appeared exclusively on the duct wall upstream of the extraction slot. No water accumulation was observed downstream of the extraction slot. This suggested that the CFD analysis was accurate in predicting the fates of drops that enter the inlet of the collector for the 25 m s^{-1} case,

and it was expected that this would hold true for the 115 m s^{-1} case as well. Unfortunately, the air flow in the interior of the collector for the low velocity wind tunnel testing was insufficient to transport the accumulated water along walls of the collector. Thus, the wind tunnel testing did not address the effectiveness of the extraction slot in removing water from the duct wall. Based on the qualitative results obtained from the NCAR wind tunnel, the decision was made to continue with the construction of the remainder of the collection system.

5.2 Observed collection efficiency during DYCOMS-II

The second opportunity for an experimental evaluation of the axial-flow cyclone cloud water collector occurred during the DYCOMS-II field project. The DYCOMS-II mission, including project objectives, location, sampling environment, and flight plans will be described in detail in Chapter 6. However, aspects pertaining to the performance of the axial-flow cyclone under flight conditions will be discussed in this section.

Early in the DYCOMS-II mission, it became obvious that the collection efficiency of the axial-flow cyclone was lower than predicted by the numerical modeling. In flight, a real time measurement of LWC provided by a Particulate Volume Monitor (PVM) model PVM-100A (Gerber Scientific, Inc.) was multiplied by a simplified collection efficiency factor derived from the numerical modeling work to provide an estimate of the volume of cloud water accumulating in each sample storage bottle during each cloud sample period. Post flight measurement of the actual volume of water collected in each storage bottle revealed that the true collection rates were well below the expected collection rates.

Unfortunately, because the collection system was mounted in a PMS canister beneath the wing of the NSF/NCAR C-130, it was impossible to observe the system during flight in order to diagnose the problem.

The in-flight calculation of the sample collection rate did not explicitly take the drop size distribution into account, but was rather based on the total LWC. To determine if this simplified

estimate of collection rate was erroneous, after returning from the field a more rigorous estimate of the expected collection rate for each sample period was made using cloud drop size distributions measurements from the RAF SPP-100. In addition to the SPP-100 drop distributions, aircraft speed, PVM-100A derived LWC, estimates of evaporation as a function of drop size, and the external aspiration efficiency and internal collection efficiency as a function of drop size were used in the more rigorous calculation of the expected collection rate. These post-campaign calculations suggested that collection rates during DYCOMS-II should have been in the range of 1 to 9.7 ml min^{-1}. These expected collection rates far exceeded the actual collection rates which varied between 0.07 and 1.2 ml min^{-1}. For sample periods in which cloud drop distribution data were available, the actual sample collection rates averaged approximately 9% of the expected sample collection rates. Figure 5.3 displays the ratio of the actual sample collection rate to the expected sample collection rate for individual DYCOMS-II sample periods. The highest ratio was experienced on RF02-6, a sample period associated with heavy drizzle. A scatter plot of actual collection rate versus expected collection rate is provided in Figure 5.4. Although the actual collection rate is a function of LWC as would be expected (Figure 5.5), the majority of microphysical and flight parameters (LWC, cloud drop number concentration, wind speed, updraft velocity, sample duration) do not show strong correlations with the actual to expected collection rate ratios. There is one interesting trend in the actual to expected sample collection ratio that arises when the ratio is plotted against volume mean drop diameter as illustrated in Figure 5.6. During some flights, the ratio decreases with increasing mean drop diameter (RF03 and RF09) while during other flights, the ratio increases with increasing mean drop diameter (RF02, RF07, and RF08). A minimum in the ratio occurs at a volume mean diameter of approximately 15 μm. Interestingly, the flights with ratios that decrease with increasing drop diameter tend to be the high drop number concentration, low drizzle cases. The flights with ratios that increase with increasing drop diameter tend to be the low drop number concentration, light drizzle cases. A satisfactory explanation for this behavior has not yet been developed.

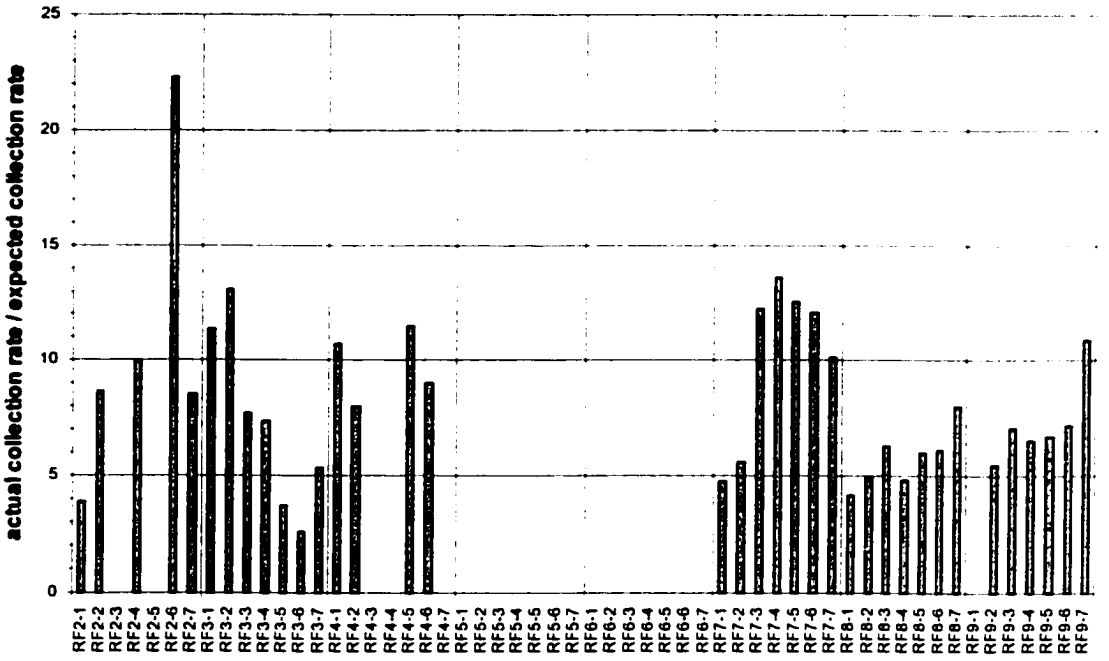

Figure 5.3. The ratio of the measured rate of sample collection to the expected rate of collection based on the drop size distribution and CFD trajectory analysis for individual DYCOMS-II samples.

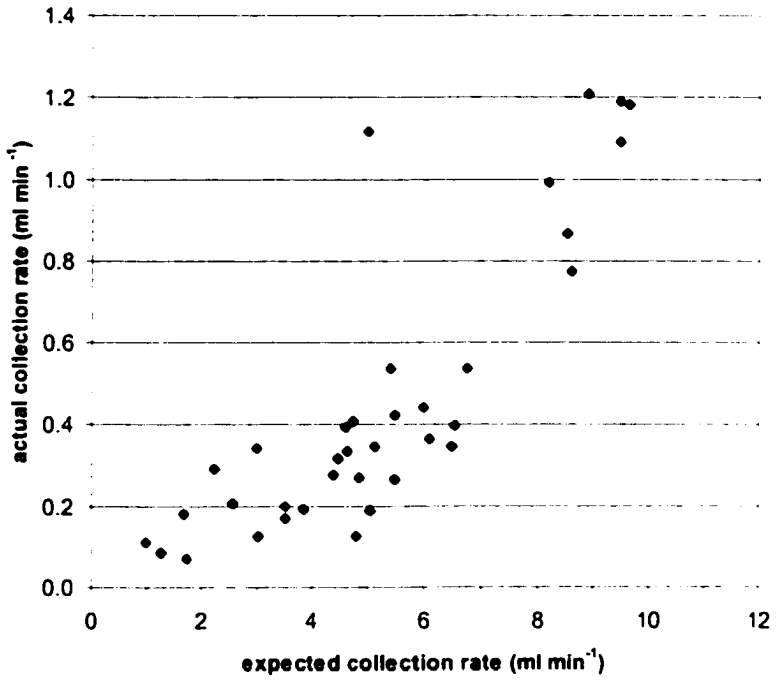

Figure 5.4. Actual versus expected rate of sample collection.

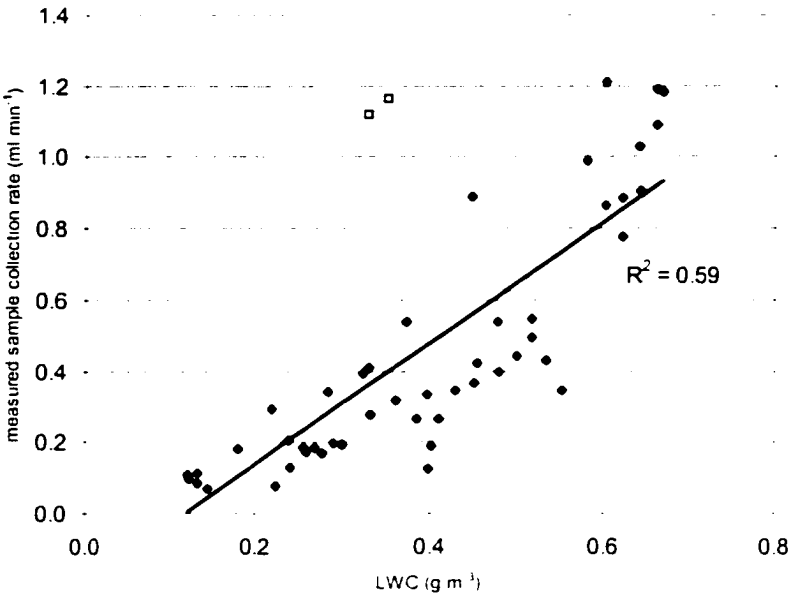

Figure 5.5. The measured rate of sample collection as a function of LWC as measured by the PVM during DYCOMS-II. If the two high drizzle sample periods (open squares) are removed, R^2=0.74.

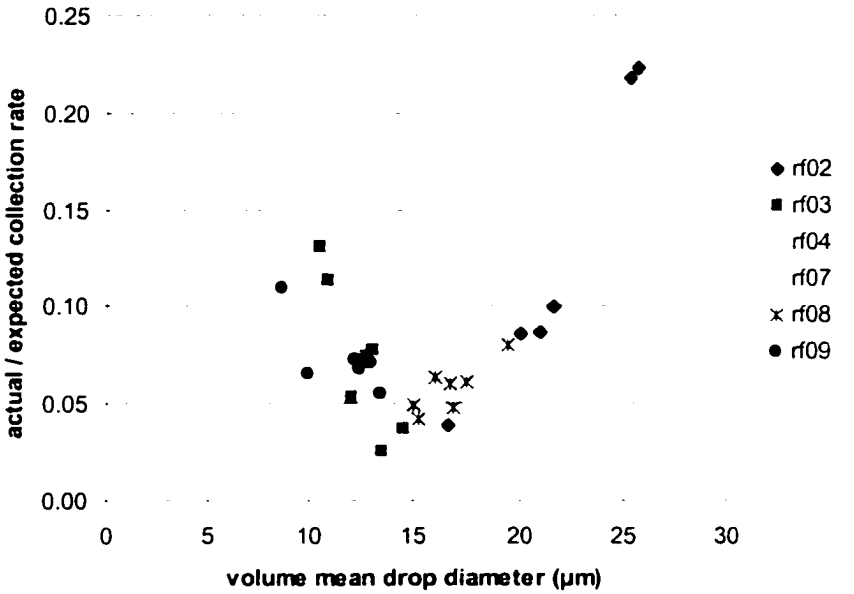

Figure 5.6. The actual to expected sample collection ratio as a function of volume mean drop diameter.

5.3 Experimental laboratory evaluation

The unexpectedly low collection efficiency experienced during the DYCOMS-II field project suggested that an important aspect of the flow dynamics or drop collection characteristics in the axial-flow cyclone was being neglected or misrepresented in the previous experimental and numerical analysis. In order to investigate the internal collection efficiency of the axial-flow cyclone in a more rigorous manner, a quantitative calibration technique was employed. In this calibration technique, fluorescent-tagged monodisperse drops were injected into the inlet of the axial-flow cyclone which was operating at flight-like flow conditions. The fluorescent tracer allows the number of drops that impact individual surfaces in the collector to be quantified, permitting drop deposition patterns in the interior of the collector to be accurately determined. After repetition of this procedure for various drop sizes, a collection efficiency curve that describes collection efficiency as a function of drop size can be constructed. This technique has been used successfully in the past to calibrate aerosol impactors (Marple et al., 1995; 1987; Hillamo and Kauppinen, 1991; Vaughn, 1989) and ground-based cloud water collectors (Straub and Collett, 2001; 2002), and to verify numerical modeling results (McFarland et al., 1997; Muyshondt et al., 1996).

5.3.1 Experimental set-up

The experimental calibration of the axial-flow cyclone took place in the Department of Atmospheric Science's Aerosol and Cloud Simulation Laboratory (Simlab) at Colorado State University. In the absence of a 115 m s^{-1} wind tunnel to generate air flow through the axial-flow cyclone, three GAST Regenair blowers (models R4P115, R4110-2, and R3105-12) provided flow through the interior of the collector. The intake ports of the three blowers were connected via rigid PVC tubing to a manifold which was in turn attached to the outlet of the axial-flow cyclone (Figure 5.7). Operating at their maximum capacity, the blowers could draw approximately 4800

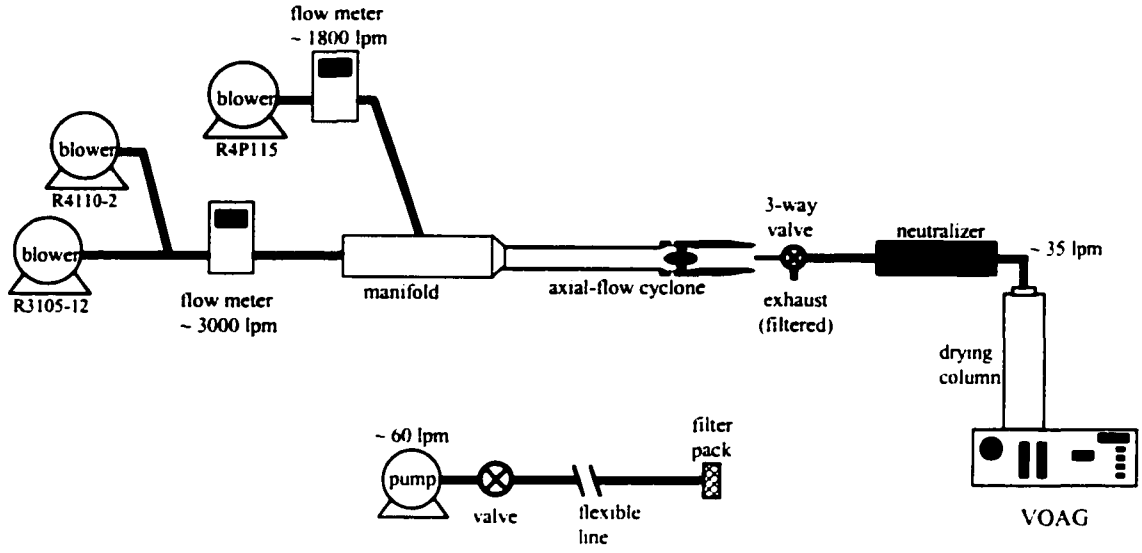

Figure 5.7. Experimental setup for the laboratory calibration of the axial-flow cyclone.

l min^{-1} of air through the axial-flow cyclone, closely approximating the expected in-flight flow rate of 4900 l min^{-1}. Flow rates were monitored by two Sierra flow meters (models 760 and 780).

Monodisperse calibration drops were generated with a Model 3450 Vibrating Orifice Aerosol Generator (VOAG) (TSI, Inc.) (Berglund and Liu, 1973). The VOAG operates by forcing a liquid solution through a small orifice, 20 μm for this work, to produce a liquid jet. The orifice is rapidly vibrated at a known frequency in order to break the liquid jet up into consistently sized drops. The liquid solution used to generate the calibration drops is composed of a volatile component that quickly evaporates and a non-volatile component that remains behind to produce the final calibration drop. For this work, isopropyl alcohol was selected as the volatile component and a mixture of oleic acid and fluorescein (EM Science, EM Industries, Inc.) was selected as the non-volatile component. Oleic acid (ρ = 0.90 g cm^{-3}) is characterized by low volatility and approximates the density of water; fluorescein (ρ = 1.53 g cm^{-3}) was included as a fluorescent tracer. After drop production in the VOAG, a dispersion air flow reduces the chances of collision and coalescence and a dilution air flow acts to evaporate the volatile component. Dispersion and dilution air flows were set to 20 cm^3 min^{-1} and 35 l min^{-1}, respectively. The

dispersion and dilution air flows also act to transport the calibration drops through the PVC distribution lines. A Model 3054 Aerosol Neutralizer (TSI, Inc.) was installed in the distribution line during the production of 4 and 5 μm drop sizes, which were found to be susceptible to enhanced collection due to electrostatic force in previous studies (Straub and Collett, 1999).

Knowledge of the flow rate of the liquid solution through the orifice (Q) and the frequency of vibration of the orifice (f) allows the calculation of the initial drop diameter, D_d:

$$D_d = \left(\frac{6Q}{\pi f}\right)^{\frac{1}{3}} \tag{5.1}$$

The volume fraction of non-volatile components in the liquid solution then determines the final drop diameter (D_p) (Olan-Figueroa et al., 1982):

$$D_p = \left[C + C\frac{C_f}{\rho_f} + I\right]^{\frac{1}{3}} D_d \tag{5.2}$$

where C is the volumetric concentration of oleic acid in solution, C_f is the concentration of fluorescein in oleic acid (mass of fluorescein per ml of oleic acid), ρ_f is the density of fluorescein, and I is the volumetric concentration of nonvolatile impurities in the volatile component. For the calibration of the axial-flow cyclone, the liquid flow rate was held constant at 0.170 ml min^{-1} by specifying a syringe pump speed of 1×10^{-3} cm s^{-1}, a value that maintains sufficient pressure in the liquid feed system to support a stable liquid jet (Straub and Collett, 1999). The vibration frequency was also held constant at 60 kHz. Drops with diameters between 4 and 20 μm were produced by altering the nonvolatile fraction of the liquid solution as indicated in Table 5.1. The concentration of fluorescein in oleic acid (C_f) was varied between drop sizes in order to maintain a constant total fluorescein mass output for each drop size. The isopropyl alcohol impurity value of 2 ppm did not affect drop size. Solutions were prepared several days in advance to provide sufficient time for the fluorescein to dissolve completely.

Drop Diameter μm	Fluorescein Cf g/ml	Non-volatile Concentration vol %	Volume of Oleic Acid ml	Mass of Fluorescein g
4	1	0.0004	0.043	0.0429
5	0.4	0.0011	0.110	0.0440
6	0.2	0.0021	0.212	0.0424
8	0.1	0.0053	0.534	0.0534
10	0.05	0.0108	1.076	0.0538
20	0.006	0.0886	8.858	0.0532

Table 5.1. Calibration drop liquid solution components required to make 100 ml total.

During calibration runs, samples of drops were collected on glass slides treated with a fluorochemical coating and viewed at 150× magnification in order to verify their sizes. The fluorochemical coating allowed drop spreading to be taken into account with a spreading factor of 1.33 (Olan-Figueroa et al., 1982) that defines the ratio between the flattened diameter and the original spherical diameter. A Nikon SMZ-U stereo zoom microscope with a Javelin Ultrachip CCTV video camera was used to capture and digitize the drop images, and the software package Image Pro Plus v1.2 was used to view and size the drops. The drop images were also used to determine the fraction of doublets and triplets which inevitably form due to drop collision and coalescence in the calibration stream. Doublets are formed when two drops coalesce and therefore have twice the mass of single drops, while triplets are formed when three drops coalesce and have three times the mass of single drops. The collection characteristics of doublets and triplets are different than for singlets, and must be accounted for in the calibration procedure (Marple et al., 1987).

Rigid PVC tubing was used to transport the calibration drops from the VOAG to the inlet of the axial-flow cyclone (Figure 5.8). Downstream of a three-way valve used to control the flow of calibration drops, the PVC tubing reduced down to an outer diameter of 2.0 cm and an inner diameter of 1.2 cm. This reduced diameter tubing was used in order to allow introduction of the calibration drops directly into the interior of the inlet of the collector. This drop delivery configuration was prompted by CFD modeling of the inlet flow field at laboratory conditions, which revealed the following: Because air is being drawn through the axial-flow

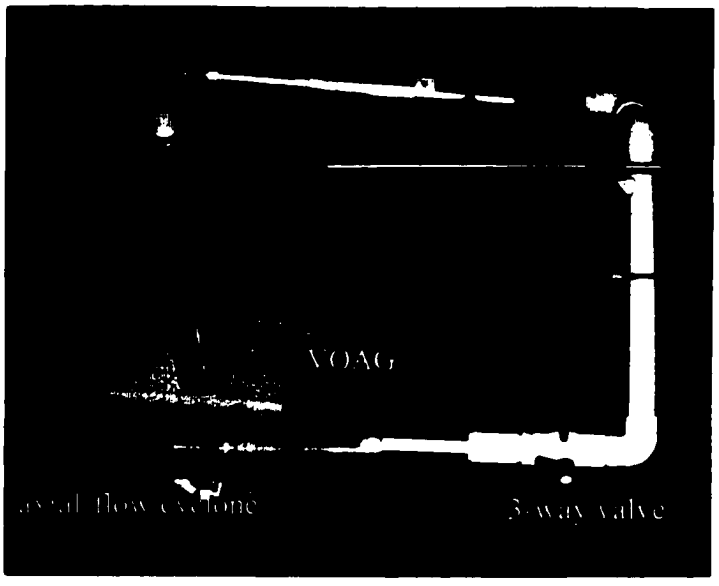

Figure 5.8. Photograph of the axial-flow cyclone calibration experimental setup.

cyclone by blowers rather than being forced through as a result of ram pressure, the inlet is superisokinetic rather than subisokinetic as indicated by the velocity field in Figure 5.9. At laboratory conditions, quiescent air accelerates from all directions to reach 30 m s^{-1} in the inlet of the collector, creating a flow field that focuses any drops released upstream of the inlet toward the centerline (Figure 5.10). These trajectories would reveal little about the true collection characteristics of the axial-flow cyclone. As an alternative, drops were instead released from a location approximately 4 cm downstream of the inlet leading edge where the flow attains a more uniform and axial structure. In the experimental setup, the small diameter of the VOAG outlet tubing was necessary to keep blockage of the axial-flow cyclone inlet to a minimum and to accelerate the calibration drops to a higher velocity, although even with a 1 cm diameter outlet, the VOAG outlet velocity was still only on the order of 10 m s^{-1}. The VOAG outlet tube extended 4 cm into the axial-flow cyclone inlet and was placed mid-way between the center hub and the duct wall as illustrated in Figure 5.11. It should be mentioned that the numerical model of the axial-flow cyclone at laboratory conditions was identical to the original modeling at flight conditions except for two features. First, instead of specifying an upstream velocity boundary

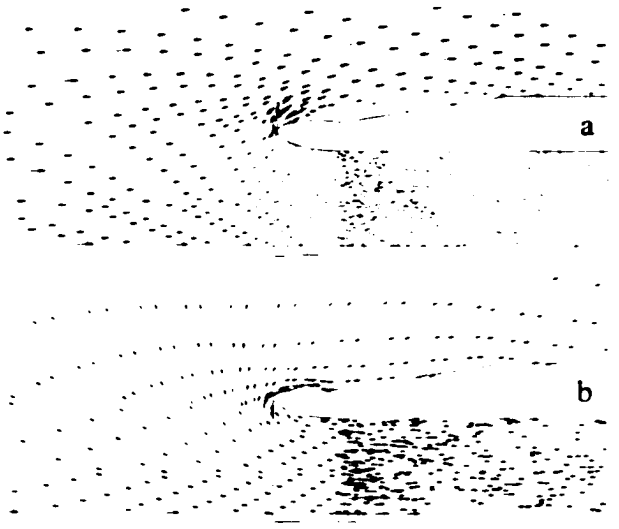

Figure 5.9. Inlet flow field for aircraft conditions (a) and lab conditions (b). Arrows represent the magnitude and direction of air flow in (a) but only the direction of air flow in (b). In both cases, inlet interior velocities are approximately 30 m s^{-1}.

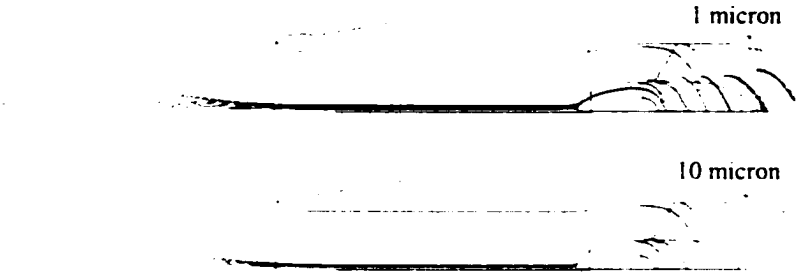

Figure 5.10. Trajectories of 1 and 10 μm drops released upstream of the axial-flow cyclone inlet at laboratory conditions.

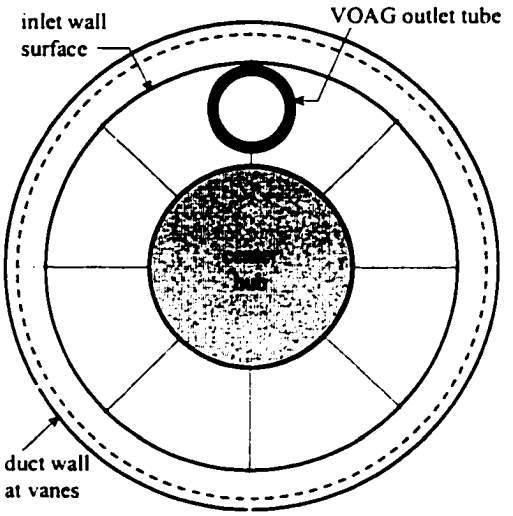

Figure 5.11. VOAG outlet tube placement during the experimental calibration.

condition, a downstream pressure was specified to simulate the presence of the blowers. Second, air material properties were modified to reflect the laboratory environment at 1500 m.

In order to quantify drop deposition patterns resulting from this calibration procedure, surfaces onto which the fluorescein-tagged drops deposited were soaked in a known volume of extract solution into which the fluorescein would dissolve. The extract solution could then be analyzed fluorometrically to ascertain the mass of fluorescein on any given surface. A 0.001 N NaOH solution was used for extraction because of its effectiveness in removing the oleic acid/fluorescein drops from the surfaces of the collector (Marple et al., 1987; Straub and Collett, 1999). Surfaces were soaked for approximately one hour in a sufficient volume of extract solution so that the resulting fluorescein concentrations were within the calibration range of a Shimadzu RF-1501 spectrofluorophotometer. The spectrofluorophotometer was calibrated with standard concentrations of 0.0025, 0.005, 0.01, 0.02, 0.04, and 0.08 $\mu g\ ml^{-1}$ of fluorescein in 0.001 N NaOH.

The extract solution concentrations were multiplied by the extract volumes to determine the total mass of fluorescein that had deposited on each of the extracted components. If no doublets or triplets were produced by the VOAG, all of the fluorescein mass could be attributed to singlets, and fluorescein mass could be used as a surrogate measure of drop number. Unfortunately, some fraction of the fluorescein mass on any given surface was due to doublets and triplets, and their presence must be taken into account. This was accomplished by following the procedure described by Straub and Collett (1999) in which the total mass of fluorescein injected into the collector is attributed to singlets, doublets, and triplets based on the generated fraction of each as determined through the microscopic analysis. The mass of fluorescein on each surface is then attributed to singlets, doublets, and triplets in the following way: the calibration process is initiated with large drop sizes for which the collection efficiency of doublets and triplets can be assumed to be 100%, and the mass of fluorescein on a surface associated with

doublets and triplets can be easily calculated. The singlet collection efficiency for those large drop sizes can then be determined. As the calibration proceeds to smaller drop sizes, the previously determined large drop collection efficiencies can be used as the collection efficiencies for appropriately sized doublets and triplets of smaller drops. In this way, the collection efficiency of doublets and triplets can always be known, and singlet collection efficiency can be determined.

During the calibration of the axial-flow cyclone, doublets typically accounted for approximately 4% of the total number of calibration drops and triplets for 1%. These low concentrations of doublets and triplets had relatively little impact on the calculated collection efficiencies, requiring a maximum collection efficiency correction of only 5%, and typically only 1 to 2%.

In addition to the quantitative monodisperse drop calibration, the flow of water in the interior of the axial-flow cyclone was qualitatively investigated. This was performed with the aid of a common spray bottle used to spray water into the inlet of the axial-flow cyclone while the three blowers were activated. Alternatively, small quantities of water were pipetted directly onto surfaces of interest. The flow of water in the interior of the collector could then be studied visually in an effort to gain some insight into the fate of sampled cloud drops after they deposit on the surfaces of the collector.

5.3.2 Experimental procedure

Separate calibrations were performed for actual drop diameters of 4, 5, 6, 8, 10, and 20 μm, with each calibration requiring 4 to 5 hours to complete. The calibration procedure began by placing a 20 ml syringe filled with solution for the desired drop size in the VOAG syringe pump. After activating the syringe pump and flushing the liquid feed system with 5 ml of solution, the drain valve was closed to start the liquid jet. The orifice vibration frequency was then adjusted to 60 kHz and the dilution and dispersion air valves were opened. To assure that consistently sized

drops were produced, the liquid feed system pressure was allowed to stabilize for 10 to 15 minutes, with the final pressure usually reading about 20 psi. During the time required for pressure stabilization, the air flow containing the calibration drops was exhausted through a filtered outlet on the 3-way valve.

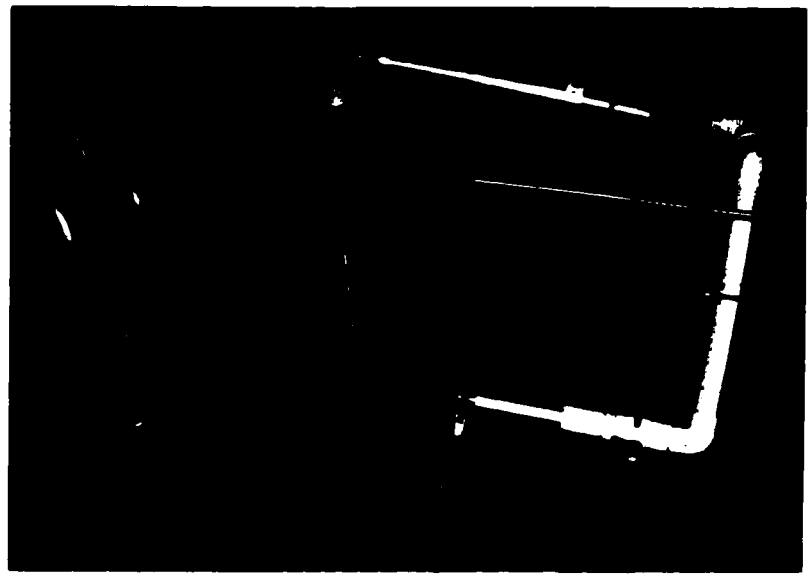

Figure 5.12. Photograph of the experimental calibration setup showing drop collection on a nylon membrane filter prior to drop injection into the axial-flow cyclone inlet.

Before injecting the drops into the collector, the VOAG outlet tubing was rotated away from the inlet of the axial-flow cyclone to allow drop collection on a nylon filter for a duration of 1 minute (Figure 5.12). The flow of calibration drops was precisely controlled by opening and closing the three-way valve which alternated the flow of drops between the filtered exhaust and the VOAG outlet. The 47 mm diameter, 1 μm pore size Nylasorb nylon membrane filter was mounted in a Plexiglas filter pack that could be placed directly in front of the VOAG outlet. A pump drew approximately 60 l min^{-1} of air through the filter to ensure that all of the calibration drops exiting the VOAG outlet would be captured. This filter measurement, along with two additional filter measurements made after injecting drops into the collector, served as a check of the magnitude and consistency of the VOAG output. Following the first filter measurement, the VOAG outlet was rotated into place in front of the axial-flow cyclone inlet and the three blowers

were sequentially activated. Calibration drops were injected into the inlet for 1 minute after which the blowers were turned off. The second and third filter measurements were then made, drops were collected on a glass slide for size verification, and finally the VOAG liquid jet was deactivated by opening the liquid feed system drain valve.

In order to quantify drop deposition patterns in the axial-flow cyclone through fluorometric analysis, the collector was disassembled and the individual components were soaked in 0.001 N NaOH extract solution. Typically, between 400 ml and 1500 ml of solution was required to soak the components of the collector. The filters were soaked as well, using 1000 ml of extract solution. The goal of the laboratory calibration, in part, was to determine the fraction of drops of a given size that reach the duct wall upstream of the extraction slot. For this reason, the axial-flow cyclone was broken down into the following sections for extraction: the inlet, the curved vane assembly, the duct containing the extraction slot, and the aluminum duct downstream of the extraction slot. The inlet refers to the entire portion of the duct upstream of the curved vane assembly. The curved vane assembly incorporates the center hub, the eight curved vanes, and a section of duct wall as a single piece. Because of this, drop deposition on those surfaces could not be differentiated. The section of the duct containing the extraction slot included surfaces both upstream and downstream of the extraction slot, in addition to the slot itself. In order to separately extract the upstream and downstream surfaces, this section was first placed in a container such that only the upstream surfaces were submerged in extract solution. After one hour, the piece was rotated 180° and placed in second container with fresh extract solution in which only the downstream surfaces were submerged. The aluminum duct was the final surface downstream of the extraction slot to be quantified for drop deposition.

After allowing the filters and the collector components to soak for one hour, the concentration of the extract solutions were measured using the spectrofluorophotometer. A six standard calibration of the spectrofluorophotometer was performed prior to every drop calibration procedure and four replicate measurements were made for each extract solution. Following the

extract measurement, each piece of the collector was washed with a dilute solution of Triton X-100 and rinsed with deionized water to ensure the removal of all fluorescein mass in preparation for subsequent calibrations.

5.3.3 Results

Including replicates, a total of 11 calibration runs were performed. One run each was completed for 4 and 8 μm drops, two runs each for 5, 10, and 20 μm drops, and three runs for 6 μm drops. The replicates provided an indication of the precision of the calibration procedure. The replicate measurements were used to calculate 95% confidence limits which are included in the collection efficiency curves displayed in this section. The 95% confidence limits were based on pooled relative standard deviations of 1.5% for the total fluorescein mass deposited on all surfaces upstream of the extraction slot and relative standard deviations of 69.8%, 7.8%, 8.7%, and 15.7% for the inlet, the curved vane assembly, the duct containing the extraction slot, and the aluminum duct downstream of the extraction slot, respectively. The higher standard deviation associated with drop collection on the inlet surface most likely results from the fact that slight run to run variations of the VOAG outlet tube alignment relative to the inlet created variability in the relatively small number of drops that deposit on the inlet.

In order to compare the experimental calibration results to the numerical trajectory simulations, calibration drop diameters are reported as equivalent aerodynamic diameters. The aerodynamic diameter is the diameter of a unit density drop that has the same fall velocity as the original drop. Because the oleic acid calibration drops have a density less than 1 g cm^{-3}, the aerodynamic diameters are slightly smaller than the physical diameters as indicated in Table 5.2.

Berglund and Liu (1973) suggest that the VOAG is a primary standard capable of producing drop diameters accurate to ± 2% of the calculated drop diameters based on the drop solution components and the VOAG operating parameters. The microscope drop diameter measurements confirmed that the drop sizes produced by the VOAG matched the desired drop

drop diameter	aerodynamic diameter µm	accuracy estimate[a] ± µm	measured standard deviation ± µm	95% confidence interval ± µm
4	3.79	0.08	N/A	N/A
5	4.74	0.09	0.36	0.16
6	5.69	0.11	0.27	0.10
8	7.59	0.15	0.23	0.17
10	9.49	0.19	0.38	0.17
20	18.97	0.38	0.68	0.31

[a]2% of drop diameter (Berglund and Liu, 1973)

Table 5.2. Actual diameters, aerodynamic diameters, and related uncertainty statistics for calibration drops produced by the VOAG.

sizes, within the approximately ± 1µm accuracy of the imaging system. This was true for all drop sizes, although a reliable measurement of 4 µm drops was not possible due to their small size and the fact that they were collected on an oiled glass slide for which spreading could not be accounted. Berglund and Liu (1973) further suggest that the standard deviation of drops generated by the VOAG is 1% of the mean drop diameter. The standard deviations obtained from the microscopic analysis are greater than 1% of drop diameter, possibly due to limitations in the imaging system. However, these more conservative standard deviations were used to calculate the 95% confidence intervals for the drop diameters listed in Table 5.2.

The VOAG output was extremely consistent over the course of a given calibration run as indicated by relative standard deviations for each set of three filters that ranged between 0.5 % and 4.4 %. In addition, all of the fluorescein mass injected into the axial-flow cyclone appeared to be recovered during the extraction process, which included the removal of calibration drops from surfaces upstream and downstream of the extraction slot. The total mass recovered from the interior surfaces of the axial-flow cyclone averaged 98.3% ± 7.3% of the pre- and post-calibration filter measurements.

The laboratory calibration revealed that the majority of drops that enter the inlet of the axial-flow cyclone deposit on wall surfaces upstream of the extraction slot. An internal collection efficiency curve was constructed for the experimental calibration based on assumptions similar to those for the CFD-based internal collection efficiency curve, i.e. that drops that deposit on the

inlet wall surface or the surfaces of the curved vanes eventually reach the duct wall and are available for collection. Because the center hub could not be separately extracted, drops that deposit there are included as drops that are assumed to be collected. The experimentally determined internal collection efficiency curve, corrected for the presence of doublets and triplets, is displayed in Figure 5.13. Also included in Figure 5.13 are internal collection efficiency curves derived from two numerical trajectory simulation cases: for flight conditions at 3000 m and for laboratory conditions. The internal collection efficiency corresponding to operation during flight at 3000 m is the same as discussed in Section 4.4.2. An additional collection efficiency curve was constructed based on the numerical modeling at laboratory conditions in order to better represent the laboratory calibration and allow comparisons between the numerical and experimental results. For the numerical modeling at laboratory conditions, drops were released from an injection surface that matches the size and placement of the VOAG outlet tube. Drop initial velocities were also selected to match the VOAG outlet velocity of 9 m s^{-1}. It is interesting

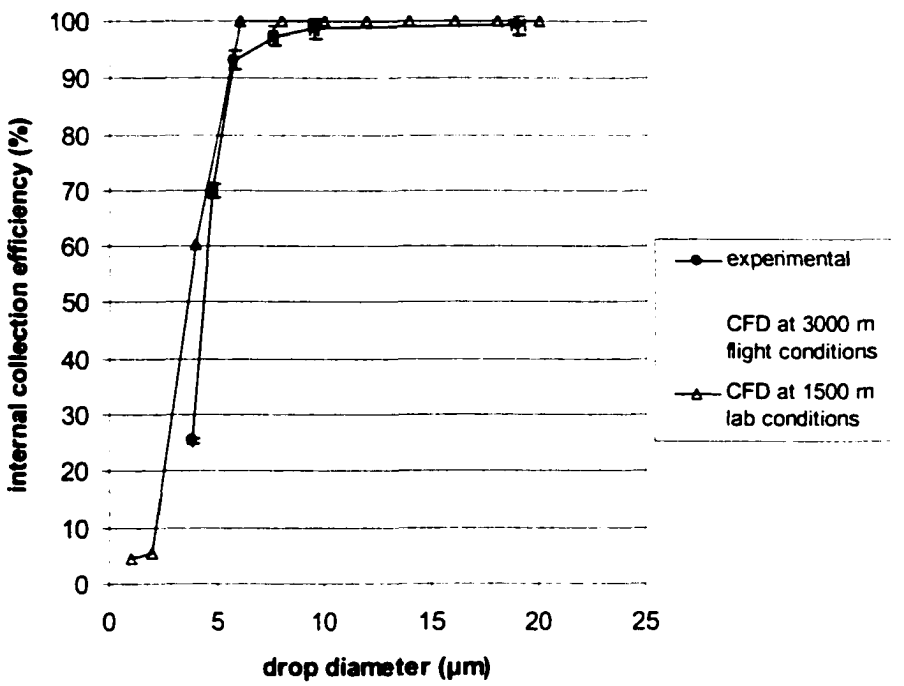

Figure 5.13. Internal collection efficiency curve for the experimental calibration of the axial-flow cyclone (filled circles). CFD predictions of internal collection efficiency at laboratory (open triangles) and flight conditions at 3000 m (open squares) are included for comparison.

to note that despite the differences in inlet air flow fields, drop injection locations, and drop injection velocities, the two numerically predicted collection efficiency curves are quite similar, displaced by only 1 μm. The experimentally determined internal collection efficiency curve agrees quite well with the numerically derived curves.

The deposition of drops on the individual surfaces of the axial-flow cyclone can also be examined. Figure 5.14 shows the fraction of drops that deposit on the inlet wall surface and the curved vane assembly as determined through the experimental analysis and corrected for the presence of doublets and triplets. Also included are numerically predicted collection curves for the corresponding surfaces. As can be seen in Figure 5.14, during the experimental calibration a portion of drops deposited on the inlet surface, while numerical drop trajectories suggest that no drops impact on the inlet. The fact that some drops were collected on the inlet during the experiments could be the result of misalignment of the VOAG outlet tube that directed drops slightly toward the inlet wall. Alternatively, the presence of the VOAG outlet tube in the inlet flow field most likely creates considerable turbulence which could lead to the turbulent deposition of drops on the inlet wall, a phenomenon not captured in the numerical modeling.

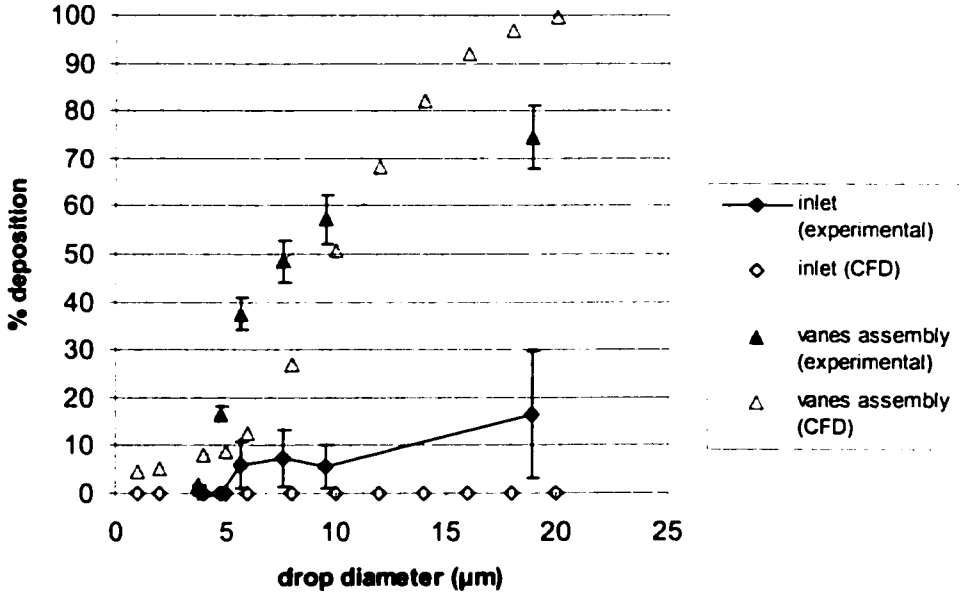

Figure 5.14. The fraction of drops entering the inlet of the axial-flow cyclone that deposit on the inlet section (diamonds) and the curved vane assembly (triangles). Curves derived from the experimental calibration (filled symbols) and CFD modeling (open symbols) are displayed.

The experimental and numerical curves depicting drop deposition on the curved vane assembly both show increasing collection with increasing drop diameter in Figure 5.14. In the experimental work, because a fraction of drops deposit on the inlet surface, fewer drops are available for deposition on the vane assembly, resulting in a collection efficiency that is biased toward lower efficiencies compared to the numerical modeling. Collection efficiency curves that take this effect into account can be constructed by neglecting drops that are removed upstream of a surface when calculating collection efficiency for a particular surface. Collection efficiency curves generated in this way can be seen in Figure 5.15. As a reminder, the curved vane assembly includes the eight curved vanes, the center hub, and the attached section of duct wall.

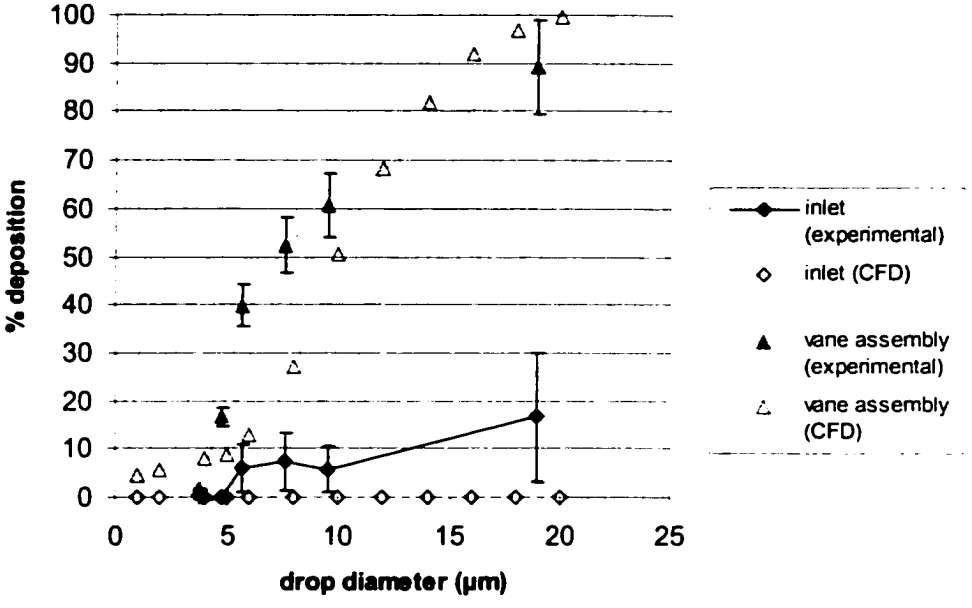

Figure 5.15. The fraction of drops that deposit on the inlet section (diamonds) and curved vane assembly (triangles), after taking drop deposition on upstream surfaces into account. Curves derived from the experimental calibration (filled symbols) and CFD modeling (open symbols) are displayed.

Figure 5.16 shows the numerically and experimentally determined fraction of drops that deposit on the duct wall between the curved vanes and the extraction slot. For drop deposition on this surface, the numerical and experimental curves exhibit the same trend, although the numerical modeling predicts higher rates of deposition than the experimental results for drops between 5 and 10 μm in diameter. Much of this discrepancy is due to the fact that a higher

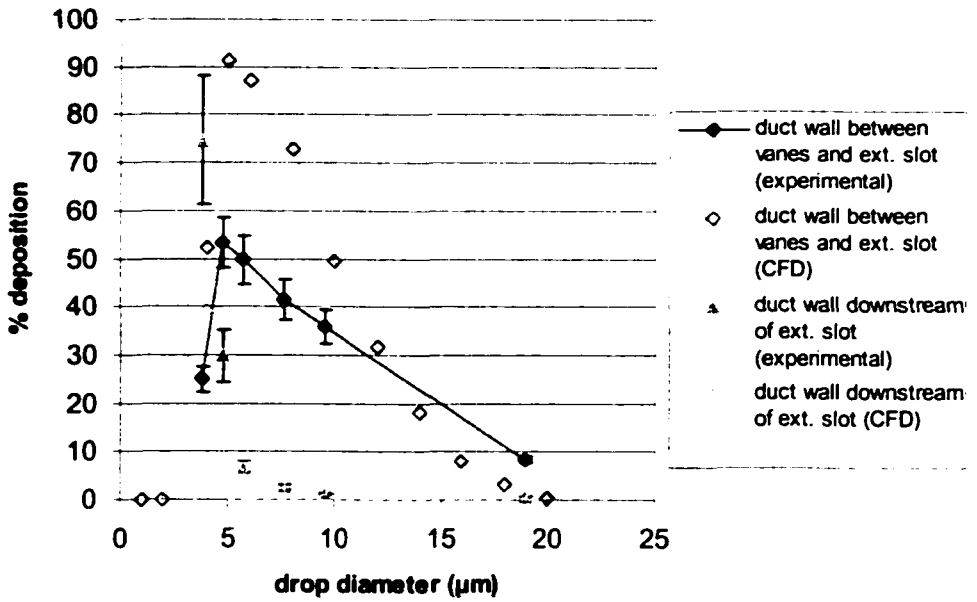

Figure 5.16. The fraction of drops entering the inlet of the axial-flow cyclone that deposit on the duct wall between the curved vanes and extraction slot (diamonds) and on the duct wall downstream of the extraction slot (triangles). Curves derived from the experimental calibration (filled symbols) and CFD modeling (open symbols) are displayed.

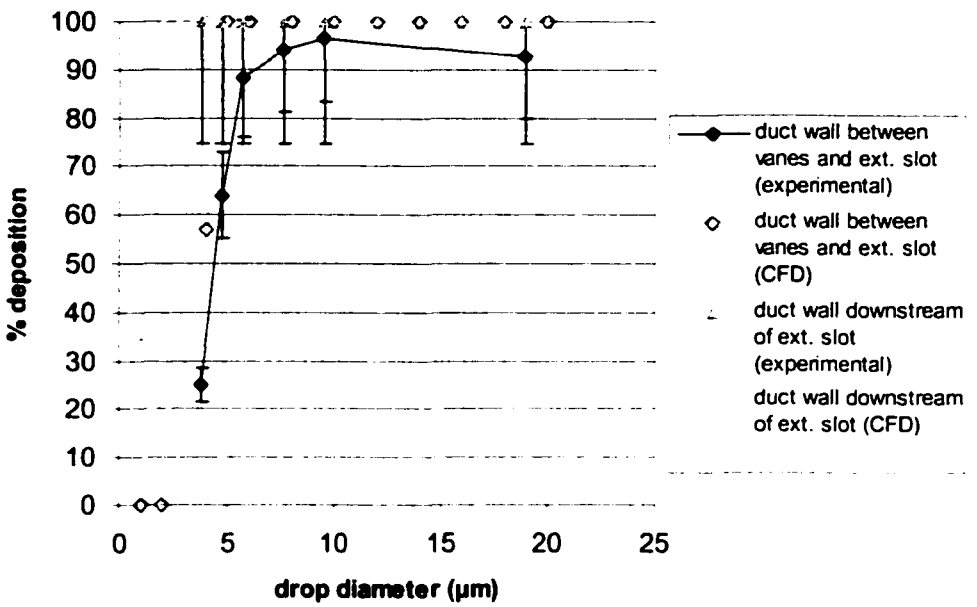

Figure 5.17. The fraction of drops that deposit on the duct wall between the curved vanes and extraction slot (diamonds) and on the duct wall downstream of the extraction slot (triangles), after taking drop deposition on upstream surfaces into account. Curves derived from the experimental calibration (filled symbols) and CFD modeling (open symbols) are displayed.

percentage of drops in that size range is removed from the air stream on the inlet and the vane assembly in the experimental calibration. This leaves fewer drops remaining in the air stream to enter the rotational flow field and deposit on the duct wall between the vanes and the extraction slot, resulting in a lower percentage of drops depositing there. Collection efficiency curves that account for the removal of drops on upstream surfaces can be seen in Figure 5.17, which shows much better agreement between the numerical and experimental curves.

Figures 5.16 and 5.17 also show numerical predictions and experimental results describing the fraction of drops that deposit on the duct wall downstream of the extraction slot, with the numerical and experimental curves in close agreement in both cases.

Finally, qualitative information about the flow of water in the interior of the axial-flow cyclone was acquired by injecting water into the inlet while the blowers were actively drawing air through the system. Although the clear Lexan duct allowed the motion of water along the surfaces of the axial-flow cyclone to be visually observed, the curvature and imperfect polishing of the duct did not present a perfect view. In addition, the relatively high 30 m s^{-1} air velocity transports water rapidly enough that the flow of water was not always obvious. However, after repeated observations a few phenomena can be described with some degree of certainty. First, it appears that drops that deposit on the curved vanes do shed off of the vanes and reach the duct wall upstream of the extraction slot as hoped. Second, drops that deposit on the center hub simply flow along the hub to the trailing edge before being re-entrained into the air stream. Because the trailing edge of the hub extends farther downstream than the extraction slot, the re-entrainment these drops occurs downstream of the extraction slot, which would indicate that these drops are not available for collection. Third, it is apparent that water that deposits on the duct wall upstream of the extraction slot is not efficiently removed by the extraction slot. Water sprayed into the inlet can be seen to deposit on the duct wall upstream of the extraction slot and shortly thereafter it appears on the duct wall downstream of the extraction slot. This suggests that some water is flowing over the extraction slot rather than into it, although the actual sequence of

events leading to this behavior is difficult to ascertain. In fact, very little water was observed to actually enter the extraction slot. The water that did enter the slot tended to pool and circulate along the upstream edge of the slot without ever descending to the bottom of the slot where it could be removed through the two sample ports. This occurred even with a vacuum applied to the extraction slot ports to simulate flight operation. The numerical trajectory modeling predicted that cloud drops positioned along the leading edge of the extraction slot should be quickly transported to the bottom of the slot due to centrifugal force. The observed water flow along the lip of the extraction slot could indicate that the presence of the extraction slot may disturb the rotational flow field in a way that is not captured in the numerical model.

5.3.4 Conclusions

The experimental laboratory calibration of the axial-flow cyclone suggests that internal drop deposition patterns are well predicted by the numerical trajectory simulations. Although there is some discrepancy in deposition patterns among the individual surfaces, the total fraction of drops that are collected on surfaces upstream of the extraction slot, as represented by the internal collection efficiency, is in good agreement for the two methods. The experimental calibration and the numerical modeling both indicate that the majority of drops that enter the axial-flow cyclone will be deposited upstream of the extraction slot.

While the experimental calibration confirms that drops do in fact deposit on surfaces upstream of the extraction slot as expected, the low collection rate observed during DYCOMS-II also demonstrates that the majority of the available cloud water remains unsampled. Although sample loss through evaporation may occur as discussed in Section 4.4.6, the magnitude is insufficient to account for a 90% reduction in sample volume. The numerical modeling described in Section 4.4.3, suggests that drops do enter the inlet of the collector despite slight misalignments of the axial-flow cyclone with the air streamlines. The laboratory tests which involved the injection of water into the axial-flow cyclone provided qualitative evidence that

drops that deposit on the curved vanes are shed off the vanes, into the rotational flow field, and deposit on the duct wall upstream of the extraction slot. Although the qualitative observations show that drops that impact the center hub may not reach the duct wall, deposition on the center hub should account for the fates of 15% of total drops at a maximum. In any event, the fact that drops that impact the center hub may remain uncollected was taken into account when calculating the expected collection rates during DYCOMS-II, and the observed collection rates still fell short of expectations by over 90%. When taken as a whole, these quantitative and qualitative observations point to the unintended flow of cloud water past, rather then into the extraction slot as the most likely explanation for the observed low collection rate. The consequence of removing only 10% of the available water from the axial-flow cyclone is minimized if there is no bias in drop sizes that are ultimately removed for storage. Based on the experimental laboratory calibration with fluorescein-tagged drops and visual observations of water flow in the axial-flow cyclone, cloud drops of all sizes should arrive at the duct wall upstream of the extraction slot. After drops deposit on the duct wall, mix with other drops, and flow toward the extraction slot as a liquid film, there is no obvious mechanism that would preferentially remove cloud water associated with any given drop size, and therefore a representative sample will likely be obtained.

6 Dynamics and Chemistry of Marine Stratocumulus, Phase II

The Dynamics and Chemistry of Marine Stratocumulus, Phase II (DYCOMS-II) field project took place during July 2001 (Stevens et al., 2002) as a sequel to the original 1986 DYCOMS field campaign (Lenschow et al., 1988). The DYCOMS-II mission consisted of nine flights in the marine boundary layer over the Pacific Ocean using the NSF/NCAR C-130 aircraft as a research platform. Participation in DYCOMS-II provided the first opportunity for aircraft deployment of the axial-flow cyclone cloud water collection system, and served as a testing and evaluation program for the system as well as an opportunity to study the chemistry of marine stratocumulus clouds. Details regarding the deployment of the collection system during DYCOMS-II, along with chemical composition data from collected cloud water samples, will be presented in this chapter.

6.1 Project objectives

The primary focus of the DYCOMS-II field project was to study the turbulent mixing of free tropospheric air into the marine boundary layer (entrainment), and the production and influences of drizzle in marine stratocumulus cloud layers. Of the nine total DYCOMS-II research flights, seven flights were designed specifically to facilitate the study of entrainment. The remaining two flights were optimized for the operation of a cloud radar system. A summary of the nine research flights, numbered RF01-RF09, is provided in Table 6.1.

Estimation of entrainment through a tracer method prompted the measurement of gaseous dimethyl sulfide (DMS), O_3, CO, and CO_2. In addition, the NSF/NCAR C-130 was outfitted with aerosol and cloud microphysics instrumentation, including an aerosol backscatter lidar, several liquid water probes, multiple PMS optical particle probes, and instrumentation for measuring

meteorological and aircraft state parameters (Figure 6.1). Cloud and aerosol microphysics instrumentation relevant to the interpretation of cloud water chemical data are listed in Table 6.2.

flight number	date	take off time UTC	landing time UTC	research flight type	day/night
RF01	7/10/2002	06:28	15:12	entrainment	night
RF02	7/11/2002	06:51	15:44	entrainment	night
RF03	7/13/2002	06:35	15:42	entrainment	night
RF04	7/17/2002	06:33	15:29	entrainment	night
RF05	7/18/2002	06:31	15:25	entrainment	night
RF06	7/20/2002	06:12	15:08	radar	night
RF07	7/24/2002	06:35	15:44	entrainment	night
RF08	7/25/2002	20:10	5:15	entrainment	day
RF09	7/27/2002	19:01	3:42	radar	day

Table 6.1. DYCOMS-II research flight summary.

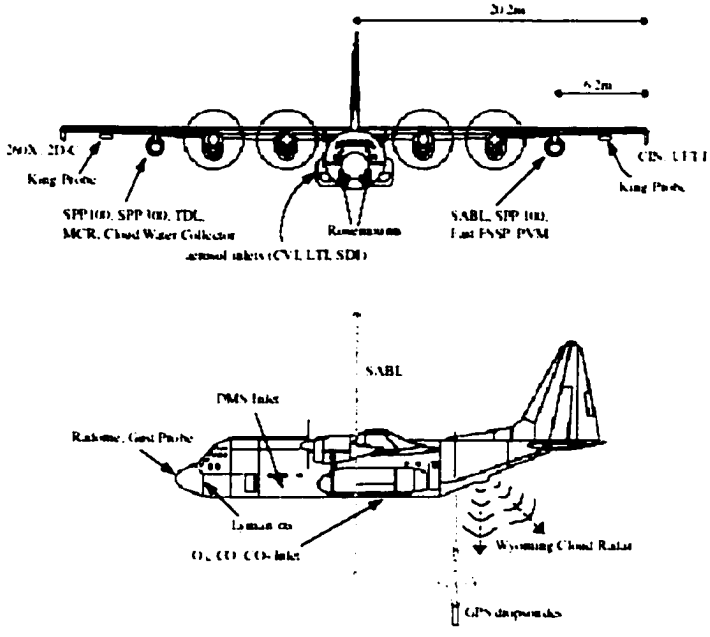

Figure 6.1. The NSF/NCAR C-130 aircraft and DYCOMS-II instrumentation layout (Stevens et al., 2002). The axial-flow cyclone cloud water collector was mounted on the instrumentation pod below the right wing.

instrument	location on aircraft	measurement	range
SPP-100 (FSSP-100)	left wing pod	cloud drop size distribution	2 - 47[a] μm
SPP-200 (PCASP)	right wing pod	aerosol size distribution	0.1 - 3 μm
SPP-300 (FSSP-300)	right wing pod	aerosol/cloud drop size distribution	0.3 - 20 μm
PMS-260X	right wing tip	cloud/drizzle drop size distribution	40 - 600 μm
Gerber PVM-100	left wing pod	integrated LWC[b]	0.002 - 10 g cm^{-3}
King Probe (Hot Wire)	left wing	integrated LWC	0.05 - 3 g cm^{-3}

[a]the range was set to 0.5 - 37 μm for RF02

[b]sensative to drop sizes between 3 and 50 μm (Gerber, 1996)

Table 6.2. Aerosol and cloud microphysics instrumentation included on the NSF/NCAR C-130 during DYCOMS-II.

A smaller suite of instrumentation was devoted to studying aerosol and cloud water chemistry, and was included primarily for CCN closure studies. In addition to CCN and condensation nuclei (CN) counters, subcloud aerosol and cloud drop residual particle composition analyses were directed by Lynn Russell (Princeton University) and Cynthia Twohy (Oregon State University). Bulk aerosol filter samples with a 1 μm upper size cut were collected on subcloud flight legs for elemental analysis through X-ray fluorescence and functional group analysis through Fourier transform infrared spectroscopy (Stevens et al., 2002). Similar analysis techniques were planned for cloud drop residual particles sampled with a counter flow virtual impactor (CVI). Further composition information was provided by single particle microscopy for the subcloud and cloud drop residual samples. Finally, the new axial-flow cyclone cloud water sampler was included on the DYCOMS-II mission, located on the instrumentation pod beneath the right wing of the NSF/NCAR C-130 (Figure 6.2).

Figure 6.2. The axial-flow cyclone cloud water collection system located beneath the right wing pod of the NSF/NCAR C-130. The collection system is housed in a PMS canister and is mounted in the lowest position on the instrumentation pod. Photo by Dick Friesen.

Despite the limited chemical measurements made during DYCOMS-II, the substantial in-cloud flight time required for the entrainment and drizzle studies served our objectives quite well by providing ample opportunity to test and evaluate the axial-flow cyclone cloud water sampler in clouds under flight conditions. It was hoped that any cloud water samples obtained during DYCOMS-II could be used to advance our knowledge of marine stratocumulus chemistry, to the extent possible given the limited supporting measurements. Detecting aqueous phase sulfur oxidation and determining the importance of various S(IV) oxidation pathways were of particular interest.

6.2 Flight details

The DYCOMS-II field project was based out of North Island Naval Air Station located on Coronado Island, just off the coast of San Diego, CA. The project targeted a region over the Pacific Ocean 400 km southwest of North Island Naval Air Station (Figure 6.3). All research

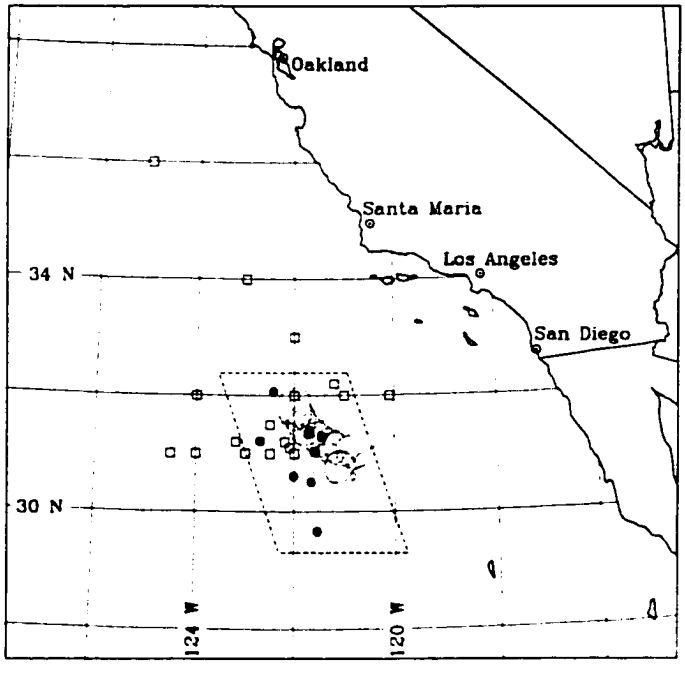

Figure 6.3. The DYCOMS-II field project target region off the coast of Southern California. The majority of flight time was spent in the area enclosed by the dashed line. The solid line represents the RF07 flight track which drifts with the mean wind. Filled circles indicate the centroid of the DYCOMS-II research flights, open squares indicate the location of research flights from previous campaigns.

flights were approximately 10 hours in length. The typical entrainment flight track (RF01-RF05, RF07-RF08) consisted of a ferry flight to the target location followed by a series of hour long legs flown at five different levels as illustrated in Figure 6.4: above cloud, below cloud, at the surface, just below cloud top and just above cloud base. At each level, the flight track consisted of one ½ hour clockwise circle and one ½ hour counterclockwise circle. Between horizontal flight legs, rapid traverses from the surface to the free troposphere provided profiles of the entire marine boundary layer. The flight tracks were Lagrangian, advecting with the mean wind in an attempt to sample the same air mass over the duration of the flight. However, wind shear in the marine boundary layer made truly Lagrangian flights impossible. In addition, air space restrictions, flight objectives, and logistical considerations created variation in the mission to mission flight tracks. The radar research flights (RF06 and RF09) featured substantially more complicated flight tracks.

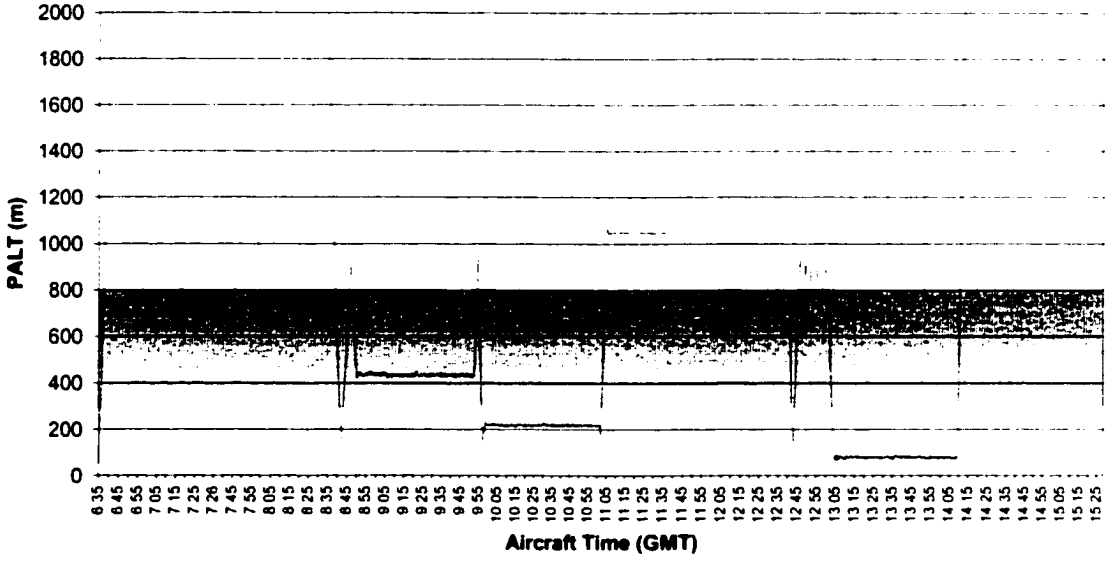

Figure 6.4. Altitude time series for RF07. The shaded area indicates the approximate cloud depth. Ferry legs were flown at 2500 to 5000 m. Horizontal research legs were typically flown at five levels: above cloud, below cloud, at the surface, just above cloud base, and just below cloud top. Between horizontal legs, profiles of the boundary layer were obtained through rapid ascents and descents. Cloud water collection was performed during the cloud base and cloud top legs.

Over the course of the project, seven nighttime flights (RF01-RF07) and two daytime flights (RF08 and RF09) were conducted. Nighttime flights were featured in order to simplify data analysis by eliminating short wave radiative forcing. Furthermore, marine stratocumulus clouds typically thicken during the night, so sampling at night enhanced the chances of encountering clouds suitable for the mission objectives. Finally, previous marine stratocumulus flights in the area occurred almost exclusively during the day, and nighttime sampling provided a contrasting case study.

6.3 Sampling environment

The marine boundary layer in the target region was well mixed throughout the duration of the DYCOMS-II project, as indicated by representative profiles of total water content and liquid water potential temperature (Figure 6.5). The well-mixed layer was topped by a strong inversion, below which the stratocumulus cloud deck formed, also observable in LWC measurements displayed in Figure 6.5. The cloud deck appeared to be very uniform and homogeneous for each of the research flights, as can be seen in GOES-10 visible satellite imagery for the periods just after RF04 and RF07 (Figure 6.6), and a photo taken during a return ferry flight (Figure 6.7).

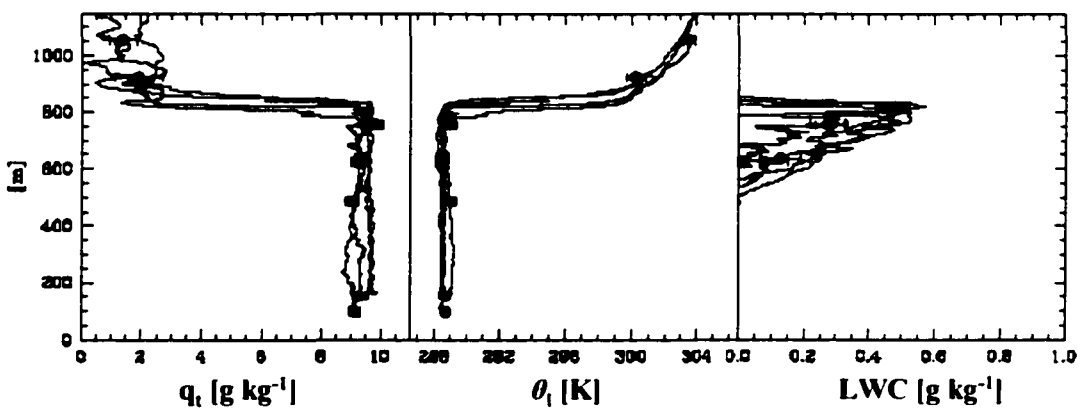

Figure 6.5. Multiple aircraft soundings obtained over the duration of RF01 showing vertical profiles of total water content (q_t), liquid water potential temperature (θ_l), and liquid water content (LWC). As indicated by the profiles of q_t and θ_l, the marine boundary layer was well mixed. The cloud layer resided just below the inversion. Stevens et al. (2002).

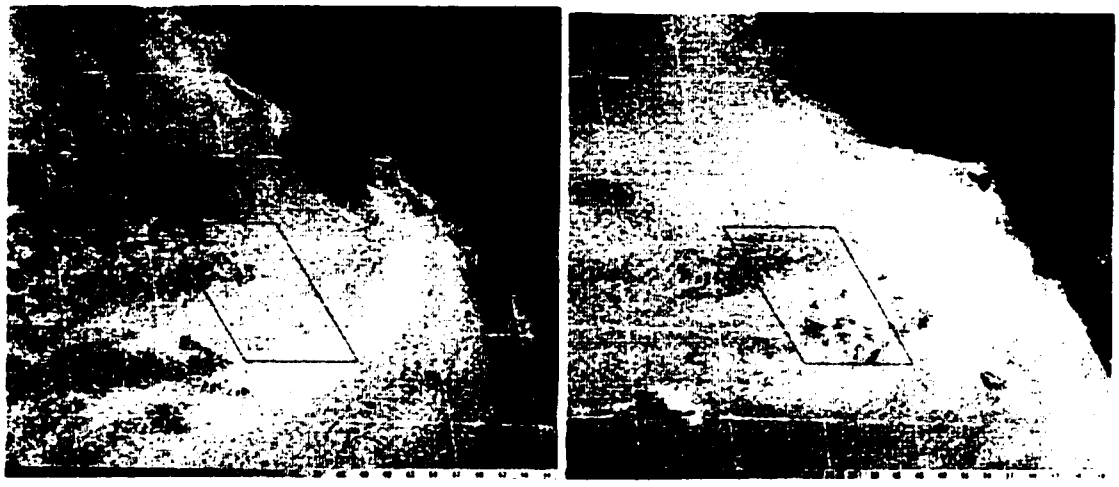

Figure 6.6. GOES-10 satellite visible images taken just after sunrise at the end of RF04 (left) and RF07 (right). The images cover latitudes from 27° N to 37°N and longitudes from 116° W to 126° W. The area enclosed by the solid line indicates the flight target region.

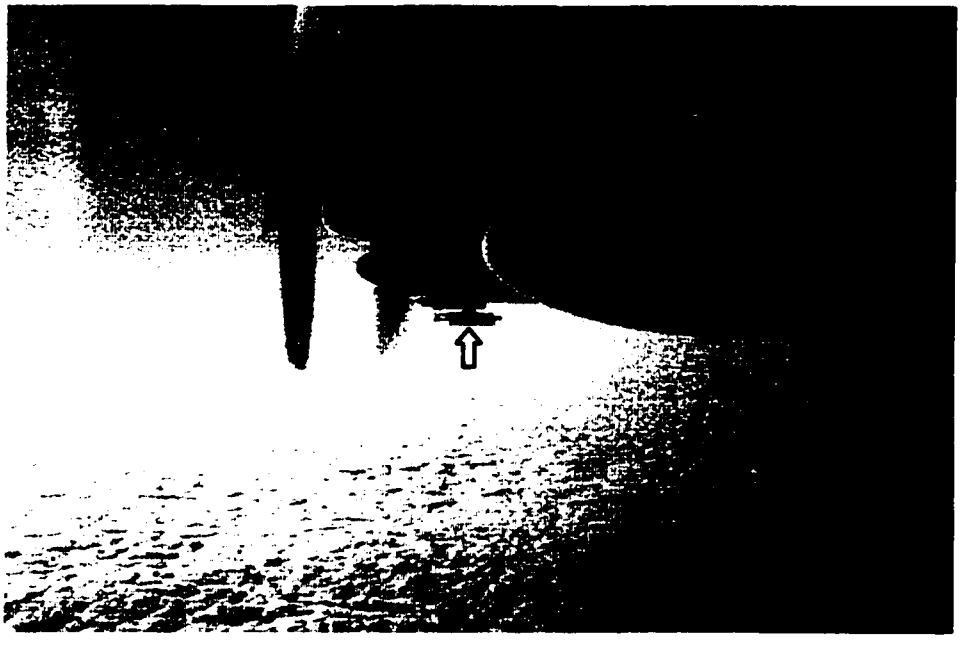

Figure 6.7. Photo of the marine stratocumulus cloud deck taken just after sunrise on a return ferry flight. The axial-flow cyclone cloud water collector can be seen in the center of the image, and is indicated by the arrow.

Despite the uniform appearance of the stratocumulus cloud layer, variabilities in drizzle, LWC, DMS concentrations, aerosol concentrations, cloud water chemical composition, and many other parameters were observed from flight to flight and even across individual flight leg circles (Stevens et al., 2002).

LWC generally increased linearly from cloud base to cloud top, typically ranging between 0.1 and 0.2 g m^{-3} during the cloud base flight legs, and 0.5 to 0.8 g m^{-3} during the cloud top legs. Ambient temperatures during sample periods ranged from 9.5° to 14.4° C. Winds were predominantly from the north-northwest and average wind speeds varied from 5 to 12 m s^{-1} between flights. Cloud drop number concentrations also varied substantially from flight to flight, ranging from 50 cm^{-3} to over 300 cm^{-3} during individual cloud water sampling periods, which could indicate the degree to which the sampled air masses can be considered of pristine marine origin. Drizzle was encountered on all flights, although the drizzle intensity varied from flight to flight. Drizzle intensity also varied considerably over the course of individual flight circles: heavy drizzle was observed in some locations while drizzle was absent at other locations. Environmental parameters for the nine DYCOMS-II flights are summarized in Table 6.3.

flight number	drizzle	wind speed[a] m s^{-1}	wind direction[a] ° (N=0/360)	cloud drop number conc[b] cm^{-3}	approx. cloud top height[c] m	approx. cloud layer depth[c] m
RF01	light	-	-	-	-	-
RF02	heavy	7.3	319	62	680	295
RF03	light	11.6	330	266	590	270
RF04	moderate	5.2	354	194	990	440
RF05	light	7.9	344	N/A[d]	770	130
RF06	moderate	6.7	333	N/A[d]	720	430
RF07	heavy	6.9	303	136	820	520
RF08	light	5.6	316	118	590	290
RF09	light	5.7	356	237	590	270

[a]averaged over the entire flight duration in the marine boundary layer

[b]SPP-100 data averaged over cloud water sample periods

[c]approximated from C-130 profile leg data

[d]SPP-100 data unavailable for RF05 and RF06

Table 6.3. Environmental parameters describing the nine DYCOMS-II research flights.

6.4 Cloud water sample collection during DYCOMS-II

With a storage limit of seven total cloud water samples per flight, the sampling strategy was to obtain two samples in the lower LWC regions near cloud base and five samples in the

higher LWC regions at cloud top. Individual samples were labeled with the research flight number and the sample bottle in which they were collected (e.g. RF02-1, RF02-2, etc.). The forward sample bottle was designated bottle 1 and the aft bottle was designated 7. Storage bottles were always filled sequentially beginning with bottle 1 and ending with bottle 7.

Seven samples could potentially be obtained for each research flight; however, not every bottle was used on every flight. Evaporation tests were conducted using one bottle each on RF02 and RF09, so no sample is available for RF02-5 and RF09-1. During RF05, three bottles contained no sample. The inlet cover remained closed while filling RF05-5, RF05-6 was an unsuccessful attempt to sample during rapid penetrations into and out of cloud top, and no attempt was made to sample into RF05-7. RF06-2 represents an unsuccessful attempt to capture a precipitation sample below cloud base. Therefore, excluding samples obtained during RF01 (see below), a total of 50 cloud water samples suitable for analysis were obtained over the course of the field campaign.

6.4.1 Collector operation

Although all of the subsystems of the cloud water collector worked as intended during the entire DYCOMS-II mission, the bulk collection efficiency was found to be anomalously low, as described in Section 5.2. Prior to participation in DYCOMS-II, collection rates were expected to be on the order of several milliliters of water per minute, based on the results of the numerical modeling effort. For those predicted sample collection rates, sample periods were expected to be several minutes in length in order to collect a sufficient volume for chemical analysis. However, low sample volumes obtained during short sample periods on RF01 revealed that the axial-flow cyclone collection efficiency was much lower than anticipated. The sample volumes from RF01 were insufficient for complete chemical analysis and therefore no results from RF01 will be reported.

A likely explanation of this low collection rate may be unintended flow of cloud water sample past, rather than into, the extraction slot. Laboratory flow testing has supported this explanation as the cause of the discrepancy, as discussed in Section 5.3. The incomplete removal of cloud water from the duct wall would reduce collection rate, but should maintain a representative cloud water sample. In order to compensate for the reduced collection efficiency of the system, sample times were increased to an average of 25 minutes for cloud base samples and 13 minutes for cloud top sample periods. Despite the low collection rate, enough cloud water was collected in nearly every sample period on flights RF02 through RF09 to enable the desired chemical analyses to be performed.

During the removal of the collection system from the C-130 at the conclusion of RF01, a small amount of water was observed in the bottom of the PMS canister. At the time, the source of the water was not readily apparent although it was presumed to originate from a leak in the sample transport tubing or a leak at the interface between the aluminum and polycarbonate sections of the axial-flow cyclone duct. At that interface, the aluminum duct simply inserts into a recess in the polycarbonate duct and is secured with a hose clamp. No o-rings were included at the interface because in theory all cloud water should be removed upstream at the extraction slot and no water would be available to leak at the interface location. After discovering that the collection efficiency was lower than expected and that water may in fact be flowing past the extraction slot, a leak at the aluminum duct interface appeared to be a possibility. To prevent potential water leaks at that location on future missions, a thin bead of silicone was used to seal the aluminum/polycarbonate duct interface on all subsequent flights. Based on the fact that sampled cloud water would be removed from the duct wall at the extraction slot with no possibility of coming into contact with the silicone at the downstream interface, no further consideration was given to the use of silicone as a sealant. Unfortunately, acetic acid vapor may have been released, ultimately depositing on surfaces of the axial-flow cyclone duct upstream of

the extraction slot which do come into contact with cloud water sample. The detection and consequences of this possible contamination will be discussed in the following sections.

6.4.2 Description of sample periods

Sample durations, collected sample volumes, and microphysical parameters, averaged for cloud base and cloud top sample periods for each flight, are listed in Table 6.4. A full listing of these parameters for individual sample periods can be found in Appendix D.

flight number	flight leg	number of samples collected	average sample duration min	average volume collected ml	average height above cloud base[a] m	average volume mean diameter[b] μm	average cloud drop number conc.[b] cm^{-3}	average LWC[c] $g\ m^{-3}$
RF02	cloud base	1	11.3	0.8	176	16.6	49	0.14
	cloud top	5	12.9	9.4	232	22.7	65	0.34
RF03	cloud base	2	16.0	5.0	2	10.6	279	0.25
	cloud top	5	11.7	3.5	154	13.1	260	0.46
RF04	cloud base	2	26.0	5.1	94	10.6	211	0.21
	cloud top	5	12.3	11.6	358	17.5	177	0.64[d]
RF05	cloud base	1	41.2	4.7	87	N/A[e]	N/A[e]	0.13
	cloud top	3	20.1	3.7	89	N/A[e]	N/A[e]	0.26
RF06	cloud base	2	16.1	1.4	102	N/A[e]	N/A[e]	0.17
	cloud top	4	9.2	5.7	329	N/A[e]	N/A[e]	0.50
RF07	cloud base	2	30.2	5.6	134	14.4	132	0.29
	cloud top	5	12.6	13.7	381	19.5	137	0.62
RF08	cloud base	0[f]	N/A	N/A	N/A	N/A	N/A	N/A
	cloud top	7	16.8	4.7	178	16.6	118	0.39
RF09	cloud base	2	37.3	3.6	68	9.2	244	0.13
	cloud top	4	16.1	5.1	205	12.7	233	0.39

[a]approximated from C-130 profile leg data
[b]SPP-100 measurements; only partial data available for RF03 and RF04
[c]Gerber PVM data
[d]PVM LWC unavailable for RF04-5 through RF04-7 sample periods, Hot Wire LWC used instead
[e]SPP-100 data unavailable for RF05 and RF06
[f]all in-cloud flight legs during RF08 were at mid-cloud or cloud top

Table 6.4. Sample durations, collected sample volumes, and microphysical parameters averaged for cloud base and cloud top sample periods for each DYCOMS-II flight.

A few notes regarding the aircraft instrumentation should be made: the SPP-100 operated only intermittently during flights RF03 and RF04. Therefore, cloud drop sizes and concentrations reported for RF03 (sample periods 2-6) and RF04 (sample periods 1,2,5,6) were calculated from data that temporally covered an average of 60% of those sampling periods. The

SPP-100 failed completely for RF05 and RF06, so cloud drop size and concentration information is unavailable for those flights. The PVM failed on RF04 during sample periods 5 through 7. King Probe LWC data, which had been tracking PVM LWC quite well during the first part of RF04, was used as a substitute measure of LWC for sample periods RF04-5 through RF04-7.

In order to investigate the origins of air masses sampled during the DYCOMS-II field project, back trajectories were calculated with the HYbrid Single-Particle Lagrangian Integrated Trajectory (HYSPLIT) model developed by NOAA's Air Resources Laboratory. The FNL global data archive set (based on spectral MRF model output) was selected for these calculations. Model vertical velocity was specified for calculating vertical motion. Three back trajectories originating from the approximate center of the DYCOMS-II target region were generated for each flight. The three back trajectories correspond to ending heights of 250 m, 500 m, and 1500 m. Because the 250 m and 500 m trajectories are fairly similar, only the 500 m trajectories are displayed in Figure 6.8. The 1500 m trajectories are displayed in Figure 6.9. All of the trajectories represent a 5 day air parcel history.

According to the HYSPLIT back trajectory analysis, the majority of the sampled air masses passed through the area north and west of the study region. The most notable exception is the trajectory corresponding to the air arriving at the target location above the boundary layer during RF09. In that case, the air mass appears to have passed over Mexico. For the most part, the air masses traveled along the coastline and a few traverse land prior to reaching the sampling location. Some error may be introduced into this analysis because the ending location, height, and time of these trajectories do not correspond exactly to individual sample periods. The absolute accuracy of these back trajectories may also diminish with time and would ideally be represented as probability distributions. In addition, the sparse observational data for model input over the remote ocean may affect the accuracy of trajectory calculations in that region. However, they do suggest that continentally influenced air may have been present at the DYCOMS-II target location, and that cloud water samples obtained there may not represent the cloud water

composition of a pristine marine environment. As will be discussed later in this chapter, there is not a strong correlation between the degree of continental influence as indicated by the back trajectory analysis and the air equivalent concentrations of species such as nitrate or sulfate that may represent anthropogenic sources.

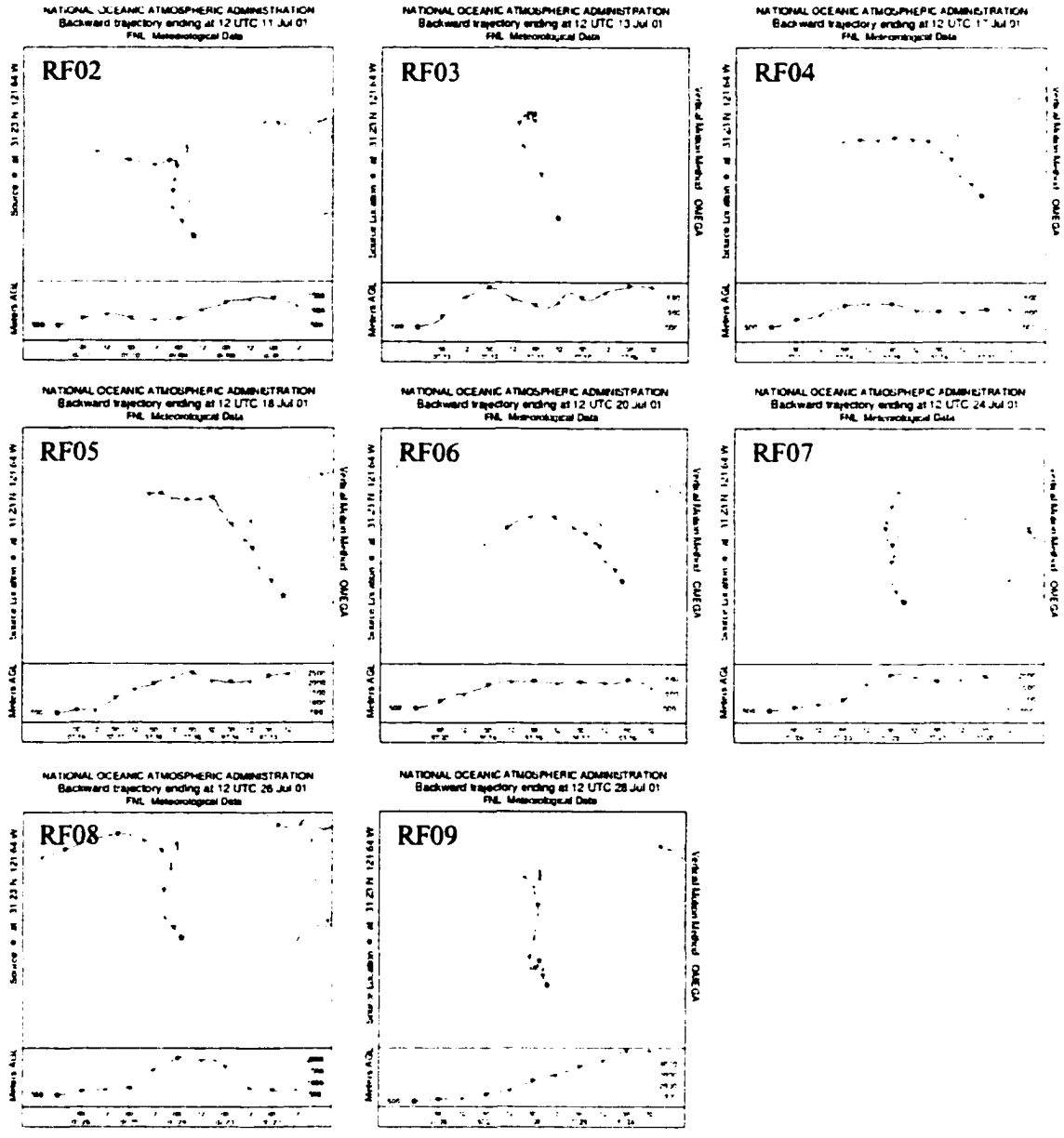

Figure 6.8. HYSPLIT back trajectories ending at 500 m at the center of the DYCOMS-II target area.

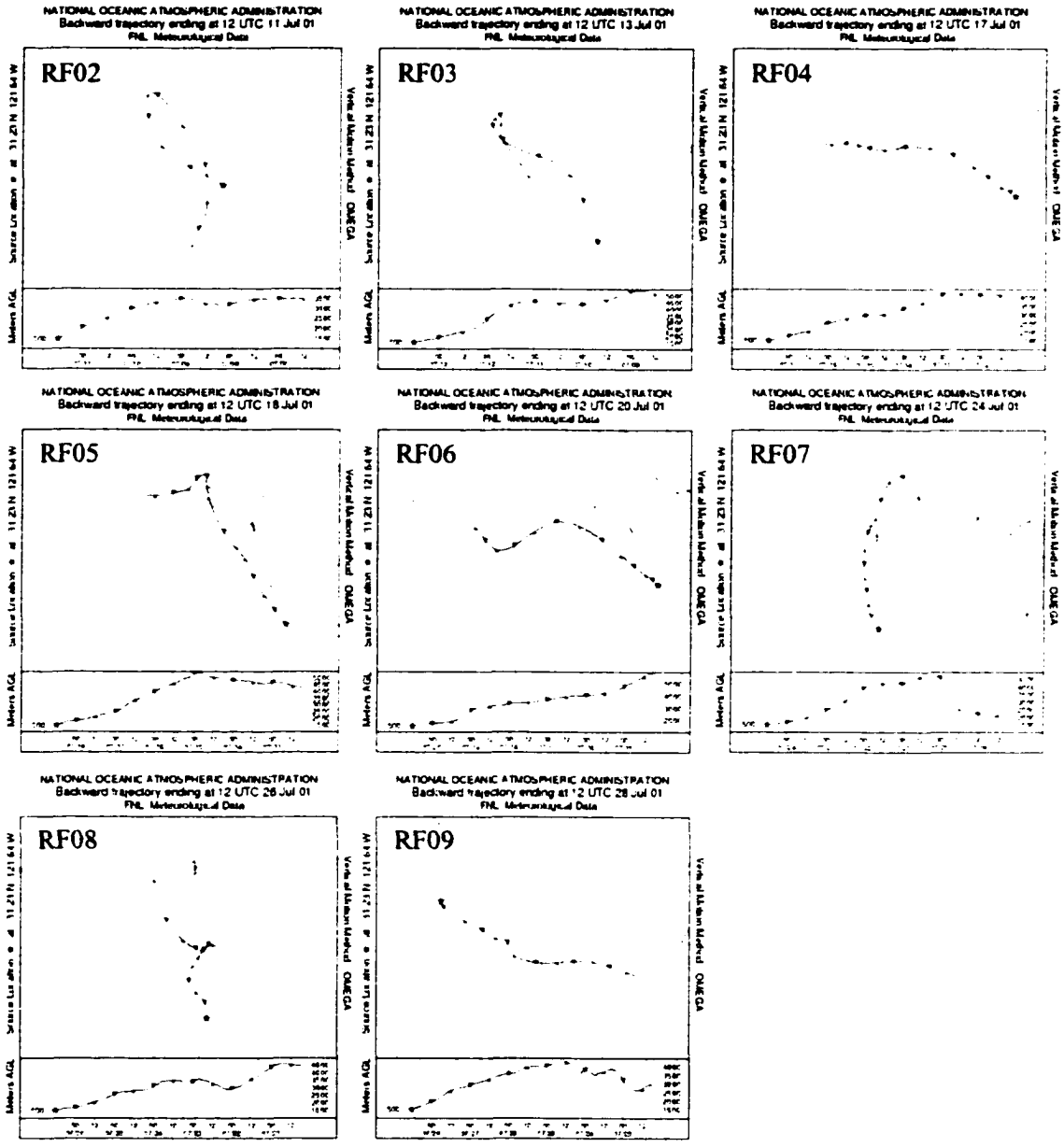

Figure 6.9. HYSPLIT back trajectories ending at 1500 m at the center of the DYCOMS-II target area.

6.5 Cloud water chemical analysis

Immediately after returning from each DYCOMS-II research flight, the collection system was removed from the NSF/NCAR C-130 aircraft following the procedures described in Appendix C. The sample storage bottles were removed from the collector and individually

weighed on a Mettler Toledo PB3002 digital balance to record the mass of collected water. Cloud water samples were then analyzed for pH and separate aliquots were prepared from the remaining cloud water sample for each species to be measured. When sufficient sample was available, aliquots were prepared for inorganic ions, S(IV), peroxides, trace metals, formaldehyde, and total organic carbon (TOC).

6.5.1 Analytical methods, uncertainties, and detection limits

In the following sections, sample preservation techniques and analytical methods will be briefly described for each measured species. More detailed information regarding the principles of analysis and the preparation of aliquot preservation solutions can be found in the Atmospheric Science Department Chemistry Group Cloud Water Manual. Sample aliquots were refrigerated at the field site for the duration of the DYCOMS-II mission. Following the completion of DYCOMS-II, samples were transported to the Colorado State University Department of Atmospheric Science analytical chemistry laboratory for analysis. Sample handling and aliquot preparation protocols used during the DYCOMS-II field project are provided in Appendix C.

A relative standard deviation (RSD) was established for each species based on replicate analyses of collected samples, except where noted, using the following expression:

$$RSD\% = \left(\frac{s_{pooled}}{\bar{x}}\right) \times 100 \tag{6.1}$$

where $\bar{x}$ is the mean value of the data set and s_{pooled} is the pooled standard deviation given by:

$$s_{pooled} = \sqrt{\frac{\sum_{i=1}^{N_1}(x_i - \bar{x}_1)^2 + \sum_{j=1}^{N_2}(x_j - \bar{x}_2)^2 + \sum_{k=1}^{N_3}(x_k - \bar{x}_3)^2 + \ldots}{N_1 + N_2 + N_3 + \ldots - N_s}} \tag{6.2}$$

where overbars denote mean values, N_1 is the number of data points in the first sample set, N_2 is the number of data points in the second data set, and N_s is the total number of data sets.

A minimum detection limit (MDL) was determined for each species from the analyses of collector blanks. Two field blanks were procured before every research flight. One blank was

taken from the axial-flow cyclone duct, curved vane assembly, and extraction slot. The second blank was from the storage system and represents a composite blank from the sample transport tubing and all seven storage bottles. Because samples from RF01 were of insufficient volume for analysis and are not reported here, only blanks from RF02 through RF09 were used in the detection limit calculations. Before every flight blanks were also taken from the portable water system used to provide deionized water (DI) in the field. The DI blanks are not included in the MDL calculations. No blank correction was performed for any of the species measured during the DYCOMS-II field campaign. The following equation was used to calculate the MDL for each species:

$$MDL = \bar{x}_b + ts_b\sqrt{\frac{N_b + N_s}{N_b N_s}} \tag{6.3}$$

where $\overline{x_b}$ is the blank mean value, s_b is the blank standard deviation, N_b is the number of blanks, N_s is the number of samples, and the t value is chosen at the 95% confidence level.

6.5.1.1 pH

An Orion model 250A pH meter and a Cole Parmer 05990-45 gel-filled electrode were used to measure cloud water pH on site immediately after every flight. For this measurement, 0.5 ml of cloud water sample was placed in a 2 ml microcentrifuge vial. The pH meter was calibrated before every set of measurements using pH 4.01 and pH 7.00 buffer solutions. A typical research flight set of seven samples required approximately 10 minutes for pH analysis. No drift in the pH meter calibration was observed during that time. Uncertainty is assumed to be ± 5 % (Moore, 2001).

6.5.1.2 Ion analysis

A single aliquot was prepared for anion and cation analysis for each sample period by placing 500 µl of sample into a polyethylene autosampler vial. Anions and cations were analyzed on parallel Dionex DX500 ion chromatograph (IC) systems. The anion system employed an

AS4A separator column in conjunction with an AG4A guard column, a self-regenerating anion suppressor, and a conductivity detector. The cation system contained a CS12 separator column with a CG12 guard column, a self-regenerating cation suppressor, and conductivity detector. The IC analyses were performed by Taehyoung Lee from 23 – 27 August 2001. Anion concentrations (Cl^-, NO_3^-, and SO_4^{2-}) and cation concentrations (Na^+, NH_4^+, K^+, Mg^{2+}, and Ca^{2+}) were measured for all 50 sample periods.

RSD and MDL statistics for the IC analysis can be found in Table 6.5. 14 replicate pairs were used to determine the RSD for each anion and cation species. The cation MDLs were calculated based on 16 blank measurements. While the MDLs calculated for Na^+, NH_4^+, and K^+ were in line with past analyses, Mg^{2+} and Ca^{2+} MDLs were exceptionally high, measuring 16.1 and 10.3 μN, respectively. Elevated field blank levels for Mg^{2+} and Ca^{2+}, averaging 14.8 and 9.2 μN respectively, were responsible for the high MDLs. Field DI blanks and measurements of Simlab DI water showed similar levels for these two cations, suggesting the problem originated within the IC itself. Following the replacement of the cation separator column, samples were rerun in May and June 2002 and those results for Mg^{2+} and Ca^{2+} are reported here. Blank concentrations were reduced to approximately 7 μN for both Mg^{2+} and Ca^{2+}.

	Sodium	Ammonium	Potassiuum	Magnesium	Calcium	Chloride	Nitrate	Sulfate
MDL (95% CL) μN	2 12	0 99	0 19	8 65	8 00	10 01	1 10*	1 18*
RSD%	2 75	8 69	4 21	2 93	5 89	2 95	1 40	2 28

*MDL from BRAVO study

Table 6.5. Mean detection limits and relative standard deviations for ionic species.

NO_3^-, and SO_4^{2-} levels in the DYCOMS-II blanks were below the IC peak detection values in most cases. In addition, few low standard checks were performed making MDL calculations impossible. As an alternative, NO_3^-, and SO_4^{2-} MDLs from the Big Bend Regional Aerosol and Visibility Observational (BRAVO) study are reported.

Although the analysis of organic acids was not originally proposed for DYCOMS-II, after returning from the field 22 samples were selected for acetate, formate, and methane sulfonic

acid (MSA) analysis by ion chromatography. The cation/anion aliquots were used for this analysis, and therefore no organic acid preservation was performed in the field. In light of this, a detailed listing of organic acid concentrations, RSDs, and MDLs will not be provided. Because MSA may be rapidly oxidized in the aqueous phase by OH (Fitzgerald, 1991), the value of the analysis is questionable. Acetate levels, as they pertain to pH measurements and the charge balance, will be discussed in the appropriate sections below. The organic acid runs were conducted from 21 – 24 September 2001.

6.5.1.3 S(IV)

Total S(IV) aliquots were prepared in the field by adding 100 µl of a S(IV) preservation solution and 100 µl of a catalase solution to 1 ml of cloud water sample. The buffered preservation solution contains formaldehyde to stabilize S(IV) as hydroxymethanesulfonate (HMS), and the catalase solution destroys H_2O_2 to prevent oxidation. At the time of analysis, the HMS was decomposed to free S(IV) and formaldehyde. Pararosaniline was then added to form a product which could be quantified with a Hach DR/400V spectrophotometer. This analysis method is based on that of Dasgupta et al. (1980) and is detailed in the Chemistry Group Cloud Water Manual. S(IV) aliquots from 46 sample periods were prepared and 38 were analyzed. The analysis occurred from 19 – 20 November 2001.

The S(IV) analysis required nearly the full aliquot volume, leaving an insufficient sample volume for replicate analysis. The RSD was therefore calculated from multiple standard replicates in this case. Eight replicates of standard 2 (2 µM), 9 replicates of standard 3 (5 µM), and 6 replicates of standard 5 (20 µM) were used. The MDL was established from 16 field blank measurements. S(IV) analysis statistics are reported in Table 6.6.

		S(IV)
MDL (95% CL)	µM	0.87
RSD%		8.39[a]

[a]RSD calculated from standard replicates

Table 6.6. Mean detection limit and relative standard deviation for S(IV).

6.5.1.4 Peroxides

Aliquots for total soluble peroxides were created by adding 200 µl of a conditioning reagent and 200 µl of a fluorescent reagent to 1 ml of cloud water sample. The conditioning reagent acted as a buffer and the fluorescent reagent contained *p*-hydroxyphenylacetic acid (POPHA) to react with available peroxides to form a stable dimer. The dimer concentration was then determined with a Shimadzu RF-1501 spectrofluorophotometer. This analysis technique does not differentiate hydrogen peroxide from organic peroxides, resulting in a measure of total soluble peroxides in the cloud water. Typically, however, hydrogen peroxide dominates total soluble peroxide concentrations in the atmosphere. The analysis follows the procedure of Lazrus et al. (1985) and is further described in the Chemistry Group Cloud Water Manual.

After an initial period of difficulty, due in part to high peroxide concentrations in the cloud samples, several modifications to the Cloud Water Manual peroxide analysis procedure were necessary to allow analysis. First, to bring the fluorescence intensity of the recommended standards within range of the RF-1501, the low sensitivity setting and a 10 nm emission slit width were specified. Second, the volumes of standards, samples, and reagent chemicals placed in the microcuvette for analysis were tripled. When using the volumes specified in the manual, a meniscus was visible in the microcuvette window and measurements were erratic. Finally, some DYCOMS-II samples were out of range of the RF-1501and a 1:4 dilution with DI water was necessary. A number of trial dilutions indicated that this process did not affect the peroxide measurements. Total peroxide aliquots were available for 44 sample periods and all were analyzed. Because the peroxide aliquots are less stable than the others, the analysis was conducted as soon as possible after returning from the DYCOMS-II field study. The peroxide analysis was initiated on 9 August 2001 and concluded on 10 August 2001.

A total of 23 pairs of replicates were used in the determination of the RSD and 16 field blanks for the MDL. The peroxide analysis statistics are displayed in Table 6.7.

		H_2O_2
MDL (95% CL)	μM	0.91
RSD%		2.06

Table 6.7. Minimum detection limit and relative standard deviation for H_2O_2.

6.5.1.5 Trace metals

A single aliquot was prepared for the measurement of total manganese and total iron for each sample period when sufficient sample was available. Trace metal aliquots were prepared by adding 100 μl of trace metal grade 9.7% HNO_3 to acidify 1 ml of cloud water sample. The analysis of the DYCOMS-II trace metal samples was performed by Hui Chang using a Varian model 640Z Zeeman-corrected graphite furnace atomic absorption spectrometer from 4 – 7 December 2001. Trace metal aliquots from 39 sample periods were prepared and 23 were analyzed.

Each trace metal sample was analyzed in replicate, making 23 replicate pairs available for the RSD calculation. Upon analysis, the cloud water collector storage system blank prepared before RF03 was found to be contaminated. Because the storage system blank was a composite from all sample bottles, the contamination could not be localized to a single bottle. Therefore, the three trace metal samples obtained during RF03 were removed from the data set and will not be reported here, resulting in a total of 20 trace metal samples. In addition, the RF03 trace metal blanks were not included in the detection limit calculation, leaving 14 field blanks for the MDL determination. The trace metal statistics are reported in Table 6.8.

		Fe	Mn
MDL (95% CL)	$\mu g\ l^{-1}$	11.63	0.41
RSD%		2.43	1.48

Table 6.8. Minimum detection limits and relative standard deviations for Fe and Mn.

6.5.1.6 Formaldehyde

A preservation solution (100 µl) containing bisulfite was added to 1 ml of cloud water sample in order to stabilize formaldehyde as HMS for storage. Just before analysis, HMS in the aliquot was decomposed back to formaldehyde to which excess 2,4-pentanedione and ammonia were added. The formaldehyde reacts with the 2,4-pentanedione and ammonia to produce diacetyldihydrolutidine (DDL) which can be quantified through fluorescence using a Shimadzu RF-1501 spectrofluorophotometer. Further details regarding the formaldehyde analysis procedure can be found in the Chemistry Group Cloud Water Manual and the technique is based on the work of Dong and Dasgupta (1987). Formaldehyde aliquots were prepared for 31 sample periods and 30 of those were analyzed. The formaldehyde analysis took place on 9 October 2001.

The RSD and MDL statistics for formaldehyde are provided in Table 6.9. There were 20 sample replicate measurements performed during the formaldehyde analysis and all were used to calculate the RSD. The 16 field blanks from RF02 through RF09 allowed the determination of the MDL.

		HCHO
MDL (95% CL)	µM	0.79
RSD%		3.18

Table 6.9. Minimum detection limit and relative standard deviation for HCHO.

6.5.1.7 Total organic carbon

Total organic carbon (TOC) aliquots were prepared by placing 15 ml of cloud water into glass vials. Due to limited sample volumes, only two TOC aliquots were prepared for the entire DYCOMS-II field project. Cloud water from two individual sample periods was required to create each 15 ml aliquot. One aliquot combined 7.5 ml of cloud water each from sample periods RF07-3 and RF07-4. The second aliquot combined 7.5 ml of cloud water each from sample

periods RF07-5 and RF07-6. In addition to these two combined samples from RF07, three blanks were analyzed. These included a DI blank, a blank from the collection surfaces in the interior of the axial-flow cyclone duct, and a composite blank from the sample storage system. All three blanks were taken prior to RF07. The TOC analysis was performed by Taehyoung Lee on 9 September 2001 using a Shimadzu model 5000A Total Organic Carbon Analyzer.

6.5.2 Chemical analysis results

6.5.2.1 pH

Sample pH ranged from 3.26 to 4.82, with a mean of 4.02 for all samples collected during the DYCOMS-II field project. Thus, all of the cloud water sampled during DYCOMS-II was more acidic than the "background" pH of 5.6 for cloud water in equilibrium with atmospheric CO_2 concentrations.

As noted earlier, the use of a silicone based sealant, although applied outside of the cloud water sample flow path, may have influenced sample composition and pH. Acetic acid vapor released from the silicone may have deposited on collection surfaces exposed to cloud water sample. As a weak acid, acetic acid dissociates into acetate and H^+, potentially acidifying cloud water samples. The organic acid IC analysis revealed anomalously high concentrations of acetate in a few of the analyzed samples. Concentrations exceeding 100 μN were observed intermittently, often with negligible concentrations in adjacent sample periods, suggesting contamination as a source. Blanks taken before reassembly of the collector, the point at which silicone was applied, always exhibited negligible acetate levels.

An estimate was made of the upper limit of pH modification due to acetic acid contamination. The IC analysis provided a measure of total acetic acid plus acetate, which was used along with the measured pH for each sample and the acetic acid/acetate equilibrium constant to determine the fraction that must have existed as acetate. Assuming that the calculated acetate concentration also represented the amount of H^+ added to the sample as a result of contamination.

the effect on pH could be determined. In reality, the dissociation of a weak acid in a sample of cloud water would not happen independently of other species in the cloud water and other aqueous phase processes, so it is impossible to determine the exact consequences of contamination. However, based on the above methodology, 20 of the 22 samples analyzed for organic acids would have experienced less than 5 % reductions in pH (0.2 pH units or less) due to acetic acid contamination. Two samples, RF02-1 and RF02-7, may have experienced pH reductions of 10.0% (0.4 pH units) and 14.5% (0.7 pH units), respectively.

6.5.2.2 Major inorganic ions

The average ionic cloud water composition for all DYCOMS-II samples is illustrated in Figure 6.10. Concentrations are expressed as μN, or μEquivalents l^{-1}. Sodium and chloride account for approximately two thirds of total ions in solution, while additional sea salt related ions, such as potassium, magnesium, calcium, and sulfate are present as well. Ammonium and nitrate were detected in low concentrations. Ammonium concentrations were below the MDL in 13 samples and are reported to be one half the MDL in those cases. Average cloud water concentrations of nitrate (31 μN) and ammonium (19 μN) measured during the DYCOMS-II field project are comparable to previously recorded measurements made in coastal stratiform clouds

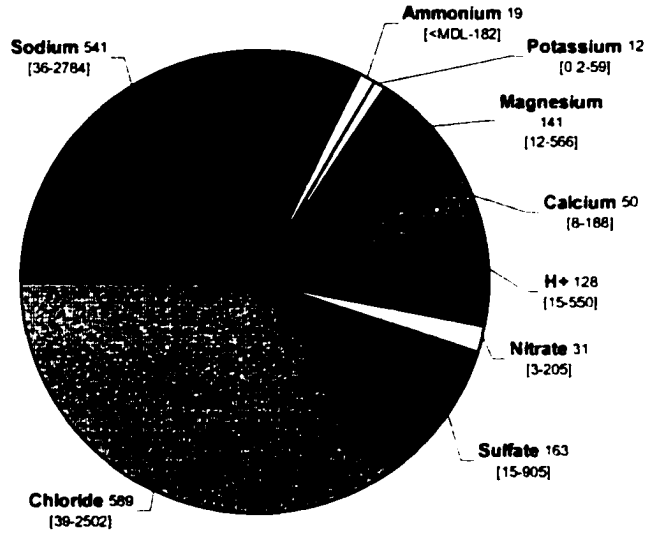

Figure 6.10. Average DYCOMS-II cloud water ionic concentrations. Average concentrations in μN follow species name and the range in μN appears in brackets.

sampled from a ground-based site in Oregon (Collett et al., 2002b). During that study, bulk cloud water nitrate concentrations averaged 23 μN and ammonium concentrations averaged approximately 50 μN. In contrast, the average DYCOMS-II sulfate concentration (163 μN) was more than double the Oregon average (69 μN). Average sodium and chloride concentrations measured during DYCOMS-II were also higher than concentrations measured in Oregon, although sea salt particle production is wind speed dependent making sodium and chloride comparisons difficult to interpret without additional meteorological information. More extensive comparisons to previous cloud water, aerosol, and gas phase studies will be presented in terms of air equivalent concentrations in Section 6.5.3.2.

An ionic charge balance was calculated for every sample as a ratio of total measured anions to total measured cations. H^+ concentrations were derived from measured pH. OH^- and predicted equilibrium bicarbonate concentrations were found to be negligible. Excluding organic acid concentrations, the anion to cation ratio ranged between 0.71 and 0.95, with an average of 0.85. For samples in which organic acids were analyzed, the average ratio increased to 0.89. However, because organic acids were not preserved in the field, their contribution to the ion balance is not fully captured. The lowest ratios were observed when total ionic concentrations were less than approximately 300 μN.

Many of the ions typically associated with sea salt were observed in proportions similar to those found in sea water, suggesting sea salt aerosol produced at the ocean surface as their source. Scatter plots of each ion concentration versus sodium concentration for the DYCOMS-II cloud water samples are displayed in Figure 6.11 along with typical sea water ratios. Sea water ratios were calculated from standard sea water elemental concentrations tabulated in the CRC Handbook of Physics and Chemistry (Lide, 2000) and closely match the measured ratios summarized by Keene et al. (1986). No significant chloride deficit was observed in the cloud water samples, unlike the typical case for polluted marine aerosols in which acid displacement reactions occur (e.g. Brimblecombe and Clegg, 1988, Munger et al., 1989). HCl displaced by

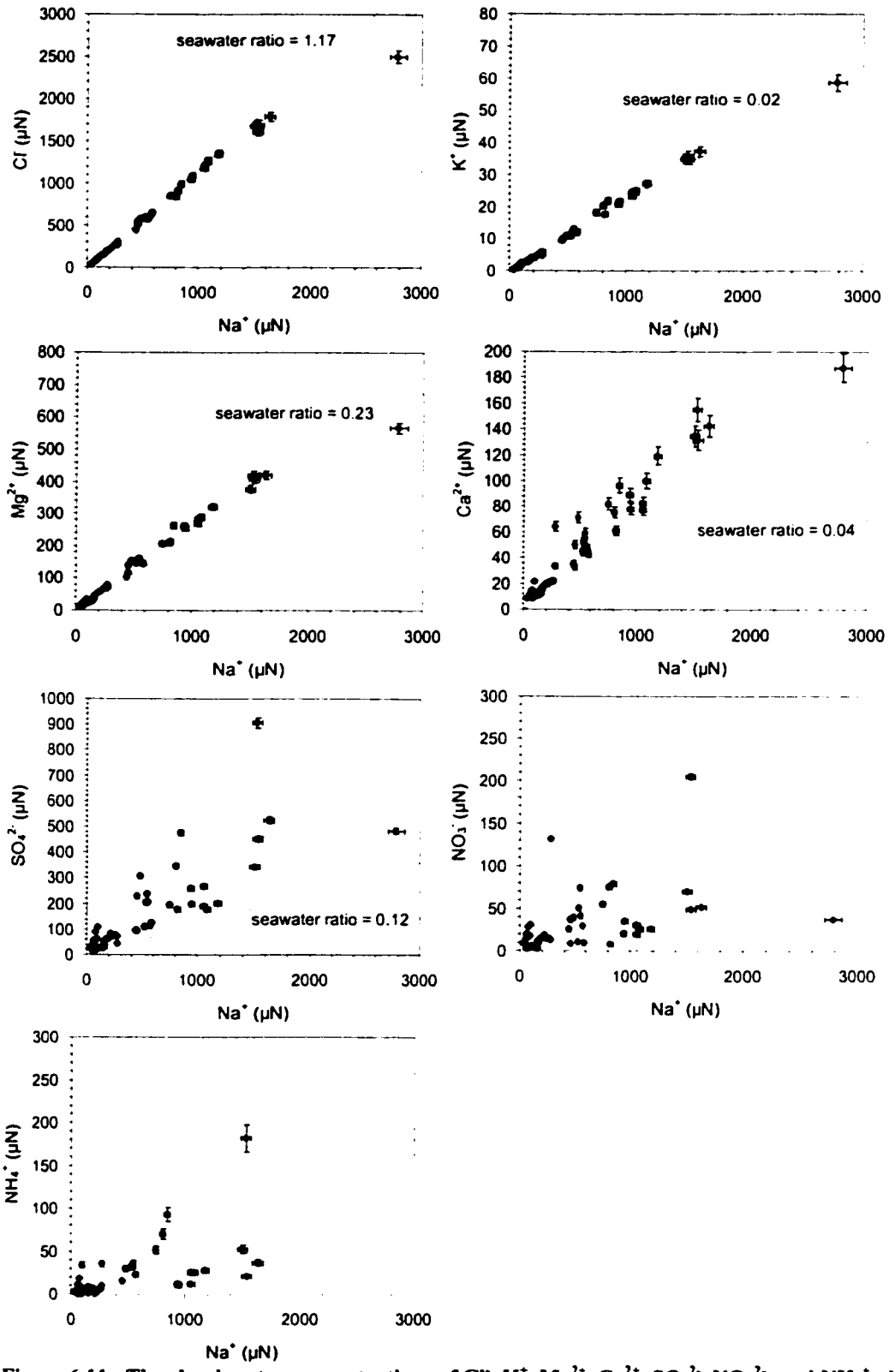

Figure 6.11. The cloud water concentrations of Cl^-, K^+, Mg^{2+}, Ca^{2+}, SO_4^{2-}, NO_3^{2-}, and NH_4^+ plotted against sodium concentration. The solid lines represent the ratio observed in sea water. Error bars indicate one sigma analytical uncertainty.

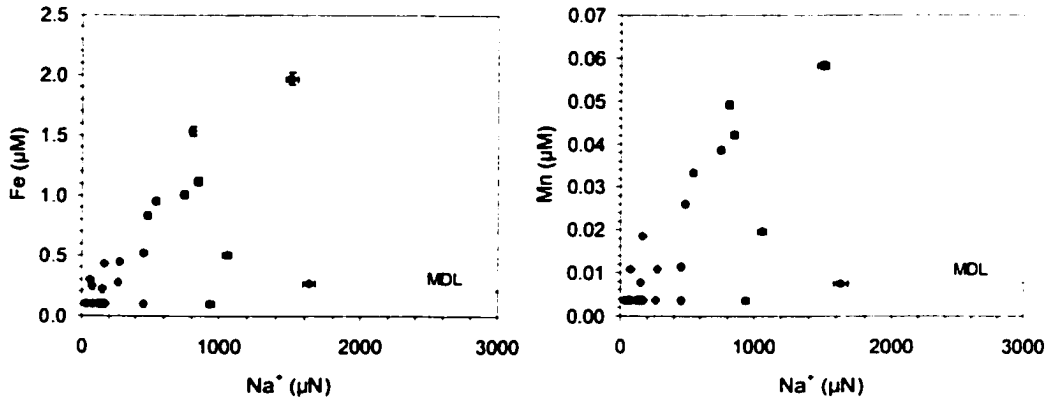

Figure 6.12. The cloud water concentrations of Fe and Mn plotted against sodium concentration. Molar seawater ratios of Fe and Mn to Na^+ are $< 1\times10^{-8}$. Fe and Mn concentrations below the MDL are reported as ½ the MDL. Error bars indicate one sigma analytical uncertainty.

NO_3^-, SO_4^{2-}, and organic acids in deliquesced, concentrated sea salt aerosols resides in the gas phase and can be reabsorbed by dilute cloud drops (Munger et al., 1989; Bator and Collett, 1997; von Glasow and Sander, 2001).

Potassium was present at sea water proportions while magnesium was slightly enriched and calcium was substantially enriched. Subtraction of the blank concentrations, which averaged approximately 7 μN for calcium and magnesium, reduces the apparent enrichment only minimally. Other researchers have noted comparable levels of calcium enrichment in marine cloud water samples collected on the coast of Washington (Vong et al., 1997) and Tenerife (Moore, 2001), in aerosols sampled off the coast of California (Parungo et al., 1987), and in rain water sampled on Bermuda (Keene et al., 1986). One possible explanation for the observed excess calcium and magnesium could be the presence of soil or mineral components which are nearly always identified in marine aerosols (Fitzgerald, 1991; Raemdonck et al., 1986). The measurement of Fe and Mn in the DYCOMS-II cloud water samples (Figure 6.12) supports the presence of a soil component due to the fact that Fe and Mn have a negligible marine source (as measured by the molar ratios of these species to Na^+ which are both $<1\times10^{-8}$) but a substantial crustal source. Evidence of Asian dust transport to the remote Pacific marine boundary layer has been presented by Uematsu et al. (1983); however, the peak period of Asian dust production and

transport is February to mid-June and may or may not have influenced the DYCOMS-II study region in July. Alternatively, calcium and magnesium enrichment may be the result of fractionation of sea salt species as aerosols are generated at the ocean surface (Sievering et al., 1999).

Sulfate was also significantly enriched in the DYCOMS-II cloud water samples compared to concentrations expected through direct injection of sea water into the marine boundary layer. Excess sulfate, referred to as non-sea salt sulfate ($nssSO_4^{2-}$), was found in every cloud water sample and accounted for 27% to 90% of the total sulfate concentration, similar to cloud water observations made during a clean marine case as part of the ACE2 HILLCLOUD experiment at Tenerife (Moore, 2001). Nitrate and ammonia do not have typical ratios defining their abundance with respect to sodium for sea water.

The limited chemical measurements made during the DYCOMS-II field project prevent the apportionment of ammonia, nitrate, and non-sea salt sulfate to particular sources. However, possible sources of these species in the marine boundary layer have been identified in previous studies. Radon measurements made during the original DYCOMS field project, which was conducted in the same vicinity as DYCOMS-II, provide strong evidence of transport from continental sources (Lenschow et al., 1988). The study of marine stratocumulus by Hudson and Frisbie (1991) during the First ISCCP Regional Experiment (FIRE) suggests that the signature of anthropogenic continental sources can be observed more than 500 km off the coast of California, coincident with the DYCOMS-II target region. Studies have also shown that nitrate concentrations in the remote marine boundary layer are strongly influenced by transport from continents (Savoie et al., 1989), although biologic sources and lightning could not be ruled out in their study. Prospero and Savoie (1989) estimate that continental sources are responsible for 40 to 70% of nitrate over the North Pacific, and attribute the highest concentrations to the transport of Asian dust in spring.

Elevated levels of ammonium, nitrate, and non-sea salt sulfate are also associated with regions of strong upwelling where biological activity is enhanced (Parungo et al., 1986; Parungo et al., 1987; Clarke et al., 1987). Upwelling results from the divergence of the ocean surface layer due to the alongshore component of wind stress, and occurs off the west coast of the U.S. primarily in summer as the Pacific subtropical high intensifies (Breaker and Gilliland, 1981; Smith, 1981). Nutrient rich water supports phytoplankton, zooplankton, and other aquatic life that release dimethyl sulfide (DMS), NO, and NH_3 which are precursors for sulfate, nitrate, and ammonium in aerosol particles and cloud drops. The production of DMS is widely considered to be the primary source of non-sea salt sulfur species in the marine boundary layer (Charlson et al., 1987, Kritz, 1982; Chen et al., 2000) and the link between DMS and non-sea salt sulfate observed in the marine boundary layer has been extensively examined (Charlson et al., 1987; Hegg et al., 1990; Pandis et al., 1994; Hertel et al., 1994; Huebert et al., 1996b). The proximity of the DYCOMS-II mission target area to a potentially significant upwelling region, and related biological emissions, may have influenced the chemical composition of the collected cloud water samples.

Emissions from ships can also be a significant source of SO_2 and NO_x in the marine boundary layer (Lawrence and Crutzen, 1999; Corbett et al., 1999); these gases can be oxidized to sulfate and nitrate, respectively. SO_2 emissions from ships can equal or exceed DMS emissions in the Northern Hemisphere (Corbett et al., 1999) and NO_x concentrations are increased by a factor of two in the remote boundary layer and by a factor of 100 or more in shipping lanes (Lawrence and Crutzen, 1999). A number of ships were observed during the DYCOMS-II mission although no record of their presence was kept. Finally, stratospheric injection and lightning can be potential sources of nitrate precursors in the remote marine boundary layer (Parungo et al., 1986; Liu et al., 1983; Kley et al., 1981).

6.5.2.3 S(IV)

Of the 38 total samples analyzed for S(IV), 22 had concentrations below the MDL of 0.87 μM. For sample periods with measured S(IV) concentrations below the MDL, a value of ½ the MDL was used for the calculation of average concentrations. Most of the values above the detection limit were recorded on flights RF03 and RF09 and for cloud base legs on other flights. The maximum S(IV) concentration was 3.3 μM and the average was 1.0 μM.

6.5.2.4 Peroxide

The analytical peroxide method used for the DYCOMS-II samples provides a measurement of hydrogen peroxide plus soluble organic peroxides. Although organic peroxides have been measured as a significant fraction of total gas phase peroxides (e.g. Heikes et al., 1996a; Heikes, 1992; Weller et al., 2000), aqueous phase measurements are usually dominated by H_2O_2 due to the lower solubility of organic peroxides (e.g. Olszyna et al., 1988; Kelly et al., 1985; Daum et al., 1984b). However, sizable contributions from organic peroxides have also been measured in a few continental cloud water samples obtained from aircraft (Kelly et al., 1985), thus the presence of organic peroxide can not be ruled out entirely.

Cloud water peroxide concentrations were considerable throughout the DYCOMS-II mission, ranging from 38 to 283 μM and averaging 114 μM. These levels may not be unexpected as peroxides are formed through peroxy radical recombination which is positively correlated with increased solar radiation, water vapor concentrations, and temperature (Lee et al., 2000). Gas phase H_2O_2 concentrations show a strong seasonality with the highest values typically recorded during the summer (Lee et al., 2000; Olszyna et al., 1988). Ozone and formaldehyde photolysis are primary sources of peroxy radicals in the marine boundary layer. Enhanced peroxide concentrations are also expected when nitrogen oxide levels are low, which is typically the case in the marine boundary layer (Weller et al., 2000; Martin et al., 1997). Overall, conditions were favorable for H_2O_2 production in the marine boundary layer during the DYCOMS-II mission.

6.5.2.5 Trace metals

Trace metal concentrations are available for 20 DYCOMS-II sample periods. No concentrations are reported from RF03 due to possible contamination as indicated by one of the blanks. Of the 20 samples, 8 Fe and 10 Mn samples were below the MDL and are therefore reported as one half the MDL. The average cloud water concentrations were 22.3 $\mu g\ l^{-1}$ and 0.7 $\mu g\ l^{-1}$ for Fe and Mn, respectively.

6.5.2.6 Formaldehyde

The average cloud water formaldehyde concentration (representing dissolved formaldehyde plus formaldehyde present in solution as the gem diol form) for the 30 analyzed DYCOMS-II sample periods was 4.7 μM, with a minimum value of 2.2 μM and a maximum value of 8.7 μM. Methane oxidation, followed by the formation and photolysis of methylhydroperoxide, is the main source of formaldehyde in the remote marine boundary layer (Ayers et al., 1997; Heikes et al., 2001). Minor sources of formaldehyde include DMS and light hydrocarbon oxidation. Formaldehyde can be directly emitted from anthropogenic sources; however, its photochemical lifetime is on the order of hours making long range transport into the remote marine boundary layer negligible (Weller et al., 2000).

6.5.2.7 Total organic carbon

The two combined TOC aliquots were both prepared from cloud water obtained during the RF07 flight leg at cloud top. RF07 was characterized by lower air equivalent cloud water concentrations of sea salt species, sulfate, nitrate, and ammonium than on many of the other flights (see Section 6.5.3.4). Therefore, just as RF07 concentrations of those species do not represent mission average concentrations, the same is most likely true for TOC concentrations. The TOC concentration for the RF07-3&4 combined sample measured 0.853 ppm, while the RF07-5&6 combined sample measured 0.841 ppm. TOC concentrations for the DI blank, axial-

flow cyclone interior blank, and storage system blank were 0.132, 0.035, and 0.065 ppm, respectively.

6.5.3 Discussion

6.5.3.1 Air equivalent concentrations

Aqueous phase cloud water concentrations of all species varied widely from sample to sample and from flight to flight during DYCOMS-II. As pointed out by Daum et al. (1984a) and Vong et al. (1997), variations in cloud water concentrations not only reflect changing source concentrations, chemical processing, and dispersion, but also changes in cloud LWC. Empirical power law relationships between cloud water ionic concentrations and LWC have been derived for several specific data sets to explain some of the variability in measured concentrations (Elbert et al., 2000; Moller et al., 1996). As LWC increases due to condensation, cloud drops will simply become more dilute, provided other factors remain constant. Although cloud drops of different sizes grow at different rates, a bulk cloud water sample should dilute at the rate of LWC increase. In marine stratocumulus clouds, LWC typically increases from cloud base to cloud top (e.g. Paluch et al., 1992; Paluch and Lenschow, 1991). The increase is related to an increase in drop diameter rather than increased number concentration (Martin et al., 1994) suggesting that the condensational growth of individual drops is the dominant process. This variation of LWC with height may exert a strong influence on the observed cloud water solute concentrations.

Figure 6.13 shows the Na^+ concentration, which is representative of other non volatile species, as a function of LWC for all cloud water samples obtained during DYCOMS-II. The samples are grouped by research flight and a power law curve fit is included for each flight. Although there is variability in the data for each flight, the general trend of lower concentrations with increasing LWC can be seen. For simple dilution, the power law exponent should be -1 as indicated by the dashed line. The average exponent for the power law relationships fit for each of the DYCOMS-II flights is -0.8, suggesting that dilution plays a role in the change in measured

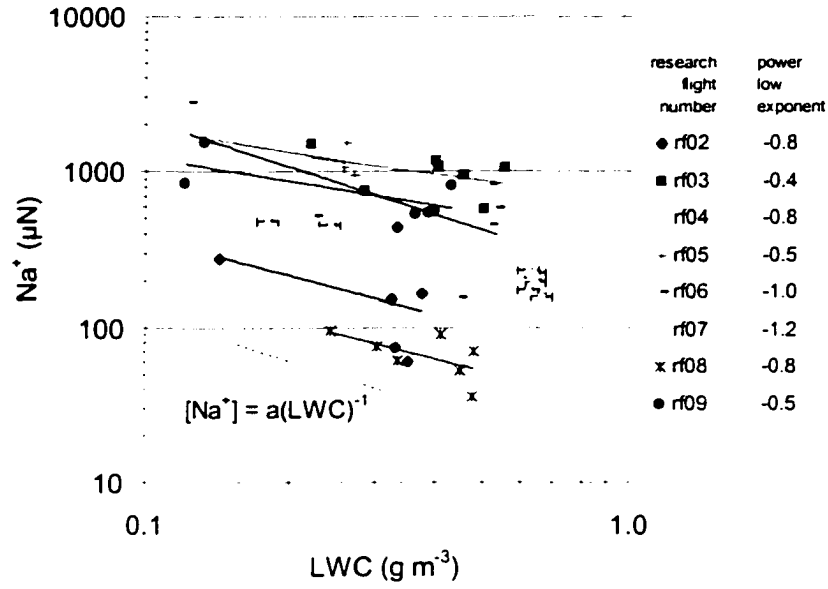

Figure 6.13. Cloud water sodium concentrations plotted against cloud LWC for individual DYCOMS-II research flights. The dashed line represents the expected variation in concentration due to dilution. One sigma LWC uncertainties are presented for RF04, and are representative of the remaining flights.

concentration on a given flight. The slightly lower than expected average dilution rate (exponent of -0.8 vs. -1) could be the result of smaller drops taking up a disproportionate amount of water, but remaining unsampled as a result of non-isokinetic sampling by the axial-flow cyclone. Alternatively, a lower than expected dilution rate could reflect the activation of additional CCN as LWC increases. CCN activation would contribute solute mass to the cloud drop population as LWC increases whereas vapor deposition to existing drops would not.

Cloud water concentrations can be converted to air equivalent concentrations to remove the effects of dilution associated with changing LWC. For the DYCOMS-II samples, air equivalent concentrations were obtained by multiplying the cloud water solute concentration by the average LWC during the sample period as measured by the PVM-100A. The PVM-100 A has a reported uncertainty of 5%. For volatile species (i.e. H_2O_2, HCHO) that may partition between the gas and aqueous phase, an additional gas phase concentration must be considered to order to arrive at a total air equivalent concentration. Calculation of equilibrium gas phase concentrations will be discussed in the following section.

Air equivalent concentrations represent the amount of solute present inside cloud drops in a given volume of air, and can be expressed on a molar basis (nmol m^{-3}), or a mass basis ($\mu g\ m^{-3}$). Air equivalent concentrations are useful for making comparisons with concurrent aerosol and gas phase measurements or with cloud water concentrations obtained during other field studies. Average air equivalent concentrations for ionic species are displayed in Figure 6.14.

6.5.3.2 Comparison to previous cloud water, aerosol, and trace gas studies

There have been few cloud water chemistry studies conducted in the remote marine environment and no known cloud water composition data, other than pH, published from those studies with which to compare DYCOMS-II results. However, the cloud water chemical composition measured during DYCOMS-II can be compared to coastal cloud water studies in which sampled air masses originated primarily from the marine boundary layer. Unfortunately, many cloud water studies do not report air equivalent concentrations, or measured cloud LWC, making comparisons difficult. The more numerous aerosol and trace gas studies conducted in the remote marine environment provide a useful comparison as well. The presentation of cloud water, aerosol, and trace gas measurements from previous field campaigns in this section is not

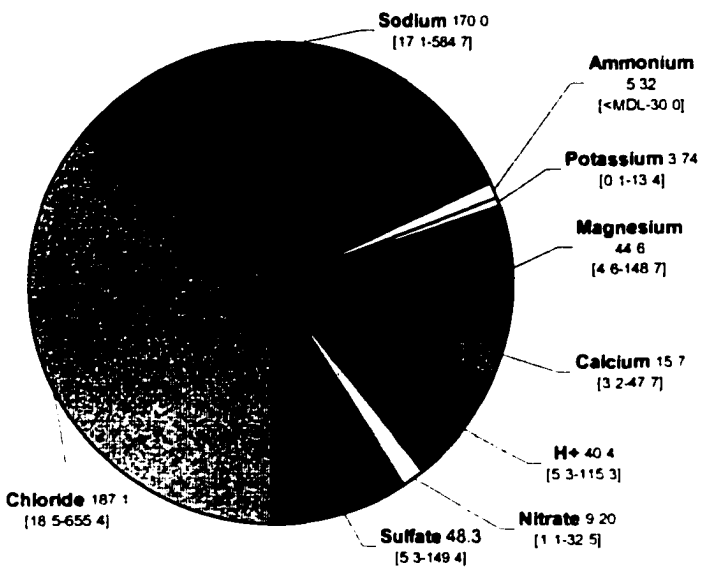

Figure 6.14. Average DYCOMS-II air equivalent ionic concentrations. Average concentrations in nEq m^{-3} follow species name and the range in nEq m^{-3} appears in brackets.

intended as a comprehensive review, but rather as an indication of the range of concentrations obtained under conditions similar to those experienced during the DYCOMS-II field project.

While most coastal cloud water studies do not report the origin of air masses present at the sampling site, coastal studies at Tenerife in the Canary Islands and Cheeka Peak Observatory (CPO) in Washington State do provide back trajectory analysis and therefore may be more suitable for comparison to DYCOMS-II measurements.

Concentrations measured at CPO in May 1993 (Vong et al., 1997) were classified according to air mass origin. A composite clean marine background cloud water composition was constructed from 48 samples with air mass back trajectories traversing the Pacific Ocean prior to sampling. These background concentrations for most species at CPO tended to be lower than those measured during DYCOMS-II. The lower concentrations may be due in part to the selection of purely maritime air mass trajectories to construct a clean marine background case, whereas the DYCOMS-II back trajectory analysis shows that some of the DYCOMS-II cloud water samples may have been obtained from continentally influenced air masses. Additionally, the spring time CPO campaign may not have been influenced as strongly by marine biological activity.

The field project conducted at Tenerife in 1995 and 1996 measured slightly higher concentrations, as averaged from 59 cloud water samples, than the DYCOMS-II campaign (Borys et al., 1998). However, although nearly all of the sample period back trajectories passed over the Atlantic Ocean for a substantial duration, a number also crossed the European continent at some point during the 6 days prior to sampling and therefore the study does not necessarily represent an uncontaminated background marine environment. The concentrations of individual solutes measured during these field campaigns at Tenerife and CPO will be compared with DYCOMS-II measurements throughout the remainder of this section.

Cloud water pH measurements obtained during the original DYCOMS mission, which included slotted-rod collectors and was carried out in the same geographic area as DYCOMS-II,

were consistent with the current reported pH values which ranged between 3.26 to 4.82, with an average of 3.90. The original DYCOMS cloud water pH readings ranged between 3.71 and 5.06 and averaged 4.02 (Lenschow et al., 1988). Unfortunately no other chemical results have been published regarding the cloud water samples collected during the original DYCOMS mission. Aircraft-based cloud water collected over the Northwest Pacific exhibited an average pH of 4.4 (Watanabe et al., 2001). However, that average is only based on 4 samples and the conditions encountered during that mission were admittedly influenced by anthropogenic sources. Two cloud water samples obtained off the coast of Washington State during periods of onshore flow, and therefore presumably of marine character, had measured pH values of 4.0 (Hegg et al., 1984b).

Comparable pH levels have also been observed for cloud water in a marine stratiform environment as sampled from coastal, ground-based sites at Tenerife and CPO. The pH measured at Tenerife ranged between 3.0 and 4.4 (Borys et al., 1998) and the mean pH measured at CPO was 4.46 (Vong et al., 1997). Slightly higher cloud water pH values, varying between 4.5 and 5.0, were measured during an ACE-2 clean marine event as reported in Moore (2001). Cloud water pH was determined to vary between 4.21 and 6.03 at Angora Peak in Oregon (Rao and Collett, 1995), between 4.05 and 5.54 approximately 100 km from the Pacific Ocean in Oregon, and between 3.65 and 5.20 along the coast of Northern California (Weathers et al., 1988).

Unfortunately, a number of factors make it difficult to directly compare concentrations of sea salt components between studies, as the production of sea salt is heavily dependent on wind speed and other parameters. There is no "background" sea salt concentration for the remote marine boundary layer (Fitzgerald, 1991). Sea salt aerosol particles that are incorporated into cloud drops primarily through nucleation scavenging are produced when bubbles at the ocean surface burst and generate up to 10 jet drops and hundreds of film drops. After partial or complete evaporation, jet drops are generally less than 1 to 2 μm radius and film drops are less than 1 μm radius (O'Dowd et al., 1997). In addition, wave breaking at high wind speeds can

directly generate spume drops greater than 10 μm radius. Although there is some disagreement as to the importance of sea salt particles acting as CCN, measurements support the assertion that sea salt particles are well mixed throughout the marine boundary layer and can account for 90% of activated CCN (O'Dowd et al., 1997).

The number and mass concentration of sea salt aerosols in the remote boundary layer is a strong function of wind speed. Figure 6.15 shows a scatter plot of sea salt mass (in cloud water) versus wind speed for the DYCOMS-II sample periods along with two curves fit to experimental data. The curves are the upper and lower limiting cases presented by Fitzgerald (1991) and are based on data from Exton et al. (1986) and Gras and Ayers (1983). Of course the wind speed measured concurrently with the DYCOMS-II cloud water samples is not necessarily representative of the wind speed at the time of sea salt aerosol production, a fact that may account for the significant scatter in the DYCOMS-II data. In addition to air mass history, factors such as particle scavenging and sea surface temperature account for the wide range of experimentally determined sea salt concentrations for a given wind speed (Fitzgerald, 1991).

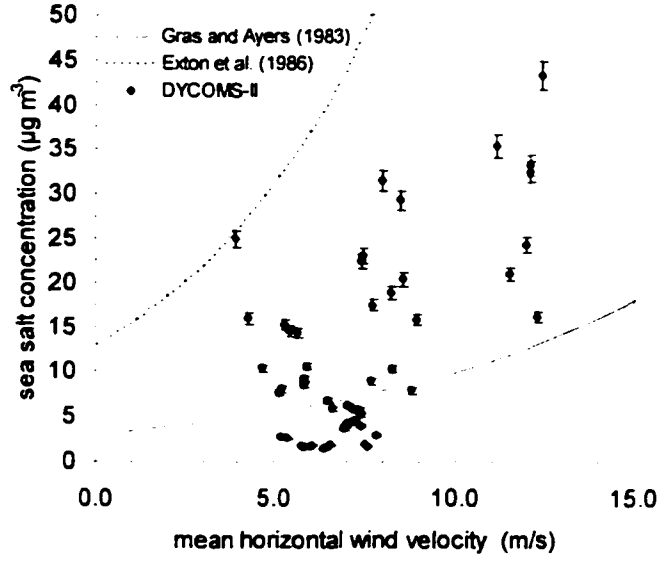

Figure 6.15. Sea salt mass concentration as a function of wind speed for DYCOMS-II cloud water samples and two curves fit to experimental data. Error bars represent one sigma analytical uncertainty.

It may be worth mentioning a few sea salt mass concentrations to verify that the DYCOMS-II measurements fall into the range of reported values. To make the following comparisons, it is assumed that the majority of sea salt aerosol particles activate to form cloud drops and are therefore contained in the cloud water samples. There is some evidence in the DYCOMS-II data that supports this assumption. When plotting cloud drop number concentration measured via the SPP-100 versus below-cloud aerosol number concentration measured via the SPP-200 for individual cloud water sampling periods (see Figure 6.21), a nearly 1:1 linear relationship is observed. Although both instruments are sensitive to finite size ranges (see Table 6.2) that may or may not cover the entire aerosol and cloud drop populations, the 1:1 linear relationship in Figure 6.21 suggests that during the DYCOMS-II mission, the majority of aerosols between 0.1 and 3 μm were activating to form cloud drops.

Comparisons between the sea salt mass measured in DYCOMS-II cloud water samples and measurements from previous aerosol studies can be based on air equivalent concentrations of sodium mass, which averaged 3.9 $\mu g\ m^{-3}$ for the DYCOMS-II cloud water samples, or total sea salt mass which averaged 12.5 $\mu g\ m^{-3}$ for DYCOMS-II cloud water samples. Air equivalent cloud water sodium concentrations averaged 1.6 $\mu g\ m^{-3}$ at CPO (Vong et al., 1997) and 3.5 $\mu g\ m^{-3}$ at Tenerife (Borys et al., 1998). A data base of all available marine aerosol chemical measurements assembled by Heintzenberg et al. (2000) puts the global average sodium concentration at 3.6 $\mu g\ m^{-3}$, in good agreement with the DYCOMS-II average. Aerosol measurements specific to the Pacific Ocean indicate sodium concentrations of 3.0 $\mu g\ m^{-3}$ (Parungo et al., 1986). Long term observations of aerosol sodium mass concentrations at 5 stations in the Atlantic range from 3.3 to 7.5 $\mu g\ m^{-3}$ (Gong et al., 1997). Fitzgerald (1991) summarizes four aerosol studies in the marine boundary layer when wind speed was less than 10 $m\ s^{-1}$ and shows total sea salt mass concentrations varying from 1.2 to 55 $\mu g\ m^{-3}$. Finally, total sea salt mass loadings measured on the coast of Antarctica are slightly lower, ranging between 0.2 and 10.2 $\mu g\ m^{-3}$ (Hall and Wolff, 1998).

Many studies have been devoted to the determination of non-sea salt sulfate concentrations in the marine boundary layer. Non-sea salt sulfate has both anthropogenic and marine sources and varies widely from study to study. The air equivalent non-sea salt sulfate concentration averaged 14.0 nmol m^{-3} for the DYCOMS-II cloud water samples, ranging between 0.9 and 53.9 nmol m^{-3}. Cloud water samples collected at CPO contained lower air equivalent concentrations, averaging 4.0 nmol m^{-3} (Vong et al., 1997). A much higher cloud water derived air equivalent concentration mean of 38.5 nmol m^{-3} was obtained at Tenerife (Borys et al., 1998). Ship-based measurements of non-sea salt sulfate aerosol in the Pacific Ocean during various field campaigns have averaged approximately 9.4 nmol m^{-3} (Parungo et al., 1987), 2.2 nmol m^{-3} (Parungo et al, 1986), 8.5 nmol m^{-3} (Clarke et al., 1987), and approximately 18 to 32 nmol m^{-3} between the equator and 20° N (Bates et al., 1992). Aircraft-based aerosol observations over the Pacific recorded average non-sea salt concentrations of 5.7 nmol m^{-3} in remote marine samples and 54.5 nmol m^{-3} in Asian influenced samples (Dibb et al., 1996). Particulate only measurements for predominantly marine air masses over the Atlantic Ocean measured 14.8 nmol m^{-3} (Huebert et al., 1996a). Average non-sea salt sulfate values in the Southern Hemisphere during ACE-1 were 6.6 nmol m^{-3} for C-130 aircraft samples and 3.4 nmol m^{-3} for ground-based filter samples (Huebert et al., 1998). Huebert et al. (1996b) reports a diurnal variation in the concentration of non-sea salt sulfate ranging from 7.8 nmol m^{-3} at sunrise to 9.4 nmol m^{-3} at sunset. These measurements were made in the remote marine boundary layer at Christmas Island during periods free from anthropogenic contributions.

Nitrate concentrations measured in cloud water sampled during the DYCOMS-II field project were higher than values measured during other remote marine boundary layer studies. The DYCOMS-II air equivalent nitrate concentration averaged 9.2 nmol m^{-3}. Nitrate concentrations derived from cloud water obtained at CPO were about half that value, averaging 4.2 nmol m^{-3}. Some of the lowest total nitrate (particulate nitrate + $HNO_3(g)$) concentrations have been measured by Savoie et al. (1989) in the remote tropical South Pacific marine boundary layer

(1.8 nmol m^{-3}) and the equatorial Pacific (2.6 nmol m^{-3}). North Pacific averages at Midway and Oahu have also been reported by Savoie et al. as 4.7 and 5.8 nmol m^{-3}. The Midway and Oahu average values are significantly exceeded when dust storms are prevalent. Particulate only measurements in marine air masses have been made in the Atlantic by Huebert et al. (1996a). In that study, the average nitrate concentration was 9.6 nmol m^{-3}, similar to the DYCOMS-II cloud value. Much higher nitrate concentrations were recorded in the cloud water study conducted by Borys et al. (1998) at Tenerife where the average air equivalent concentration was 33.9 nmol m^{-3}.

Trace metals, presumably mostly of crustal origin, have been observed in similar concentrations to those measured in the DYCOMS-II cloud water samples, which averaged 7.1 ng m^{-3} and 0.23 ng m^{-3} for Fe and Mn, respectively. Raemdonck et al. (1986) report an average aerosol Fe concentration of 8.2 ng m^{-3} derived from cascade inertial impactor measurements made during a cruise in the remote Tropical Pacific. Additional remote marine Fe concentrations summarized by Raemdonck et al. range between 3.3 and 10 ng m^{-3}. Mn concentrations during that study were below the detection limit of 0.23 ng m^{-3} except for two samples with concentrations of 0.63 and 0.31 ng m^{-3}. A background marine Mn concentration of 0.3 ng m^{-3} was obtained from the cloud water samples collected by Vong et al. (1997) at CPO.

Ammonium concentrations in DYCOMS-II cloud water samples averaged 19.3 μM. If gas and aqueous phase ammonia are in equilibrium in marine stratocumulus, it is expected that nearly all of the ammonia will reside in the cloud drops due to its high solubility at typical cloud pH values (Quinn et al., 1987), although a fraction could potentially remain as interstitial ammonium sulfate aerosol. Assuming that the measured ammonium concentration in the DYCOMS-II cloud water samples represents the total available ammonium, the air equivalent ammonium concentration was 5.3 nmol m^{-3}.

These concentrations compare favorably with previous measurement studies in the marine environment. For air masses of marine origin arriving at CPO, cloud water concentrations of ammonium averaged 11.1 μM, and air equivalent concentrations averaged 3.3 nmol m^{-3} (Vong

et al., 1997). Again, the air equivalent cloud water measurements of Borys et al. (1998) are much higher, averaging 55.6 nmol m^{-3}. Ammonium in the particulate phase only was measured by Huebert et al. (1996a) in predominantly marine only air masses in the Atlantic, and averaged 12.6 nmol m^{-3}.

Concentrations of gas phase ammonia over the surface of the ocean, based on measured sea water concentrations of total ammonia near Cape Grim, Tasmania and the assumption of Henry's law equilibrium, are predicted to be between 3.6 and 8.7 nmol m^{-3} (Quinn et al., 1987). This range of background ammonia concentrations has been supported by gas phase measurements in air of marine origin at Cape Grim (Ayers and Gras, 1983; 1980). Sea water ammonia concentrations in the North Pacific were found to be comparable to those measured at Cape Grim (Quinn et al., 1988), suggesting that similar equilibrium gas phase concentrations should be experienced. In fact, simultaneous aerosol and gas phase ammonia concentrations were made at the coastal CPO site in May 1987 and from a research vessel off the coast of North America (Quinn et al., 1988). Air masses originating in the North Pacific were measured, yielding average values of total ammonia of 7.2 nmol m^{-3} and 6.9 nmol m^{-3} for the ship and coastal site, respectively. During the study, the ocean was found to be a net source of ammonia. Unfortunately, the source of the ammonia measured in ocean surface waters was not discussed in the papers reviewed for this work.

Cloud water measurements of peroxides have been made during many ground-based and aircraft-based field campaigns (e.g. Olszyna et al., 1988; Kelly et al., 1985; Macdonald et al., 1995; Barth et al., 1989; Noone et al., 1991; Richards, 1995; Rao and Collett, 1995; Collett et al., 1999; Hoag et al., 1999). Some of the highest readings were obtained at Whitetop Mountain during the summer where a mean concentration of 57 μM and a maximum concentration of 247 μM were recorded (Olszyna et al., 1988). Richards (1995) measured aqueous phase H_2O_2 concentrations in the Los Angeles Basin and found increasing concentrations toward the coast

reaching a maximum of 163 μM just off the coast. Cloud water H_2O_2 concentrations ranging from 0.3 to 112 μM were measured via aircraft off the U.S. Atlantic coast by Barth et al. (1989).

Few cloud water H_2O_2 measurements have been made in the remote marine environment, so gas phase H_2O_2 concentrations measured in the marine boundary layer may be more appropriate for comparison to DYCOMS-II H_2O_2 levels. In the presence of clouds, H_2O_2 partitions between the gas and aqueous phases. Therefore, a total equivalent gas phase H_2O_2 concentration for the DYCOMS-II sample periods was required for this comparison. Total gas phase H_2O_2 was calculated by adding the gas phase concentration assumed to be in Henry's law equilibrium to the air equivalent H_2O_2 concentration residing in the cloud water (all measured soluble peroxides were assumed to be present as hydrogen peroxide for this calculation). The temperature dependent Henry's law constant from Lind and Kok (1994) was used for this work and total gas phase concentrations are expressed in ppb.

The resulting total gas phase H_2O_2 concentrations for the DYCOMS-II sample periods ranged from 0.54 to 2.47 ppb and averaged 1.42 ppb. These values appear to be in line with previous gas phase H_2O_2 observations made in the marine boundary layer environment. Aircraft-based gas phase measurements made in the North Pacific in the fall of 1991 by Heikes et al. (1996a) showed average concentrations of approximately 1.5 ppb for altitudes and latitudes comparable to those experienced during the DYCOMS-II mission. H_2O_2 concentrations obtained from the Mauna Loa Observatory in May and June 1988 (Heikes, 1992) averaged 1.05 ppb for sample periods influenced by unpolluted, free tropospheric air. Aircraft measurements of gas phase H_2O_2 in the marine boundary layer of the Southern Atlantic Ocean in September and October of 1992 averaged 1.9 ppb and ranged between 0.3 ppb and 4.9 ppb during individual flights (Heikes et al., 1996b). Finally, ship-based observations of H_2O_2 in the North Atlantic in June 1992 averaged 0.63 ppb (Martin et al., 1997), and in October and November varied between approximately 0.5 and 2.0 ppb (Weller et al., 2000).

As with peroxides, formaldehyde may partition between the aqueous and gas phases when clouds are present. An equivalent total gas phase concentration was constructed by first multiplying the cloud water formaldehyde concentration by LWC to generate an air equivalent concentration. To that product the gas phase formaldehyde concentration required to be in Henry's law equilibrium with the aqueous phase measurements was added. The temperature dependent Henry's law constant from Seinfeld and Pandis (1998) was used. Because a fraction of the measured formaldehyde may have been complexed with S(IV) in the sampled cloud water, the assumption of Henry's law equilibrium may not be entirely valid. However, the concentration of S(IV) in the majority of samples was either below the MDL or a small fraction of the formaldehyde concentration, suggesting that most of the formaldehyde was not complexed with S(IV).

Because formaldehyde is only slightly soluble even when accounting for gem diol formation in solution, most remains in the gas phase in a typical cloud. The measured cloud water air equivalent concentration averaged 0.05 ppb for the DYCOMS-II samples. Based on Henry's law equilibrium, the average equilibrium gas phase concentration would be 0.27 ppb. The addition of those values results in a total gas phase equivalent concentration for the DYCOMS-II sample periods that averages 0.32 ppb.

The average estimated DYCOMS-II formaldehyde concentration of 0.32 ppb is consistent with previous gas phase studies. Formaldehyde measurements by Ayers et al. (1997) at Cape Grim in November and December 1993 revealed a diurnal cycle with an average daytime maximum of approximately 0.45 ppb and a nighttime minimum of approximately 0.3 ppb. Aircraft-based measurements in the central Pacific in 1999 were stratified according to altitude and show that formaldehyde concentrations decrease with increasing altitude (Heikes et al., 2001). The highest concentrations were recorded in the 0 to 1 km surface layer with a median of value of approximately 0.35 ppb for a latitude/longitude box near the DYCOMS-II target location. Heikes et al. (2001) also summarize a range of previous formaldehyde sampling

missions in the marine boundary layer and report that past measurements agree well with their own. The average formaldehyde concentration at Mauna Loa Observatory, located at an elevation of 3.4 km, was 0.1 ppb in May and June 1988 (Heikes, 1992). The maximum concentration during that period was 0.32 ppb. Finally, ship-based formaldehyde concentrations in the Atlantic marine boundary layer ranged from 0.5 to >1.2 ppb in October and November 1996 (Weller et al., 2000).

The use of Henry's law to predict gas phase concentrations of H_2O_2, HCHO, and NH_3 from measured cloud water solute concentrations involves a number of assumptions that may or may not be satisfied. For Henry's law to be valid at any given time, gas phase diffusion, interfacial transport, hydrolysis/ionization, and aqueous phase diffusion must not present mass transport limitations for the species of interest (Seinfeld and Pandis, 1998). The solubility of the species and the size of the cloud drops both play a role in determining how rapidly the species reaches equilibrium. Species that are more soluble require more time to reach equilibrium. Larger cloud drop sizes also require longer equilibration times. For a soluble species in a population of cloud drops, size dependent condensational growth and size dependent gas exchange rates can create non-equilibrium cloud water concentrations across the drop size spectrum (Ogren and Charlson, 1992). Rapidly varying LWC, the presence of organic films, and aqueous phase chemical reactions may act to further prevent cloud drops from reaching equilibrium with the gas phase. For example, the depletion of H_2O_2 as a result of S(IV) oxidation reactions may prevent cloud water H_2O_2 concentrations from equilibrating with the gas phase. Similarly, due to its complexation with S(IV), cloud water HCHO concentrations may not attain equilibrium with the gas phase.

The appropriateness of assuming Henry's law equilibrium for H_2O_2 has been investigated by a number of authors. Simultaneous measurements of gas and aqueous phase H_2O_2 by Barth et al. (1989) have indicated that cloud water concentrations were always lower than predicted by Henry's law. However, gas and aqueous phase H_2O_2 were found to be in equilibrium by Noone

et al. (1991) and within 25% of equilibrium by Macdonald et al. (1995). In order to investigate the validity of assuming Henry's law equilibrium during the DYCOMS-II field campaign, gas phase measurements of H_2O_2, HCHO, and NH_3 would have been required. Unfortunately, the C-130 did not include instrumentation to obtain these measurements.

6.5.3.3 Cloud water concentration trends

As mentioned previously, the effects of cloud LWC on cloud water chemical concentrations were apparent during the DYCOMS-II field project. As LWC increased from cloud base to cloud top during a given flight, the concentrations of most species decreased as drops grew through condensation and became more dilute (see Figure 6.13). However, while cloud drop dilution was responsible for concentration variations during the course of an individual flight, the cloud water chemical concentrations varied widely from flight to flight. For example, the average sodium concentration during RF08 was very low (69 μM) compared to the averages for RF03 (1015 μM) or RF05 (1293 μM).

Part of the flight to flight variation in solute concentration appears to be related to cloud drop size. On flights with smaller average drop diameters, cloud drops tended to be more concentrated and on flights with larger average drop diameters, cloud drops tended to be more dilute. This can be seen in Figure 6.16 which shows sodium concentration as a function of volume mean drop diameter for flights when drop size distributions are available (RF02-RF04 and RF07-RF09). The effects of dilution as drops increase in size during several individual flights can also be seen in this figure. Similar relationships hold for the remaining cation species (Figure 6.17) and anion species (Figure 6.18). Cloud water pH was also strongly correlated with the volume mean drop diameter as illustrated in Figure 6.19.

If the clouds present in the study region were experiencing simple dilution and no other processes were occurring, ionic concentration should exhibit a power law dependence on volume mean drop diameter with an exponent of -3 as indicated by the dashed lines in Figures 6.17

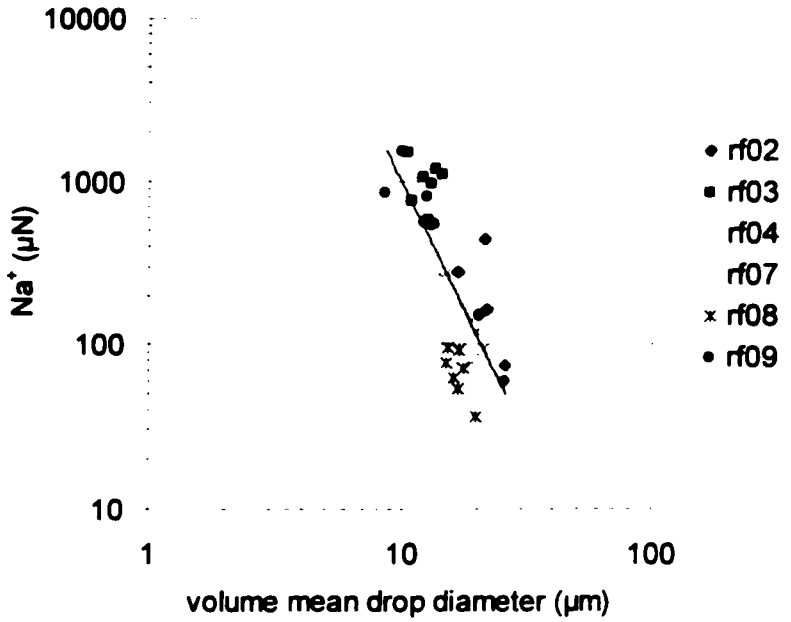

Figure 6.16. Cloud water sodium concentration as a function of volume mean drop diameter for individual research flights. Error bars represent one sigma analytical uncertainty.

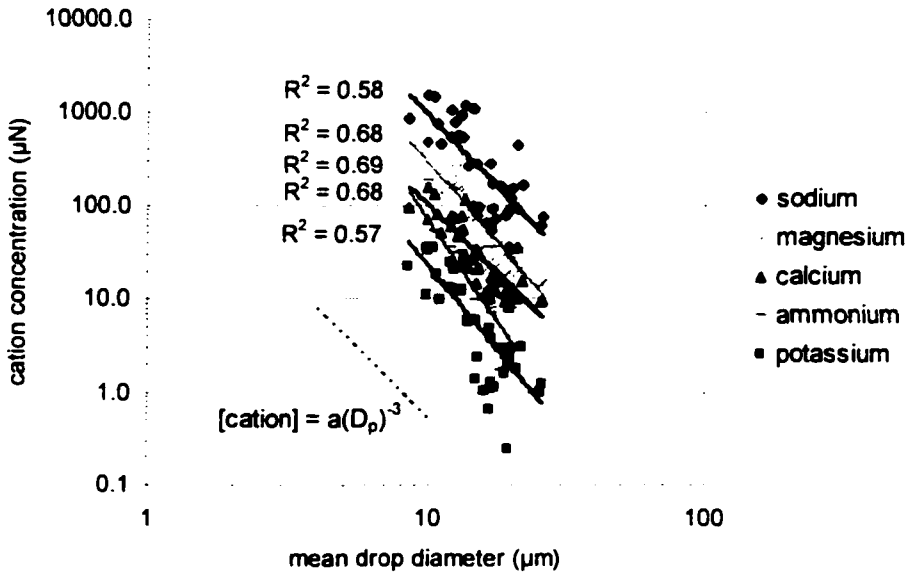

Figure 6.17. Concentrations of Na^+, Mg^{2+}, Ca^{2+}, NH_4^+, and K^+ as a function of volume mean drop diameter. The expected decrease in concentration with drop size due to dilution is indicated by the dashed line. Power law curve fit exponents are -3.2 for Na^+, -3.5 for Mg^{2+}, -2.9 for Ca^{2+}, -4.4 for NH_4^+, and -3.6 for K^+.

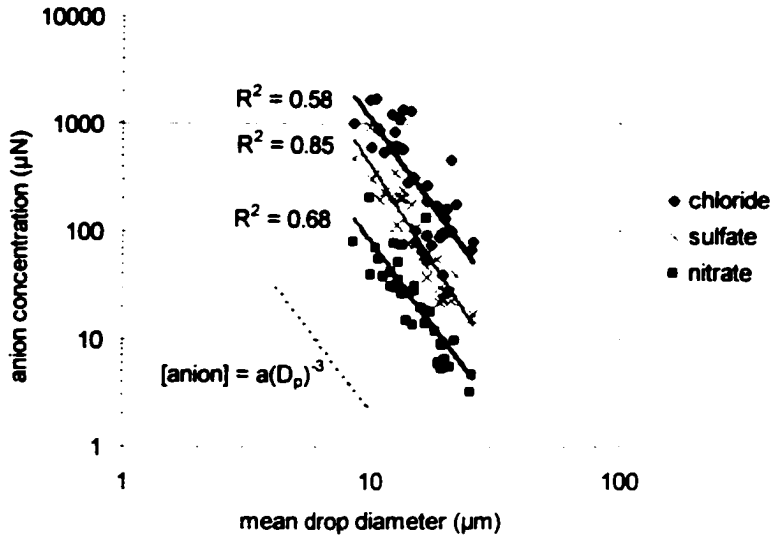

Figure 6.18. Concentrations of Cl^-, SO_4^{2-}, and NO_3^- as a function of volume mean drop diameter. The expected decrease in concentration with drop size due to dilution is indicated by the dashed line. Power law curve fit exponents are -3.2 for Cl^-, -3.6 for SO_4^{2-}, and -3.1 for NO_3^-.

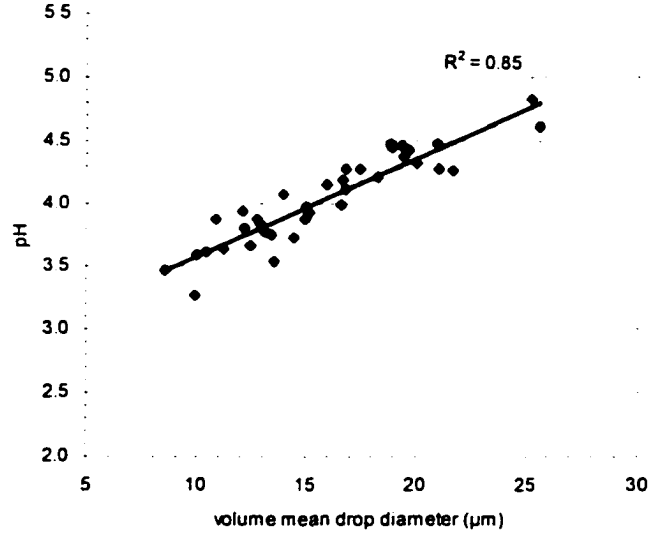

Figure 6.19. The variation of cloud drop pH with volume mean drop diameter for all samples collected during DYCOMS-II. Error bars represent one sigma uncertainty.

and 6.18. An investigation of cloud drop chemical concentration as a function of volume mean drop diameter was performed by Adzuhata et al. (2001) for samples collected over a relatively long period of time. While their data exhibited much greater variability than the DYCOMS-II

cloud water samples, the authors found exponents greater than -3 (large drops were more concentrated than would be expected through simple dilution). This was attributed to scavenging of interstitial aerosol over the lifetime of the cloud, offsetting dilution to a certain extent.

When the DYCOMS-II sample concentrations are plotted versus mean drop diameter as a single group in Figures 6.17 and 6.18, the power law curve fit exponents were nearly all less than -3, and averaged -3.4. Given that the DYCOMS-II cloud water samples were obtained over a month long period rather than a single cloud event, it is not unexpected that the observed exponents do not exactly coincide with the theoretical exponents describing simple dilution. In fact, it is somewhat surprising that samples collected over a month long period characterized by various background conditions and subject to cloud processes in addition to dilution show the reasonably strong trends that they do. The curves indicate that mean drop size plays a significant role in the cloud water chemical concentrations observed during DYCOMS-II.

The size of cloud drops encountered during individual DYCOMS-II sample periods was closely related to the cloud drop number concentration. As illustrated in Figure 6.20, when more drops were present to compete for water vapor, the mean drop diameter tended to be smaller, an observation consistent with other marine stratocumulus studies (Hudson and Svensson, 1995).

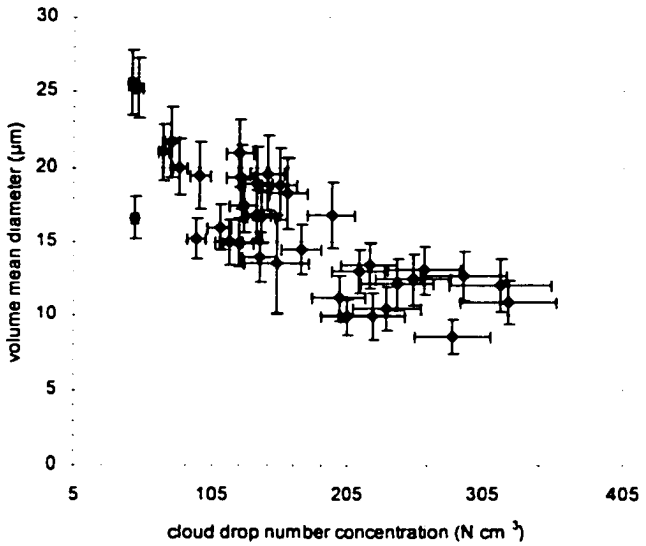

Figure 6.20. The relationship between volume mean drop diameter and cloud drop number concentration for the DYCOMS-II cloud water sample periods.

Therefore, on any given flight, if high cloud drop number concentrations were experienced, the mean drop diameter was smaller and the drops were more concentrated.

The number of cloud drops experienced during a given flight, in turn, was correlated with the aerosol number concentration present below cloud, as shown in Figure 6.21. This figure is based on data from individual cloud water sample periods and corresponding below-cloud flight segments during flights RF03, RF07, and RF08. The below cloud aerosol number concentrations were derived from the SPP-200, which is sensitive to diameters from 0.1 to 3.0 μm, and therefore does not represent the entire aerosol population. However, it can be seen that higher number concentrations of below cloud aerosol particles tend to be associated with higher cloud drop number concentrations. During flights with elevated cloud drop number concentrations, the limited available water vapor is distributed over a larger number of activated cloud drops. In this case, each individual drop contains less water resulting in higher solute concentrations. Overall, it appears that the cloud water ionic concentrations recorded during DYCOMS-II were dependent on the number of aerosol particles present in the marine boundary layer at any given time.

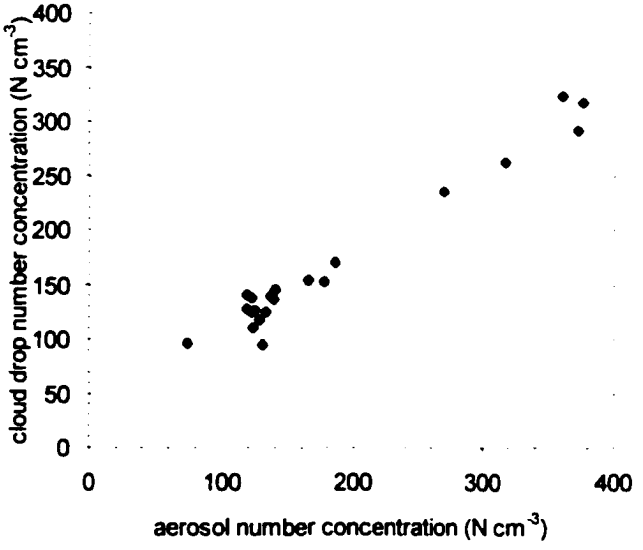

Figure 6.21. Cloud drop number concentration (SPP-100) versus below cloud aerosol number concentration (SPP-200) corresponding to cloud water sample periods during RF03, RF07, and RF08.

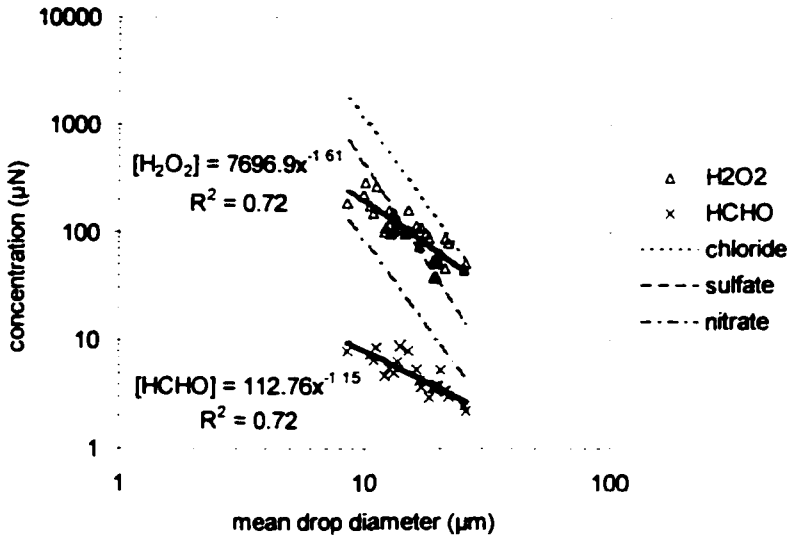

Figure 6.22. Measured concentrations of H_2O_2 and HCHO as a function of volume mean diameter. The decrease in concentration with drop size for chloride, sulfate, and nitrate are included for reference. The power law curves fit to the measured data have exponents of -1.61 for H_2O_2 and -1.15 for HCHO.

The concentrations of gas phase species, including H_2O_2 and HCHO, are also correlated with the volume drop diameter (Figure 6.22). In this case the power law exponents are quite a bit greater than for the low volatility ionic species which partition entirely to the aqueous phase. The fact that gas phase species can partition between the gas and aqueous phases makes a complete explanation of this behavior difficult without concurrent gas phase measurements. However, theoretical trends in trace gas species can be calculated if the aqueous and gas phases are assumed to be in Henry's law equilibrium, and it is assumed that the rising parcel of air is a closed system in which the total concentration of the trace gas is constant. In that case, as cloud drops experience condensational growth the aqueous concentration of trace gas species decreases due to dilution. As gas phase species enter the cloud drops to maintain equilibrium, the gas phase concentration decreases and a new equilibrium is established. In a closed system, therefore, gas phase concentrations will decrease with height. The equilibrium aqueous phase concentration also decreases with height, although the total amount of the trace gas species in the aqueous phase increases due to an increase in cloud LWC.

Because the decrease in aqueous phase trace gas concentration is no longer just a function of drop dilution, a perfect power law can no longer be expected even under idealized conditions. However, an approximate power law fit to theoretical calculations based on Henry's law equilibrium in a closed system can be used to compare with the observed DYCOMS-II data. Curves indicating the theoretical decrease in aqueous phase trace gas concentration with increasing mean drop diameter are shown in Figure 6.23. The theoretical curves placed in Figure 6.23 do not represent absolute expected concentrations for a given drop size, but only the expected trend resulting from drop dilution. The curves are constructed to coincide with the highest observed trace gas concentrations for convenience only. As can be seen, the DYCOMS-II data are in better agreement with the theoretical trend in H_2O_2 than HCHO. Because of the lower solubility of HCHO, the gas phase HCHO reservoir is not depleted as rapidly and a nearly flat theoretical curve results.

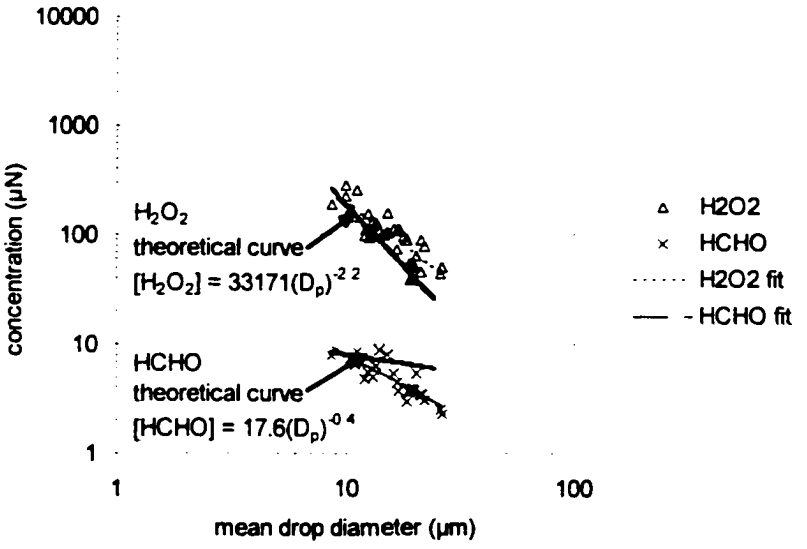

Figure 6.23. Measured concentrations of H_2O_2 and HCHO as a function of volume mean diameter along with theoretical dilution curves for a closed system. The theoretical power law curve fits are -2.2 for H_2O_2 and -0.4 for HCHO.

The observed values of total HCHO were calculated as the sum of the measured aqueous phase concentration and a calculated gas phase concentration. If the gas phase concentration is not actually in equilibrium with the measured aqueous phase concentration as assumed, that could

be partially responsible for the discrepancy between the theoretical and observed trends with drop diameter. Alternatively, the observed HCHO data could simply be reflecting an increase in the total concentration of HCHO that happens to be coincident with smaller cloud drops representative of a more polluted air mass. It is also worth noting that the theoretically derived trends in trace gas concentration due to cloud drop dilution do not take entrainment, mass transfer limitations, precipitation scavenging, or aqueous phase reactions into account, all of which may play a role in determining the compositional makeup of cloud drops.

6.5.3.4 Air equivalent concentration trends

The air equivalent concentrations of most measured species varied considerably from flight to flight. Flight averaged air equivalent concentrations of Na^+ and Cl^-, which are representative of all of the sea salt species, are shown in Figure 6.24. Much higher concentrations were recorded on RF03, RF05, RF06, and RF09 than during the remaining flights. Air equivalent cloud water concentrations of sea salt are related to the cloud drop number concentration as can be seen in Figure 6.25. The variability in Figure 6.25 is not reduced perceptibly when the sum of Na^+ and non-sea salt sulfate (another source of CCN that may be uncorrelated with sea salt

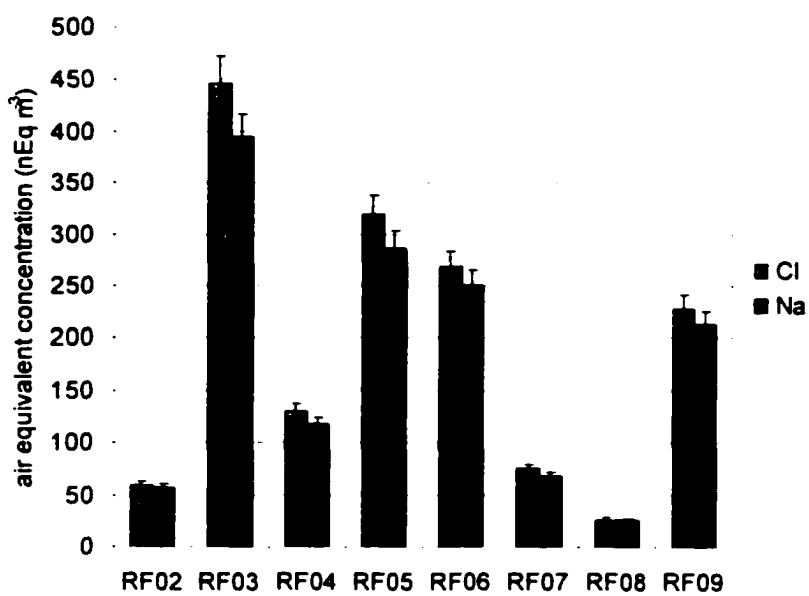

Figure 6.24. Flight averaged sodium and chloride air equivalent concentrations. Error bars indicate one sigma analytical uncertainty.

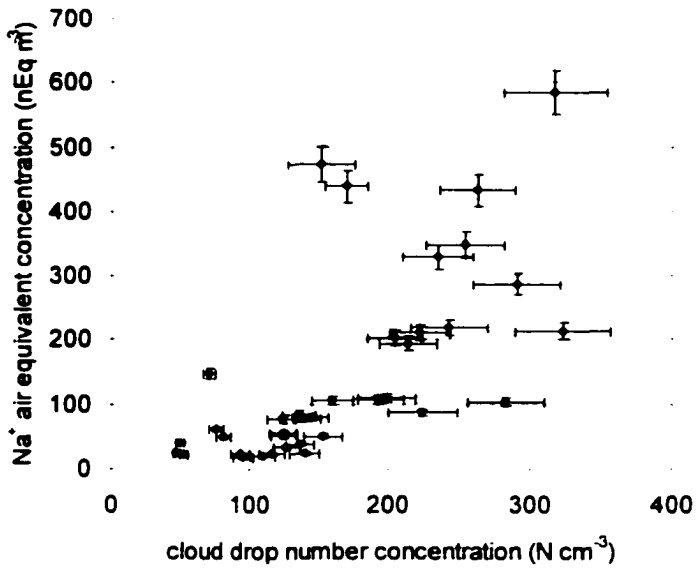

Figure 6.25. Sodium air equivalent concentration versus cloud drop number concentration.

particles) is plotted against cloud drop number concentration. Although there is significant scatter in the data, Figure 6.25 suggests that periods with higher cloud water derived air equivalent concentration are associated with periods when greater numbers of aerosol particles activate to form cloud drops. The number of CCN is determined by a range of factors including, among others, updraft velocity and aerosol number concentration and size distribution.

Sea salt mass and number concentrations in the marine environment are known to increase with increasing wind speeds (e.g. Fitzgerald, 1991). While the highest wind speeds were encountered during RF03, which features the highest sea salt mass concentration, a scatter plot of sea salt concentration (in cloud drops) versus wind speed for all DYCOMS-II cloud water sample periods only shows a hint of a correlation (see Figure 6.15). This may be due to the fact that sample period wind speeds may not be representative of wind speeds at the time of aerosol formation.

Complicating this analysis are the frequent periods of drizzle encountered during the DYCOMS-II mission. Based on mission summaries prepared in the field and discussions at the DYCOMS-II Data Workshop, the research flights were roughly categorized in the following way:

heavy drizzle on RF02 and RF07, moderate drizzle on RF04 and RF06, and light or no drizzle on RF03, RF05, RF08, and RF09. This classification of the extent of drizzle encountered during individual flights is admittedly crude; in future analyses, data from the Wyoming Cloud Radar (WCR) can be used to quantify the extent of drizzle when they become available. The heavy drizzle days were characterized by some of the lowest sea salt concentrations while the light drizzle days were typically associated with the highest concentrations of sea salt. This observation can be interpreted in a number of ways regarding cause and effect. Drizzle can be viewed as a mechanism that removed aerosol mass from the atmosphere through precipitation scavenging, and extensive drizzle resulted in low sea salt concentrations. Alternatively, low concentrations of sea salt particles could have been responsible for a broad cloud drop size distribution that promoted the formation of drizzle, and therefore low aerosol concentrations resulted in heavy drizzle. The issues surrounding the formation and maintenance of drizzle in marine stratocumulus are of common interest to many groups that participated in DYCOMS-II and further insight will hopefully be available after additional collaboration. An interesting case study may be RF08 which was considered a light drizzle day yet experienced the lowest sea salt mass concentrations of the entire mission.

The highest non-sea salt sulfate, nitrate, and ammonium concentrations were observed on RF09 (Figure 6.26). In addition, RF03, RF04, and RF05 also displayed high concentrations of these species. Trace metal concentrations show that elevated levels were encountered during RF09 (Figure 6.27) with much lower concentrations on all other flights (trace metal concentrations measured for RF03 samples were similar in magnitude to RF09, but are not reported due to possible blank contamination on that flight). Total concentrations of trace gas species (aqueous phase + calculated equilibrium gas phase) are more consistent from flight to flight than other species, although the highest concentrations of HCHO were observed on RF03 and RF09 (Figure 6.28). An examination of the air mass back trajectories (see Figures 6.8 and 6.9) reveals no consistent correlations between measured concentrations of these species and air

mass history that can be applied to every flight. It may be worth noting, however, that the 1500 m back trajectory for RF09 indicates that the air mass sampled during that flight recently passed over Mexico. Although the back trajectory analysis overall is inconclusive, the cloud water solute observations suggest that RF09 was the most influenced by continental sources, possibly both natural and anthropogenic in origin.

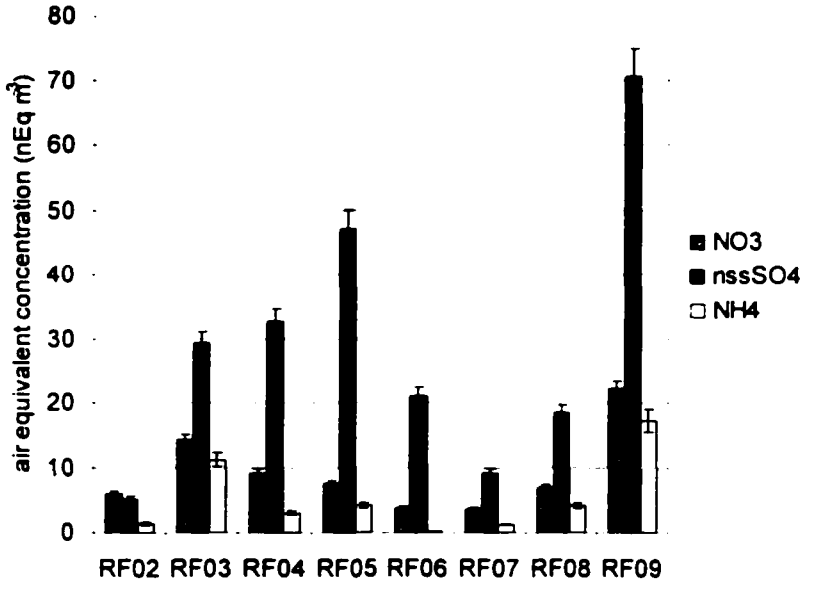

Figure 6.26. Flight averaged nitrate, sulfate, and ammonium air equivalent concentrations. Error bars indicate one sigma analytical uncertainty.

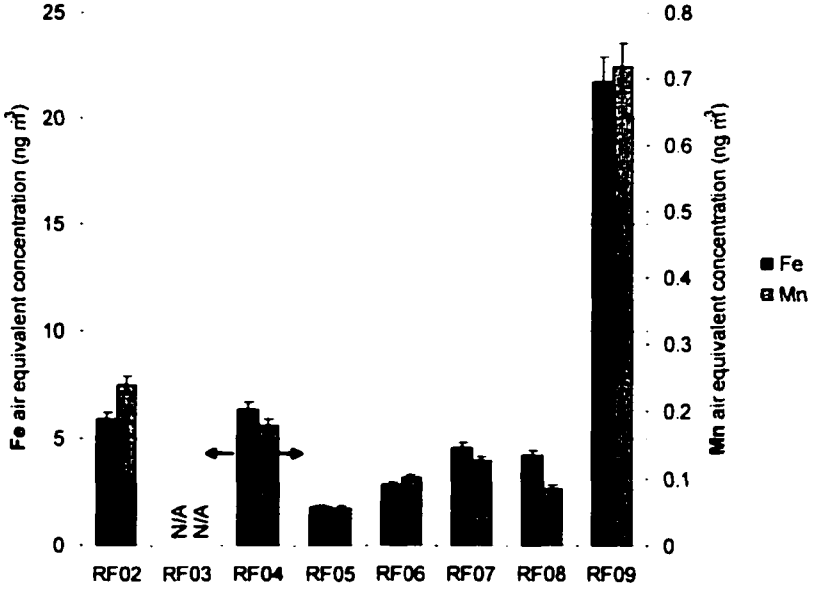

Figure 6.27. Flight averaged trace metal air equivalent concentrations. Error bars indicate one sigma analytical uncertainty.

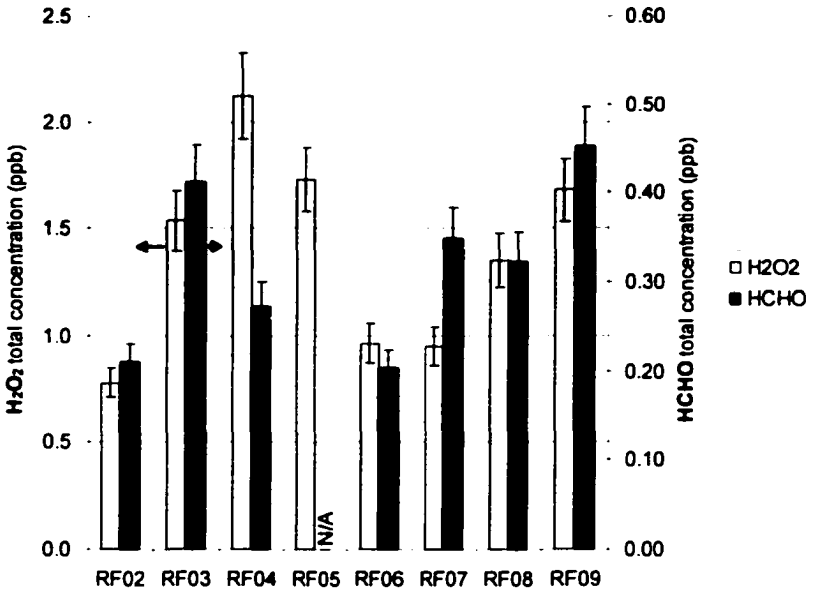

Figure 6.28. Flight averaged H_2O_2 and HCHO total (aqueous phase + equilibrium gas phase) concentrations. Error bars indicate one sigma analytical uncertainty.

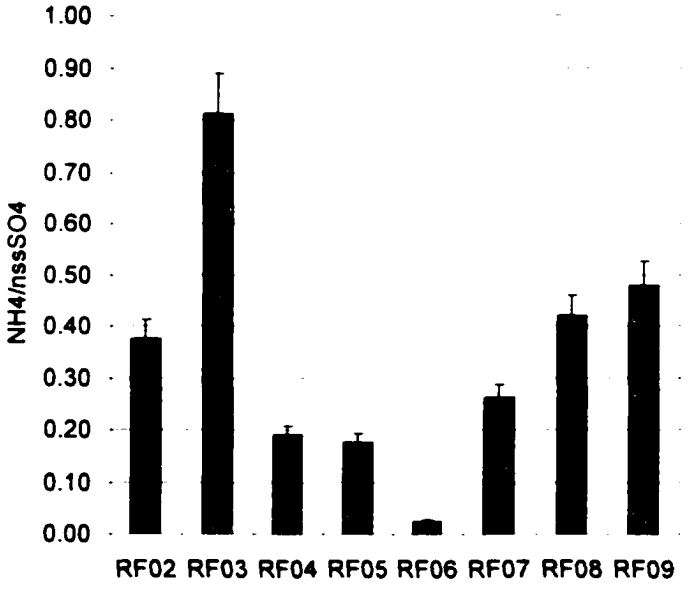

Figure 6.29. Flight averaged ratios of ammonium to non-sea salt sulfate. Error bars indicate one sigma analytical uncertainty.

The flight averaged molar ratios of ammonium to non-sea salt sulfate are displayed in Figure 6.29. The average ratio for the entire DYCOMS-II mission was 0.36. A ratio less than 2 suggests that there is insufficient ammonium to neutralize the non-sea salt sulfate in the sampled

cloud water. Huebert et al. (1996a) report an overall average ratio of 0.65 for aerosol measurements made from Santa Maria Island in the Atlantic, and a ratio of 0.37 for the subset of aerosols sampled in clean marine air. Although others have also observed ratios < 1 (e.g. Clark et al., 1987), a ratio of approximately 1 appears to be more common for aerosols and precipitation in the marine environment (Covert, 1988; Quinn et al., 1988).

6.5.3.5 SO_4^{2-} production in the marine boundary layer

As noted in the introductory chapter of this dissertation, the aqueous phase conversion of dissolved SO_2 to sulfate accounts for the majority of total global sulfate production. The production of sulfate in cloud drops tends to acidify the drops and, in the case of non-precipitating clouds, is a source of non-volatile aerosol mass that can influence radiative forcing and future cloud cycles. In the remote marine boundary layer, DMS produced through biological activity is considered a significant source of SO_2 which can ultimately be oxidized to sulfate. For these reasons, evidence of aqueous phase sulfate production in remote marine stratocumulus clouds was of interest.

Complicating the analysis of in-cloud sulfate production is the fact that the DYCOMS-II flights were not truly Lagrangian. Although the flight legs were configured to drift with the mean wind at a given level, wind shear with height prevents the same parcel of air from being sampled at cloud base and at cloud top. In addition, the air mass properties were not homogeneous through the duration of a flight leg at a given level. The horizontally non-homogeneous nature of the marine boundary layer was observed in many fields, including DMS concentrations, LWC, and drizzle rates (Stevens, 2002). This inhomogeneity also characterized the cloud water samples and was clearly observed during RF07. During the hour long flight leg at cloud top, five cloud water sample periods covered three distinct sections of the flight circle. Two sections were sampled twice each and the third section was sampled a single time. While the duplicate sample periods in which sampling occurred in the same part of the cloud agreed quite well, variations of

up to 50% were observed across the individual sections of the flight circle. Although this same variability presumably existed on the remaining research flights, the sample periods tended to overlap one another making it difficult to define separate sections of the flight circle for comparison purposes.

Due to the variability encountered at cloud base and cloud top, the cloud base and cloud top sample air equivalent concentrations were averaged for each flight. The average cloud base and cloud top concentrations of non-sea salt sulfate are displayed as a function of height above cloud base in Figure 6.30. The in-cloud legs flown during RF05 and RF08 were at nearly the same level, so no distinction could be made between cloud base and cloud top for those flights. It should be emphasized that cloud base was identified from aircraft soundings through the depth of the boundary layer just before and just after the hour long in-cloud flight legs. Therefore, cloud base was not measured for individual sample periods and may have varied considerably in space and time over the course of an individual in-cloud flight leg, and is likely a source of uncertainty

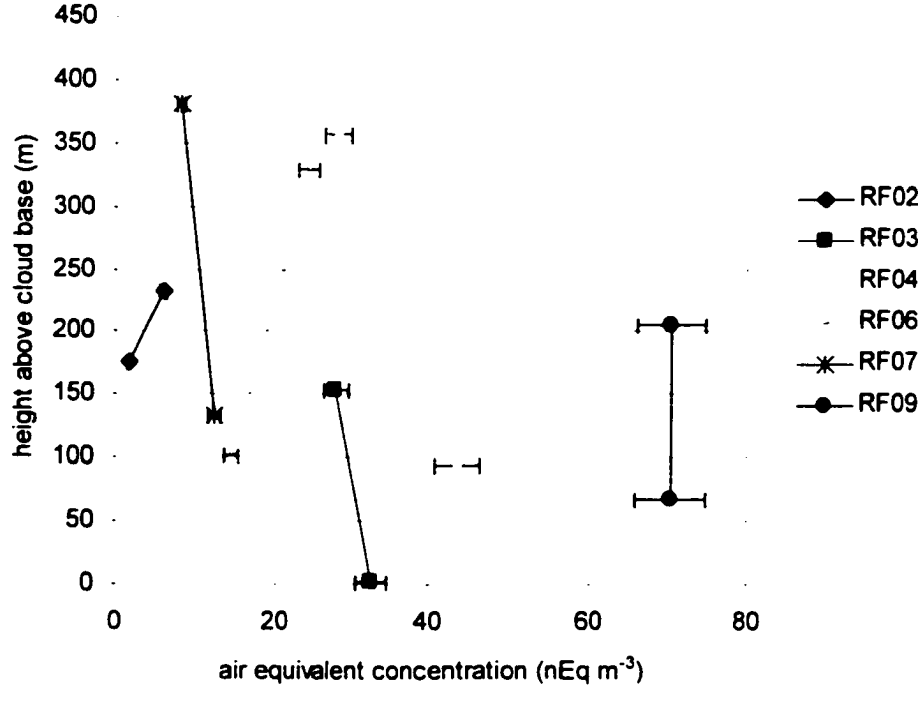

Figure 6.30. Cloud base and cloud top averaged non-sea salt sulfate concentrations. Error bars indicate one sigma analytical uncertainty.

that is not indicated in Figure 6.30. Given this caveat, it can be seen that there is not a systematic increase in air equivalent non-sea salt sulfate concentrations from cloud base to cloud top that would provide an indication of in-cloud sulfate production. In fact, non-sea salt sulfate appears to decrease from cloud base to cloud top during several flights.

The concentration of non-sea salt sulfate, as with other species, can be influenced by a number of in-cloud processes including aerosol scavenging and removal through precipitation scavenging, making it difficult to assess the contribution of aqueous phase chemical reactions to the total measured non-sea salt sulfate concentration. To examine the extent of in-cloud S(IV) oxidation, it is useful to ratio the non-sea salt sulfate concentration to a tracer species that mimics the behavior of non-sea salt sulfate except for chemical production. In that way, the influence of all other processes affecting sulfate concentrations can be excluded. Because of the relatively few chemical measurements made during the DYCOMS-II mission, the choice of a tracer species was limited. Liu et al. (1993) suggest the use of ammonium as a tracer because it is typically measured in sufficient concentrations and is also typically associated with sulfate in the precursor aerosol. Using ammonium as a tracer, the fraction of sulfate formed through aqueous phase oxidation can be estimated as:

$$\left[SO_4^{2-}\right]_{produced} = \left(\frac{\left[SO_4^{2-}\right]_T}{\left[NH_4^+\right]_T} - \frac{\left[SO_4^{2-}\right]_B}{\left[NH_4^+\right]_B}\right)\left[NH_4^+\right]_T \qquad (6.1)$$

where the subscript T refers to measurements at cloud top and the subscript B refers to measurements at cloud base. The sulfate concentrations used in equation 6.1 consist only of the non-sea salt fraction. Because ammonium was below detection limits in every sample obtained during RF06 and nearly every sample during RF02, those flights were not used for the analysis of sulfate production. The four flights in which cloud base and cloud top segments could be differentiated and had ammonium concentrations above detection limits for the majority of samples were RF03, RF04, RF07, and RF09.

Based on the use of ammonium as a tracer, the estimated concentrations of sulfate produced in the aqueous phase via equation 6.1, along with one sigma standard deviations, are: 1.89 ±2.39 nEq m^{-3} for RF03, 4.92 ±4.33 nEq m^{-3} for RF04, 3.36 ±1.13 nEq m^{-3} for RF07, and 2.62 ±4.42 nEq m^{-3} for RF09. These values represent 6.7%, 17.4%, 42.2%, and 3.7% of the measured cloud top non-sea salt sulfate concentration for RF03, RF04, RF07, and RF09, respectively. While the quantity of sulfate produced in the aqueous phase is predicted to be positive for each of these four cases, the uncertainty encompasses or nearly encompasses 0 for three out of the four flights. As a further indicator of aqueous phase sulfate production, the species responsible for oxidizing S(IV) to sulfate should be observed to decrease from cloud base to cloud top. As will be discussed below, the primary oxidant for all DYCOMS-II sample periods is expected to be H_2O_2. Total H_2O_2 concentrations (cloud water plus estimated gas concentrations) for these four flights are illustrated in Figure 6.31. Although the variation is within the error estimates, decreases in total H_2O_2 concentration are suggested on RF03, RF04, and RF07, and an increase is suggested during RF09.

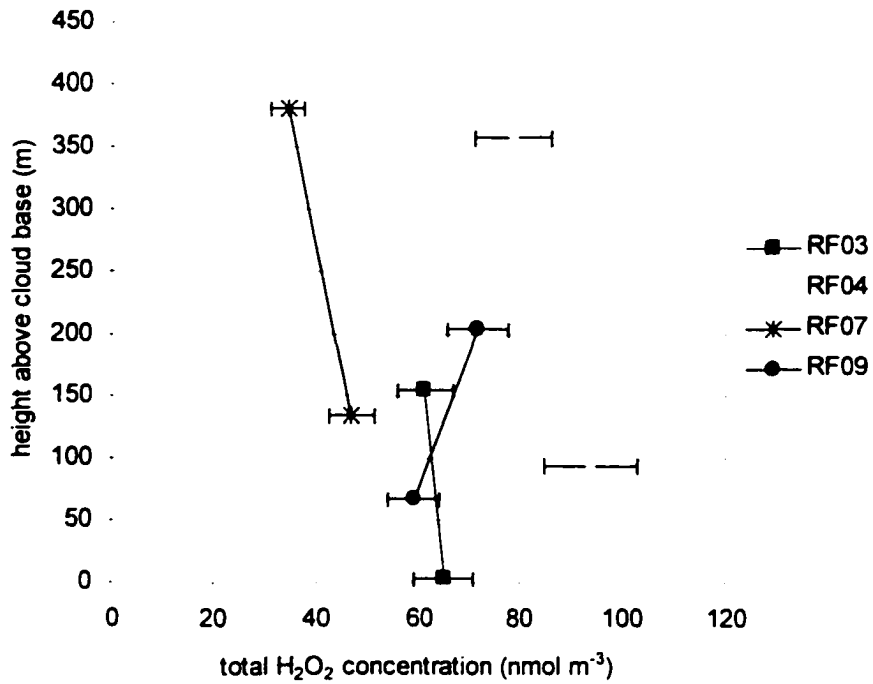

Figure 6.31. Cloud base and cloud top averaged H_2O_2 concentrations. Error bars indicate one sigma analytical uncertainty

In addition to the caveats stated above for this analysis, there are additional reasons that a stronger sulfate production signal might be difficult to detect during the DYCOMS-II mission. For example, the cloud base legs were typically flown about 100 m above cloud base to ensure that the aircraft stayed within cloud for the duration of the hour long flight leg. Therefore, by the time the cloud base samples were obtained, some fraction of the available sulfur dioxide may have already been absorbed and oxidized. Average oxidation timescales for the H_2O_2 pathway are 0.8, 1.5, 6.6, and 0.5 s for RF03, RF04, RF07, and RF09 (see below). Based on an updraft velocity of 1 m s^{-1}, the timescale for a parcel to rise from cloud base to the lowest flight leg where sampling occurred would have been 2, 94, 134, and 68 s for RF03, RF04, RF07, and RF09. A comparison between these timescales suggests that aqueous S(IV) oxidation via H_2O_2 would have had sufficient time to proceed before reaching the altitude of the lowest in-cloud flight legs. Further, it has been argued that a significant fraction of sulfur oxidation in the remote marine boundary layer occurs in deliquesced sea salt aerosol particles before they participate as CCN in cloud formation (Sievering et al., 1999; 1991; Gurciullo et al., 1999).

Another question of interest that can be addressed with the DYCOMS-II cloud water sample analysis is the dominant aqueous oxidation pathway for the further conversion of S(IV) to sulfate. In the aqueous phase, the major S(IV) oxidants include H_2O_2, O_3, and trace metal catalyzed O_2. While oxidation by O_3 and trace metal catalyzed O_2 is important at higher pH values, oxidation by H_2O_2 typically dominates at low pH. The high H_2O_2 concentrations and low pH values characteristic of the DYCOMS-II cloud water samples suggest that the H_2O_2 oxidation pathway was the most significant at the time of collection.

The relative importance of the various oxidation pathways was calculated based on published oxidation rate laws for H_2O_2 (Hoffmann and Calvert, 1985), O_3 (Hoffmann, 1986), and trace metal catalyzed O_2 (Ibusuki and Takeuchi, 1987). The S(IV) oxidation rates are given by the following equations:

H_2O_2:
$$-\frac{dS(IV)}{dt} = \frac{k_1[H^+][H_2O_2][HSO_3^-]}{1+K[H^+]} \quad (6.2)$$

O_3:
$$-\frac{dS(IV)}{dt} = (k_2[SO_2 \cdot H_2O] + k_3[HSO_3^-] + k_4[SO_3^{2-}])[O_3] \quad (6.3)$$

O_2:
$$-\frac{dS(IV)}{dt} = k_5[Fe(III)][Mn(II)][S(IV)][H^+]^{-0.74} \quad \text{for pH<4.2} \quad (6.4a)$$

$$-\frac{dS(IV)}{dt} = k_6[Fe(III)][Mn(II)][S(IV)][H^+]^{0.67} \quad \text{for pH>4.2} \quad (6.4b)$$

where $K=13\ M^{-1}$, $k_1=7.5\times10^7\ M^{-1}s^{-1}$, $k_2=2.4\times10^4\ M^{-1}s^{-1}$, $k_3=3.7\times10^5\ M^{-1}s^{-1}$, $k_4=1.5\times10^9\ M^{-1}s^{-1}$, $k_5=3.7\times10^7\ M^{-1}s^{-1}$, and $k_6=2.5\times10^{13}\ M^{-1}s^{-1}$.

The measured pH was used to determine the H^+ concentration used in equations 6.2, 6.3 and 6.4. The H^+ concentration also defines the equilibrium fraction of S(IV) that would exist as $SO_2 \cdot H_2O$, HSO_3^-, and SO_3^{2-}, an important factor in all of the oxidation rate equations. At the pH values observed during DYCOMS-II, nearly all of the S(IV) should be present in the form of HSO_3^-. The concentrations of H_2O_2, Fe(III), and Mn(II) were taken from the DYCOMS-II cloud water chemical analysis. Fe(III) was assumed to comprise 25% of total Fe while Mn(III) was assumed to be 100% of total Mn (Xu et al., 1999). At the time of this analysis, ozone concentrations measured during DYCOMS-II were only available for RF03. The RF03 average concentration of 27 ppb was therefore assumed to be representative of the remaining flights and was also assumed to be in Henry's law equilibrium with the cloud water for all sample periods.

The resulting oxidation rates are displayed in Figure 6.32 in terms of a molar change in S(IV) per second per ppb of SO_2 present. As suspected, the H_2O_2 pathway is predicted to be the

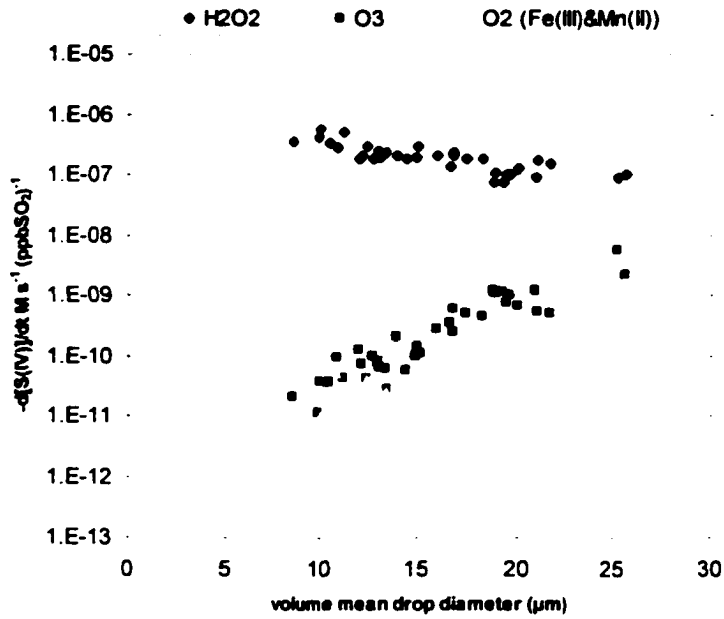

Figure 6.32. Potential S(IV) oxidation rates for H_2O_2, O_3, and O_2 catalyzed by trace metals.

dominant S(IV) oxidation pathway for the conditions experienced during each of the DYCOMS-II sample periods. The relative importance of the trace metal catalyzed O_2 oxidation pathway is insensitive to changes in the fraction of Fe and Mn assumed to exist as Fe(III) and Mn(II) in the cloud water samples. Oxidation by O_3 becomes more important as drop size increases, mainly due to the increase in drop pH that accompanied increases in mean drop diameter. Any input of SO_2 into the remote marine environment that is absorbed by cloud drops would therefore be expected to be rapidly oxidized by the abundant H_2O_2. Most of the measured values of total S(IV) in the DYCOMS-II cloud water samples were below detection limits, supporting this assessment. It is often the case that very little S(IV) is detected in clouds in which excess H_2O_2 is found (Daum et al., 1984b; Kelly et al., 1985; Macdonald et al., 1995). This may reflect rapid oxidation of S(IV) within the cloud or in the collected cloud water prior to S(IV) stabilization. When total S(IV) concentrations were occasionally measured above the detection limits, it may indicate the presence of HMS in the cloud drops. HMS is formed as S(IV) complexes with HCHO and provides a S(IV) reservoir that is not easily oxidized (Rao and Collett, 1995; Richards

et al., 1983). When both species are above the detection limit, air equivalent concentrations of cloud water total S(IV) are correlated with air equivalent HCHO concentrations (Figure 6.33). The complexation of S(IV) with HCHO is dependent on drop pH and the concentrations of HSO_3^- and SO_3^{2-}. In addition, oxidation reactions compete with the complexation reactions for available S(IV). Timescales for these competing reactions have been examined by Rao and Collett (1995) to determine regimes in which the rates of S(IV) complexation may be sufficiently fast that S(IV) is consumed before it can be oxidized. Following the procedure of Rao and Collett (1995), timescales for complexation and oxidation by H_2O_2 and O_3 were calculated for the DYCOMS-II sample periods and are displayed in Figure 6.34. As can be seen, the timescale for S(IV) complexation with HCHO is orders of magnitude greater than that for either oxidation pathway. In addition, as would be expected from the oxidation rate calculations described above, the timescale for S(IV) oxidation by O_3 is much longer than the H_2O_2 oxidation timescale. Therefore, if additional SO_2 were absorbed by cloud drops during the DYCOMS-II, the complexation of S(IV) would not be expected to hinder S(IV) oxidation by H_2O_2 or O_3.

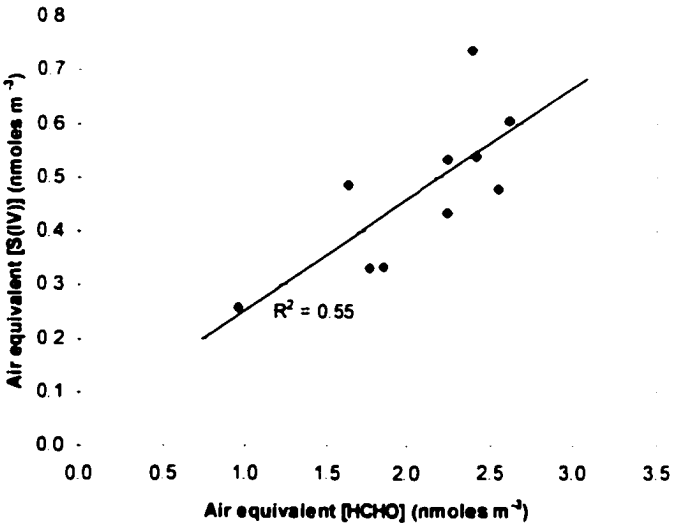

Figure 6.33. Scatter plot of air equivalent S(IV) and HCHO concentrations.

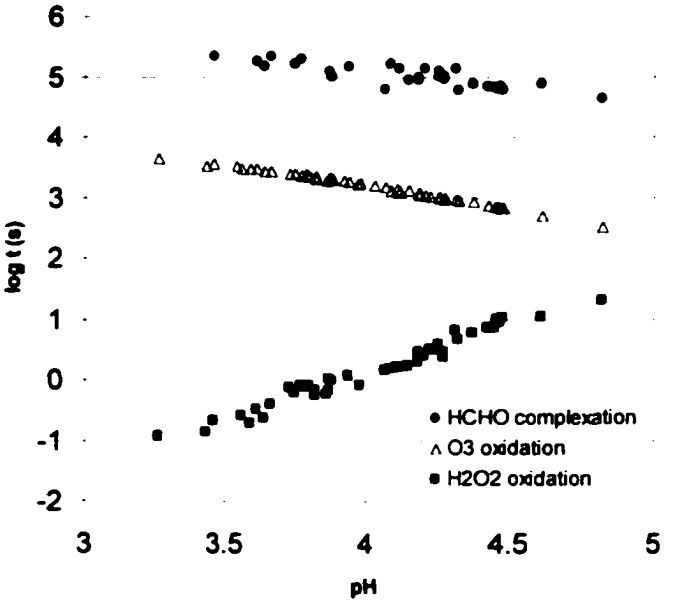

Figure 6.34. Characteristic times for S(IV) complexation and oxidation by H_2O_2 and O_3.

7 Conclusions and Recommendations

7.1 Conclusions

To facilitate the study of cloud formation and processing mechanisms, numerous cloud water sampling instruments have been developed over the years. Most have been intended to collect cloud water samples from ground-based platforms, although the desire to obtain samples from clouds that are inaccessible from surface sites has led to the design of aircraft-based collectors as well. Cloud water samples acquired from aircraft platforms have been used for the investigation of cloud nucleation, aerosol and trace gas scavenging, S(VI) production, cloud water acidification, the influence of anthropogenic pollution, the distribution of trace species in the atmosphere, and the general characterization of cloud water composition at geographical locations around the world.

Although aircraft-based cloud water collectors have been used in the past to capture sufficient volumes of cloud water for chemical analysis, a review of the scientific literature reveals that the collection characteristics of these instruments have rarely been evaluated. Collector performance is often unknown or limited to theoretically derived 50% cut diameters or bulk collection efficiencies based on field observations. In addition, collectors that depend on inertial impaction for drop collection may be susceptible to drop shatter and re-entrainment which can create biases in the sampled size distribution. For the most part, aircraft-based collectors have been designed for particular aircraft making it difficult to transfer a single collector to multiple aircraft for use during various field campaigns.

The preceding chapters of this dissertation have described the design, construction, evaluation, and field use of a new aircraft-based cloud water collector intended to address the

limitations of previous designs. The new collection system utilizes an axial-flow cyclone to separate cloud drops from the air stream via centrifugal force in a rotational flow field. Up to seven cloud water samples can be stored during a single research flight. The desire to create a portable system was met by housing the entire collection system in a Particle Measurement Systems canister to take advantage of standard mechanical and electrical interfaces. The tendency for cloud drops to shatter and be re-entrained as a result of high velocity impacts on solid surfaces was diminished by selecting an axial-flow cyclone design rather than employing simple inertial impaction as a collection technique. Ease of use and straightforward installation and removal of the collection system were considered in the design phase and confirmed during field usage.

CFD analysis of the axial-flow cyclone indicates that sampling is subisokinetic due to the presence of the vane unit mounted in the cyclone duct that generates the required rotational air flow. For operation at 115 m s^{-1}, the free stream velocity is reduced to approximately 30 m s^{-1} in the interior of the collector, equivalent to a flow rate of 4,900 l min^{-1} through the 6 cm diameter axial-flow cyclone duct. Accompanying the deceleration of the air flow, a 6000 Pa increase in static pressure and 6 K increase in static temperature were predicted.

Simulations of cloud drop trajectories suggest that the rotational flow field in the axial-flow cyclone is sufficient to quickly move entrained cloud drops to the duct wall where they can be removed for storage. Collection efficiency curves were compiled for operation at 1000 m and 3000 m and the 50% cut diameters were determined to be approximately 8 μm in both cases. The predicted sample collection rate in a cloud with a 12 μm mean diameter and a LWC of 0.3 g m^{-3} is approximately 4 g min^{-1}. The external aspiration efficiency was largely a function of the sub-isokinetic sampling conditions and was responsible for the reduced collection efficiency at small drop sizes. For the most part, the collection efficiency curves were independent of slight misalignments between the inlet and air streamlines. An investigation into the potential for drop shatter and re-entrainment indicates that drops larger than 46 μm will be vulnerable to shatter if

drops impact on a liquid film coated surface. If surfaces are assumed to be dry, drops larger than 30 μm are expected to shatter.

The 6 K rise in air temperature experienced in the inlet of the axial-flow cyclone increases saturation vapor pressure and has implications for sample evaporation. Evaporation of cloud drops suspended in the air stream should be negligible for drop sizes of interest. Calculations meant to bound evaporation from wall surfaces indicate that losses should be less than 10% for operation in clouds with LWC greater than 0.2 g m^3. A reduction in the predicted evaporation losses could be achieved by reducing the exposure of cloud water to the low velocity, elevated temperature region between the inlet and the curved vane unit. However, this low velocity region beneficially decelerates large drops before impact on the curved vane assembly and thereby inhibits drop shatter. The final inlet geometry represents a compromise between the competing factors of evaporation and drop shatter.

The CFD-based trajectory simulations were verified with an experimental laboratory calibration involving fluorescein-tagged monodisperse drops. Air was drawn through the axial-flow cyclone at a flow rate equivalent to that experienced during aircraft operation. Because air flow through the axial-flow cyclone was achieved through a suction flow, external aspiration efficiency could not be studied. However, the experimentally determined internal drop deposition patterns agreed well with the numerical simulations and lend support to the CFD modeling effort.

Participation in the DYCOMS-II field campaign in July 2001 provided the first opportunity to evaluate the operation of the collection system under flight conditions. All of the subsystems worked as intended throughout the duration of the project. However, the rate of cloud water collection was well below the anticipated collection rate. The observed collection rate varied between 0.07 and 1.2 g min^{-1} in comparison to expected collection rates of 1.0 to 9.7 g min^{-1}. Because the laboratory calibration demonstrated that drop deposition patterns in the interior of the axial-flow cyclone were as expected, attention was focused on inefficient extraction of accumulated cloud water from the duct wall as the likely cause of reduced collection

rates. Unfortunately the flow of calibration drops after deposition could not be investigated quantitatively with the experimental method employed. However, a qualitative visual inspection of water drops sprayed into the inlet of the collector while being operated at flight-like flow rates confirmed that water tended to flow over, rather than into, the extraction slot. A redesigned extraction slot should be the first step in augmenting collection rates.

Despite the lower than expected collection rate, sufficient volumes of cloud water were obtained during most of the DYCOMS-II sample periods to permit chemical analysis. Over the course of the project, 50 samples suitable for analysis were collected during seven nighttime and two daytime flights. While a limited number of cloud water sampling studies conducted from coastal, ground-based locations have reported solute concentrations for marine stratocumulus clouds, there have been no *in situ* cloud water studies that have reported solute concentrations for stratocumulus clouds residing in the remote marine boundary layer. Therefore, the cloud water solute composition data compiled in this dissertation represents a valuable and previously unavailable data set.

Based on the DYCOMS-II sample analysis, new insight has been gained into the chemistry of stratocumulus clouds in the remote marine environment. As would be expected in a marine environment, sodium and chloride were the two most abundant ions in all DYCOMS-II samples. When ratioed to sodium, chloride and potassium were found to be present in proportions similar to those found in sea water. On the other hand, sulfate, magnesium, and calcium were enriched to varying degrees, suggesting contributions from sources other than sea salt. The analysis may indicate that pristine marine conditions were not always encountered during cloud water sampling periods. Back trajectories that show sampled air masses passing over land during the five days prior to sampling support this conclusion. However, no consistent correlation between air mass back trajectory and air equivalent concentrations (defined as the amount of solute contained in cloud water per unit volume of air) was established, perhaps a sign that emissions from ships or biological activity influenced the study region. Alternatively, the

lack of correlation between air mass origin and air equivalent solute concentration could be the result of deficiencies in the back trajectory analysis calculation. Limited supporting aerosol and gas composition measurements and periods of drizzle encountered throughout the DYCOMS-II mission complicated the analyses.

Based on the DYCOMS-II data, trends in cloud water concentration with cloud LWC and volume mean diameter were established. The trends with cloud LWC show that dilution played a role in cloud drop solute concentration during individual flights. The trends with volume mean diameter demonstrate that variations in solute concentration are related to cloud drop size which is in turn related to below-cloud aerosol number concentration. Air equivalent concentrations were calculated to eliminate dependence on LWC and allow a comparison with geographically similar aerosol, trace gas, and cloud water studies. The air equivalent concentrations of most species measured during DYCOMS-II fell within the range of previous coastal ground-based cloud water studies and *in situ* aerosol and trace gas studies.

The DYCOMS-II cloud water samples also presented an opportunity to examine aqueous phase S(IV) oxidation in marine stratocumulus. Using ammonium as a tracer species, there was only limited evidence of in-cloud sulfate production. A comparison of rate laws suggested H_2O_2 as the dominant oxidant for in-cloud S(IV) conversion to sulfate. At the conditions encountered during DYCOMS-II, the rate of S(IV) complexation with HCHO is insufficient to compete with S(IV) oxidation. Given the abundance of H_2O_2, sulfate production is limited only by the availability of SO_2.

Overall, the new aircraft-based cloud water collection system described in this dissertation satisfied the majority of the project objectives, and provides a working prototype from which improved versions can be developed. The collection system is portable and is capable of providing well defined samples of cloud water for chemical analysis, and its use during DYCOMS-II has contributed to our knowledge of marine cloud chemistry.

7.2 Recommendations

As is common with newly developed instrumentation, the first operational use of the cloud water collection system revealed a few design and procedural shortcomings. The principal deficiency in the system is the lower than expected sample collection rate. The numerical modeling, supported by the experimental laboratory calibration, suggests that cloud drops that enter the inlet of the axial-flow cyclone reach the duct wall upstream of the extraction slot and therefore should be available for removal and storage. Through visual analysis of the axial-flow cyclone during operation at simulated flight conditions, it appears that the extraction slot does not efficiently remove cloud water from the duct wall. While inefficiency of the extraction slot should still yield a sample representative of the cloud water entering the inlet of the axial-flow cyclone, an increase in the sample collection rate will require a modification of the extraction slot.

Unfortunately, the shear driven flow of liquid water drops along a surface is not easily predictable through empirical calculations or numerical modeling. That difficulty, along with time constraints and a lack of an available wind tunnel test facility, prevented a thorough understanding of the extraction slot performance prior to participation in the DYCOMS-II field project. However, with the benefit of recent laboratory evaluation, general recommendations for design improvements can be made.

The performance of the current extraction slot design may be enhanced with additional ports to drain water from the slot. Visual observations of water flow in the axial-flow cyclone at flight-like conditions provide evidence that a fraction of the water flowing into the extraction slot simply circulates around the upstream edge without moving to the bottom of the slot for removal. The two ports currently in place may be insufficient to drain this accumulated water from the entire extraction slot. The existing hardware could be modified without significant expense to evaluate the benefits of additional extraction ports. Unfortunately, the increase in the rate of

sample collection will be limited because visual observations also show that the majority of the available water never enters the extraction slot in the first place. Therefore, this option will probably not render perfect extraction efficiency. In addition, there is limited space surrounding the axial-flow cyclone in the current PMS enclosure to incorporate the fittings required to support extra extraction ports.

A second extraction slot could be incorporated into the duct wall just downstream of the current slot to remove water that bypasses the first slot. While sequential extraction slots would enhance sample collection rates, the gains may be modest. There is no guaranty that the second slot would remove a greater fraction of cloud water than the first slot. If the removal efficiency of a second slot was similar to the first, an additional 10% of the available water would be acquired and the majority of the cloud water would continue to remain uncollected. Supplemental extraction slots would also increase the length of the system, possibly reducing the number of storage bottles that can be accommodated in the PMS enclosure.

A change in the design of the extraction slot would probably offer the most benefit. The experimental laboratory evaluation has demonstrated that liquid drops rapidly reach the duct wall just downstream of the vane assembly. In addition, water was observed flowing uniformly along the duct wall in a helical pattern upstream and downstream of the extraction slot. This behavior suggests that a disturbance in the near wall flow field due to the presence of the extraction slot may responsible for the unexpected water flow behavior. The slot may generate sufficient turbulence that water flow into the slot is impeded. This conclusion would support the development of an extraction slot that minimally disrupts the rotational flow field. A shallower slot may offer less flow distortion, although the exact dimensions of an ideal slot may be a matter of trial and error. Flow disruption could be further minimized by employing an annular cavity coupled with a very thin slot that is flush with the interior surface of the duct (Figure 7.1). By drawing a vacuum on the annular cavity, a high velocity suction flow would be produced along the entire length of the slot to draw cloud water from the wall surface and into the cavity without

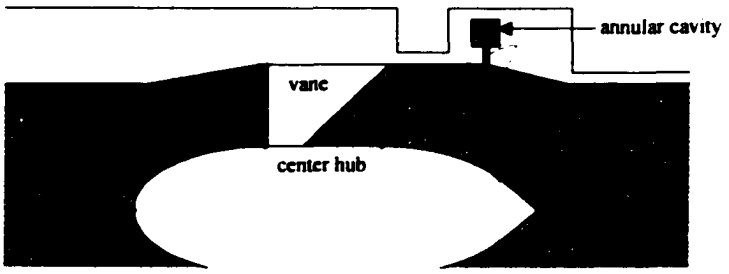

Figure 7.1. Alternate extraction slot design.

disturbing the main rotational flow field. Alternatively, a short section of the duct wall could be fabricated from a porous material through which cloud water can flow. Again a vacuum on the outer surface of the porous material would draw water off the duct wall without influencing the rotational flow field. Finding and maintaining a chemically inert porous insert would be the main concern with this option.

Extraction slot modifications can be made without replacing the entire axial-flow cyclone duct. A new polycarbonate section containing the extraction slot can be machined and interchanged with the current section. If a new extraction slot section is produced, the inclusion of an o-ring seal at the junction with the aluminum duct is recommended. This would alleviate any potential leaks at that location and would make the use of other sealants that can compromise sample composition, such as silicone, unnecessary. If extraction slot modifications are impractical within the confined space of a PMS canister, or if additional sample storage containers are desired in future versions of the collector, a larger custom enclosure could be fabricated. A custom enclosure must incorporate a standard PMS mounting interface and comply with weight restrictions, but otherwise may be of any reasonable size or shape. A standard PMS canister was utilized for the prototype cloud water collection system for convenience, although it would have been preferable to design an enclosure that conforms to the specifications of the cloud water collection system rather than the other way around.

A wind tunnel evaluation of the cloud water collection system was originally proposed as part of this development project. Unfortunately, wind tunnels that are capable of generating 100

m s^{-1} air speeds and liquid water drops of appropriate size and known concentration are relatively few in number, are difficult to schedule test time in, and the costs associated with their use can be prohibitive. These factors, along with a limited development period before deployment on the DYCOMS-II field project, prevented experimental wind tunnel work from being undertaken. Although future wind tunnel testing may not be helpful in addressing the inefficiency of the current extraction slot design, an effort to schedule test time in an appropriate wind tunnel facility would be advantageous. Operation of the collection system at well controlled wind tunnel conditions would allow CFD predictions of total air flow rate through the system to be verified. Wind tunnel testing would also permit the external aspiration efficiency to be evaluated experimentally for typical flight conditions and for various angles of attack. In addition, it may be possible to investigate evaporative losses experimentally in a wind tunnel setting. The calculations performed to bound evaporation from wall surfaces in the cloud water collector rely on a number of assumptions, including the fraction of the duct wall that is wetted, and would benefit from verification.

Further evaluation of the collection system could be accomplished if the system were deployed on a second field project with a stronger chemistry focus. More comprehensive below cloud aerosol composition, cloud interstitial aerosol, and trace gas measurements would provide additional bounds for expected cloud water composition and concentrations that could be compared to measured values. The inclusion of a second cloud water sampler of a different design would provide a valuable intercomparison study.

In the longer term, adapting the cloud water collection system for automated operation would extend the applicability of the system. Seats on research aircraft are typically in high demand, and instrumentation that can be placed on board without the need for an accompanying, dedicated researcher may offer an advantage. Because the current version of the axial-flow cyclone is operated via LabVIEW, certain aspects of automation would be straightforward. The system is already configured to import real time LWC data from a serial feed and predict the

volume of water accumulating in each sample bottle. Of course, due to extraction slot issues the prediction is not currently accurate but could be easily corrected. Alternatively, sensors could be placed in or near the sample bottles to monitor the actual accumulated volume. In either case, only minor changes to the current LabVIEW VI would be required to automatically open valves when the appropriate conditions are encountered and to close the valves when adequate sample is obtained. The more difficult aspect of automating the cloud water collection system is determining appropriate times to initiate sampling. Real-time LWC monitoring can be used to identify when current conditions are suitable for sampling, but cannot determine if the in-cloud flight leg will be long enough in duration for a sufficient sample volume to be obtained. Some knowledge of the anticipated flight plan would be required and threshold LWC values would have to be selected with care.

Finally, while the cloud water composition data obtained during the DYCOMS-II field project has already yielded interesting conclusions regarding marine stratiform clouds present in the study region, further analysis would be worthwhile. The upcoming release of two data sets may be particularly valuable for extending conclusions that can be drawn from the cloud water composition data. These data sets focus on subcloud aerosol particle composition and cloud drop residual particle composition from filter samples obtained during the DYCOMS-II mission. The subcloud aerosol composition may provide a useful baseline composition from which in-cloud sulfate production can be reevaluated. The cloud drop residual composition, sampled with a CVI, invites comparisons to be made with bulk cloud water samples from the axial-flow cyclone cloud water collector. However, there are several issues that may hinder direct comparison and must be taken into consideration. First, the methods used to analyze the aerosol and cloud drop residual samples supply elemental and functional group composition rather than ionic composition. Second, both the subcloud aerosol and cloud drop residual sampling systems employed a 1 μm cutoff to exclude coarse mode aerosols from the analysis. The axial-flow cyclone does not possess an upper size cut so that nearly all activated CCN are potentially sampled. Third, the

cloud drop residual sample stream is exposed to a high temperature, dry air flow in order to evaporate the liquid water from the sample. In the process volatile or semi-volatile solutes may be lost as well. During preliminary discussions at the DYCOMS-II Data Workshop, it was unclear the extent to which certain species, such as Cl^-, were affected. Despite these concerns, the DYCOMS-II cloud water composition data, together with subcloud aerosol and cloud drop residual particle composition data, provide a unique data set that will be useful for investigations into the aerosol / cloud water / trace gas system in the marine boundary layer.

References

Adzuhata, T., Inotsume, J., Okamura, T., Kikuchi, R., Ozelki, T., Kajikawa, M., and Ogawa, R. (2001). Evaluation of ionic pollutants of acid fog and rain using a factor analysis and back trajectories. *Analyt. Sci.* 17:71-76.

Akiyama, T., and Marui, T. (1989). Dust collection efficiency of a straight-through cyclone – effects of duct length, guide vanes and nozzle angle for secondary rotational air flow. *Powder Technol.* 58:181-185.

Anderson, J.D. (1992). Discretization of partial differential equations, in Computational Fluid Dynamics; An Introduction. J.F. Wendt, ed. Springer-Verlag, Berlin. pp. 95-100.

Anderson, T.L., Covert, D.S., and Charlson, R.J. (1994). Cloud droplet number studies with a counterflow virtual impactor. *J. Geophys. Res.* 99:8249-8256.

Asgharian, B., and Godo, M. N. (1997). Transport and deposition of spherical particles and fibers in an improved virtual impactor. *Aerosol Sci. Technol.* 27:499-506.

Ayers, G.P., Gillett, R.W., Granek, H., de Serves, C., and Cox, R.A. (1997). Formaldehyde production in clean marine air. *Geophys. Res. Lett.* 24:401-404.

Ayers, G.P., and Gras, J.L. (1983). The concentration of ammonia in Southern Ocean air. *J. Geophys. Res.* 88:10655-10659.

Ayers, G.P., and Gras, J.L. (1980). Ammonia gas concentrations over the Southern Ocean. *Nature.* 284:539-540.

Barth, M.C., Hegg, D.A., and Hobbs, P.V. (1989). Measurements of atmospheric gas-phase and aqueous phase hydrogen peroxide concentrations in winter on the east coast of the United States. *Tellus.* 41B:61-69.

Bates, T.S., Calhoun, J.A., and Quinn, P.K. (1992). Variations in the methanesulfonate to sulfate molar ratio in submicrometer marine aerosol particles collected over the Southern Pacific Ocean. *J. Geophys. Res.* 97:9859-9865.

Bator, A., and Collett, J.L. Jr. (1997). Cloud chemistry varies with drop size. *J. Geophys. Res.* 102:28071-28078.

Baumgardner, D., and Huebert, B. J. (1993). The airborne aerosol inlet workshop: meeting report. *J. Aerosol Sci.* 24:835-846.

Bergin, M.H., Pandis, S.N., Davidson, C.I., Jaffrezo, J.-L., Dibb, J.E., Russell, A.G., and Kuhns, H.D. (1996). Modeling of the processing and removal of trace gas and aerosol species by Arctic radiation fogs and comparison with measurements. *J. Geophys. Res.* 101:14465-14478.

Berglund, R.N., and Liu, B.Y.H. (1973). Generation of monodisperse aerosol standards. *Environ. Sci. Technol.* 7:147-153.

Bigg, E.K. (1986). Discrepancy between observations and prediction of concentrations of cloud condensation nuclei. *Atmos. Res.* 20:82-86.

Bird, R.B., Stewart, W.E., Lightfoot, E.N. (1960). Transport Phenomena. John Wiley & Sons, New York, New York. pp. 389-412, 636-642, 642-652.

Birmili, W., Yuskiewicz, B., Wiedensohler, A., Stratmann, F., Choularton, T.W., Bower, K.N. (1999). Climate-relevant modification of the aerosol size distribution by processes associated with orographic clouds. *Atmos. Res.* 50:241-263.

Bogen, J. (1974). Trace elements in precipitation and cloud water in the area of Heidelberg, measured by instrumental neutron activation analysis. *Atmos. Environ.* 8:835-844.

Borys, R.D., Lowenthal, D.H., Wetzel, M.A., Herrera, F., Gonzalez, A., and Harris, J. (1998). Chemical and microphysical properties of marine stratiform cloud in the North Atlantic. *J. Geophys. Res.* 103:22073-22085.

Borys, R.D., Hindman, E.E., DeMott, P.J. (1988). The chemical fractionation of atmospheric aerosol as a result of snow crystal formation and growth. *J. Atmos. Chem.* 7:213-239.

Boucher, O., Lohmann, U. (1995). The sulfate-CCN-cloud albedo effect. *Tellus.* 47B:281-300.

Bower, K.N., and Choularton, T.W. (1993). Cloud processing of the cloud condensation nucleus spectrum and its climatological consequences. *Q. J. R. Meteorol. Soc.* 119:655-679.

Breaker L.C, and Gilliland, R.P. (1981). A satellite sequence on upwelling along the California coast, in Coastal Upwelling. F.A. Richards, ed. American Geophysical Union, Washington, D.C. pp. 87-94.

Brimblecombe, P., and Clegg, S.L. (1988). The solubility and behavior of acid gases in the marine aerosol. *J. Atmos. Chem.* 7:1-18.

Brock, F.V., Semmer, S.R., and Jirak, C. (1995). Passive solar radiation shields: Wind tunnel testing. 9th AMS Symposium on Meteorological Observations and Instrumentation, 27-31 March, Charlotte, North Carolina. pp 89-93.

Burkholz, A. (1989). Droplet Separation. VCH Publishers, New York, NY. pp. 191-199.

Carmichael, A.D. (1966). The aerodynamic design of axial-flow and radial-inflow turbines, in Gas Turbine Engineering Handbook. J.W. Sawyer, ed. Gas Turbine Publications, Stamford, CT. pp. 56-66.

Charlson, R.J., Seinfeld, J.H., Nenes, A., Kulmala, M., Laaksonen, A., and Facchini, M.C. (2001). Reshaping the theory of cloud formation. *Science.* 292:2025-2026.

Charlson, R.J., Langner, J., Rodhe, H., Leovy, C.B., and Warren, S.G. (1991). Perturbation of the northern hemisphere radiative balance by backscattering from anthropogenic sulfate aerosols. *Tellus.* 43AB:152-163.

Charlson, R.J., Lovelock, J.E., Andreae, M.O., and Warren, S.G. (1987). Oceanic phytoplankton, atmospheric sulphur, cloud albedo and climate. *Nature.* 326:655-661.

Chen, G., Davis, D.D., Kasibhatla, P., Bandy, A.R., Thornton, D.C., Huebert, B.J., Clarke, A.D., and Blomquist, B.W. (2000). A study of DMS oxidation in the tropics: comparison of Christmas Island Field Observations of DMS, SO_2, and DMSO with model simulations. *J. Atmos. Chem.* 37:137-160.

Chen, Q., and Ahmadi, G. (1997). Deposition of particles in a turbulent pipe flow. *J. Aerosol Sci.* 28:789-796.

Chuang, P.Y., Collins, D.R., Pawlowska, H., Snider, J.R., Honsson, H.H., Brenguier, J.L., Flagan, R.C., and Seinfeld, J.H. (2000). CCN measurements during ACE-2 and their relationship to cloud microphysical properties. *Tellus.* 52B:843-867.

Chylek, P., Banic, C.M., Johnson, B., Damiano, P.A., Isaac, G.A., Leaitch, W.R., Liu, P.S.K., Boudala, F.S., Winter, B., Ngo, D. (1996). Black carbon: Atmospheric concentrations and cloud water content measurements over southern Nova Scotia. *J. Geophys. Res.* 101:29105-29110.

Clarke, A.D., Ahlquist, N.C., and Covert, D.S. (1987). The Pacific marine aerosol: evidence for natural and acid sulfates. *J. Geophys. Res.* 92:4179-4190.

Collett, Jr., J.L., Sherman, D.E., Moore, K.F., Hannigan, M.P., and Lee, T. (2002a). Aerosol particle processing and removal by fogs: observations in chemically heterogeneous central California radiation fogs. *Water, Air, Soil Poll: Focus.* 1:303-312.

Collett, Jr., J.L., Bator, A., Sherman, D.E., Moore, K.F., Hoag, K.J., Demoz, B.B., Rao, X., Reilly, J.E. (2002b). The chemical composition of fogs and intercepted clouds in the United States. *Atmos. Res.*, in press.

Collett, Jr., J.L., Hoag, K.J., Sherman, D.E., Bator, A., and Richards, L.W. (1999). Spatial and temporal variations in San Joaquin Valley fog chemistry. *Atmos. Environ.* 33:129-140.

Collett, Jr., J.L., Prevot, S.H., Staehelin, J., and Waldvogel, A. (1991a). Physical factors influencing winter precipitation chemistry. *Environ. Sci. Technol.* 25:782-788.

Collett, Jr., J.L., Daube, B.C., and Hoffmann, M.R. (1991b). Spatial and temporal variations in precipitation and cloud interception in the Sierra Nevada of central California. *Tellus.* 43B:390-400.

Corbett, J.J., Fischbeck, P.S., and Pandis, S.N. (1999). Global nitrogen and sulfur inventories for oceangoing ships. *J. Geophys. Res.* 104:3457-3470.

Cossali, G.E., Coghe, A., and Marengo, M. (1997). The impact of a single drop on a wetted solid surface. *Experiments in Fluids.* 22:463-472.

Couture, M.D., Banic, C.M., Schemenauer, R.S., Leaitch, W.R., and Wiebe, H.A. (1998). Comparison of the chemistry of fog water from mountain sites and cloud water from airborne platforms. 1st International Conference on Fog and Fog Collection, 19-24 July, Vancouver, Canada.

Covert, D.S., Gras, J.L., Wiedensohler, A., and Stratmann, F. (1998). Comparison of directly measured CCN with CCN modeled from the number-size distribution in the marine boundary layer during ACE 1 at Cape Grim, Tasmania. *J. Geophys. Res.* 103:16597-16608.

Covert, D.S. (1988). North Pacific marine background aerosol: average ammonium to sulfate molar ratio equals 1. *J. Geophys. Res.* 93:8455-8458.

Crowe, C., Sommerfeld, M., and Tsuji, Y. (1998). Multiphase Flows with Droplets and Particles. CRC Press, Boca Raton, Fla, pp. 191-203.

Dasgupta P.K., DeCesare, K., and Ullrey, J.C. (1980). Determination of atmospheric sulfur dioxide without tetrachloromercurate (II) and the mechanism of the Schiff reaction. *Analyt. Chem.* 52:1912-1922.

Daum, P.H., and Springston, S.R. (1993). Tropospheric sampling with aircraft, in Measurement Challenges in Atmospheric Chemistry. L. Newman, ed. American Chemical Society, Washington, D.C. pp. 101-132.

Daum, P.H., Schwartz, S.E., and Newman. (1984a). Acidic and related constituents in liquid water stratiform clouds. *J. Geophys. Res.* 89:1447-1458.

Daum, P.H., Kelly, T.J., Schwartz, S.E., and Newman. (1984b). Measurements of the chemical composition of stratiform clouds. *Atmos. Environ.* 18:2671-2684.

Dibb, J.E., Talbot, R.W., Klemm, K.I., Gregory, G.L., Singh, H.B., Bradshaw, J.D., and Sandholm, S.T. (1996). Asian influence over the western North Pacific during the fall season: Inferences from lead 210, soluble ionic species and ozone. *J. Geophys. Res.* 101:1779-1792.

Dickerson, R.R., Huffman, G.J., Luke, W.T., Nunnermacker, L.J., Pickering, K.E., Leslie, C.D., Lindsey, C.G., Slinn, W.G.N., Kelly, T.J., Daum, P.H., Delany, A.C., Greenberg, J.P., Zimmerman, P.R., Boatman, J.F., Ray, J.D., Stedman, D.H. (1987). Thunderstorms: An important mechanism in the transport of air pollutants. *Science.* 235:460-465.

Dixon, R.W., and Charlson, R.J. (1994). Development of a new real-time method for measuring S(IV) in cloud water using a counter-flow virtual impactor. *Tellus.* 46B:193-204.

Dong, S., and Dasgupta, P.K. (1987). Fast fluorometric flow injection analysis of formaldehyde in atmospheric water. *Environ. Sci. Technol.* 21:581-588.

Donnell, E.A., Fish, D.J., Dicks, E.M. (2001). Mechanisms for pollutant transport between the boundary layer and the free troposphere. *J. Geophys. Res.* 106:7847-7856.

Dye, J.E. (1983). A spray device for ground testing of the Johnson-Williams liquid water content meter. Preprints: 5th AMS Symposium on Meteorological Observations and Instrumentation, 11-15 April, Toronto, Canada. pp. 362-364.

Elbert, W., Hoffman, M.R., Kramer, M., Schmitt, G., Andreae, M.O. (2000). Control of solute concentrations in cloud and fog water by liquid water content. *Atmos. Environ.* 34:1109-1122.

Exton, H.J., Latham, J., Park, P.M., Smith, M.H., and Allen, R.R. (1986). The production and dispersal of maritime aerosol, in Oceanic Whitecaps. E.C. Monahan and G. MacNiocaill, eds. Reidel, Hingham, MA. pp. 175-193.

Feingold, G., and Chuang, P.Y. (2002). Analysis of the influence of film-forming compounds on droplet growth: implications for cloud microphysical processes and climate. *J. Atmos. Sci.* 59:2006-2018.

Feingold, G., Kreidenweis, S.M., and Zhang, Y. (1998). Stratocumulus processing of gases and cloud condensation nuclei 1. Trajectory ensemble model. *J. Geophys. Res.* 103:19527-19542.

Feingold, G., Kreidenweis, S.M., Stevens, B., Cotton, W.R. (1996). Numerical simulations of stratocumulus processing of cloud condensation nuclei through collision-coalescence. *J. Geophys. Res.* 101:21391-21402.

Feingold, G., and Heymsfield, A.J. (1992). Parameterizations of condensational growth of droplets for use in general circulation models. *J. Atmos. Sci.* 49:2325-2342.

Ferziger, J. H., and Peric, M. (1999). Computational Methods for Fluid Dynamics. Springer, Berlin, pp.25-37,67-83,162-168.

Fitzgerald, J.W. (1991). Marine aerosols: a review. *Atmos. Environ.* 25A:533-545.

Flossman, A.I. (1994). A 2-D spectral model simulation of the scavenging of gaseous and particulate sulfate by a warm marine cloud. *Atmos. Res.* 32:233-248.

Fluent Incorporated. (1999). FLUENT User's Guide. Lebanon, N.H., Vol. 1-4.

Fox, J. (2000). Personal communication.

Freitas, C.J. (1995). Perspective: Selected benchmarks from commercial CFD codes. *ASME Journal of Fluids Engineering.* 117:208-218.

Fuzzi, S., Orsi, G., and Mariotti, M. (1985). Wet deposition due to fog in the Po Valley, Italy. J. *Atmos. Chem.* 3:289-296.

Garrett, T.J., and Hobbs, P.V. (1995). Long range transport of continental aerosols over the Atlantic Ocean and their effects on cloud structures. *J. Atmos. Sci.* 52:2977-2984.

Gerber, H. (1996). Microphysics of marine stratocumulus clouds with two drizzle modes. *J. Atmos. Sci.* 53:1649-1662.

Gong, S.L., Barrie, L.A., Prospero, J.M., Savoie, D.L., Ayers, G.P., Blanchet, J.-P., and Spacek, L. (1997). Modeling sea-salt aerosols in the atmosphere 2. Atmospheric concentrations and fluxes. *J. Geophys. Res.* 102:3819-3830.

Gong, H., Anand, N. K., and McFarland, A. R. (1993). Numerical prediction of the performance of a shrouded probe sampling turbulent flow. *Aerosol Sci. Technol* 19:294-304.

Gras, J.L. (1995). CN, CCN, and particle-size in southern-ocean air at Cape-Grim. *Atmos. Res.* 35:233-251.

Gras, J.L., and Ayers, G.P. (1983). Marine aerosols at southern mid-latitudes. *J. Geophys. Res.* 88:10661-10666.

Griffiths, W. D., and Boysan, F. (1996). Computational Fluid Dynamics (CFD) and empirical modeling of the performance of a number of cyclone samplers. *J. Aerosol Sci.* 27:281-304.

Gurciullo, C., Lerner, B., Sievering, H., and Pandis, S.N. (1999). Heterogeneous sulfate production in the remote marine environment: Cloud processing and sea-salt particle contributions. *J. Geophys. Res.* 104:21719-21731.

Hall, J.S., and Wolff, E.W. (1998). Causes of seasonal and daily variations in aerosol sea-salt concentrations at a coastal Antarctic station. *Atmos. Environ.* 32:3669-3677.

Hegg, D.A. (1990). Heterogeneous production of cloud condensation nuclei in the marine atmosphere. *Geophys. Res. Lett.* 17:2165-2168.

Hegg, D.A., Radke, L.F., and Hobbs, P.V. (1990). Particle production associated with marine clouds. *J. Geophys. Res.* 95:13917-13926.

Hegg, D.A., and Hobbs, P.V. (1988). Comparisons of sulfate and nitrate production in clouds on the mid-Atlantic and Pacific Northwest coasts of the United States. *J. Atmos. Chem.* 7:325-333.

Hegg, D.A., and Hobbs, P.V. (1986). Sulfate and nitrate chemistry in cumuliform clouds. *Atmos. Environ.* 20:901-909.

Hegg, D.A., Hobbs, P.V., and Radke, L.F. (1984a). Measurements of the scavenging of sulfate and nitrate in clouds. *Atmos Environ.* 18:1939-1946.

Hegg, D.A., Radke, L.F., and Hobbs, P.V. (1984b). Measurements of transformations in the physical and chemical properties of clouds associated with onshore flow in Washington State. *J. Climate Appl. Meteor.* 23:979-984.

Hegg, D.A., and Hobbs, P.V. (1981). Cloud water chemistry and the production of sulfate in clouds. *Atmos. Environ.* 15:1597-1604.

Heikes, B., Snow, J., Egli, P., O'Sullivan, D., Crawford, J., Olson, J., Chen, G., Davis, D., Blake, N., and Blake, D. (2001). Formaldehyde over the central Pacific during PEM-Tropics B. *J. Geophys. Res.* 106:32717-32731.

Heikes, B.G., Lee, M., Bradshaw, J., Sandholm, S., Davis, D.D., Crawford, J., Rodriguez, J., Liu, S., McKeen, S., Thornton, D., Bandy, A., Gregory, G., Talbot, R., and Blake, D. (1996a). Hydrogen peroxide and methylhydroperoxide distributions related to ozone and odd hydrogen over the North Pacific in the fall of 1991. *J. Geophys. Res.* 101:1891-1905.

Heikes, B.G., Lee, M., Jacob, D., Talbot, R., Bradshaw, J., Singh, H., Blake, D., Anderson, B., Fuelberg, H., and Thompson, A.M. (1996b). Ozone, hydroperoxides, oxides of nitrogen, and

hydrocarbon budgets in the marine boundary layer over the South Atlantic. *J. Geophys. Res.* 101:24221-24234.

Heikes, B.G. (1992). Formaldehyde and hydroperoxides at Mauna Loa Observatory. *J. Geophys. Res.* 97:18001-18013.

Heintzenberg, J., Covert, D.C., and Van Dingenen, R. (2000). Size distribution and chemical composition of marine aerosols: a compilation and review. *Tellus.* 52B:1104-1122.

Heintzenberg J., Ogren, J.A., Noone, K.J., and Gardneus, L. (1989). The size distribution of submicrometer particles within and about stratocumulus cloud droplets on Mt. Areskutan, Sweden. *Atmos. Res.* 24:89-101.

Hertel, O., Christensen, J., and Hov, O. (1994). Modelling of the end products of the chemical decomposition of DMS in the marine boundary layer. *Atmos. Environ.* 28:2431-2449.

Hillamo, R. E., and Kauppinen, E. I. (1991). On the performance of the Berner low pressure impactor. *Aerosol Sci. Technol.* 14:33-47.

Hindman, E.E., Carter, E.J., Borys, R.D., and Mitchell, D.L. (1992). Collecting supercooled cloud droplets as a function of droplet size. *J. Atmos. Oceanic Technol.* 9:337-353.

Hindman, E.E. (1988). Airborne "cloud sieving". Preprints of the 10th International Cloud Physics Conference, 15-20 August, Homburg von der Höhe, Germany. pp. 229-231.

Hoag, K.J., Collett, Jr., J.L., and Pandis, S.N. (1999). The influence of drop size-dependent fog chemistry on aerosol processing by San Joaquin Valley fogs. *Atmos. Environ.* 33:4817-4832.

Hoffmann, M.R. (1986). On the kinetics and mechanism of oxidation of aquated sulfur dioxide by ozone. *Atmos. Environ.* **20**:1145-1154.

Hoffmann, M.R., and Calvert, J.G. (1985). Chemical Transformation Modules for Eulerian Acid Deposition Models. Volume II. The Aqueous-Phase Chemistry, National Center for Atmospheric Research, Boulder, CO.

Hoppel, W.A., Frick, G.M., and Fitzgerald, J.W. (1994). A cloud chamber study of the effect that nonprecipitating water clouds have on the aerosol size distribution. *Aerosol Sci. Technol.* 20:1-30.

Hoppel, W.A., Frick, G.M., Larson, R.E. (1986). Effect of nonprecipitating clouds on the aerosol size distribution in the marine boundary layer. *Geophys. Res. Lett.* 13:125-128.

Horlock, J.H. (1966). Axial Flow Turbines – Fluid Mechanics and Thermodynamics. Butterworth & Co. Ltd., London. pp. 72-128.

Hudson, J.G., and Svensson, G. (1995). Cloud microphysical relationships in California marine stratus. *J. Appl. Met.* 34:2655-2666.

Hudson, J.G., and Frisbie, P.R. (1991). Cloud condensation nuclei near marine stratus. *J. Geophys. Res.* 96:20795-20808.

Huebert, B.J., Howell, S.G., Zhuang, L., Heath, J.A., Litchy, M.R., Wylie, D.J., Kreidler-Moss, J.L., Coppicus, S., and Pfeiffer, J.E. (1998). Filter and impactor measurements of anions and cations during the First Aerosol Characterization Experiment (ACE 1). *J. Geophys. Res.* 103:16493-16509.

Huebert, B.J., Zhuang, L., Howell, S., Noone, K., and Noone, B. (1996a). Sulfate, nitrate, methanesulfonate, chloride, ammonium, and sodium measurements from ship, island, and aircraft during the Atlantic Stratocumulus Transition Experiment/ Marine Aerosol Gas Exchange. *J. Geophys. Res.* 101:4413-4423.

Huebert, B.J., Wylie, D.J., Zhuang, L., and Heath, J.A. (1996b). Production and loss of methanesulfonate and non-sea salt sulfate in the equatorial Pacific marine boundary layer. *Geophys. Res. Lett.* 23:737-740.

Huebert, B. J., Lee, G., and Warren, W. L. (1990). Airborne aerosol inlet passing efficiency measurement. *J. Geophys. Res.* 95:16369-16381.

Huebert, B.J., Vanbramer, S., and Tschudy, K.L. (1988). Liquid cloudwater collection using modified Mohnen slotted rods. *J. Atmos. Chem.* 6:251-263.

Huebert, B.J., and Baumgardner, D. (1985). A preliminary evaluation of the Mohnen slotted-rod cloud water collector. *Atmos. Environ.* 19:843-846.

Husain, L., Rattigan, O.V., Dutkiewicz, V., Das, M., Judd, C.D., Khan, A.R., Richter, R., Balasubramanian, R., Swami, K., and Walcek, C.J. (2000). Case studies of the $SO_2 + H_2O_2$ reaction in clouds. *J. Geophys. Res.* 105:9831-9841.

Husain, L. (1989). A technique for determining in-cloud formation of SO_4. *Geophys. Res. Lett.* 16:57-60.

Ibusuki, T., and Takeuchi, K. (1987). Sulfur dioxide oxidation by oxygen catalyzed by mixtures of manganese (II) and iron (III) in aqueous solutions at environmental reaction conditions. *Atmos. Environ.* 21:1555-1560.

Isaac, G.A., Leaitch, W.R., and Strapp, J.W. (1990). The vertical distribution of aerosols and acid related compounds in air and cloudwater. *Atmos. Environ.* 24A:3033-3046.

Isaac, G.A., and Daum, P.H. (1987). A winter study of air, cloud and precipitation chemistry in Ontario, Canada. *Atmos. Environ.* 21:1587-1600.

Jaeschke, W., Gunther, A. (2001). Chemical composition of size segregated cloud drops collected with an airborne two stage impactor. 2nd International Conference on Fog and Fog Collection, 15-20 July, St. John's, Newfoundland, Canada. pp. 65-68.

Jaeschke, W. (1986). Multiphase atmospheric chemistry, in Chemistry of Multiphase Atmospheric Systems. W. Jaeschke, ed. Springer-Verlag, Berlin. pp. 3-13.

Jiusto, J.E. (1967). Aerosol and cloud microphysics measurements in Hawaii. *Tellus.* 19:359-368.

Jones, A., Roberts, D.L., and Slingo, A. (1994). A climate model study of indirect radiative forcing by anthropogenic sulphate aerosols. *Nature.* 370:450-453.

Jurcik, B., and Wang, H. C. (1995). On the shape of impactor efficiency curves. *J. Aerosol Sci.* 26:1139-1147.

Karamchandani, P., and Venkatram, A. (1992). The role of non-precipitating clouds in producing ambient sulfate during summer: results from simulations with the acid deposition and oxidant model (ADOM). *Atmos. Environ.* 26A:1041-1052.

Keene, W.C., Pszenny, A.A.P., Galloway, J.N., and Hawley, M.E. (1986). Sea-salt corrections and interpretation of constituent ratios in marine precipitation. *J. Geophys. Res.* 91:6647-6658.

Kelly, T.J., Daum, P.H., and Schwartz, S.E. (1985). Measurements of peroxides in cloudwater and rain. *J. Geophys. Res.* 90:7861-7871.

Khemani, L.T., Momin, G.A., Naik, M.S., Prakasa Rao, P.S., Safai, P.D., and Murty, A.S.R. (1987). Influence of alkaline particulates on pH of cloud and rain water in India. *Atmos. Environ.* 21:1137-1145.

Khemani, L.T., Sharma, S.K., Murty, A.S.R., and Ramana Murty, Bh.V. (1982). A simple gadget for collection of cloud/rain water from aircraft. Proceedings of the Conference on Cloud Physics, 15-16 Nov, Chicago, Illinois. pp. 303-305.

Kim, C.H., and Lee, J.W. (2001). A new collection efficiency model for small cyclones considering the boundary layer effect. *J. Aerosol Sci.* 32:251-269.

Kim, H.T., Lee, K.W., and Kuhlman, M.R. (2001). Exploratory design modifications for enhancing cyclone performance. *J. Aerosol Sci.* 32:1135-1146.

Kim, Y.J., and Boatman, J.F. (1992). The collection efficiency of a modified Mohnen slotted-rod cloud-water collector in summer clouds. *J. Atmos. Oceanic Technol.* 9:35-41.

King, W.D. (1984). Air flow and particle trajectories around aircraft fuselages. I: Theory. *J. Atmos. Oceanic Technol.* 1:5-13.

Kley, D., Drummond, J.W., McFarland, M., and Liu, S.C. (1981). Tropospheric profiles of NO_x. *J. Geophys. Res.* 86:3153-3168.

Kritz, M.A. (1982). Exchange of sulfur between the free troposphere, marine boundary layer, and the sea surface. *J. Geophys. Res.* 87:8795-8803.

Laj, P., Fuzzi, S., Lazzari, A., Ricci, L., Orsi, G., Berner, A., Dusek, U., Schell, D., Gunther, A., Wendisch, M., Wobrock, W., Frank, G., Martinsson, B.G., and Hillamo, R. (1998). The size dependent composition of fog droplets. *Cont. Atmos. Phys.* 71:115-130.

Laucks, M.L., and Twohy, C.H. (1998). Size-dependent collection efficiency of an airborne counterflow virtual impactor. *Aerosol Sci. Technol.* 28:40-61.

Launder, B. E. (1989). Second-moment closure: present... and future? *Int. J. Heat and Fluid Flow.* 10:282-300.

Launder, B. E., and Spalding, D. B. (1974). The numerical computation of turbulent flows. *Computer Methods in Applied Mechanics and Engineering.* 3:269-289.

Lawrence, M.G., and Crutzen, P.J. (1999). Influence of NOx emissions from ships on tropospheric photochemistry and climate. *Nature.* 402:167-170.

Lazrus, A., Kok, G.L., Gitlin, S.N., Lind, J.A., and McLaren, S.E. (1985). Automated fluorometric method for hydrogen peroxide in atmospheric precipitation. *Analyt. Chem.* 57:917-922.

Leaitch, W.R., Banic, C.M., Isaac, G.A., Couture, M.D., Liu, P.S.K., Gultepe, I., Li, S.-M., Kleinman, L., Daum, P.H., and MacPherson, J.I. (1996). Physical and chemical observations in marine stratus during the 1993 North Atlantic Regional Experiment: Factors controlling cloud drop number concentrations. *J. Geophys. Res.* 101:29123-29135.

Leaitch, W.R., Isaac, G.A., Strapp, J.W., Banic, C.M., and Wiebe, H.A. (1992). The relationship between cloud droplet number concentrations and anthropogenic pollution: Observations and climatic implications. *J. Geophys. Res.* 97:2463-2474.

Leaitch, W.R., Strapp, J.W., Wiebe, H.A., Anlauf, K.G., and Isaac, G.A. (1986a). Chemical and microphysical studies of nonprecipitating summer cloud in Ontario, Canada. *J. Geophys. Res.* 92:11821-11831.

Leaitch, W.R., Strapp, J.W., and Isaac, G.A. (1986b). Cloud droplet nucleation and cloud scavenging of aerosol sulphate in polluted atmospheres. *Tellus.* 38B:328-344.

Lee, M., Heikes, B.G., and O'Sullivan, D.W. (2000). Hydrogen peroxide and organic hydroperoxide in the troposphere: a review. *Atmos. Environ.* 34:3475-3494.

Lei, H-C., Tanner, P.A., Huang, M.-Y., Shen, Z.-L., and Wu, Y.-X. (1997). The acidification process under the cloud in southwest China: Observation results and simulation. *Atmos. Environ.* 31:851-861.

Lelieveld, J., and Heintzenberg, J. (1992). Sulfate cooling effect on climate through in-cloud oxidation of anthropogenic SO_2. *Science.* 258:117-120.

Lenschow, D.H., Paluch, I.R., Bandy, A.R., Pearson, R. Jr., Kawa, S.R., Weaver, C.J., Huebert, B.J., Kay, J.G., Thornton, D.C., and Driedger, A.R. III. (1988). Dynamics and chemistry of marine stratocumulus (DYCOMS) Experiment. *BAMS.* 69:1058-1066.

Leonard, B. P. (1979). A stable and accurate convective modelling procedure based on quadratic upstream interpolation. *Computer Methods in Applied Mechanics and Engineering.* 19:59-98.

Lide, D.R., ed. (2000). Handbook of Chemistry and Physics. CRC Press. Boca Raton, Florida 33431. p. 14-14.

Lillis, D., Cruz, D.N., Collett, Jr., J.L., Richards, L.W., and Pandis, S.N. (1999). Production and removal of aerosol in a polluted fog layer: model evaluation and fog effect on PM. *Atmos. Environ.* 33:4797-4816.

Lind, J.A., and Kok, G.L. (1994). Correction to "Henry's law determinations for aqueous solutions of hydrogen peroxide, methylhydroperoxide, and peroxyacetic acid". *J. Geophys. Res.* 99:21119.

Liu, P.S.K., Leaitch, W.R., Macdonald, A.M., Isaac, G.A., Strapp, J.W., and Wiebe, H.A. (1993). Sulphate production in summer cloud over Ontario, Canada. *Tellus.* 45B:368-389.

Liu, S.C., McFarland, M., Kley, D., Zafiriou, O., and Huebert, B. (1983). Tropospheric NO_x and O_3 budgets in the equatorial Pacific. J. Geophys. Res. 88:1360-1368.

Macdonald, A.M., Anlauf, K.G., Banic, C.M., Leaitch, W.R., and Wiebe, H.A. (1995). Airborne measurements of aqueous and gaseous hydrogen peroxide during spring and summer in Ontario, Canada. *J. Geophys. Res.* 100:7253-7262.

MacInnes, J. M., and Bracco, F. V. (1992). Stochastic particle dispersion modeling and the tracer-particle limit. *Phys. Fluids A* 4:2809-2824.

MacPherson, J.I., and Baumgardner, D. (1988). Airflow about King Air wingtip-mounted cloud particle measurement probes. *J. Atmos. Oceanic Technol.* 5:259-273.

Marple, V. A., Olson, B. A., and Miller, N. C. (1995). A low-loss cascade impactor with stage collection cups: calibration and pharmaceutical inhaler applications. *Aerosol Sci. Technol.* 22:124-134.

Marple, V.A., Rubow, K.L., Turner, W., and Spengler, J.D. (1987). Low flow rate sharp cut impactors for indoor air sampling: design and calibration. *JAPCA.* 37:1303-1307.

Marple, V. A., and Rubow, K. L. (1986). Theory and design guidelines, in Cascade Impactor Sampling and Data Analysis. J.P. Lodge, Jr. and T.L. Chan, eds. AIHA, Akron, pp.79-102.

Martin, D., Tsivou, M., Bonsang, B., Abonnel, C., Carsey, T., Springer-Young, M., Pszenny, A., and Suhre, K. (1997). Hydrogen peroxide in the marine atmospheric boundary layer during the Atlantic Stratocumulus Transition Experiment/ Marine Aerosol and Gas Exchange experiment in the eastern subtropical North Atlantic. *J. Geophys. Res.* 102:6003-6015.

Martin, G.M., Johnson, D.W., and Spice, A. (1994). The measurement and parameterization of effective radius of droplets in warm stratocumulus clouds. *J. Atmos. Sci.* 51:1823-1842.

Maser, R., Franke, H., Preiss, M., and Jaeschke, W. (1994). Methods provided and applied in a research aircraft for the study of cloud physics and chemistry. *Beitr. Phys. Atmos.* 67:321-334.

Maser, R., and Jaeschke, W. (1992). Study of cloud water chemistry – new instrumentation for aircraft measurements, in Nucleation and Atmospheric Aerosols. N. Fukuta and P.E. Wagner, eds. A. Deepak Publishing, Hampton, Virginia. pp. 497-500.

Mason, B.J. (1992). Acid rain: its causes and its effects on inland waters. Clarendon Press, Oxford.

Maynard, A.D. (2000). A simple model of axial flow cyclone performance under laminar flow conditions. *J. Aerosol Sci.* 31:151-167.

McFarland, A. R., Gong, H., Muyshondt, A., Wente, W. A., and Anand, N. K. (1997). Aerosol deposition in bends with turbulent flow. Environ. *Sci. Technol.* 31:3371-3377.

McFarland, D. (2001). Personal communication.

Mitra, S.K., Pruppacher, H.R., and Brinkmann, J. (1992). A wind tunnel study on the drop to particle conversion. *J. Aerosol Sci.* 23:245-256.

Mohnen, V.A. (1980). Cloud water collection from aircraft. *Atmos. Technol.* 12:20-25.

Moller, D., Acker, K., and Wieprecht, W. (1996). A relationship between liquid water content and chemical composition in clouds. *Atmos. Res.* 41:321-335.

Moore, K.F. (2001). Drop size-dependent chemical composition in clouds and fogs. Department of Atmospheric Science Report No. 713. Colorado State University, Fort Collins, CO.

Morsi, S. A., and Alexander, A. J. (1972). An investigation of particle trajectories in two-phase flow systems. *Journal of Fluid Mechanics.* 55:193-208.

Mothes, H., and Loffler, F. (1988). Prediction of particle removal in cyclone separators. *Int. Chem. Eng.* 28:231-240.

Mundo, CHR., Sommerfield, M., and Tropea, C. (1995). Droplet-wall collisions: experimental studies of the deformation and breakup process. *Int. J. Multiphase Flow.* 21:151-173.

Munger, J.W., Collett, Jr., J.L., Daube, Jr., B., and Hoffmann, M.R. (1989). Chemical composition of coastal stratus clouds: dependence on droplet size and distance from the coast. Atmos. Environ. 23:2305-2320.

Munson, B.R., Young, D. F., and Okiishi, T. H. (1990). Fundamentals of Fluid Mechanics. John Wiley & Sons, New York, pp.146,319-338,372-373,484-502.

Muyshondt, A., McFarland, A. R., and Anand, N. K. (1996). Deposition of aerosol particles in contraction fittings. *Aerosol Sci. Technol.* 24:205-216.

Nieuwstadt, F.T.M., and Dirkzwager, M. (1995). A fluid mechanics model for an axial cyclone separator. *Ind. Eng. Chem. Res.* 34:3399-3404.

Noone, K.B., Noone K.J., Heintzenberg, J., Ström, J., and Ogren, J.A. (1993). In situ observations of cirrus cloud microphysical properties using the counterflow virtual impactor. *J. Atmos. Oceanic Technol.* 10:294–303.

Noone, K.J., Ogren, J.A., Noone, K.B., Hallberg, A., Fuzzi, S., and Lind, J.A. (1991). Measurements of the partitioning of hydrogen peroxide in a stratiform cloud. *Tellus.* 43B:280-290.

Noone, K.J., Ogren, J.A., and Heintzenberg, J. (1990). An examination of clouds at a mountain-top site in central Sweden: The distribution of solute within cloud drops. *Atmos. Res.* 25:3-15.

Noone, K.J., Charlson, R.J., Covert, D.S., Ogren, J.A., and Heintzenberg, J. (1988a). Cloud droplets: Solute concentration is size dependent. *J. Geophys. Res.* 93:9477-9482.

Noone, K.J., Ogren, J.A., Heintzenberg, J., Charlson, R.J., and Covert, D.S. (1988b). Design and calibration of a counterflow virtual impactor for sampling of atmospheric fog and cloud droplets. *Aerosol Sci. Technol.* 8:235-244.

Norment, H.G. (1988). Three-dimensional trajectory analysis of two drop sizing instruments: PMS OAP and PMS FSSP. *J. Atmos. Oceanic Technol.* 5:743-756.

Oddie, B.C.V. (1962). The chemical composition of precipitation at cloud level. *Q. J. R. Meteor. Soc.* 88:535-538.

O'Dowd, C.D., Smith, M.H., Consterdine, I.E., and Lowe, J.A. (1997). Marine aerosol, sea-salt, and the marine sulphur cycle: a short review. *Atmos. Environ.* 31:73-80.

Ogawa, A. (1984). Separation of Particles from Air and Gases, Volume II. CRC Press, Inc., Boca Raton, FL. pp. 1-19.

Ogren, J.A., and Charlson, R.J. (1992). Implications for models and measurements of chemical inhomogeneities among cloud droplets. *Tellus.* 44B:208-225.

Ogren, J.A., Heintzenberg, J., Zuber, A., Noone, A.J., and Charlson, R.J. (1989). Measurements of the size-dependence of solute concentrations in cloud droplets. *Tellus.* 41B, 24–31.

Ogren, J.A., Heintzenberg, J., and Charlson, R.J. (1985). In-situ sampling of clouds with a droplet to aerosol converter. *Geophys. Res. Lett.* 12:121-124.

Olan-Figueroa, E., McFarland, A.R., and Ortiz, C.A. (1982). Flattening coefficients for DOP and oleic acid droplets deposited on treated glass slides. *Am. Ind. Hyg. Assoc.* 43:395-399.

Olszyna, K.J., Meagher, J.F., and Baily, E.M. (1988). Gas-phase, cloud and rain-water measurements of hydrogen peroxide at a high-elevation site. *Atmos. Environ.* 22:1699-1706.

Paluch, I.R., Lenschow, D.H., Hudson, J.G., and Pearson, R. Jr. (1992). Transport and mixing processes in the lower troposphere over the ocean. *J. Geophys. Res.* 97:7527-7541.

Paluch, I.R., and Lenschow, D.H. (1991). Stratiform cloud formation in the marine boundary layer. *J. Atmos. Sci.* 48:2141-2158.

Pandis, S.N., Russell, L.M., and Seinfeld, J.H. (1994). The relationship between DMS flux and CCN concentrations in remote marine regions. *J. Geophys. Res.* 99:16945-16957.

Parungo, F.P., Nagamoto, C.T., Madel, R., Rosinski, J., and Haagenson, P.L. (1987). Marine aerosols in Pacific upwelling regions. *J. Aerosol Sci.* 18:277-290.

Parungo, F.P., Nagamoto, C.T., Rosinski, J., and Haagenson, P.L. (1986). A study of marine aerosols over the Pacific Ocean. *J. Atmos. Chem.* 4:199-226.

Parungo, F., Nagamoto, C., Nolt, I., Dias, M., and Nickerson, E. (1982). Chemical analysis of cloud water collected over Hawaii. *J. Geophys. Res.* 87:8805-8810.

Patankar, S. V. (1980). Numerical Heat Transfer and Fluid Flow. Hemisphere Publishing Corp., Washington, D. C.

Petrenchuk, O.P. (1973). Estimation of condensation nuclei chemical composition from the results of cloud water analysis. Proceedings of the 8th International Conference on Nucleation, 24-29 Sept., Leningrad, U.S.S.R. pp. 445-449.

Petrenchuk, O.P., and Drozdova, V.M. (1966). On the chemical composition of cloud water. *Tellus.* 18:280-286.

Preiss, M., Maser, R., Franke, H., Jaeschke, W., and Graf, J. (1994). Distribution of trace substances inside and outside of clouds. *Beitr. Phys. Atmos.* 67:341-351.

Prospero, J.M., and Savoie, D.L. (1989). Effect of continental sources on nitrate concentrations over the Pacific Ocean. *Nature.* 339:687-689.

Pruppacher, H.R., and Klett, J.D. (1997). Microphysics of Clouds and Precipitation. Kluwer Academic Publisher, Dordrecht, The Netherlands, pp.287, 379-399, 537-546.

Quinn, P.K., Charlson, R.J., and Bates, T.S. (1988). Simultaneous observations of ammonia in the atmosphere and ocean. *Nature.* 335:336-338.

Quinn, P.K., Charlson, R.J., and Zoller, W. (1987). Ammonia, the dominant base in the remote marine troposphere: a review. *Tellus.* 39B:413-425.

Raemdonck, H., Maenhaut, W., and Andreae, M.O. (1986). Chemistry of marine aerosol over the Tropical and Equatorial Pacific. *J. Geophys. Res.* 91:8623-8636.

Range, K., and Feuillebois, F. (1998). Influence of surface roughness on liquid drop impact. *J. Colloid and Interface Sci.* 203:16-30.

Rao, X., and Collett, J.L. Jr. (1998). The drop size-dependence of iron and manganese concentrations in clouds and fogs: Implications for sulfate production. *J. Atmos. Chem.* 30:273-289.

Rao, X., and Collett, J.L., Jr. (1995). Behavior of S(IV) and formaldehyde in a chemically heterogeneous cloud. *Environ. Sci. Technol.* 29:1023-1031.

Rattigan, O.V., Reilly, J., Judd, C.D., Moore, K.F., Das, M., Sherman, D.E., Dutkiewicz, V.A., Collett, Jr., J.L., and Husain, L. (2001). Sulfur dioxide oxidation in clouds at Whiteface Mountain as a function of drop size. *J. Geophys. Res.* 106:17347-17358.

Reilly, J.E., Rattigan, O.V., Moore, K.F., Judd, C., Sherman, D.E., Dutkiewicz, V.A., Kreidenweis, S.M., Husain, L., and Collett, Jr., J.L. (2001). Drop size-dependent S(IV) oxidation in chemically heterogeneous radiation fogs. *Atmos. Environ.* 35:5717-5728.

Rein, M. (1993). Phenomena of liquid drop impact on solid and liquid surfaces. *Fluid Dynamics Res.* 12:61-93.

Richards, L.W. (1995). Airborne chemical measurements in nighttime stratus clouds in the Los Angeles Basin. *Atmos. Environ.* 29:27-46.

Richards, L.W., Anderson, J.A., Blumenthal, D.L., McDonald, J.A., Kok, G.L., and Lazrus, A.L. (1983). Hydrogen peroxide and sulfur (IV) in Los Angeles cloud water. *Atmos. Environ.* 17:911-914.

Samenfink, W., Elsaβer., A., Dullenkopf, K., and Wittig, S. (1999). Droplet interaction with shear-driven liquid films: analysis of deposition and secondary droplet characteristics. *Int. J. Heat Fluid Flow.* 20:462-469.

Savoie, D.L., Prospero, J.M., Merrill, J.T., and Uematsu, M. (1989). Nitrate in the atmospheric boundary layer of the tropical South Pacific: implications regarding sources and transport. *J. Atmos. Chem.* 8:391-415.

Schanot, A. (2000). Personal communication.

Schell, D., Wobrock, W., Maser, R., Preiss, M., Jaeschke, W., Georgii, H.W., Gallagher, M.W., Bower, K.N., Beswick, K.M., Pahls, S., Facchini, M.C., Fuzzi, S., Wiedensohler, A., Hansson, H.C., and Wendisch, M. (1997). The size-dependent chemical composition of cloud droplets. *Atmos. Environ.* 31:2561-2576.

Scott, W. D. (1978). The pH of cloud water and the production of sulfate. *Atmos. Environ.* 12:917-921.

Scott, W.D., and Laulainen. (1979). On the concentration of sulfate in precipitation. *J. Appl. Meteor.* 18:138-147.

Seinfeld, J.H., and Pandis, S.N. (1998). Atmospheric chemistry and physics: from air pollution to climate change. Wiley-Interscience, New York, NY, pp.337, 470-483,803.

Shirolkar, J.S., Coimbra, C.F.M., and McQuay, M.Q. (1996). Fundamental aspects of modeling turbulent particle dispersion in dilute flows. *Prog. Energy Combust. Sci.* 22:262-399.

Sievering, H., Lerner, B., Slavich, J., Anderson, J., Posfai, M., Cainey, J. (1999). O_3 oxidation of SO_2 in sea-salt water: size distribution of non-sea-salt sulfate during the First Aerosol Characterization Experiment (ACE 1). *J. Geophys. Res.* 104:21707-21717.

Sievering, H., Boatman, J., Galloway, J., Keene, W., Kim, Y., and Laria, M. (1991). Heterogeneous sulfur conversion in sea-salt aerosol particles: the role of aerosol water content and size distribution. *Atmos. Environ.* 25A:1479-1487.

Sinner, T., Hoffmann, P., and Ortner, H.M. (1994). Determination of pH-value, redox-potential, transition metals concentration and Fe(II)- and Fe(III)-content in cloud water samples. *Beitr. Phys. Atmos.* 67:353-357.

Smith, R.L. (1981). A comparison of the structure and variability of the flow field in three coastal upwelling regions: Oregon, Northwest Africa, and Peru, in Coastal Upwelling. F.A. Richards, ed. American Geophysical Union, Washington, D.C. pp. 87-94.

Snider, J.R., and Brenguier, J.-L. (2000). Cloud condensation nuclei and cloud droplet measurements during ACE-2. *Tellus.* 52B:828-842.

Stevens, B., Lenschow, D.H., Vali, G., Gerber, H., Bandy, A., Blomquist, B., Brenguier, J., Bretherton, C.S., Campos, T., Chai, S., Faloona, I., Haimov, S., Friesen, D., Laursen, K., Leon, D., Lilly, D.K., Loehrer, S., Malinowski, S., Rivera, M., Rogers, D.C., Russell, L., Savic-Jovcic, V., Snider, J., Straub, D., Szumowski, M., Tschudi, M., Twohy, C., Wetzel, M., van Zanten, M. C. (2002). Dynamics and Chemistry of Marine Stratocumulus – DYCOMS-II. Submitted to the Bulletin of the American Meteorological Society.

Stow, C.D., and Hadfield, M.G. (1981). An experimental investigation of fluid flow resulting from the impact of a water drop with an unyielding dry surface. *Proc. R. Soc. Lond. A* 373:419-441.

Strapp, J.W., Leaitch, W.R., Anlauf, K.G., Bottenheim, J.W., Joe, P., Schemenauer, R.S., Wiebe, H.A., Isaac, G.A., Kelly, T.J., and Daum, P.H. (1988). Winter cloud water and air composition in central Ontario. *J. Geophys. Res.* 93:3760-3772.

Straub, D.J., and Collett, J.L. Jr. (2002). Development of a multi-stage cloud water collector: Part 2 - Numerical and experimental calibration. *Atmos Environ.* 36:45-56.

Straub, D. J., and Collett, J. L. Jr. (2001). Numerical and experimental performance evaluation of the 3-Stage FROSTY Supercooled Cloud Collector. *Aerosol Sci. Technol.* 34:247-261.

Straub, D. J., and Collett, J. L. Jr. (1999). Numerical and experimental performance evaluation of two multi-stage cloud collectors. Department of Atmospheric Science Report No. 676. Colorado State University, Fort Collins, CO.

Strauss, W. (1975). Industrial Gas Cleaning; the principles and practice of the control of gaseous and particulate emissions. Pergamon Press, Oxford. pp. 216-265.

Strom, J., Heintzenberg, J., Noone, K.J., Noone, K.B., Ogren, J.A., Albers, F., and Quante, M. (1994). Small crystals in cirriform clouds: a case study of residual size distribution, cloud water content, and related cloud properties. *Atmos. Res.* 32:125-141.

Swanson, P. D., Muzzio, F. J., Annapragada, A., and Abjei, A. (1996). Numerical analysis of motion and deposition of particles in cascade impactors. *Int. J. Pharm.* 142:33-51.

Tanner, R.L. (1987). Chemical instrumentation of atmospheric wet deposition processes, in The Chemistry of Acid Rain. R.W. Johnson, G.E. Gordon, W. Calkins, and A.Z. Elzerman, eds. American Chemical Society, Washington, D.C. pp. 289-302.

Twohy, C.H., Schanot, A.J. and Cooper, W.A. (1997). Measurement of condensed water content in liquid and ice clouds using an airborne counterflow virtual impactor. *J. Atmos. Oceanic Technol.* 14:197-202.

Twohy, C.H., and Rogers, D. (1993). Airflow and water-drop trajectories at instrumentation points around the Beechcraft King Air and Lockheed Electra. *J. Atmos. Oceanic Technol.* 10:566-578.

Twohy, C.H., Clark, A.D., Warren, S.G., Radke, L.F., and Charlson, R.J. (1989). Light-absorbing material extracted from cloud droplets and its effect on cloud albedo. *J. Geophys. Res.* 94:8623-8631.

Twomey, S. (1991). Aerosols, clouds and radiation. Atmos. Environ. 25A:2435-2442.

Twomey, S. (1977). The influence of pollution on the shortwave albedo of clouds. *J. Atmos. Sci.* 34:1149-1152.

Twomey, S. (1974). Pollution and the planetary albedo. *Atmos. Environ.* 8:1251-1256.

Uematsu, M., Duce, R.A., Prospero, J.M., Chen, L., Merrill, J.T., and McDonald, R.L. (1983). Transport of mineral aerosol from Asia over the North Pacific Ocean. *J. Geophys. Res.* 88:5343-5352.

Vaughan, N.P. (1989). The Anderson impactor: calibration, wall losses and numerical simulation. *J. Aerosol. Sci.* 20:67-90.

Vaughan, N.P. (1988). Construction and testing of an axial flow cyclone preseparator. *J. Aerosol Sci.* 19:295-305.

von Glasow, R., and Sander, R. (2001). Variations of sea salt aerosol pH with relative humidity. *Geophys. Res. Lett.* 28:247-250.

Vong, R.J., Baker, B.M., Brechtel, F.J., Collier, R.T., Harris, J.M., Kowalski, A.S., McDonald, N.C., and McInnes, L.M. (1997). Ionic and trace element composition of cloud water collected on the Olympic Peninsula of Washington State. *Atmos. Environ.* 31:1991-2001.

Walters, P.T., Moore, M.J., and Webb, A.H. (1983). A separator for obtaining samples of cloud water in aircraft. *Atmos. Environ.* 17:1083-1091.

Watanabe, K., Ishizaka, Y., and Takenaka, C. (2001). Chemical characteristics of cloud water over the Japan Sea and the Northwestern Pacific Ocean near the central part of Japan: airborne measurements. *Atmos. Environ.* 35:645-655.

Weathers, K.C., Likens, G.E., Bormann, F.H., Bicknell, S.H., Bormann, B.T., Daube, B.C. Jr., Eaton, J.S., Galloway, J.N., Keene, W.C., Kimball, K.D., McDowell, W.H., Siccama, G.T., Smiley, D., and Tarrant, R.A. (1988). Cloudwater chemistry from ten sites in North America. *Environ. Sci. Technol.* 22:1018-1026.

Weller, R., Schrems, O., Boddenberg, A., Gab, S., and Gautrois, M. (2000). Meridional distribution of hydroperoxides and formaldehyde in the marine boundary layer of the Atlantic (48°N-35°S) measured during the Albatross campaign. *J. Geophys. Res.* 105:14401-14412.

Wilson, J.C., and Seebaugh, W.R. (2001). Measurement of Aerosol from Aircraft, in Aerosol Measurement Principles, Techniques, and Applications. P.A. Baron and K.Willeke, eds. Wiley & Sons, New York, pp 887-901.

Wilson, D.G., and Korakianitis, T. (1998). The Design of High-Efficiency Turbomachinery and Gas Turbines. Prentice Hall, Upper Saddle River, NJ. pp. 283-341.

Winters, W., Hogan, A., Mohnen, V., and Barnard, S. (1979). ASRC airborne cloud water collection system. ASRC-SUNYA Publication 728, Albany, NY.

Xu, G., Sherman, D.E., Andrews, E., Moore, K., Straub, D.J., Hoag, K., and Collett, Jr., J. (1999). The influence of chemical heterogeneity among cloud drop populations on processing of chemical species in winter clouds. *Atmos. Res.* 51:119-140.

Yum, S.S., Hudson, J.G., and Xie, Y. (1998). Comparisons of cloud microphysics with cloud condensation nuclei spectra over the summertime Southern Ocean. *J. Geophys. Res.* 103:16625-16636.

Zhang, Y., Kreidenweis, S.M., and Feingold, G. (1999). Stratocumulus processing of gases and cloud condensation nuclei 2. Chemistry sensitivity analysis. *J. Geophys. Res.* 104:16061-16080.

Zhang, Z.Q., and Liu, B.Y.H. (1989). On the empirical fitting equations for aspiration coefficients for thin-walled sampling probes. *J. Aerosol. Sci.* 20:713-720.

Appendix A. Supplemental system design information

Appendix A contains detailed information regarding the design of the axial-flow cyclone cloud water collection system. This appendix primarily supports the material presented in Chapter 3.

A.1 Axial-flow cyclone duct

The two polycarbonate sections of the axial-flow cyclone duct are fastened together with eight 4-40 threaded rods and nuts, which secure the vane unit in place as well. O-ring seals are placed at the interfaces between the vane unit and the polycarbonate sections of the duct to create a leak free system. The axial-flow cyclone can be relatively easily disassembled to remove the vane unit and for cleaning and inspection. As suggested by DFS, the inlet lip is not sharp-edged, but rather curved with a series of parabolic arcs to discourage flow separation due to non-isoaxial sampling at flight velocities (Fox, 2000). Design drawings for the axial-flow cyclone duct can be found in Appendix B.

The extraction slot was machined into the inner surface of the polycarbonate duct 5.5 cm downstream of the leading edge of the curved vanes. The 0.6 cm deep slot extends around the entire circumference of the duct. Two 2 mm diameter ports extend through the polycarbonate duct and into the extraction slot to allow accumulated cloud water to be drawn out. The ports are oriented such that one is at the bottom of the collector and the other is rotated 60° clockwise when viewed from the front of the collector (Figure A.1). The extraction ports terminate at the outer wall of the duct in 1/8" FNPT fittings.

Downstream of the extraction slot, the duct transitions to aluminum for its remaining length. The aluminum duct section simply slides into a recess machined into the polycarbonate

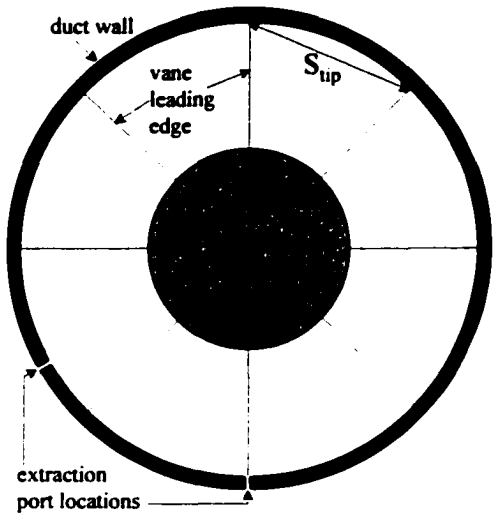

Figure A.1. Schematic front view of the curved vane unit showing blade spacing at the hub and tip and the locations of the two extraction ports. The diameter of the center hub is 3 cm and diameter of the duct wall is 7 cm.

portion of the duct and is secured with a stainless steel hose clamp. By loosening the hose clamp, the aluminum duct can be easily detached to allow access to the downstream side of the vane assembly. The aluminum duct is made from commercially available 6.35 cm OD, 0.165 cm wall thickness, 6061-T6 aluminum tubing. The transition to aluminum was a practical consideration intended to reduce machining costs, reduce weight, and to minimize the space occupied by the duct. Because all sampled cloud water is removed from the duct at the extraction slot, the choice of materials for the downstream portion of the duct was not constrained by requirements to be chemically inert, making aluminum a viable option. The aluminum portion of the duct further acts as a support structure to which many of the remaining collector components are secured.

A.2 Design of curved vane geometry

In an effort to reduce the complexity and cost of manufacture of the vane unit, the vane cross section did not incorporate an airfoil shape as is the case for the majority of high performance, high efficiency turbine blades. This omission was deemed acceptable because the velocities through the system are relatively low, because extreme efficiency was not required for

this application, and because there were not strict outlet flow conditions that needed to be satisfied.

The number of blades in a given axial-flow turbine application can be selected by the designer (Horlock, 1966), so an eight blade configuration was chosen for the axial-flow cyclone. By choosing the number of blades, the blade spacing (S) is automatically defined (Figure A.2). Because the circumference of interest is different at the blade root (at the 3 cm diameter center body) and at the blade tip (at the 7.0 cm duct wall) different blade spacings are defined at the root (S_{hub}) and the tip (S_{tip}).

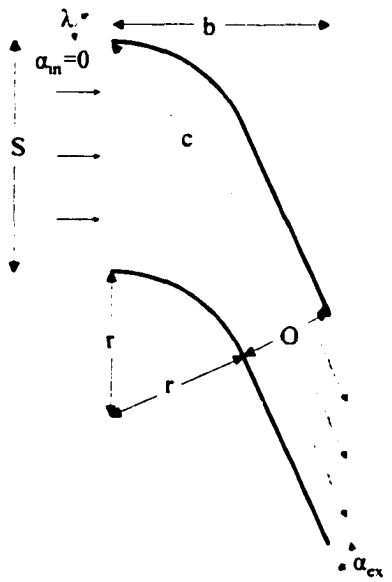

Figure A.2. Parameters describing the curved vane camber line, or cross sectional geometry. S is the blade spacing, b is axial chord, c is chord length, r is the radius of curvature, O is the nozzle width, α_{in} is the inlet flow angle, α_{ex} is the outlet flow angle, and λ is the setting angle.

Based on the blade spacing, the axial chord (b) (Figure A.2) is then calculated for the root and tip using the following equation (Wilson and Korakianitis, 1998):

$$\left(\frac{b}{S}\right)_{opt} = \left|\frac{2}{C_{L,opt}}\cos^2\alpha_{ex}\left(\tan\alpha_{in} - \tan\alpha_{ex}\right)\right| \qquad (A.1)$$

where S is the blade spacing, b is the axial chord, $C_{L,opt}$ is the optimum lift coefficient, α_{ex} is the outlet flow angle, and α_{in} is the inlet flow angle. The ratio (b/S) is referred to as the axial solidity and reaches an optimal value, $(b/S)_{opt}$, when pressure losses across the blades due to flow separation and friction are a minimum. The optimal lift coefficient ($C_{L,opt}$) should be approximately 0.8, as suggested by the empirical correlations described by Horlock (1966) and Carmichael (1966). For the axial-flow cyclone cloud water collector, the flow approaching the curved vanes is purely axial, making $\alpha_{in} = 0$. The outlet angle (α_{ex}) was selected to be 65° to provide a compromise between pressure drop and the ability to extract collected cloud water from the duct walls (Walters, 1983). By reducing α_{ex} from 65°, the static pressure drop across the vane unit could be reduced allowing the airflow to maintain a higher axial velocity through the collector, bringing it nearer to isokinetic sampling conditions. However, the reduction in α_{ex} would also reduce the tangential velocity in the collector, making removal of cloud water from the duct surface more difficult as the flow remains more axially directed.

The chord length (c) can be obtained from the relation (Wilson and Korakianitis, 1998):

$$c = \frac{b}{\cos\lambda} \tag{A.2}$$

where c is chord length, b is the axial chord, and λ is the setting angle. The setting angle is defined as the angle between the chord line and the axial direction, and can be determined from Figure 7.4 of Wilson and Korakianitis (1998).

After calculation of the blade spacing, the axial chord, and the chord length for the blade root and tip, the layout of the vane root and tip cross sectional geometries could be completed. The camber line, which defines the cross sectional shape of the blade, was based on these calculated dimensions and simple geometrical relationships to define the remaining pertinent dimensions that fully defined the shape of the blade. The camber line was constructed from a straight line segment positioned at the desired outlet angle and an arc that is tangential to that line segment and also possesses an axially-directed leading edge. Camber lines were defined at the

hub radius (1.5 cm) and at the duct wall radius (3.5 cm). For the purpose of creating a digital solid model of the vanes for manufacturing, additional camber lines were defined at 1 cm and 4 cm radii, and the blade itself was defined as the interpolated surface between those camber lines and trimmed at the center hub radius (1.5 cm) and duct wall radius (3.5 cm).

The design of the vane geometry was performed with the assumption of a zero blade thickness. However, a minimum wall thickness of 0.1 cm was recommended for proper fabrication through SLS. Distributing the wall thickness evenly about the camber line would have decreased the width of the vane nozzle (labeled O in Figure A.2) resulting in an increased pressure drop across the vanes and a reduced flow rate. Instead, the wall thickness was distributed about the camber line as illustrated in Figure A.3, in an effort to maintain the desired outlet nozzle width. This distribution reduced the outlet angle of the vanes by approximately 1°, negligibly influencing the rotational flow field.

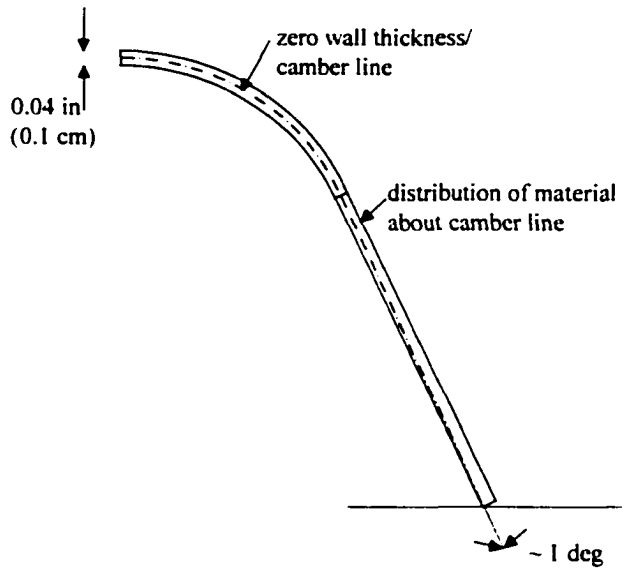

Figure A.3. Rather than distributing the wall material equally across the curved vane camber line, the thickness distribution was shifted at the vane outlet in order to preserve the designed nozzle width. This altered the outlet flow angle by approximately 1°.

A.3 Inlet cover motor

The inlet cover is driven by a geared 24 V DC Barber-Colman motor (model number EYQF-63600-750) that provides 60.3 oz-in of torque at 38 RPM. The motor was fused with a 3/8 Amp slow-blow fuse (Buss MDL 3/8) to cut power to the motor and prevent overheating in the event the cover mechanism seized.

While the motor and associated support structure are mounted inside the PMS canister, a chain drive couples the motor to two threaded rods that penetrate through the forward end cap of the canister to actuate the inlet cover. As the rods are retracted into the canister, the inlet cover opens and as the rods are extended out of the canister, the inlet cover closes. At the locations where the rods pass through the end cap, o-rings around the rods provide a water tight seal. Apart from the cover itself, the remaining mechanical components were fabricated from anodized aluminum and stainless steel.

A.4 Storage system

Cloud water is transported from the axial-flow cyclone extraction slot to the storage bottles through thin wall 1/4 in OD, 3/16 in ID FEP Teflon tubing. A polypropylene three-way compression fitting joins the two lines originating from the two extraction slot ports to a single sample transport line that runs along the aluminum duct. In order to route the semi-rigid FEP tubing in the confined space of the PMS canister, a heat gun was used to make the tubing pliable so that it could be molded into the desired position. At each of the seven sample bottle locations, a polypropylene tee compression fitting branches off the sample transport line and connects to the 1/8 in NPT inlet port of a Teflon solenoid valve (Bio-Chem Valve, 100T2-S804). These valves were selected for their small size, all Teflon flow path, and availability with a large 0.125 in diameter orifice that reduced the pressure drop through the storage system. Each of the solenoid valves is mounted on an aluminum stand and secured to the aluminum flow-through duct with a stainless steel hose clamp.

The outlet port of each solenoid valve connects directly to the lid of a sample storage bottle by way of a polypropylene 90° elbow fitting (see Figure 3.11). A large barbed fitting on the inside of the lid extends through the lid and is threaded into the elbow fitting. Thus, the sample bottle lids are permanently incorporated into the structure of the collector and only the sample bottles are removed and replaced between flights. A food grade polypropylene gasket is placed between the elbow fitting and the outer surface of the lid to maintain a leak proof seal. The storage bottles are angled forward slightly in order to accommodate them in the PMS canister (see Figure 3.12). In this seven valve, seven storage bottle arrangement, sample flow to a specific bottle is initiated by opening the valve associated with that bottle, while keeping the remaining six valves closed.

A.5 Sensors

A.5.1 Vacuum system flow meter

A microbridge mass airflow sensor (Honeywell, AWM5104VN) with a 0 to 20 lpm range was installed in-line with the vacuum generator to monitor the suction flow rate (see Figure 3.13). The Honeywell flow meter was designed to nominally operate at 12 V, but accepted an upper limit of 15 V. Unfortunately, while the flow meter behaved ideally when supplied with 15 V DC from a highly regulated power supply, when supplied with 15 V from the Lambda switching power supply the flow meter response became erratic. After an investigation, it was discovered that the flow meter's built-in electronics are susceptible to the type of rapid voltage fluctuations that are typically produced in a switching power supply. This problem was rectified with two bypass capacitors which effectively filtered out the high frequency voltage fluctuations (McFarland, 2001). A 1 μF capacitor was placed across the 28 V aircraft supply terminals and a 0.33 μF capacitor was placed across the 15 V flow meter input supply terminals.

At 12 V, the flow meter provided a linear 1 to 5 V response for flows from 0 to 20 l min^{-1}. However, operation of the flow meter at 15 V changed the response voltages and prompted a new calibration. In the laboratory, a vacuum pump was used to draw air through the Honeywell flow meter while a Gilian Gilibrator-2 was placed in line to accurately measure the flow rate. In this configuration, the Honeywell flow meter output was linear between 1.40 V and 7.61 V for flow rates ranging from 0.21 to 28.5 l min^{-1}. The following equation was derived from the calibration data to convert output voltages (V) to flow rates (Q) in l min^{-1}:

$$Q = 4.502(\mathrm{V}) - 6.082 \qquad \text{(A.3)}$$

A.5.2 Canister temperature

The system temperature was monitored with a National Semiconductor LM35 integrated circuit temperature sensor. The LM35 sensor required a 5 V power supply, which was provided by a Fairchild Semiconductor LM7805 voltage regulator that reduced the voltage from the 15 V supply. The LM35 provided a 10 mV °C^{-1} response for temperatures in the range of 0 to 100° C, although additional circuitry was necessary for the sensor to operate in this configuration. As illustrated in Figure 3.15, this circuitry included two 1N914 diodes placed in series in the 5 V return line and a 75 Ω resistor in line with a 1 μF capacitor across the sensor's output terminals.

A.6 Actuation

A.6.1 Inlet cover motor

The inlet cover was closed by operating the 28 V DC motor in the clockwise direction, and opened by operating the motor in the counterclockwise direction. As with any DC motor, the direction of shaft rotation can be reversed simply by reversing the voltage potential across the motor leads. Reversing the voltage potential on demand was accomplished by incorporating a two pole, double throw (2 Form C) DC/DC relay (NAIS TXS2SA-4.5V) that could be switched with a 5 V signal produced by the data acquisition and control system. With the relay in the

unenergized position (no control voltage applied), the motor rotates in the clockwise direction to close the cover. When a 5 V control voltage is supplied to the relay, the relay reverses the voltage potential across the motor, and the motor rotates in the counterclockwise direction to open the cover. Two micro limit-switches were used to stop the inlet cover when the fully open or fully closed positions were reached. To protect the switches from inductively produced high voltage spikes that can occur as the motor is de-energized, 1N4000 diodes were placed across the terminals (McFarland, 2001).

In order to monitor the status of the inlet cover, a simple circuit was devised (see Figure 3.15). A 15 kΩ resistor was wired to each of the motor's supply leads and then to ground. If the motor was energized to rotate in the counterclockwise direction (to open the cover), a voltage drop would develop across one of the 15 kΩ resistors. If the motor was energized to rotate in the clockwise direction (to close the cover), a voltage drop would develop across the other 15 kΩ resistor. By including a 100 kΩ resistor in line with each of the 15 kΩ resistors, the current passing through the monitoring circuits was negligible, and the voltage drop across the 15 kΩ resistors was approximately 3.6 V, a value that was within the range of the data acquisition system. When the motor was not powered, the voltage drop across the 15 kΩ resistors was 0 V. By monitoring the voltages across the 15 kΩ resistors, the periods in which the inlet cover was in the process of opening or closing could be identified and recorded.

A.6.2 Storage system valves

Relays were also used to open the storage system valves as needed. One Crydom MODC5 solid state I/O switching module, essentially a DC control/DC output relay with photo-isolation and circuit protection, was used per valve. The high voltage side of each relay was in the normally open position, so that the 15 V circuit that provided power to the valve was broken and the valve remained closed. With the application of a 5 V control voltage to the relay, the 28

V circuit was closed, which energized the valve solenoid coil and opened the valve. The valve remained open as long as the 5 V control voltage was applied to the relay.

A.7 System wiring

Twenty three component lead wires pass into and out of the electronics enclosure through a sealed fitting: two lead wires extend from the housing to each of the storage system valves (purple), the inlet cover motor (brown), the micro switch that stops the inlet cover in the closed position (yellow), the micro switch that stops the inlet cover in the open position (green), and three wires extend to the flow meter (blue for the +15 V lead; green for the return lead; gray for the output voltage lead). The six wires running to the motor and two micro switches are bundled and have a 6-pin Molex disconnect fitting in line so that the inlet portion of the axial-flow cyclone (where motor and switches are mounted) can be detached from aluminum duct (where the electronics housing is mounted).

Also exiting the electronics housing through a sealed fitting is a bundle of 19 wires for data acquisition, control, and power that arrive from the aircraft cabin. In the bundle are eight wires that transmit 5 V control signals for relay actuation (blue), one digital I/O ground wire (purple), four pairs of wires that transmit analog data acquisition signals from the collection system (green for the temperature, flow meter, door closing monitor circuit; gray for the door opening monitor circuit), one 28 V power supply wire (white), and one 28 V return wire (black). This 19 wire bundle terminates in a 24 terminal Amphenol fitting (see Figure 3.10). The terminal numbers that correspond to the individual sensors, relays, and power supplies are presented in Figure 3.15. When the collection system is placed in the PMS canister, the Amphenol fitting is plugged into a corresponding fixed Amphenol fitting in the aft end of the canister which is held in place by a specially designed Lexan support bracket. Connected to the fixed Amphenol fitting is a short cable which travels through the PMS canister strut and into the C-130 instrumentation pod. There, the cable terminates in two Bendex fittings which plug into

the aircraft power and wiring system. One Bendex fitting attaches two wires to the aircraft DC power supply terminal and provides the 28 V DC power to the collection system. The second Bendex fitting connects the remaining 17 wires to another cable that traverses the interior of the wing and terminates in the aircraft cabin at which point it attaches to a specially designed wiring harness and LabVIEW terminal board.

A.8 Analog data acquisition

The DAQCard analog inputs are used in their double ended configuration, in which the voltage potential between a pair of wires is measured. In this configuration, the signal voltage is being measured as a voltage differential rather than as a single voltage relative to ground. Due to the distance between signal generation in the PMS canister and signal acquisition in the cabin, double ended inputs are recommended to avoid complications caused by ground level voltage variations between the two locations. However, even in the differential measurement mode, LabVIEW references the ground potential of the computer on which it is running and requires that the ground potential of any signal generator (i.e. flow meter, temperature sensor, etc.) not differ greatly from the computer ground. Luckily on the NSF/NCAR C-130, the AC power supplying the laptop computer shares a common ground with the DC power supplying the sensors in the collection system. Unfortunately, a shared ground is not used on all research aircraft, and additional circuitry in the form of bias resistors may need to be incorporated into the electronics of the collection system if that is the case.

Appendix B. Axial-flow cyclone design drawings

Appendix B contains design drawings for the major components of the axial-flow cyclone cloud water collector. Design drawings for the remaining collector parts, including the fasteners, bearings, and linkages comprising the inlet cover system, are available but have not been included here due to space considerations. All of the design drawings were generated at NCAR's Design and Fabrication Services (DFS). The original design drawing files are archived at the DFS.

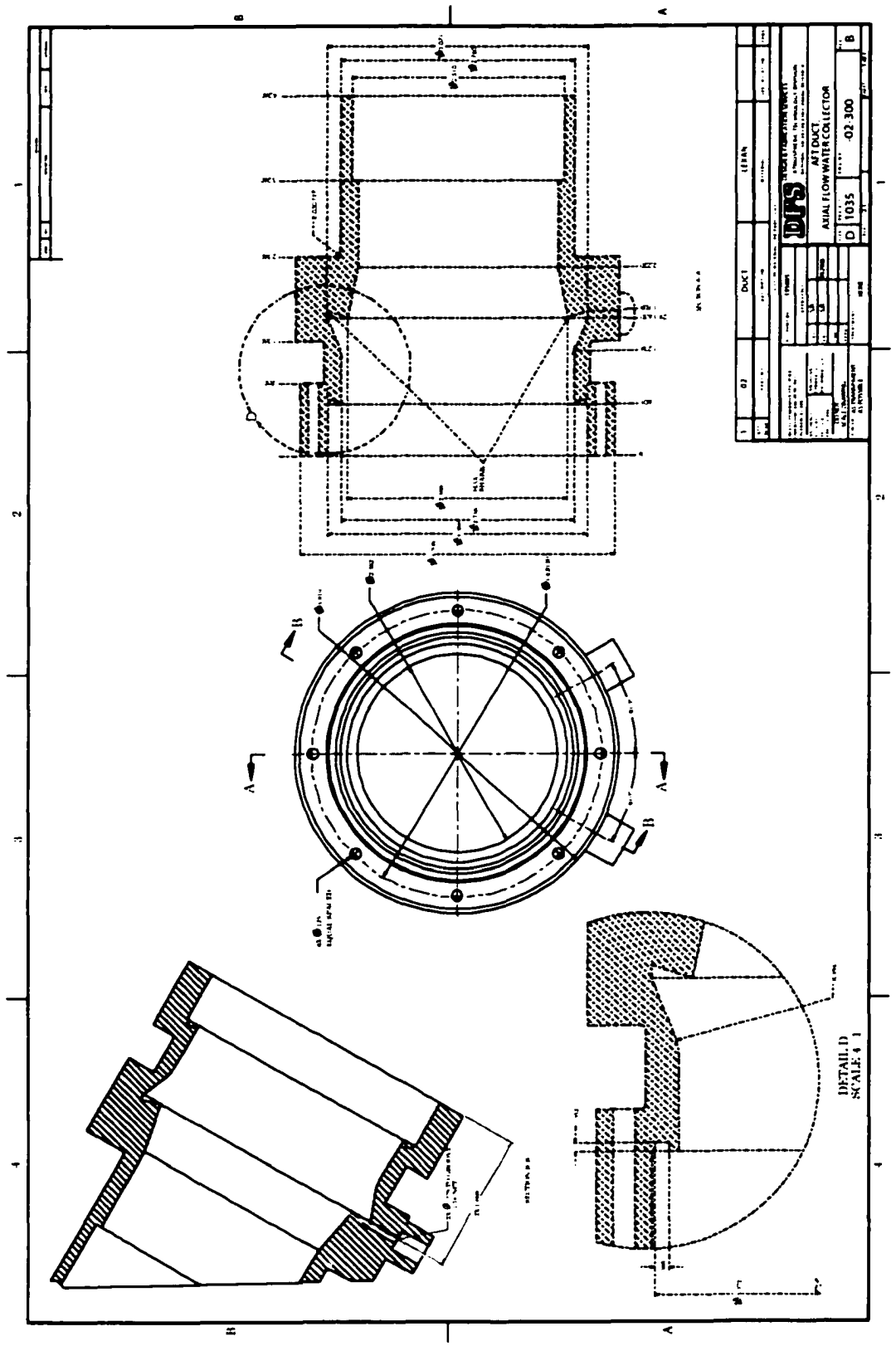

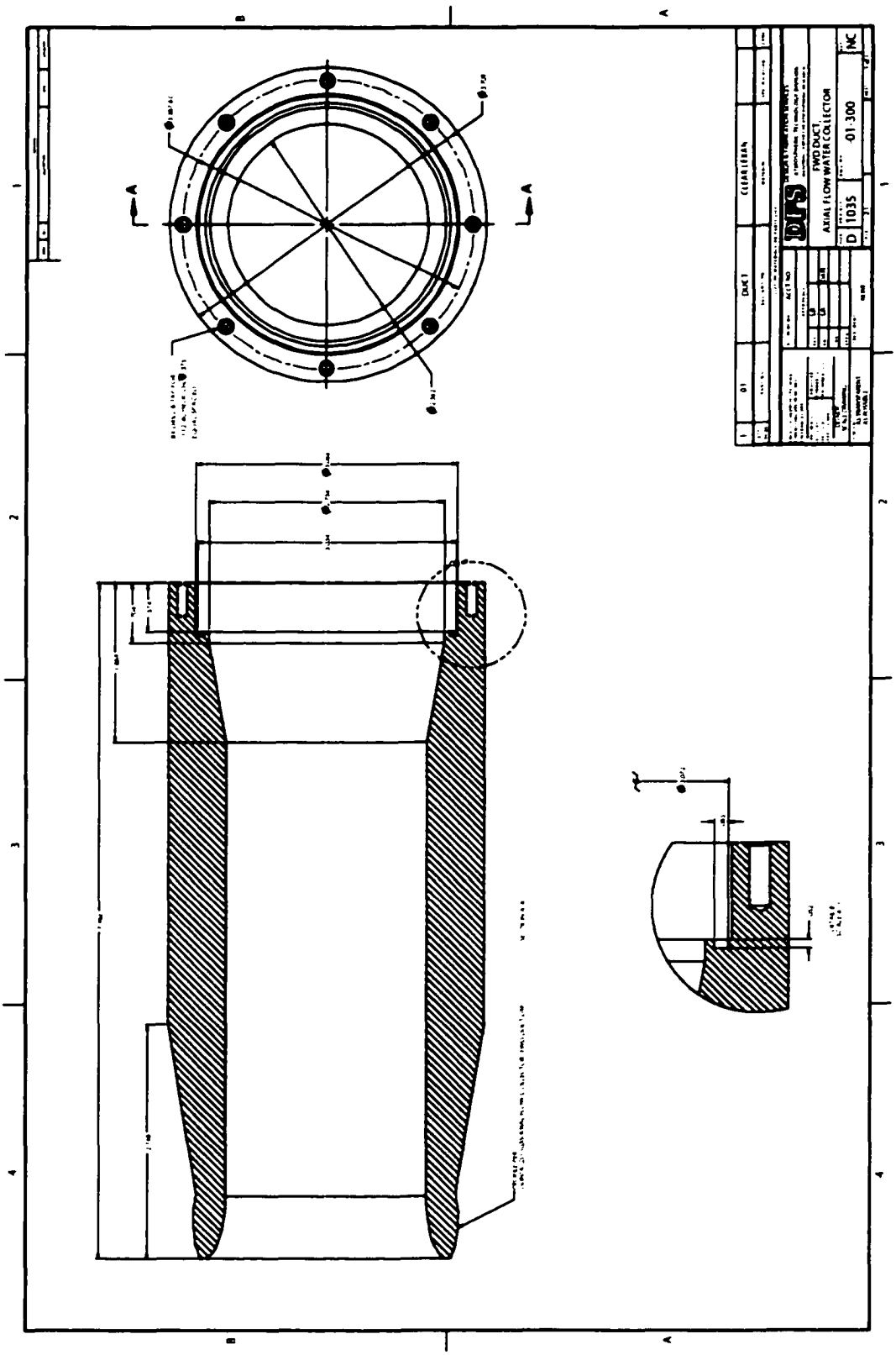

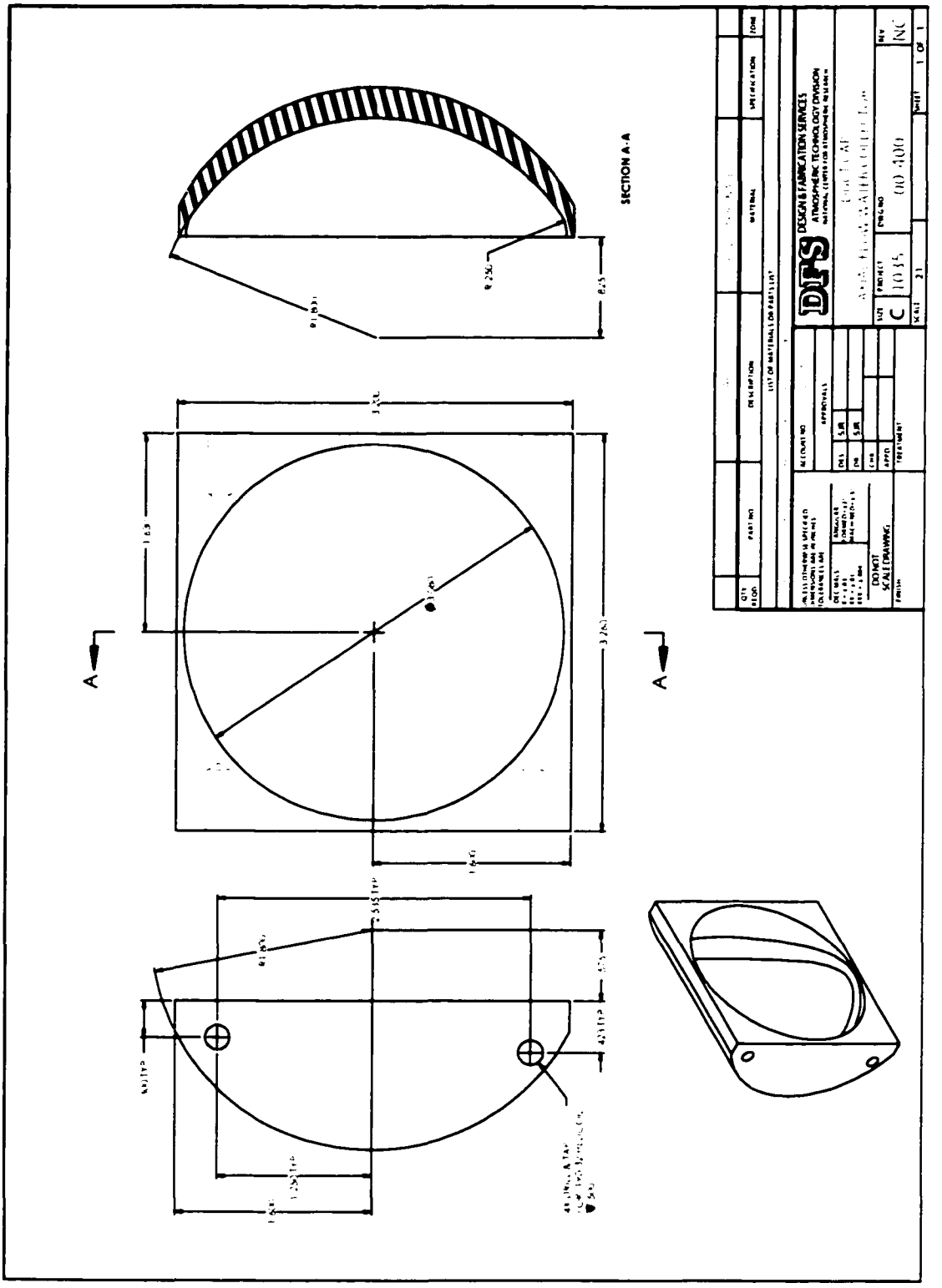

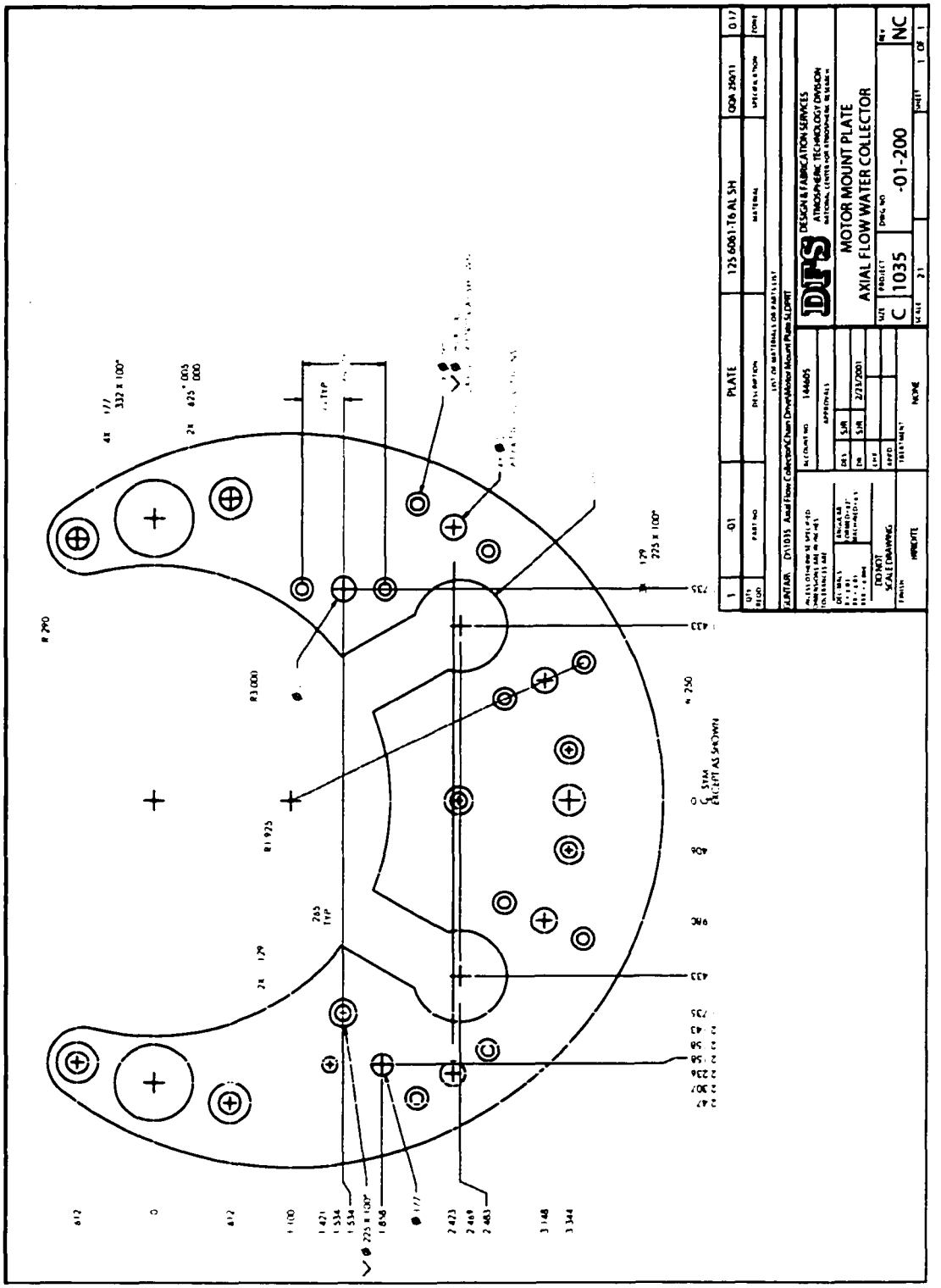

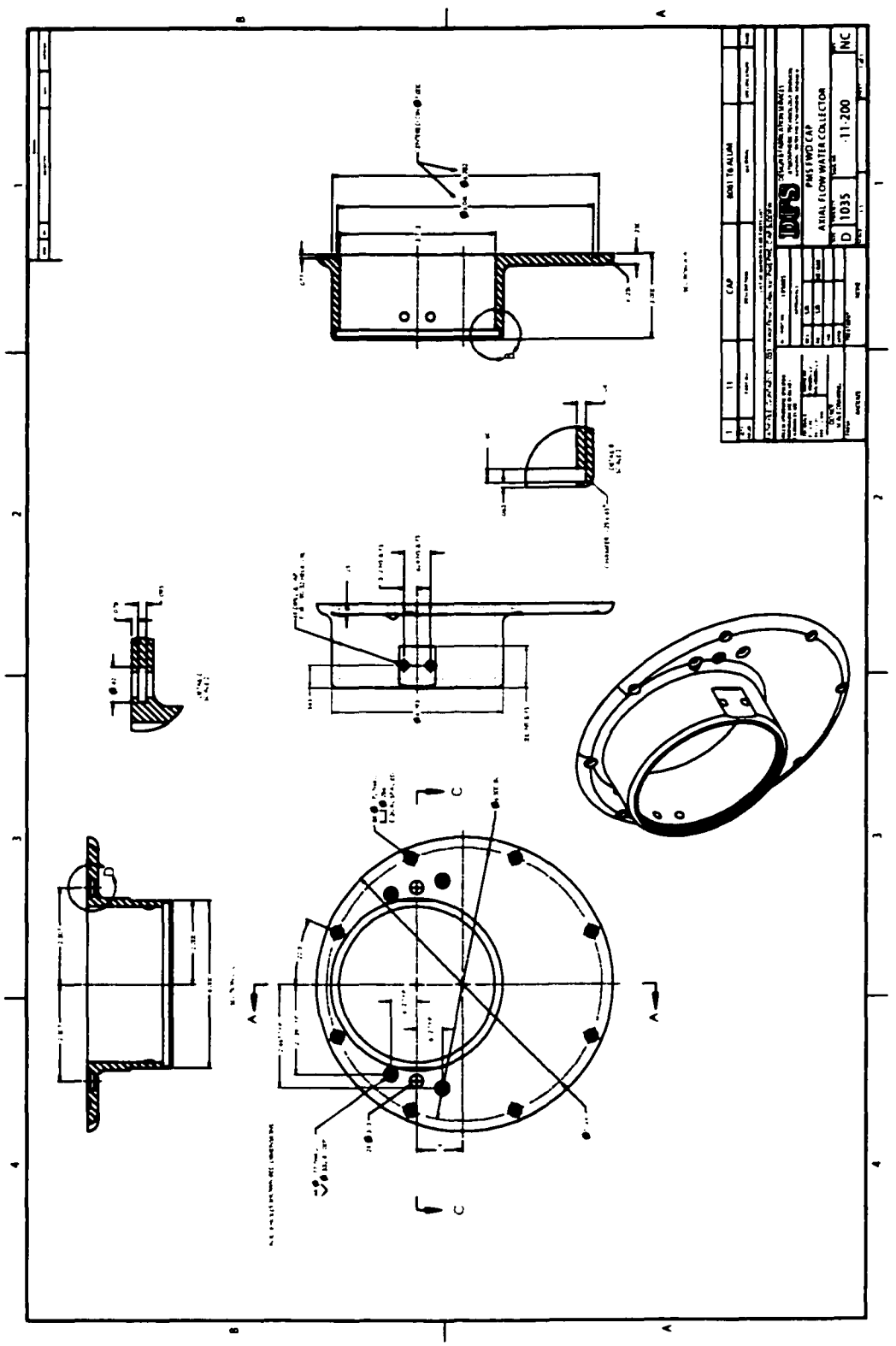

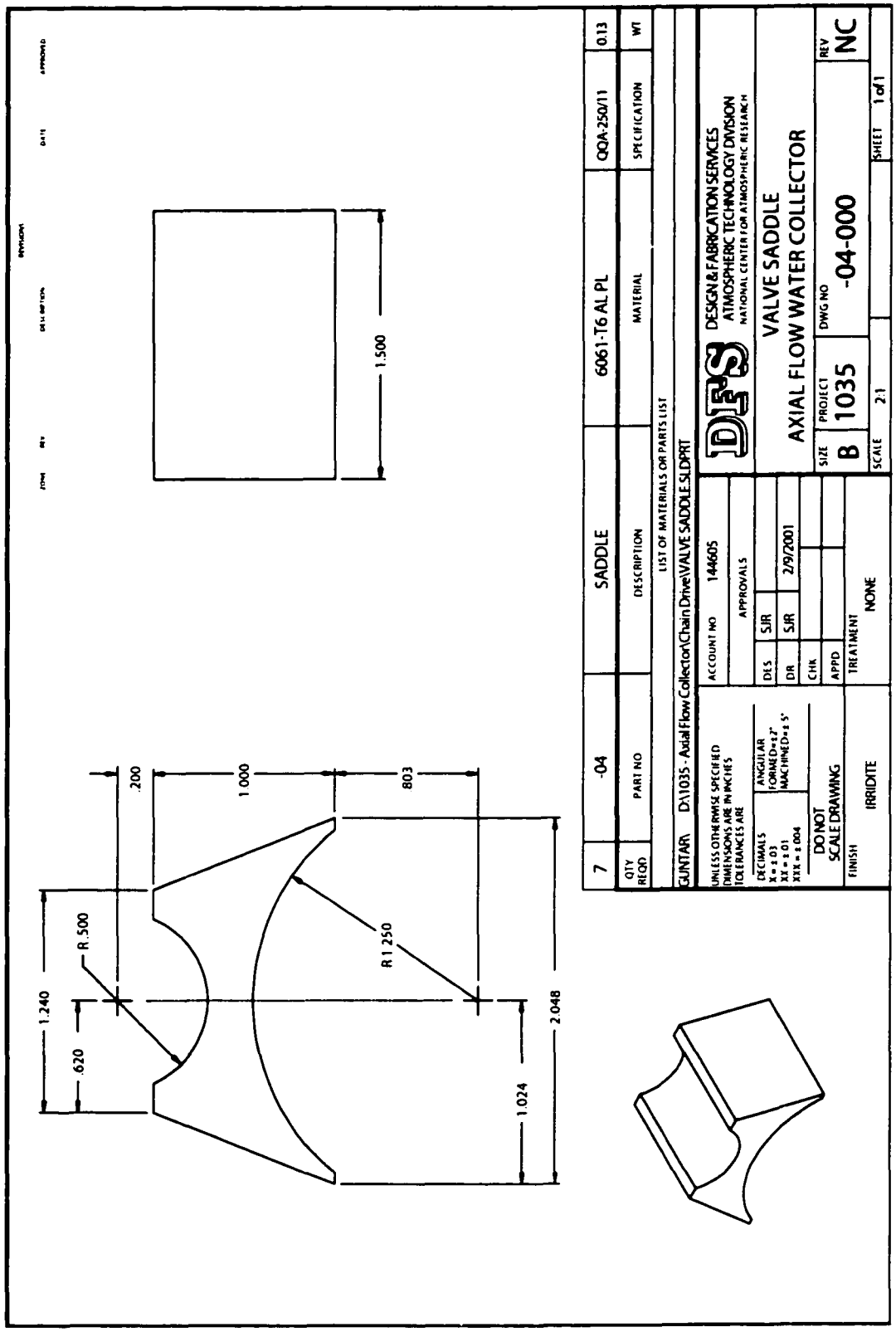

Appendix C. Axial-flow cyclone operating procedures and DYCOMS-II sample handling protocol

C.1 PMS canister modifications required for system installation

The cloud water collection system can be mounted in any PMS aircraft canister without removal of the canister from the aircraft. The forward and aft standard end caps must first be removed. The canister electrical connectors, which consist of two Amphenol fittings, must be repositioned in order to accommodate the axial-flow cyclone. The two Amphenol fittings are first detached from the standard aluminum mounting plate at the aft end of the canister. The standard aluminum plate is then removed from the canister and replaced with a custom Lexan mounting plate (Figure C.1). The Lexan plate contains an opening through which the axial-flow

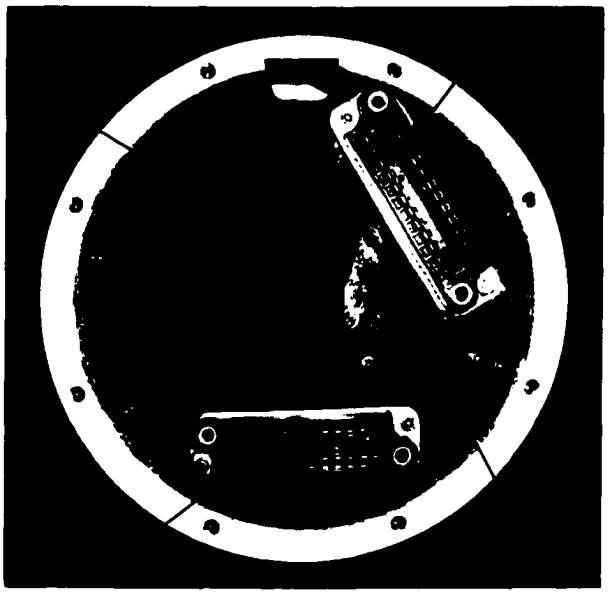

Figure C.1. Aft end view of canister without cloud water collection system installed showing Lexan mounting plate for Amphenol fittings.

cyclone duct can pass as well as mounting locations for the Amphenol fittings. The Lexan plate is secured inside the aft edge of the PMS canister with three brackets. One of the Amphenol fittings faces the rear of the canister so that the axial-flow cyclone electronics can be conveniently connected to the aircraft wiring system when the cloud water collector is installed.

C.2 Installation and removal procedures

For ease of installation and removal, the cloud water collection system consists of a single, self-contained structure. The entire structure can easily slide into and out of a PMS canister between flights to allow access to the system for sample removal and cleaning. The PMS canister requires some minor modifications (described above), after which the collection system can be installed.

In preparation for the installation of the collection system on the C-130 aircraft, the data acquisition and control wire bundle is temporarily stowed by placing the Amphenol fitting in the aluminum duct outlet. The structure of the cloud water collector can then be simply inserted into the front end of the PMS canister with the inlet positioned in the upper right quadrant of the canister. With the axial-flow cyclone duct situated in the upper right quadrant of the canister, the aluminum duct will pass through the opening in a Lexan plate that is mounted in the aft end of the canister. The collector is pushed into the canister until the front end cap contacts the front end of the canister at which point eight 8-5/8"stainless steel hex head bolts are used to secure the forward end cap to the canister.

After the Amphenol fitting is withdrawn from the aluminum duct it can be plugged into the fixed Amphenol fitting mounted on the Lexan plate. The aft end cap is then slipped over the axial-flow cyclone aluminum exit duct that protrudes from the aft end of the canister. The vacuum system quick disconnect fitting is then reconnected to complete the flow path from the scarf tube to the vacuum generation system. Finally, the excess vacuum system tubing and

excess control wiring is tucked into the aft end cap which can then be secured to the canister with eight 8-3/4"stainless steel hex head bolts. Removing the collector from the aircraft is accomplished by repeating these steps in the reverse order.

C.3 Cleaning and blank procedures

When the collection system is removed from the aircraft after sampling, it is placed in a specially designed stand for transport and servicing. The sample bottles are removed and the collector can be cleaned in preparation for subsequent flights. Before cleaning the collector, the polycarbonate portion of the axial-flow cyclone duct (containing most of the surfaces that are exposed to cloud water during sampling including the inlet, vane unit, and extraction slot) is separated from the aluminum duct to allow access to the curved vane assembly and extraction slot. To do this, the motor and microswitch lead wires must be disconnected at the Molex fitting and the sample transfer line must be disconnected at the compression fitting attached to the first Teflon valve.

After the polycarbonate section is separated from aluminum duct, the inlet cover can be opened and the entire assembly can be liberally flushed with DI water. The sample lines and valves can also be flushed by drawing DI water through the storage system sample transfer line and through each valve as they are sequentially opened. Separate blanks are typically taken from the polycarbonate duct and from the sample storage system after the washing procedure. The collector can then be reassembled and new sample storage bottles installed, using Teflon tape on the threads to provide an air tight seal. The collection system is then ready to be reinstalled on the aircraft following the procedures described in Section C.2. The detailed protocol developed for the removal and cleaning of the cloud water collection system is described below.

1. Removal of collector from aircraft

    • remove 8 bolts from canister aft closure and place bolts in a storage container

- disconnect vacuum line at the quick disconnect fitting
- disconnect electrical connection (Amphenol fitting) by first removing the nut on the right hand side and then pulling the fitting from its socket
    - place fitting inside collector exit duct so that it is out of the way
- remove canister aft closure by sliding it off exit duct
- remove 8 bolts from canister forward closure and place bolts in a storage container
- gently slide collector out from the front end of the canister and place in stand

2. Remove sample bottles
    - individually remove sample bottles from collector and cap with appropriate, matching cap (caps that have been pre-weighed with bottles prior to flight)
    - place a set of 7 "cleaning" bottles on collector
    - prepare aliquots from each bottle according to the Sample Handling and Aliquot Protocol (Section C.3)

3. Separate polycarbonate section of duct (inlet section and extraction slot section) from aluminum duct
    - disconnect motor electrical connection (6-pin white Molex connector)
    - remove electrical wiring straps (plastic wire ties) that secure extra wiring to aluminum duct
    - disconnect sample line compression fitting at valve #1 and cover both ends with parafilm
    - loosen hose clamps and slide polycarbonate duct from aluminum duct

4. Clean interior surfaces of axial-flow cyclone duct

- attach 28V power supply (+28 V and return) to motor leads at Molex connector to open inlet cover
- using a spray bottle, hold polycarbonate section upside down over a plastic tub and spray DI liberally into the aft end toward aft end of vane assembly
    - if necessary, use toothbrush or cotton swabs to clean surfaces
- place polycarbonate section (and everything attached) on short stainless steel duct and place (with inlet up) in plastic tub
- using a spray bottle, spray DI water liberally into inlet
    - if necessary, use toothbrush or cotton swabs to clean surfaces

5. Take blank from axial-flow cyclone interior surfaces

- place polycarbonate section in stand (angled downward a bit to allow water sprayed into inlet to flow to extraction ring)
- attach sample distribution line (extending from extraction slot) to large separator bottle (separator bottle is a 500 ml bottle with fittings that are identical to the smaller sample storage bottles on the collector)
- attach 2nd fitting on separator bottle to small vacuum pump (~ several l min^{-1} capacity) and turn pump on (this will draw air and water from extraction slot and into separator bottle)
- using a spray bottle, spray DI water into inlet
- allow water to run into extraction ring where it will be removed to separator bottle
- collect blank sample from separator bottle
- place polycarbonate section on short SS duct and allow to dry

6. Clean sample lines and storage bottles

- attach a short length of Teflon tubing to the compression fitting attached to valve #1 and place free end of tubing into a large bottle of DI water
- attach small vacuum pump (~ several l min^{-1} capacity) to vacuum line at the quick disconnect fitting attached to the flow meter
- connect electrical fitting (Amphenol) to NI terminal block
    - terminal block is plugged into DAQcard in laptop computer via 68 pin NI cable
    - connect white lead from terminal block to +28 V terminal on regulated power supply
    - connect black lead from terminal block to return terminal on regulated power supply
- clean valve #1
    - turn small vacuum pump on
    - open valve #1 (using LabVIEW)
    - wait until ~ 100 ml of DI water is drawn into bottle #1
    - close valve #1
    - remove bottle #1 and dump out water
    - replace bottle #1 and draw additional DI into that bottle by opening and closing valve #1
    - repeat above procedure for remaining six bottles

7. Take blanks from sample lines and storage bottles
    - place "blank" bottles on collector and draw ~ 100 ml DI into each bottle by sequentially opening Teflon valves (using LabVIEW)
    - when blanks from all bottle positions are taken, combine blanks into one single blank
        - take 10 ml of water from each blank bottle and place in a single, clean bottle that has been labeled

- replace "cleaning" bottles on collector, remove Teflon line from large bottle of DI, and draw air through each valve (by sequentially opening valves) to dry
- weigh and label 7 new, clean bottles and place on collector for following flight
    - use Teflon tape on bottle threads to eliminate leaks

8. Reassemble collector
    - attach 28V power supply (+28 V and return) to motor leads at Molex connector to close inlet cover
    - slide polycarbonate section onto aluminum duct (line up alignment marks) and tighten hose clamps
    - reconnect motor electrical connection (6-pin white Molex connector)
    - strap electrical wiring into place with 2 plastic wire ties
    - reconnect sample distribution line (from extraction slot) at valve #1 compression fitting
    - place Amphenol electrical fitting into collector duct exit to aid in collector installation on aircraft
    - place collector in specially designed stand for transport to aircraft

9. Place collector on aircraft
    - remove collector from stand and gently slide collector (exit duct first) into canister
        - make sure exit duct and wiring clears the aft end Lexan support bracket
    - attach canister forward closure to canister by inserting and tightening 8 bolts
    - at aft end of canister:
        - connect vacuum line at the quick disconnect fitting
        - connect electrical connection (Amphenol fitting)
    - attach canister aft closure to canister by inserting and tightening 8 bolts

C.4 DYCOMS-II sample handling protocol

1. Record sample name, start time, and finish time on log sheet
    - note times during flight
    - use UTC as reference
2. Weigh sample in bottle and record
    - label and weigh empty bottles prior to flight
    - make sure outside of bottle is dry
    - make sure scale is zeroed
3. pH measurement
    - place one 1.5 ml PE microcentrifuge vial into holder
    - pipette 0.5 ml of sample into vial
    - rinse pH electrode with DI water. Touch tip of electrode to clean beaker or pipette tip to remove excess DI.
    - if sufficient sample is available, rinse electrode with approximately 40 µl of sample.
    - place electrode into the sample, making sure it is in contact with the sample
    - record the pH (and measurement time) on log sheet when reading has stabilized. The meter will beep and show "ready" on the display.
    - rinse electrode with DI water and return to 4.01 buffer solution or vial of retained sample.
    - check the calibration of the pH electrode before the preparation of every set of aliquots (after every flight)
4. IC
    - pipette 500 µl of sample into a PP autosampler vial

- seal vial using the lid with a Teflon septum. Do not over tighten the lid. Do not use the septumless tops.
- label vial (sample name plus "IC") and record on log sheet. Note if aliquot is less than 500 µl.

5. S(IV)
   - pipette 1.0 ml of sample into a 1.5 ml glass vial with Teflon-lined cap (Wheaton 224800)
   - add 100 µl S(IV) PRESERVATION SOLUTION
   - add 100 µl CATALASE SOLUTION
   - close cap and mix completely
   - label vial (sample name plus "S(IV)") and record on log sheet
6. Peroxides
   - pipette 1.0 ml of sample into a 1.5 ml glass vial with Teflon-lined cap (Wheaton 224800)
   - add 200 µl CONDITIONING REAGENT
   - add 200 µl FLUORESCENT REAGENT
   - close cap and mix completely
   - label vial (sample name plus "H2O2") and record on log sheet
7. Metals
   - pipette 1.0 ml of sample into a 1.2 ml cryovial
   - add 100 µl 9.7% HNO_3 SOLUTION
   - close cap and mix completely
   - label vial (sample name plus "Metals") and record on log sheet
8. HCHO (Formaldehyde)
   - pipette 1.0 ml of sample into a 1.5 ml glass vial with Teflon-lined cap (Wheaton 224800)

- add 100 µl HCHO PRESERVATIVE SOLUTION
- close cap and mix completely
- label vial (sample name plus "HCHO") and record on log sheet

9. TOC
    - fill (minimum ~5 ml) 15 ml glass vial
    - close cap and label vial (sample name plus "TOC") and record on log sheet
10. Duplicates
    - if sufficient time and sample permits, a duplicate of each type of aliquot should be made per flight.
    - label vial (sample name plus "aliquot type" plus DUP)
11. Peroxidase and Catalase Checks
    - perform for each set of aliquots (after every flight)
    - Peroxidase activity check:
        - pipette 1.0 ml DI into a 1.5 ml glass vial
        - add 100 µl 1.0 mM H2O2 SOLUTION
        - add 200 µl CONDITIONING REAGENT
        - add 200 µl FLUORESCENT REAGENT
        - close cap and mix completely
        - label with date and "PerChk"
    - Catalase activity check:
        - pipette 1.0 ml DI into a 1.5 ml glass vial
        - add 100 µl 1.0 mM H2O2 SOLUTION
        - add 100 µl CATALASE SOLUTION
        - mix completely
        - add 200 µl CONDITIONING REAGENT
        - add 200 µl FLUORESCENT REAGENT

- close cap and mix completely
- label with date and "CatChk"

12. Sample Storage
    - aliquots and samples should be refrigerated as soon as possible
    - aliquot chemicals should be refrigerated as soon as possible
    - keep track of which set of aliquot chemicals are being used
        - record on log sheet

Appendix D. Tabulated DYCOMS-II sample period data

sample name	sample date	sample start time GMT	sample end time GMT	sample duration min	altitude m	approximate height above cloud base[b] m
RF2-1	7/10/2002	9:34:02	9:47:13	11.28[a]	476	176
RF2-2	7/10/2002	11:07:35	11:21:35	14.00	633	233
RF2-3	7/10/2002	11:21:40	11:34:51	13.18	632	232
RF2-4	7/10/2002	11:35:00	11:47:21	12.35	633	233
RF2-5	-	-	-	-	-	-
RF2-6	7/10/2002	11:47:32	12:00:57	13.42	632	232
RF2-7	7/10/2002	12:01:07	12:12:25	11.30	631	231
RF3-1	7/11/2002	8:28:08	8:42:34	14.43	327	2
RF3-2	7/11/2002	8:44:38	9:22:35	17.52[a]	328	3
RF3-3	7/11/2002	10:04:41	10:15:20	10.65	479	154
RF3-4	7/11/2002	10:15:24	10:24:49	9.42	480	155
RF3-5	7/11/2002	10:24:53	10:37:11	12.30	481	156
RF3-6	7/11/2002	10:37:21	10:48:36	11.25	478	153
RF3-7	7/11/2002	10:48:57	11:03:41	14.73	478	153
RF4-1	7/13/2002	8:34:19	8:58:03	23.73	644	94
RF4-2	7/13/2002	8:58:18	9:26:35	28.28	644	94
RF4-3	7/13/2002	11:29:02	11:40:15	11.22	906	356
RF4-4	7/13/2002	11:40:20	11:52:35	12.25	906	356
RF4-5	7/13/2002	11:52:44	12:06:58	14.23	908	358
RF4-6	7/13/2002	12:07:19	12:18:53	11.57	906	356
RF4-7	7/13/2002	12:19:02	12:31:26	12.40	914	364
RF5-1	7/18/2002	8:21:13	9:02:27	41.23	687	87
RF5-2	7/18/2002	11:01:08	11:18:04	16.93	738	88
RF5-3	7/18/2002	11:18:09	11:37:22	19.22	741	91
RF5-4	7/18/2002	11:37:32	12:01:32	24.00	740	90
RF5-5	-	-	-	-	-	-
RF5-6	-	-	-	-	-	-
RF5-7	-	-	-	-	-	-
RF6-1	7/20/2002	8:15:49	8:30:20	13.17[a]	586	411
RF6-2	-	-	-	-	-	-
RF6-3	7/20/2002	8:53:47	9:12:22	18.58	273	98
RF6-4	7/20/2002	10:38:25	10:40:51	2.43	622	247
RF6-5	7/20/2002	11:18:13	11:27:27	9.23	703	328
RF6-6	7/20/2002	11:27:43	11:39:46	12.05	703	328
RF6-7	7/20/2002	12:34:42	12:48:23	13.68	482	107

sample name	sample date	sample start time GMT	sample end time GMT	sample duration min	altitude m	approximate height above cloud base[b] m
RF7-1	7/24/2002	8:52:29	9:20:33	28.07	434	134
RF7-2	7/24/2002	9:20:42	9:52:56	32.23	434	134
RF7-3	7/24/2002	11:38:34	11:51:06	12.53	701	401
RF7-4	7/24/2002	11:51:20	12:04:00	12.67	699	399
RF7-5	7/24/2002	12:04:12	12:16:47	12.58	682	382
RF7-6	7/24/2002	12:17:01	12:29:52	12.85	664	364
RF7-7	7/24/2002	12:29:58	12:42:16	12.30	661	361
RF8-1	7/25/2002	22:16:21	22:37:05	20.73	435	135
RF8-2	7/25/2002	22:37:10	22:55:10	18.00	454	154
RF8-3	7/25/2002	22:55:14	23:19:13	23.98	474	174
RF8-4	7/26/2002	2:44:07	2:59:58	15.85	483	183
RF8-5	7/26/2002	3:00:06	3:15:24	15.30	484	184
RF8-6	7/26/2002	3:15:35	3:30:11	14.60	510	210
RF8-7	7/26/2002	3:30:16	3:39:13	8.95	509	209
RF9-1	-	-	-	-	-	-
RF9-2	7/27/2002	21:33:26	21:53:24	19.97	524	199
RF9-3	7/27/2002	21:53:28	22:06:34	13.10	504	179
RF9-4	7/27/2002	22:08:05	22:43:43	35.63	388	63
RF9-5	7/28/2002	0:23:10	0:43:18	20.13	547	222
RF9-6	7/28/2002	0:43:28	0:54:48	11.33	544	219
RF9-7	7/28/2002	0:55:06	1:34:04	38.97	397	72

sample name	volume mean diameter[c] μm	cloud drop # concentration[c] N cm^{-3}	PVM LWC g m^{-3}	horizontal wind speed m s^{-1}	ambient temperature ° C	TAS m s^{-1}
RF2-1	16.6	48.6	0.143	7.8	12.0	108.4
RF2-2	21.0	69.9	0.332	8.3	11.2	108.3
RF2-3	25.2	51.3	0.353	7.6	11.2	108.8
RF2-4	21.6	75.5	0.374	7.2	11.5	108.2
RF2-5	-	-	-	-	-	-
RF2-6	25.6	46.5	0.330	7.5	11.2	109.4
RF2-7	20.0	81.2	0.325	6.9	11.2	109.2
RF3-1	10.8	323.2	0.285	12.3	12.6	107.0
RF3-2	10.4[d]	234.9[d]	0.219	11.9	12.6	108.7
RF3-3	13.1[d]	262.4[d]	0.455	12.1	12.1	108.9
RF3-4	12.7[d]	291.0[d]	0.501	11.5	12.0	109.2
RF3-5	14.5[d]	170.3[d]	0.403	12.1	12.1	109.0
RF3-6	13.5[d]	151.8[d]	0.400	11.1	12.2	109.5
RF3-7	12.0	317.2	0.553	12.4	12.2	109.6

sample name	volume mean diameter[c] μm	cloud drop # concentration[c] N cm^{-3}	PVM LWC g m^{-3}	horizontal wind speed m s^{-1}	ambient temperature °C	TAS m s^{-1}
RF4-1	10.0[d]	224.1[d]	0.180	6.5	11.1	108.5
RF4-2	11.2[d]	198.8[d]	0.241	5.8	11.3	109.7
RF4-3	n/a[e]	n/a[e]	0.640	4.7	9.9	111.4
RF4-4	n/a[e]	n/a[e]	0.622	5.9	9.9	112.5
RF4-5	18.2[d]	160.4[d]	0.660[f]	5.1	10.2	110.8
RF4-6	16.8[d]	192.9[d]	0.622[f]	5.2	9.8	110.3
RF4-7	n/a[e]	n/a[e]	0.643[f]	5.8	9.8	109.5
RF5-1	n/a[e]	n/a[e]	0.133	8.9	9.5	109.8
RF5-2	n/a[e]	n/a[e]	0.261	8.5	10.0	109.0
RF5-3	n/a[e]	n/a[e]	0.257	8.5	9.8	108.0
RF5-4	n/a[e]	n/a[e]	0.271	8.2	9.8	109.4
RF5-5	-	-	-	-	-	-
RF5-6	-	-	-	-	-	-
RF5-7	-	-	-	-	-	-
RF6-1	n/a[e]	n/a[e]	0.447	7.4	12.6	108.9
RF6-2	-	-	-	-	-	-
RF6-3	n/a[e]	n/a[e]	0.123	7.4	13.7	107.9
RF6-4	n/a[e]	n/a[e]	0.516	8.0	11.3	109.0
RF6-5	n/a[e]	n/a[e]	0.533	7.4	10.6	109.1
RF6-6	n/a[e]	n/a[e]	0.517	7.7	10.6	108.8
RF6-7	n/a[e]	n/a[e]	0.224	7.7	12.0	109.1
RF7-1	14.9	124.0	0.279	7.2	12.6	109.3
RF7-2	13.9	139.2	0.292	7.4	12.5	108.4
RF7-3	19.6	145.2	0.668	6.6	11.2	108.8
RF7-4	20.9	125.0	0.603	7.0	11.3	109.0
RF7-5	18.8	153.9	0.660	7.0	11.4	109.7
RF7-6	19.3	125.8	0.580	7.4	11.4	107.3
RF7-7	18.9	136.7	0.602	7.0	11.3	108.2
RF8-1	15.2	93.8	0.241	5.7	12.9	107.9
RF8-2	15.0	117.1	0.302	6.0	12.8	108.7
RF8-3	16.0	110.2	0.334	5.8	13.0	108.4
RF8-4	16.8	137.3	0.411	5.2	12.7	107.0
RF8-5	16.6	140.7	0.451	6.5	12.5	108.3
RF8-6	17.5	127.6	0.479	5.3	12.3	107.5
RF8-7	19.4	96.1	0.477	6.4	12.5	107.9
RF9-1	-	-	-	-	-	-
RF9-2	13.4	222.0	0.386	5.3	12.4	111.7
RF9-3	13.0	214.1	0.362	5.6	12.4	111.3
RF9-4	9.9	204.7	0.133	5.4	12.9	109.9
RF9-5	12.4	254.3	0.430	3.9	12.2	111.0
RF9-6	12.1	242.8	0.397	4.3	12.1	110.9
RF9-7	8.5	283.4	0.121	8.8	12.8	110.2

[a]sample period consists of two individual periods

[b]approximated from C-130 profile leg data

[c]derived from SPP-100 data

[d]SPP-100 failed intermittantly during these sample periods

[e]SPP-100 failed completely during these sample periods

[f]PVM LWC unavailable for RF04-5 through RF04-7 sample periods, Hot Wire LWC used instead

Appendix E. Tabulated DYCOMS-II cloud water composition

sample name	sample volume collected	pH	Chloride	Nitrate	Sulfate	Sodium	Ammonium	Potassium	Magnesium	Calcium
	ml	-	µN	µN	µN	µN	µN	µN	µN	µN
RF2-1	0.77	3.99	269.5	131.1	45.4	277.5	34.9	4.8	69.5	64.0
RF2-2	5.75	4.28	449.9	26.6	94.9	441.5	0.5[a]	9.7	103.6	35.5
RF2-3	15.33	4.82	67.6	3.1	15.0	60.1	0.5[a]	1.0	14.9	9.4
RF2-4	6.65	4.26	179.9	9.4	38.6	163.1	0.5[a]	3.0	35.5	15.4
RF2-5	-	-	-	-	-	-	-	-	-	-
RF2-6	14.98	4.61	80.2	4.6	16.7	74.3	0.5[a]	1.2	14.0	9.7
RF2-7	4.47	4.33	158.9	6.3	28.3	152.4	7.8	3.0	29.5	12.8
RF3-1	4.94	3.87	856.5	55.2	195.0	750.8	51.2	18.3	207.5	82.1
RF3-2	5.13	3.61	1682.8	69.4	342.7	1505.3	52.2	35.0	378.0	134.6
RF3-3	4.51	3.77	1090.3	35.3	199.9	951.3	11.0	21.5	254.7	77.9
RF3-4	4.18	3.87	624.0	30.1	113.9	573.2	22.8	12.2	147.9	47.4
RF3-5	2.31	3.73	1269.0	26.7	179.0	1088.4	25.5	24.8	289.4	99.9
RF3-6	1.4	3.54	1351.1	26.0	201.0	1183.2	27.7	27.2	321.4	119.3
RF3-7	5.11	3.94	1186.3	30.7	191.1	1058.3	25.7	24.3	269.2	77.3
RF4-1	4.29	3.59	585.6	39.6	307.7	481.5	29.9	11.0	153.7	71.3
RF4-2	5.82	3.64	545.9	37.1	229.4	453.9	15.4	9.6	139.1	50.3
RF4-3	11.56	4.09	235.4	18.9	83.6	222.0	0.5[a]	4.2	59.5	20.1
RF4-4	10.83	4.12	253.2	15.1	75.8	231.2	3.6	4.8	62.1	20.9
RF4-5	15.5	4.21	169.8	11.8	53.7	158.9	1.7	2.9	39.6	15.3
RF4-6	8.97	4.28	190.3	13.9	61.4	172.9	6.9	3.7	47.7	17.3
RF4-7	11.2	4.19	210.1	15.8	65.2	195.7	6.5	4.0	55.9	19.6
RF5-1	4.7	3.43	1787.4	51.4	523.0	1632.6	36.1	37.3	419.8	142.8
RF5-2	2.9	3.56	1694.9	48.7	451.5	1536.9	21.1	34.7	408.7	131.9
RF5-3	3.58	3.86	1212.3	19.8	266.9	1059.9	11.4	23.5	283.3	82.3
RF5-4	4.47	3.82	1050.5	21.1	260.4	942.2	12.1	21.0	260.4	89.0
RF5-5	-	-	-	-	-	-	-	-	-	-
RF5-6	-	-	-	-	-	-	-	-	-	-
RF5-7	-	-	-	-	-	-	-	-	-	-

[a]below detection limit

sample name	sample volume collected ml	pH -	Chloride µN	Nitrate µN	Sulfate µN	Sodium µN	Ammonium µN	Potassium µN	Magnesium µN	Calcium µN
RF6-1	11.7	4.32	172.8	3.1	32.5	155.6	0.5[a]	2.9	31.8	12.0
RF6-2	-	-	-	-	-	-	-	-	-	-
RF6-3	1.78	3.79	2502.1	37.2	482.6	2784.1	0.5[a]	58.6	566.0	187.6
RF6-4	1.33	3.97	918.9	7.9	177.3	823.6	0.5[a]	17.8	213.2	61.0
RF6-5	3.98	4.23	657.8	10.4	125.4	584.6	0.5[a]	12.1	146.6	43.2
RF6-6	5.97	4.26	511.4	9.1	95.6	457.7	0.5[a]	10.2	117.5	32.7
RF6-7	1.02	4.03	602.3	11.3	111.4	526.7	0.5[a]	11.1	147.5	44.8
RF7-1	4.72	3.88	311.3	13.2	74.0	275.7	9.6	5.9	78.4	33.5
RF7-2	6.41	4.07	288.1	14.8	76.9	268.1	6.3	5.7	73.3	22.1
RF7-3	14.83	4.43	131.8	5.4	28.3	119.2	0.5[a]	2.3	24.9	10.7
RF7-4	15.33	4.47	101.6	5.3	23.1	93.2	0.5[a]	1.8	19.7	10.0
RF7-5	14.98	4.48	86.9	5.8	22.0	76.7	1.8	1.5	18.1	9.2
RF7-6	12.74	4.46	96.9	5.2	22.4	89.0	1.8	1.9	18.4	9.1
RF7-7	10.64	4.45	152.9	5.9	30.2	139.8	2.3	2.9	31.6	11.4
RF8-1	2.63	3.92	99.9	30.8	107.8	95.6	33.8	2.4	33.4	21.4
RF8-2	3.44	3.98	78.9	28.2	89.2	76.4	18.3	1.3	27.5	14.9
RF8-3	6.67	4.15	63.9	19.5	57.7	61.5	10.8	1.0	20.7	11.6
RF8-4	4.18	4.11	89.2	18.1	62.2	90.8	7.8	1.3	26.2	14.0
RF8-5	5.6	4.19	54.3	13.9	37.2	52.8	4.1	0.6	15.0	10.2
RF8-6	5.83	4.28	73.7	17.2	50.6	70.4	10.5	1.1	21.5	12.5
RF8-7	4.83	4.38	38.7	8.7	24.3	35.7	2.8	0.2	12.3	8.3
RF9-1	-	-	-	-	-	-	-	-	-	-
RF9-2	5.34	3.75	577.6	74.6	239.1	546.0	32.4	12.5	149.2	54.8
RF9-3	4.16	3.82	591.8	51.1	205.7	534.2	31.6	11.7	156.0	52.3
RF9-4	2.98	3.26	1613.2	204.9	905.1	1528.4	181.9	35.8	421.1	155.0
RF9-5	6.94	3.66	843.4	75.7	347.7	808.8	69.9	20.4	210.0	75.4
RF9-6	3.79	3.8	585.6	41.4	207.1	551.0	35.5	13.1	162.1	59.4
RF9-7	4.27	3.46	994.9	78.9	475.1	849.4	92.5	21.9	263.0	96.5

[a]below detection limit

sample name	HCHO µM	H2O2 µM	S(IV) µM	Fe ug/l	Mn ug/l	acetate µN
RF2-1						65.5
RF2-2	3.4	87.2	0.4[a]			0.0
RF2-3	2.5	44.0	0.4[a]			
RF2-4	3.0	77.4	0.4[a]	24.2	1.0	0.0
RF2-5	-	-	-	-	-	-
RF2-6	2.2	49.9	0.4[a]	13.6	0.6	
RF2-7	5.3	62.3	0.4[a]	12.5	0.4	38.1
RF3-1	6.5	145.0	1.2	56.4	2.1	51.9
RF3-2	7.4	171.7	2.2	110.1	3.2	23.8
RF3-3	4.9	100.1	1.2			
RF3-4		94.8	0.4[a]			20.1
RF3-5		96.6	1.0			
RF3-6			0.9			
RF3-7	4.7	96.8	1.1	28.3	1.1	32.6
RF4-1		283.2	1.2	46.7	1.4	28.7
RF4-2	8.5	257.2	0.4[a]	29.1	0.6	0.0
RF4-3	3.2	107.6	0.4[a]			
RF4-4	3.6	109.1	0.4[a]			
RF4-5	2.9	86.5	0.4[a]			
RF4-6	3.7	108.8	0.4[a]	5.8[a]	0.2[a]	
RF4-7	4.8	104.9	0.4[a]			
RF5-1		269.8	3.7	15.0	0.4	
RF5-2		196.2				
RF5-3		168.8	1.7			
RF5-4		163.5		5.8[a]	0.2[a]	
RF5-5	-	-	-	-	-	-
RF5-6	-	-	-	-	-	-
RF5-7	-	-	-	-	-	-

[a]below detection limit

If no value is reported, sample was not analyzed

sample name	HCHO µM	H2O2 µM	S(IV) µM	Fe ug/l	Mn ug/l	acetate µN
RF6-1	2.3	42.4	0.4[a]	5.8[a]	0.2[a]	
RF6-2	-	-	-	-	-	-
RF6-3						
RF6-4						
RF6-5		70.8	0.4[a]			
RF6-6	3.6	64.7	0.4[a]	5.8[a]	0.2[a]	
RF6-7						
RF7-1	8.0	103.3	1.6	25.2	0.6	39.3
RF7-2	8.7	107.8	1.6	15.5	0.2[a]	0.1
RF7-3	3.6	50.1	0.4[a]	5.8[a]	0.2[a]	0.2
RF7-4	3.3	45.5	0.4[a]			
RF7-5	3.8	37.8	0.4[a]	5.8[a]	0.2[a]	0.2
RF7-6	3.7	38.2	0.4[a]			
RF7-7	3.6	53.1	0.4[a]	5.8[a]	0.2[a]	0.0
RF8-1						
RF8-2		154.9				
RF8-3	5.3	112.1	1.0	16.7	0.2[a]	
RF8-4		107.7				0.1
RF8-5	4.3	72.7	0.4[a]			
RF8-6		95.1				
RF8-7	3.8	53.2	0.4[a]	5.8[a]	0.2[a]	2.8
RF9-1	-	-	-	-	-	-
RF9-2	6.2	125.0	1.4	53.3	1.8	
RF9-3		131.5				0.1
RF9-4		221.1	3.3			7.4
RF9-5	5.5	156.9	1.7	85.9	2.7	0.1
RF9-6		109.6				0.1
RF9-7	7.9	186.0	2.1	62.5	2.3	1.2

[a]below detection limit

If no value is reported, sample was not analyzed

sample name	Chloride µN	Nitrite µN	Nitrate µN	Sulfate µN	Sodium µN	Ammonium µN	Potassium µN	Magnesium µN	Calcium µN	acetate µN
RF2-BLKI					-0.5	0.4	-0.6	6.6	7.5	
RF2-BLKB	7.2		0.3		-0.3	-0.3	-0.5	6.3	6.9	-0.6
RF2-DI					-0.6	-0.4	-0.4	6.2	6.8	n/a
RF3-BLKI					-0.7	-0.1	-0.5	6.3	6.7	-0.5
RF3-BLKB					-0.7	-0.3	-0.4	6.5	7.8	
RF3-DI					-0.7	-0.4	-0.6	6.2	6.7	n/a
RF4-BLKI					-0.7	0.2	-0.5	6.2	7.2	-0.2
RF4-BLKB	7.3				-0.2	-0.4	-0.4	6.7	7.2	-0.6
RF4-DI					-0.7	-0.4		6.3	6.9	n/a
RF5-BLKI			1.0		-0.3	-0.2	-0.2	6.5	7.0	
RF5-BLKB	8.9		3.9		2.7	-1.4		6.9	6.7	
RF5-DI					-0.4	-1.6		6.9	7.0	n/a
RF6-BLKI	7.9				-0.1	-1.1	-0.1	7.2	6.5	
RF6-BLKB					-0.5	-1.4	-0.3	7.0	6.3	
RF6-DI					-0.6	-1.4	-0.2	6.3	6.4	n/a
RF7-BLKI	6.5				-0.4	-1.4	-0.1	10.0	6.7	
RF7-BLKB	7.7				-0.2	-1.2	-0.1	7.0	7.8	
RF7-DI	6.3				-0.3		-0.3	6.5	6.0	n/a
RF8-BLKI				0.3	0.8	-2.2	-0.5	6.8	7.5	
RF8-BLKB								6.5	7.3	
RF8-DI					1.1	-2.2	-0.6	6.3	7.1	n/a
RF9-BLKI		-0.2			1.0	-2.0		6.0	6.3	
RF9-BLKB					1.0	-2.1	-0.7	6.1	6.1	0.5
RF9-DI					0.8	-2.0	-0.7	5.9	6.8	n/a

If no value is reported, blank was below IC peak detection limit

sample name	HCHO µN	H2O2 µN	S(IV) µN	Fe µN	Mn µN
RF2-BLKI	0.4	-0.1	0.2	9.0	0.1
RF2-BLKB	0.7	-0.2	0.4	1.7	0.0
RF2-DI	0.7	-0.2	0.2	5.4	0.1
RF3-BLKI	0.4	-0.3	0.5	3.4	0.1
RF3-BLKB	0.5	-0.4	0.5	n/a	n/a
RF3-DI	0.6	-0.4	0.4	3.4	1.3
RF4-BLKI	0.6	-0.1	0.6	9.3	0.1
RF4-BLKB	0.6	-0.3	0.6	7.8	0.1
RF4-DI	0.6	-0.3	0.5	8.6	0.1
RF5-BLKI	0.3	-0.2	0.3	6.2	0.1
RF5-BLKB	0.3	-0.3	0.3	6.2	0.6
RF5-DI	0.2	-0.1	0.3	6.2	0.3
RF6-BLKI	0.5	0.5	0.3	2.5	0.0
RF6-BLKB	0.2	0.4	0.2	7.3	0.1
RF6-DI	0.3	0.4	0.5	4.9	0.1
RF7-BLKI	0.2	0.6	0.4	2.4	0.0
RF7-BLKB	0.4	0.4	0.3	2.0	0.0
RF7-DI	0.4	0.6	0.7	2.2	0.0
RF8-BLKI	0.8	0.5	0.7	3.5	0.0
RF8-BLKB	0.5	0.5	0.6	8.5	0.1
RF8-DI	n/a	1.0	0.7	6.0	0.1
RF9-BLKI	0.3	0.5	0.7	5.3	0.0
RF9-BLKB	0.5	0.5	0.8	2.4	0.0
RF9-DI	0.5	0.5	0.8	3.8	0.0